DESIGN OF LOW-DIMENSIONAL MATERIALS FOR ENERGY STORAGE, COMPUTING, AND CATALYSIS BASED ON ELECTRONIC STRUCTURE CONSIDERATIONS

A Dissertation

by

ABHISHEK PARIJA

Submitted to the Office of Graduate and Professional Studies of
Texas A&M University
in partial fulfillment of the requirements for the degree of

DOCTOR OF PHILOSOPHY

Chair of Committee,	Sarbajit Banerjee
Co-Chair of Committee,	James D. Batteas
Committee Members,	Timothy Hughbanks
	Xiaofeng Qian
Head of Department,	Simon North

August 2019

Major Subject: Chemistry

ABSTRACT

The known crystal structures of solids often correspond to the most thermodynamically stable arrangements of atoms. Yet, oftentimes there exist a richly diverse set of alternative structural arrangements that lie at only slightly higher energies and can be stabilized under specific constraints (temperature, pressure, alloying, point defects). Such metastable phase space holds tremendous opportunities for accessing non-equilibrium structural motifs and distinctive chemical bonding, and ultimately for the realization of novel function.

In the first section of this dissertation, we explore challenges with the prediction, stabilization, and utilization of metastable polymorphs of V_2O_5. Specifically, we highlight the tunability of electronic structure, the potential richness of bonding motifs, and their implications for functional properties with a focus on their ability to serve as intercalation hosts for monovalent and multivalent cations. We have examined five metastable phases (ζ-, γ'-, ρ'-, ε'-, δ') of V_2O_5, which offer some specific advantages with respect to thermodynamically stable α-V_2O_5 in terms of a higher chemical potential difference (giving rise to a larger open-circuit voltage), providing access to "frustrated" oxygen coordination environments (underpinning low barriers for ion migration), and mitigating polaronic diffusion. We demonstrate that a wide diversity of cation diffusion pathways can be accessed within 1D tunnel-structured and 2D layered metastable polymorphs by alteration of the cross-linking of layers, stacking sequence of layers, and the layer-thickness. The ζ-V_2O_5 polymorph predicted to be an excellent insertion host for multivalent cations has indeed been experimentally realized and is at this time the best-in-

class cathode material for Mg batteries in terms of showing an unparalleled combination of high voltage (1.65 V *vs.* Mg), high capacity (100 mAh/g), and excellent cyclability (>100 cycles).

In the second section of this dissertation, we examine a 1D tunnel-structured β′-$Cu_xV_2O_5$ phase, which exhibits a metal—insulator transition that is strongly dependent on the copper stoichiometry, *x*. Density functional theory (DFT) calculations, photoemission spectroscopy, and single crystal diffraction have been used to probe the mechanistic underpinnings of the metal-insulator transition. We demonstrate the melting of this polaronic state as a result of a subtle rearrangement in the site occupancies and atom positions of copper ions results in the delocalization of the electrons in the charge ordered network, ultimately manifesting in metallic behavior. The switching behavior observed in individual nanowires of β'-$Cu_xV_2O_5$ has parallels to the spiking behavior of neurons, and given the highly energy efficient electronic phase transition underpinned by preservation of the structural framework, is a potential vector for neuromorphic computing.

Water splitting, the sum of water oxidation and hydrogen evolution half-reactions, remains a formidable challenge since it requires the concerted transfer of four electrons and four protons. The 2H polymorph of MoS_2, a semiconducting transition metal dichalcogenide, has gained prominence as a catalyst for the hydrogen evolution reaction (HER) but requires a much greater overpotential as compared to Pt. Specifically, the edges of MoS_2 nanostructures are known to be the active sites for hydrogen evolution reaction. However, modification of edge sites to reduce the enthalpy of hydrogen adsorption has been stymied by the absence of a precise understanding of the atomistic and electronic

structure of active sites. In the third section of this dissertation, first-principles DFT calculations along with element-specific X-ray absorption spectroscopy and imaging have been used to probe edge electronic structure, which has further been correlated to catalytic performance. Modeling of excited state spectra allows for assignment of X-ray absorption features to specific structural and bonding motifs. In addition, the final section demonstrates that the incorporation of Se-dopants provides a powerful means to modulate edge electronic structure and reactivity. The role of Se atoms is to increase the valance band maximum (VBM) for facile O_2 evolution and decrease the conduction band minimum (CBM) for facile H_2 evolution.

DEDICATION

There are many people who have inspired and guided me toward my success throughout my Ph.D. life and journey in chemistry at Texas A&M University. This dissertation is foremost dedicated to my loving wife Sheetal Digari. This dissertation is also dedicated to my father, mother, and all my family members. Without their encouraging love and support, I could not have completed this Ph.D. journey.

ACKNOWLEDGEMENTS

First, I would like to thank my advisor, Prof. Sarbajit Banerjee, for the years of guidance, mentorship, and support of my Ph.D. research. I would also like to acknowledge Dr. David Prendergast for his immense support in the field of theoretical chemistry which contributed in the further development of my research and the completion of the dissertation.

I would also like acknowledge my co-advisor Prof. James D. Batteas, and committee members Prof. Timothy Hughbanks and Prof. Xiaofeng Qian for their support and time towards me and my dissertation.

Thanks also goes to friends, colleagues, department faculty, and staff for making my time at Texas A&M University a great experience. Finally, thanks all the past and present Banerjee Group members for their support and friendship through my graduate career.

CONTRIBUTORS AND FUNDING SOURCES

Contributors

The work in this dissertation was guided by a dissertation committee comprised of Professor Sarbajit Banerjee (advisor), Professor James D. Batteas (co-advisor), Professor Timothy Hughbanks of the Department of Chemistry and Professor Xiaofeng Qian of the Department of Materials Science and Engineering.

I acknowledge Texas A&M Supercomputing Facility and Molecular Foundry at Lawrence Berkeley National Laboratory for computational resources. DFT simulations were performed as part of a User Project with David Prendergast at The Molecular Foundry (TMF), Lawrence Berkeley National Laboratory. I also acknowledge Dr. Eli Rotenberg, Dr. Sirine Fakra, and Dr. David Shapiro for their guidance and support in performing various X-ray techniques at Advanced Light Source.

Some of the samples in Chapter V were prepared by Zhuotong Liu in collaboration with Prof. James D. Batteas. I also acknowledge Justin Andrews, Joseph Handy, Dr. Junsang Cho, and Theodore Alivio for their support in performing some of the experiments and characterization of the samples.

Funding Sources

This work in this dissertation was supported by National Priorities Research Program award (NPRP9-160-2-088) from the Qatar National Research Fund, Molecular Foundry-Advanced Light Source (ALS) doctoral fellowship, and National Science Foundation.

TABLE OF CONTENTS

LIST OF FIGURES

Page

LIST OF TABLES

Page

CHAPTER I

INTRODUCTION AND MOTIVATION: MATERIALS DESIGN BASED ON ELECTRONIC STRUCTURE CONSIDERATION*

I.1. Traversing energy landscapes away from equilibrium: strategies for accessing and utilizing metastable phase space

The design of new compounds with properties tailored to exhibit specific function is a grand challenge in the physical sciences but is greatly hindered by the immense span of the terra incognita, spanning ternary, quaternary, and more complex combinations across the periodic table that remain almost entirely unexplored. Limiting the search for specific function to current crystallographic databases essentially corresponds to sampling of a sparse and often fairly random set of possibilities across multidimensional configurational landscapes and not surprisingly has been of limited utility. One alternative involves examining hypothetical compounds; however, predicting the structure of a crystalline compound given just its composition continues to be a formidable challenge that has considerably limited the scope of computationally aided materials design.[1–3] Increasingly efficient treatments of electron densities and energies in density functional theory (DFT) have enabled the accurate prediction of a variety of structure-dependent properties for periodic solids; however, when the structure of a compound under a given set of conditions is not known, the a priori prediction of its properties becomes rather

difficult. Approaches for crystal structural prediction from first-principles tend to emphasize searching for the minimum energy structural arrangement of atoms, which while useful, neglect the considerable range of new functionality potentially accessible within metastable polymorphs, the identification of energetically proximate bistable wells whose reversible transformations can allow for switching of properties, and the recognition of specific structural motifs that could underpin specific functionality. From a fundamental perspective, the search for lowest energy structures often constrains ideas of chemical bonding to equilibrium forms.[4–6] Indeed, constructs such as formal oxidation states, coordination preferences, and the extent of covalency/ionicity constitute the fundamental tenets of chemistry and are often used to rationalize structure and reactivity. However, much of the conventional chemical intuition on these matters tends to be derived from the behavior of compounds at equilibrium. Metastable compounds in close proximity to thermodynamic equilibria can manifest starkly different behavior from their equilibrium counterparts and thereby provide access to a diversity of atomic arrangements and chemical bonding and function much richer than accessible when considering equilibrium configurations alone.[4,7–10] Such structures are often characterized by electronic structure peculiarities, closely coupled electron and lattice degrees of freedom, and magnetic frustration, which are a direct result of the stabilization of unusual oxidation states, multicenter bonding, and topologically enforced coordination environments; these characteristics, in turn, underpin the manifestation of unusual physical phenomena and reactivity. In **Chapters I-III**, we examine strategies for exploring metastable phase space

with an emphasis on recent progress in expanding the available repertoire of metastable phases of V_2O_5.

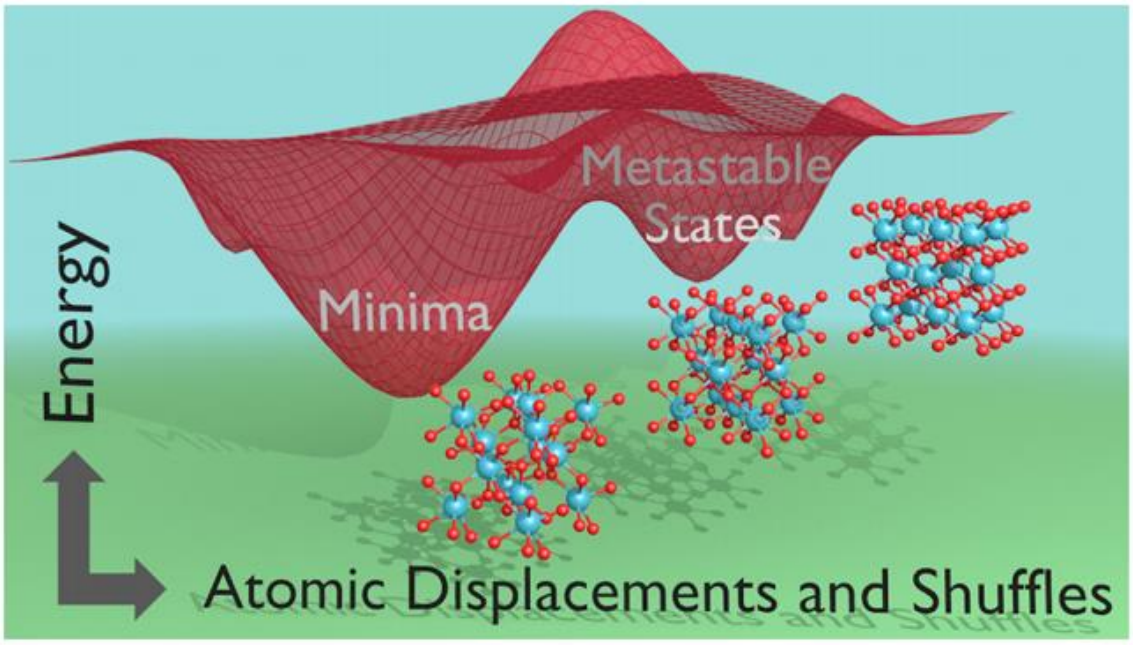

Figure I. 1. Schematic illustration of a "smooth" energy landscape with distinctly separated wells corresponding to the thermodynamically stable phase and two metastable polymorphs. Several polymorphs of HfO_2 (a VO_2 analogue) are depicted in the sketch; the monoclinic phase represents the thermodynamic minimum, whereas tetragonal and cubic polymorphs are accessible at temperatures of ca. 1700 and ca. 2200 °C, respectively.

Metastable compounds that represent local minima on the energy landscape have specific features that render them higher in energy as compared with the global minimum (**Figure I. 1**). Such features span the gamut from unfavorable "frustrated" coordination geometries to strained bonding of structural units (e.g., arising from the rigidity of polyanionic units) and elements of electron correlation and magnetic frustration. Despite such intrinsic instabilities, their position on the energy landscapes often renders them isolable and even "bottle-able" when (a) the path and angle of descent in the

multidimensional energy landscape are controlled during synthesis to deposit the material in a shallow metastable well from which it cannot readily be dislodged or (b) upon perturbation of thermodynamically stable structures along specific coordinates such as through the application of pressure, or alternately, chemical pressure/strain induced by incorporating dopants.

Metastable phases characterized by unusual bonding motifs can often be deployed to realize new functionality. Diamond presents an iconic example of a metastable phase and is a high pressure metastable allotrope of carbon that can nonetheless be kinetically trapped and stabilized under ambient temperature and pressure conditions; its covalent sp^3-bonded network yields remarkable hardness that finds a wide variety of industrial applications for drilling and cutting of other materials.[11,12] In a similar vein, whereas the 2H phase of MoS_2 is the thermodynamically stable phase in the bulk, a metallic 1T phase is stabilized as a result of the decreased formal oxidation state of molybdenum centers upon Li-ion intercalation and shows vastly improved activity as an electrocatalyst for the hydrogen evolution reaction.[13−15] A trigonal prismatic [MoS_6] coordination geometry is preferentially adopted when the Mo center has a $3d^2$ electronic configuration, whereas the octahedral [MoS_6] coordination geometry is stabilized with a $3d^3$ configuration. The remarkable performance of olivine Li_xFePO_4 as a cathode material at high rates was initially puzzling given the poor miscibility of Li-rich and Li-poor Li_xFePO_4 phases until the discovery that for small particle sizes the energy dissipative nucleation and growth of the Li-rich phase is circumvented by instead stabilizing a metastable solid-solution phase that continuously incorporates lithium ions; solid-solution formation circumventing phase

segregation has indeed been predicted to be fairly generalizable to a variety of cathode materials below a critical size.[16,17] The stabilization of metastable austenitic phases is furthermore well known in ferrous metallurgy, wherein phase transformations to thermodynamically stable phases provide a means of energy dissipation and toughening upon the application of mechanical strain.[18,19]

Metastable compounds have thus far typically been discovered through a combination of serendipity and ad hoc exploratory synthesis.[20,21] Hence, crucially missing is the fundamental understanding of which metastable materials can be successfully synthesized, design rules for stabilizing such polymorphs, mapping of transformation pathways between polymorphs (toward or further away from equilibrium), and an understanding of how their specific structural motifs and potential transformations can be harnessed to realize novel function.[22–24] We start by reviewing some fundamental governing physical principles and highlighting some illustrative examples. Next, through the specific case studies of V_2O_5 and MoS_2, we demonstrate synthetic strategies, tunability of electronic structure, and functional implications of stabilizing such compounds.

I.2. Predicting viable metastable compounds and their transformations

Structure Prediction and Identification of Viable Polymorphs

In light of the vast configurational possibilities for stabilizing different structural arrangements given a specific composition, it is important to develop design rules for predicting structure and exploring energy landscapes to a priori identify viable metastable frameworks for stabilization. Such an approach is imperative to facilitate initial screening for functionality using first-principles calculations as well as to guide synthetic

prioritization. As a notable example of evolutionary algorithm approaches, Zurek and coworkers have developed XtalOpt,[25] which coupled to DFT calculations has been used to successfully predict a variety of metastable phases stabilized under constraints such as high pressure. For instance, this approach has recently been used to predict the structure of PH_2 phases found to be superconducting at high pressures[26] as well as to predict the existence and manifestation of superconductivity within a metastable *I4/mmm*-$BaGe_3$ phase.[27] The superconductivity of the latter phase has indeed now been experimentally verified, which represents a major milestone for first principles structure prediction.[28] In another approach,[29] Stevanović performed DFT calculations on a large set of random superlattices of MgO, ZnO, and SnO_2 crystal systems to successfully predict the probability of the occurrence of a given structure, which, in turn, is reflective of the accessible metastable polymorphs in these systems. The development of materials property databases powered by high-throughput first-principles calculations has provided additional opportunities for the use of machine learning to extract correlative patterns across large data sets.[30–33] One notable insight from these studies suggests that the most viable metastable polymorphs are those that represent the energetically lowest polymorphs under a specific set of constraints (e.g., temperature, chemical potential, surface confinement, tensile or compressive stress); rapid quenching of these structures upon the removal of the constraint can leave the metastable phases trapped within shallow valleys.[34,35] From a practical perspective, if constraints under which a considered phase is the energetic minimum cannot be identified, then devising a synthetic strategy becomes rather challenging.

Explorations of Transformation Pathways

The pathways along which metastable polymorphs traverse to the thermodynamic minimum or to other polymorphs determine the energetic barriers and thus their accessibility and stability. Energetically proximate polymorphs are of particular interest as a result of their being switchable upon the application and removal of external stimuli. For instance, the metal—insulator transitions of VO_2 and NbO_2 are accompanied by monoclinic to tetragonal and undistorted rutile to body-centered distorted rutile transitions, respectively.[6,36,37] Energetic proximity is, of course, a necessary but not sufficient criterion for obtaining bistable systems; the energy barriers for transitions between two phases are fundamentally a function of the pathway linking the two polymorphs. The barriers between the insulating and metallic phases in these materials, reflective of varying structural and electronic contributions, are vastly different, as reflected in transition temperatures of 67 and 807 °C in VO_2 and NbO_2, respectively. The determination of energy landscapes and transformation paths is thus critical to accessing metastable polymorphs. While exceedingly computationally expensive given the multiple degrees of freedom, calculations of energy landscapes as a function of structural degrees of freedom, taking into account potential constraints such as templates, strain, finite size, or surface confinement, can provide important inputs to synthetic strategies.

The generalized solid-state nudged elastic band formalism is one of the most commonly used algorithms to successfully predict minimal energy transformations; it allows for the computation of the structure and energetics of transition states and thereby allows for evaluation of the energetic barriers and kinetics of polymorphic

transformations.[38–40] However, a primary drawback of NEB-based approaches is the requirement of an a priori assumption with regards to the initial and final states of the transformation. Recently, Stevanović and coworkers[24] have developed a structure mapping algorithm, which uses an optimal mapping approach that is diffusionless in nature and minimizes the dissociation of chemical bonds. In another example, Arroyave and coworkers have developed a mathematical framework for the rapid exploration of energy landscapes in phase-transforming materials, allowing for the identification of metastable intermediates based on the implementation of novel multidimensional string methods to identify transformation paths between arbitrary minima in the energy landscape.[41] It is anticipated that the development of more efficient algorithms and a greater deployment of high-performance computing resources will substantially increase the understanding of complete energy landscapes and allow for insights into how transformation pathways can be altered. The role of defects, strain, and dopants on transformation pathways remain underexplored, primarily owing to the computational expense of calculating landscapes for large supercells across multiple configurational degrees of freedom.

I.3. Strategies for the synthesis of metastable compounds

Solution Phase Synthesis and Topochemical Methods

Potential energy landscapes such as plotted in **Figure I. 1** are essentially representations of the free energy of a system plotted as a function of configurational degrees of freedom. As a system relaxes toward equilibrium, from a high-energy state, it explores the landscape in search of a means to most efficiently dissipate the excess free

energy. Conventional ceramic and metallurgical processing routes provide an excess of energy, and thus the material is usually able to efficiently explore the path toward equilibrium without being trapped in metastable states. In contrast, solution-phase synthesis routes have the potential to carefully "deposit" the material in a local minimum that can effectively "trap" the system within forms exhibiting unusual chemical bonding motifs. Such local "traps" can further be modulated through the inclusion of defects, impurities, disorder, and interfaces, all of which serve to direct the trajectory of a material down its descent from a higher energy state.

Topochemical modification routes represent a particularly intriguing approach wherein leaching of specific anionic or cationic structural components provides a means of stabilizing open framework structures, which, in turn, can again be intercalated with other cations or anions such that the final structure represents the atomistic arrangements defined by the initial template.[45,46] Performing these reactions at low temperatures and with reactivities of leaching agents matched to ensure that slow diffusion assures preservation of the metastable frameworks by limiting the amount of energy available to facilitate recrystallization to the thermodynamic form. As a recent elegant example of this approach, Powell and coworkers[42] have shown that upon starting with roxbyite-type $Cu_{2-x}S$ solution-mediated cation exchange yields metastable wurtzite polymorphs of CoS and MnS (**Figure I. 2A**). As another example, the topochemical deintercalation of Ca-ions from $CaGe_2$ has allowed for stabilization of germanane, a 2D analogue of graphene.[47] Indeed, Goldberger and colleagues have recently elaborated this strategy to stabilize 1T, 2H, and 6R germanane polytypes by topochemical deintercalation of cations from 1T

$EuGe_2$, 2H α-$CaGe_2$, and 6R β-$CaGe_2$ Zintl phases.[48] The reaction of GdOCl nanocrystals with XeF_2 has allowed for stabilization of a metastable GdF_3 polymorph, providing an example of topochemical alteration of the anion sublattice.[49] In a subsequent section, we discuss at some length the myriad V_2O_5 polymorphs that can be accessed using topochemical methods.

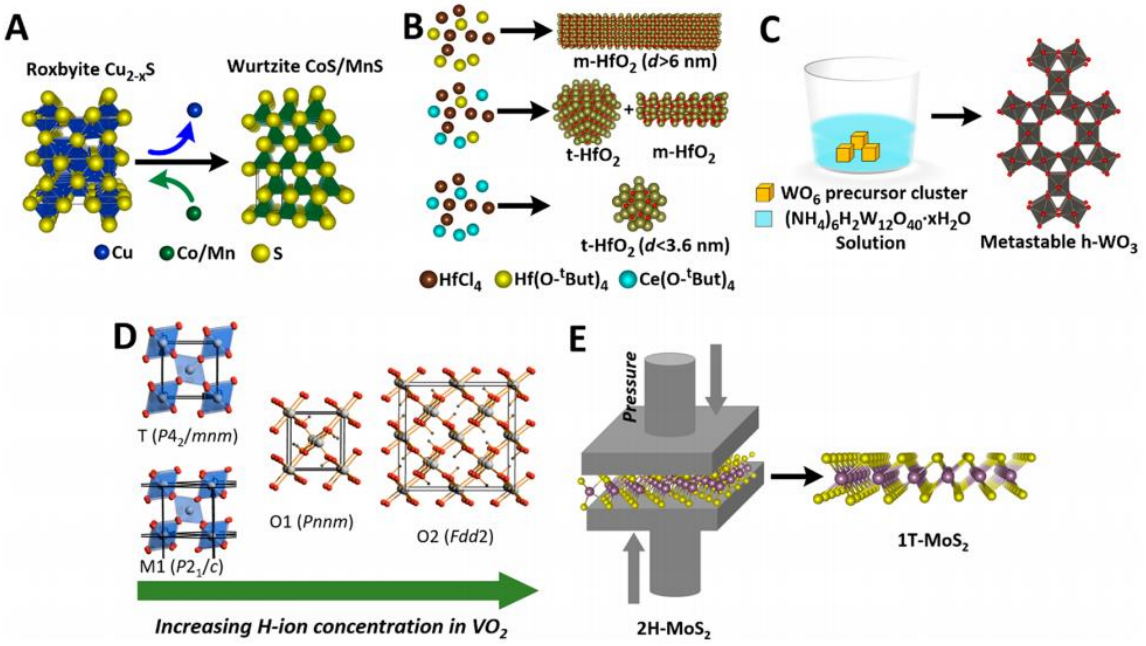

Figure I. 2. Schematic illustration of strategies for the stabilization of metastable polymorphs: (A) Topochemical modification: Roxbyite-$Cu_{2-x}S$ is topochemically converted to the metastable wurtzite polymorphs of CoS and MnS via solution-mediated cation exchange.[42] (B) Dimensional confinement: The metastable tetragonal phase is stabilized below a critical size of ca. 3.6 nm. (C) Templated growth: The metastable hexagonal WO_3 phase is stabilized by templated growth of WO_6 nuclei in a precursor solution of $(NH_4)_6H_2W_{12}O_{40}\cdot xH_2O$.[43] (D) Dopant incorporation: increasing interstitial doping of hydrogen in M1 ($P2_1/c$) phase of VO_2 stabilizes the metastable O1 (*Pnnm*) and O2 (*Fdd2*) phases, respectively. Reprinted with permission from ref 67. Copyright 2014 American Chemical Society. (E) Pressure: A pressure-induced structural distortion accompanied by a semiconducting—metallic electronic transition is achieved during the conversion of 2H-MoS_2 to 1T-MoS_2.[44]

.

Finite Size Effects on Phase Stability

Surfaces and dimensional confinement provide the second primary strategy for the synthesis of metastable polymorphs. At nanoscale dimensions, surface free-energy (as well as strain energy) terms can be opposite in sign to bulk free-energy descriptors and enable the stabilization of unusual structural motifs under conditions that represent constrained equilibrium rather than kinetic trapping.4,8 The size dependence of free energy can be written as

$$G^0 = G_{bulk} + \sum_i \gamma_i A_i \ \ldots \text{(I.1)}$$

where G_{bulk} is the bulk free energy and γ and A are the surface energy and surface area of a given facet i.[4] If there are two polymorphs a and b, for which $G_a < G_b$ but $\gamma_b < \gamma_a$, then the differences in surface energy can bring about a crossover of thermodynamic phase stabilities below a certain critical size. For example, the rutile phase of TiO_2, with $P4_2/mnm$ symmetry, become more stable than the anatase phase, with $I4_1/amd$ symmetry, at a critical diameter of ca. 14 nm.[50] More than 50 years ago, Garvie discovered that below a grain size of 30 nm ZrO_2 can be stabilized in the tetragonal phase at room temperature. This remarkable stabilization originates from the surface energy contribution outweighing the bulk free energy because the tetragonal phase exposes considerably lower energy surface facets.[51,52] A full account of the different energy terms involved in the phase transformation is warranted to understand the pronounced size dependence of phase stability; the relevant terms will be contrasted in a subsequent section to highlight the differences between HfO_2 and ZrO_2, which has made stabilization of high-temperature polymorphs of the former a much more challenging endeavor.[53,54] In contrast with ZrO_2,

the critical size for stabilization of tetragonal HfO_2 is found to be almost an order of magnitude lower, ca. 3.6 nm, as shown in **Figure I. 2B.**

Templated Growth

A third approach involves nucleation and growth of materials from specific epitaxially matched templates that favor the growth of a metastable polymorph over the thermodynamically stable phase. The growth of metastable phases under these conditions reflects the strain-induced crossover of thermodynamic stability in specific systems and is an interesting corollary to pressure-induced transitions. Classical examples include stabilization of α-Sn and α-Sn:Ge alloys using molecular beam epitaxy.[55] Similarly, MgS and MnS have been grown in the metastable zinc-blende phase by molecular beam epitaxy onto GaAs (100) substrates.[56] An insulating metastable monoclinic M2 phase is stabilized under strain for VO_2 thin films and individual nanorods;[57] indeed, a solid-state "triple point" has been identified wherein the M2 phase as well as the insulating monoclinic M1 phase (the thermodynamic minimum) and a rutile phase can coexist along a strain—temperature phase diagram.[58] Remarkably, similar strain effects have been observed upon the incorporation of W dopants within otherwise freestanding nanorods reflective in large measure of the equivalence of chemical strain; slivers of M2 domains spanning only a few unit cells are stabilized at the interface between M1 and rutile phases and minimize the strain mismatch between these polymorphs.[59,60]

As a variation on this theme, Iversen has followed the stabilization of various polymorphs of WO_3 (**Figure I. 2C**), utilizing in situ pair distribution function methods, and has demonstrated the remarkable preservation of structural motifs from molecular

precursors to extended solids, reflecting a close structural relationship between the precursors and incipient nuclei that strongly alters the relative phase stabilities from the bulk phase diagram.[43] Such an idea of seeded growth wherein the final polymorph shows structural homologies to the precursor has further been noted for MnO_2 nanocrystals grown under hydrothermal conditions.[61]

Dopant Effects on Phase Diagrams

The inclusion of extrinsic dopants or variation of the concentration of intrinsic point defects can profoundly alter phase diagrams. The stabilization of cubic and tetragonal ZrO_2 by aliovalent doping is well established and is a result of the altered local coordination environments,[62] oxidation states, and size of the dopant atoms that are oftentimes better accommodated in a higher energy metastable polymorph as compared with the (often close-packed) phase that represents the thermodynamic minimum. Ramprasad has recently presented a detailed computational exploration of dopants that can potentially stabilize the ferroelectric orthorhombic phases of HfO_2.[63,64] Such studies are illustrative of approaches for the rational design of doping schemes that are thus far only sparsely explored.

An intriguing set of ideas that has attracted recent attention is the use of diffusive dopants to reversibly alter phase stabilities, providing a means to access metastable phase space through postsynthetic modification. By coupling the diffusion of dopants to applied strain, chemical potential gradients, or voltage fields, the phase of a material can be changed "on the fly", thereby providing a powerful means of dynamically modifying phase diagrams. In recent work, voltage-driven insulator (2H)—metal (1T′) transitions

have been evinced in $MoTe_2$ upon electrostatic modulation; electrostatic doping can be induced through intercalation of Li-ions instead of direct electrical biasing of the 2D materials.[65,66] Other examples of diffusive dopants that alter phase stability are observed for hydrogen (**Figure I. 2D**) and boron interstitial dopants in VO_2; the former stabilizes an orthorhombic phase, whereas the latter stabilizes the rutile metallic phase.[67,68]

Pressure-Induced Stabilization of Metastable Phases.

The pressure applied on materials can be tuned suitably to unravel novel metastable phase space. Indeed, Nayak and coworkers, have demonstrated the conversion of the thermodynamically stable 2H-phase of MoS_2 to the 1T-phase upon the application of pressure.[44] A structural distortion, followed by an electronic transition from semiconducting to metallic state, has been observed at ca. 19 GPa (**Figure I. 2E**). Ab initio calculations reveal an increased overlap of the valence and conduction bands due to compression as the possible origin of the phase transition. In another example, Flores-Livas and researchers have been able to synthesize multiple metastable phases of phosphorus by applying pressure up to 170 GPa.[69] Several of the metastable phases showed excellent superconducting properties, entirely inaccessible in the thermodynamically stable-phase red phosporous. Applying high pressure in conjunction with moderate temperature can easily overcome the barrier to stabilize metastable polymorphs. For example, the high-pressure phase β-V_2O_5 can be synthesized by coupling temperature and pressure.[70]

I.4. Metastability and intercalation chemistry

Nonequilibrium Intercalation and Metastability in $LiFePO_4$ and MnO_2

Metastability—as a concept, recurring motif, and design tool—[73,74] is deeply intertwined in intercalation chemistry and has become increasingly important, particularly with the rise of secondary batteries exploiting intercalation phenomena. Indeed, the success of the Li-ion battery is founded on the use of materials that in their fully charged states are in fact metastable[79] or alternatively pass through metastable intermediate states, thereby circumventing immiscibility gaps and eschewing energetically costly nucleation and growth mechanisms.[16,80] More specifically, in the case of lithium cobalt oxide and related cathode materials, full cells are typically assembled using the thermodynamically stable discharged phases ($LiCoO_2$). Upon charging, metastable materials of the type $Li_{1-x}CoO_2$ are formed as x approaches unity, albeit the depth of discharge is typically limited to $x = 0.5$ to avoid oxygen evolution due to surface peroxide formation.[79,81,82] In the case of Li_xFePO_4, both end members (i.e., $FePO_4$ and $LiFePO_4$) are thermodynamically stable; however, there is severely limited Li solubility in both phases, which suggests that lithiation/deliathiation proceeds according to nucleation and growth of the fully lithiated phase growing at the expense of the delithiated phase.[83] Below a certain particle size regime, however, much higher rates are observed. The increased rates in smaller particles have been attributed to the stabilization of metastable compositions (with increased Li solubility) that bridge the miscibility gap of the thermodynamically stable end members to allow for complete solid-solution formation across the entire cycling range (i.e., $0 < x < 1$ in Li_xFePO_4).[80,84]

Perhaps more recognized is the utilization of various polymorphs of a given composition as cathode materials in attempts to vary the function while retaining composition. Indeed, this approach is ubiquitous in the exploration of novel cathode materials, particularly in the case of MnO_2, where several polymorphs such as α-MnO_2 and δ-MnO_2 are directly accessible from hydrothermal synthesis.[61,85] In other cases, metastable binary materials are stabilized via selective removal of an ionic species (e.g., stabilization of metastable λ-MnO_2 by extraction of Li from the thermodynamically stable $LiMn_2O_4$ spinel-type structure).[86,87] Indeed, such an approach provides access to a broad palette of Mn−O connectivity encompassing polymorphs with 3D (β-MnO_2, thermodynamic minimum), 2D (δ-MnO_2, spinel λ-MnO_2), and quasi-1D (hollandite α-MnO_2, ramsdellite R-MnO_2, and γ-MnO_2) crystal structures.[88] Despite the extensive use of these materials as cathode materials, no generalized approach to their discovery has been proposed in the literature.

Finally, there has recently been increased attention to moving beyond Li toward multivalent-ion batteries (Mg^{2+}, Ca^{2+}, Zn^{2+}, Al^{3+}),[73,75,89,90] each of which has distinct inherent benefits such as the storage of twice the electrons per intercalated ion, increased safety, increased crustal abundance (and thereby decreased cost and greater sustainability), and the prospect of utilizing metal anodes (a prospect precluded in the design of Li-ion batteries as a result of safety considerations with handling metallic lithium). As we have recently shown,[73] the use of metastable materials as cathodes in multivalent ion intercalation batteries can give rise to many interesting properties derived from the fact that both the "charged" oxide (MO_x, where M is a redox-active transition

metal) and the discharged phases ($M'MO_x$, where M' is an electrochemically intercalated multivalent cation) are metastable.

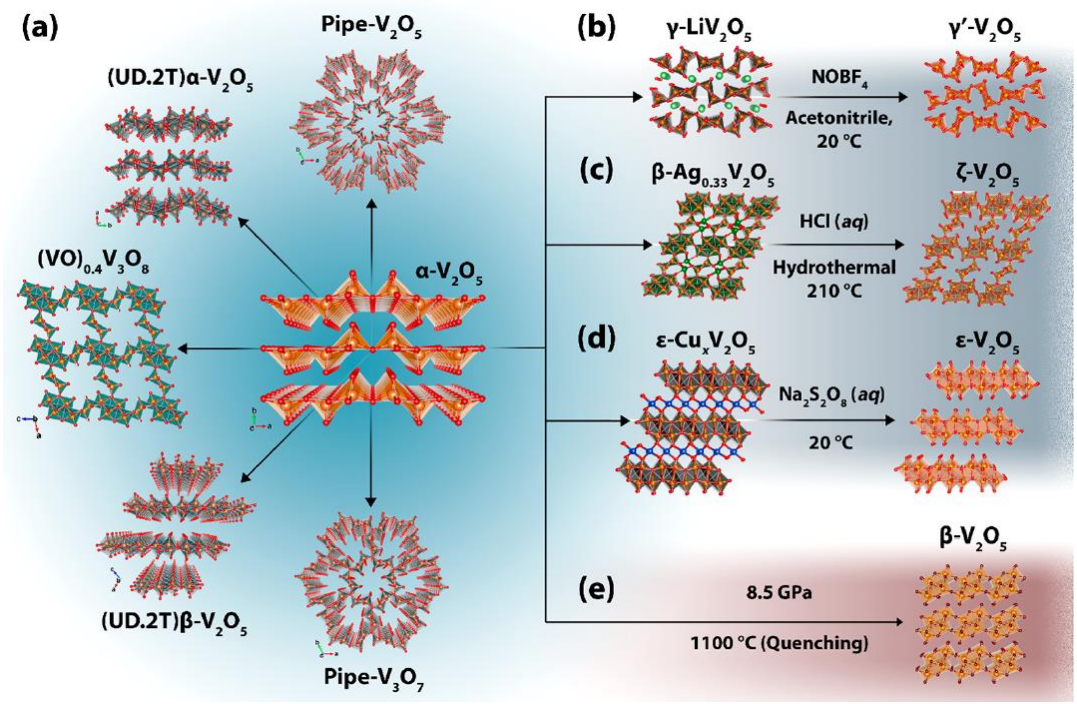

Figure I. 3. Metastable binary vanadium oxide phases depicted alongside parent ternary MxV2O5 phases. (a) Thermodynamically stable α-V_2O_5 phase is depicted at the center of the schematic. Several predicted vanadium oxide phases with starkly different vanadium−oxygen connectivity are arranged on the left in a semicircle. These phases represent synthetic targets for topochemical stabilization from previously reported ternary vanadium oxide bronzes if the vanadium—oxygen connectivity of the parent compounds can be preserved upon deintercalation. Moving counterclockwise from the top of the semicircle, these ternary bronzes are $Cs_{0.3}V_2O_5$, $Ba_{0.4}(VO)_{0.4}V_2O_5{\cdot}H_2O$, CsV_2O_5, $(H_2N(C_2H_4)_2NH_2)_{0.5}V_2O_5$, and $Cs_{0.35}V_3O_7$. (b−d) Three topochemically stabilized metastable phases of V_2O_5 (γ′-, ζ-, and ε′-) delineating synthetic parameters used for topochemical deintercalation of the inserted cations from the ternary bronzes. (e) Another metastable vanadium oxide polymorph (β-V_2O_5) is depicted. This polymorph has been stabilized through application of high pressure and temperature and is stabilized at room temperature by rapid quenching (as reported in ref 70).

Indeed, in the case of the recently studied β-$Mg_{0.33}V_2O_5$−ζ-V_2O_5 system, the entire compositional range is metastable. Recent success examining metastable compositions as

cathode materials and the structure−function relationships that arise will be discussed below with an eye toward seeking fundamental descriptors for the design and stabilization of additional cathode materials.

Metastable Vanadium Oxides as Intercalation Hosts

Metastable phase space is vast when compared with thermodynamically stable phase space, notionally encompassing different possible configurations of atoms, and therefore is difficult to explore in a systematic manner without computational guidance or chemical intuition.[34] One example of the latter approach, as observed in the case of spinel-derived λ-MnO_2, is to realize unique binary connectivity (i.e., MO_x where M = V, Cr, Mn, Fe, Ni, Co) from motifs observed in thermodynamically stable ternary phases (i.e., M″MeO_x, where M″ is a third cation—not necessarily the one that is sought to be intercalated). Such an approach is predicated on the stability of the M—O frameworks and allows for established soft-chemistry synthetic techniques to be used to remove the intercalated ions from known ternary phases to stabilize metastable binary phases. The topochemically stabilized frameworks represent kinetically trapped species that under reaction conditions are unable to recrystallize into the thermodynamically stable form; such an approach provides a considerable set of target structures for the exploration of metastability. **Figure I. 3** illustrates a broad palette of ternary $M_xV_2O_5$ and topochemically modified V_2O_5 structures either realized experimentally or examined using first-principles calculations.

The multiple available redox states ($V^{5+} \rightarrow V^{4+} \rightarrow V^{3+}$), the high oxidizing potential of the redox couples (ca. 3.8 V vs Li), and the large theoretical specific capacity

(443 mAh g^{-1} for $Li_3V_2O_5$) make V_2O_5 an exceedingly promising system from the perspective of energy-storage metrics. The large number of structural motifs and plethora of observed vanadium−oxygen connectivity and coordination observed in binary vanadium oxide materials have few parallels in other transition metals.[91] The observed structural diversity grows exponentially when moving beyond binary vanadium oxides to consider ternary vanadium oxide bronzes. The presence of intercalated cations forces the rearrangement of the vanadium oxide lattice, often resulting in unique structural motifs that are highly dependent on the identity and stoichiometry of the intercalated cation. Indeed, the intercalation of cations into V_2O_5 results in the formation of ternary $M_xV_2O_5$ (or for that matter other mixed valence $M_xV_yO_z$) materials, where the identity of "M" spans several groups of the periodic table from alkali[92–96] and alkaline metals,[97,98] to transition metals[99–101] and post-transition-metal main group cations[98] and even organic cations.[102,103] Whittingham and coworkers have exhaustively reviewed and systematically categorized the diversity of vanadium−oxygen structural connectivity, with an emphasis on open frameworks.[91] Many of these structures can potentially be fully or partially deintercalated to form metastable binary vanadium oxides with a broad range of vanadium−oxygen connectivity not observed in the thermodynamically stable layered phase of V_2O_5. These compounds suggest a powerful starting point for fundamental explorations of a "rugged" energy landscape with multiple accessible members, each with its own electronic structure and specific diffusion pathways for intercalated cations.

To date, there are six known polymorphs of V_2O_5. In addition to the thermodynamically stable α-V_2O_5 phase (**Figure I. 3a**, center),[104] there are five metastable

polymorphs of V_2O_5, including the high-pressure β-V_2O_5 phase (**Figure I. 3e**), the chimie-douce-stabilized γ′-V_2O_5 (**Figure I. 3b**),[105] the closepacked-3D high-pressure δ-V_2O_5,[106] the ε′-V_2O_5 double-layered phase closely related to the xerogel phase (**Figure I. 3d**),[71] and the tunnel-structured 1D polymorph ζ-V_2O_5 (**Figure I. 3c**).[71,73,107] Although metastable, the structure of δ-V_2O_5 is close-packed, as would be expected for a polymorph stabilized above 8.5 GPa and 1100 °C.[106] In **Chapters II** and **III**, a broader palette of potential metastable compounds notionally derived along the lines of **Figure I. 3** has been examined as potential intercalation hosts using first-principles calculations.

Crystallographic Relationships and First-Principles Evaluation of Thermodynamic and Kinetic Aspects of Intercalation

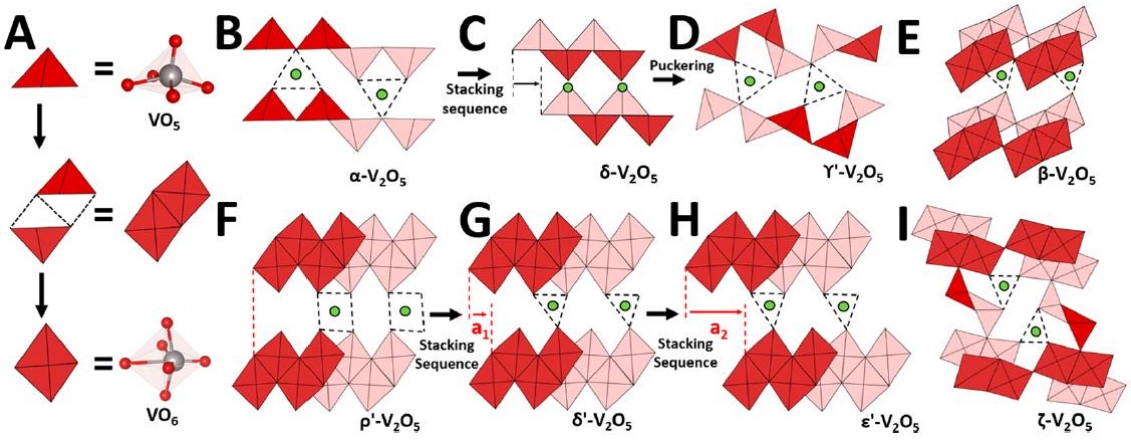

Figure I. 4. Schematic representation of crystallographic relationships between various polymorphs of V_2O_5. The fundamental building units of the V_2O_5 crystallographic system comprise [VO_5] square pyramids and distorted [VO_6] octahedral units. The gray and red spheres represent vanadium and oxygen atoms, respectively, the solid red pyramids represent [VO_5] units, and the solid red quadrilaterals represent [VO_6] units; a change in shading indicates that the units are in different planes. The polymorphs of V_2O_5 represented are (B) α-V_2O_5, (C) δ-V_2O_5, (D) γ′-V_2O_5, (E) β-V_2O_5, (F) ρ′-V_2O_5, (G) δ′-V_2O_5, (H) ε′-V_2O_5, and (I) ζ-V_2O_5.

Selecting ternary $M_xV_2O_5$ phases as initial precursor structures mitigates a primary issue with computational screening that often yields predicted structures that are not synthetically viable. Given the complexity involved in synthetic stabilization and electrochemical measurements, first-principles DFT calculations are nevertheless useful for evaluating the specific candidates derived from examining ternary vanadium oxides. In recent work, we have used such calculations to predict thermodynamic aspects such as structural parameters, lattice alteration upon intercalation, and open-circuit voltage as well as kinetic parameters such as diffusion barriers and diffusion pathways for various metastable polymorphs of V_2O_5.[74,75,92,108]

Crystallographic Relationships

α-V_2O_5 is the thermodynamic sink of the V−O phase diagram (and indeed mined as a naturally occurring ore) and is a good starting point to understand the structure of other metastable phases of V_2O_5.[109,110] It is a layered structure comprising [VO_5] pyramidal units sharing corners and edges to form 2D single-layered lamellar sheets (**Figure I. 4B**). These sheets are held together by van der Waals forces along the c direction to form a layered crystal structure with *Pmmn* symmetry.[111] **Figure I. 4** depicts the approximate crystallographic relationships between this structure and several metastable polymorphs. The metastable single-layered δ-V_2O_5 (thus labeled to distinguish it from the double-layered δ′-phase discussed below) with a space group symmetry of *Amma*,[104] can be conceptualized to be derived from topochemical deintercalation of lithium from δ-$Li_xV_2O_5$ ($0.88 < x < 1.0$).[112] The overall lamellar structures of α-V_2O_5 and δ-V_2O_5 are similar; however, the alternate sheets are shifted from each other by half a unit

cell in the *c* direction (**Figure I. 4C**). The γ′-V_2O_5 phase can be derived from δ-V_2O_5 by rotation of the two edge-shared [VO_5] pyramidal units by 90° in opposite directions along V1−O1 and V2−O2, respectively, as shown in **Figure I. 4D**. This puckering occurs only along alternate [VO_5] pairs of the lamellar sheet. As a result, the apical V−O bonds are slightly skewed along the crystallographic *b* axis, in contrast with α-V_2O_5 and δ-V_2O_5, where they all point in the same direction. In contrast, ρ′-V_2O_5, δ′-V_2O_5, and ε′-V_2O_5 comprise double-layered V_4O_{10} units sharing corners and edges, which are held together by van der Waals forces along the crystallographic c direction. Notably, these three double-layered polymorphs differ from each other in terms of stacking of the V_4O_{10} double layers along the *a* direction. The δ′-V_2O_5 and ε′-V_2O_5 polymorphs can be derived from the ρ′-V_2O_5 phase by sliding of the alternate double layers along the crystallographic *a* direction (**Figure I. 4F−H**). β-V_2O_5, a high-pressure phase with a space group symmetry of $P2_1/m$,[70] comprises two [VO_6] units that share an edge to form a double-layered unit; these units share corners in the a and *b* crystallographic direction to form a double-layered 2D sheet (**Figure I. 4E**). The structure can be conceptualized to result from the parent α-V_2O_5 phase by bringing the layers together along the *c* axis and sliding along the direction delineated by arrows in **Figure I. 4E**. The metastable phase ζ-V_2O_5 is distinct in adopting a 1D tunnel structure with a space group symmetry of *C2/m*.[74,107] It comprises three distinct vanadium centers: (a) distorted V(1)O_6 octahedra connected at edges, (b) distorted V(2)O_6 octahedra connected at corners, and (c) V(3)O_5 pentagonal square pyramids.

	OCV-Li (V)	OCV-Mg (V)	E^{hull}-V_2O_5 (meV)	E^{hull}-$Li_xV_2O_5$ (meV)	E^{hull}-$Mg_xV_2O_5$ (meV)	Li-ion diffusion barrier (eV)	Mg-ion diffusion barrier (eV)	change in oxygen coordination environment
α	3.35	2.59	0	45	118	0.11-0.16	1.15-1.23	8→3→8
γ′	3.44	2.73	6	27	50	0.18-0.15	0.71-1.16	4→3→5→3→5
ζ	3.71	3.28	24	23	–17	0.13-0.14	0.62-0.86	4→3→5→3→5
ρ′	3.74	2.86	30	38	85	0.07-0.07	0.28-0.46	6→4→6→4→6
δ′	3.59	2.80	32	53	149	0.07-0.19	0.54-1.07	4→3→5→3→5
ε′	3.72	2.92	32	47	83	0.10-0.11	0.21-0.24	4→4→4→4→4

Table I. 1. Calculated Open-Circuit Voltages (OCVs) for Li- and Mg-Ion Intercalation in Several Polymorphs of V_2O_5. Energy-above-hull (E^{hull}), which predicts the stability of the polymorphs with respect to their stable constituents in meV/atom, is also noted. An E^{hull} value of 0 meV/atom represents the polymorph that is the ground state of the system. Migration energy barriers in electron volts per unit supercell and the change in oxygen coordination environment for Li- and Mg-ions are also noted for each polymorph.

This phase can be related to the δ′-phase through several slip, condensation, and distortion processes, and indeed the reversible interconversion of Ca-intercalated frameworks β-$Ca_xV_2O_5$ to δ-$Ca_xV_2O_5$ has been experimentally realized.[113]

Calculated Thermodynamic and Kinetic Parameters

The fundamental cell voltage of a battery is derived from the difference in chemical potential between the anode and cathode selected for the cell, which, in turn, is dependent on the change in Gibbs free energy between the charged and discharged states. As such, varying the framework connectivity via selection of polymorph (by selection of metastable materials) can serve as a handle to tune the electrochemical potential of one-half of the cell and thus the voltage of the entire cell, all without changing composition.

The average open-circuit voltages for Li-ion and Mg-ion in various polymorphs of V_2O_5 calculated using DFT are contrasted for different polymorphs of V_2O_5 in **Table I. 1**.[74,75,92] The voltages are computed with respect to the bulk metal anode (body-centered Li and hexagonal close-packed Mg) in each case.[73,92,114,115] Two main inferences can be drawn from the computed voltages. First, the open-circuit voltages (OCVs) follow the same trend as the standard reduction potential in the aqueous electrochemical series (−3.04 V vs SHE for Li and −2.37 V for Mg). Second, the OCVs for the cation intercalated metastable phases of V_2O_5 are higher in comparison with α-V_2O_5. The primary origin of the higher voltages is the relative instability of the metastable polymorphs in comparison with α-V_2O_5. As shown in **Table I. 1**, metastable phases γ′-V_2O_5, ζ-V_2O_5, ρ′-V_2O_5, δ′-V_2O_5, and ε′-V_2O_5 are 6, 24, 30, 32, and 32 meV per V_2O_5 unit unstable in energy than α-V_2O_5. The intercalated phases of α-V_2O_5 are relatively more stable than intercalated phases of metastable V_2O_5. However, the difference in energy between the intercalated metastable phases and its discharged phase is higher in comparison with the same differential in energy for α-V_2O_5.

The stability of the cathode further represents an important parameter. **Table I. 1** plots the energy of decomposition (E^{hull}) for different polymorphs. A cathode material with an E^{hull} value of zero is considered to be thermodynamically stable, whereas a positive E^{hull} value suggests instability. α-V_2O_5 is considered to be the thermodynamic sink with a E^{hull} value of zero. In contrast, γ′-V_2O_5, ζ-V_2O_5, ρ′-V_2O_5, δ′-V_2O_5, and ε′-V_2O_5 are only 6, 24, 30, 32, and 32 meV higher in energy, respectively, suggesting the potential accessibility of several energetically proximate polymorphs close at room temperature.

Similarly, α-LiV_2O_5, γ-LiV_2O_5, β′-$Li_{0.66}V_2O_5$, ρ-$Li_{0.5}V_2O_5$, δ-LiV_2O_5, and ε-LiV_2O_5 are 45, 27, 23, 38, 53, and 47 meV higher in energy, suggesting their potential viability. However, α-MgV_2O_5 and δ-MgV_2O_5 are highly unstable with high Ehull values of 118 and 149 meV, suggesting that these phases are unlikely to be good intercalation hosts. Remarkably, β-$Mg_{0.33}V_2O_5$ is −17 meV more stable and γ-MgV_2O_5, ρ-$Mg_{0.5}V_2O_5$, and ε-MgV_2O_5 are only 50, 85, and 83 meV above the thermodynamic stable state, suggesting that they might be readily accessible at room temperature. In general, double-layered and tunneled-structured V_2O_5 phases appear to be much more stable as compared with single-layered V_2O_5. The migration energy barrier (E_b) is defined as the maximum energy required for an intercalant to hop between two low energy-lying intercalant positions through the transition-state geometry. To provide a perspective of the numerical values, a 60 meV change in barrier energy is enough to change the diffusivity of the intercalants by one order of magnitude. For a micrometer-sized particle to be used as a viable cathode material, diffusion barriers (except γ′-V_2O_5) is around or below 650 meV, suggesting their viability as cathode materials.

Cation Diffusion Pathways in V_2O_5 Polymorphs

Table I. 1 indicates that minor changes in coordination framework of the polymorphs can give rise to substantial changes in the diffusion barrier.[72] **Figure I. 5** illustrates the change in the local coordination environment of intercalated cations in four polymorphs of V_2O_5, namely, α-V_2O_5, γ′-V_2O_5, ζ-V_2O_5, and ρ′-V_2O_5. In α-V_2O_5, the migration of the intercalating cation occurs across the layers of staggered 1D chains of oxygen atoms along the crystallographic *b* direction. Notably, the change in coordination

environment is 8 → 3 → 8 along oxygen coordinated sites with the cation resident in a trigonal planar environment in its transition state.[74,117]

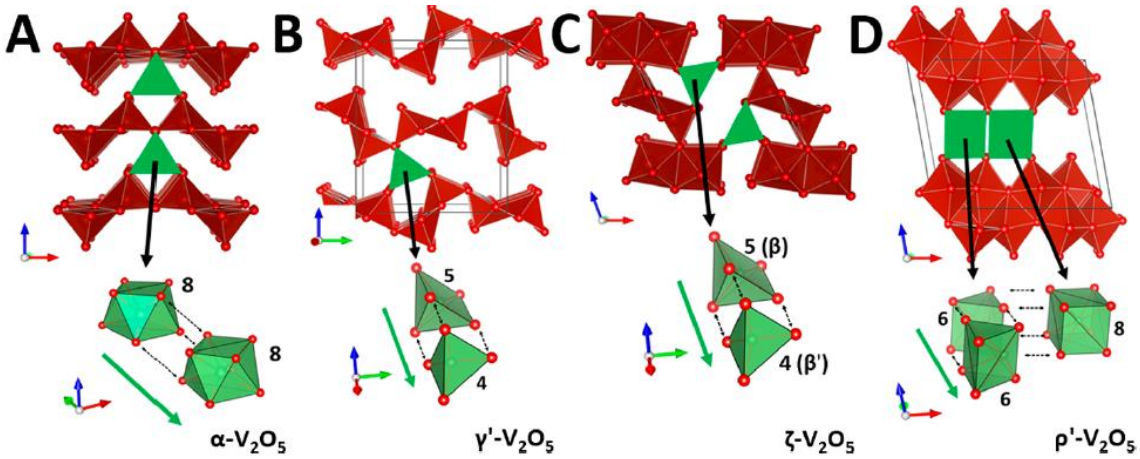

Figure I. 5. Cation-oxygen coordination environment during mono/multivalent ion diffusion in (A) thermodynamically stable phase α-V_2O_5 and metastable phases, (B) γ′-V_2O_5, (C) ζ-V_2O_5, and (D) ρ′-V_2O_5. The green arrow shows the lowest energy pathway for diffusion, and the numbers indicate the change in the coordination number during the process of diffusion. Panel (A,C) is reprinted with permission from ref 73. Copyright 2018 Elsevier. Panel (B,D) is reprinted with permission from ref 75. Copyright 2017 American Chemical Society.

The large diffusion barrier can be attributed to the large change in coordination number and suboptimal coordination environment of the cation in the spatially constrained transition state. In contrast, several of the metastable polymorphs offer much more spacious transition states, and cation diffusion is accompanied by smaller alterations of coordination number, as illustrated in **Figure I. 3** and delineated in **Table I. 1**, giving rise to substantially lower diffusion barriers. A major advantage of metastable compounds is thus the ability to access a variety of conduction pathways for intercalated ions, which can substantially alter the kinetics of diffusion.

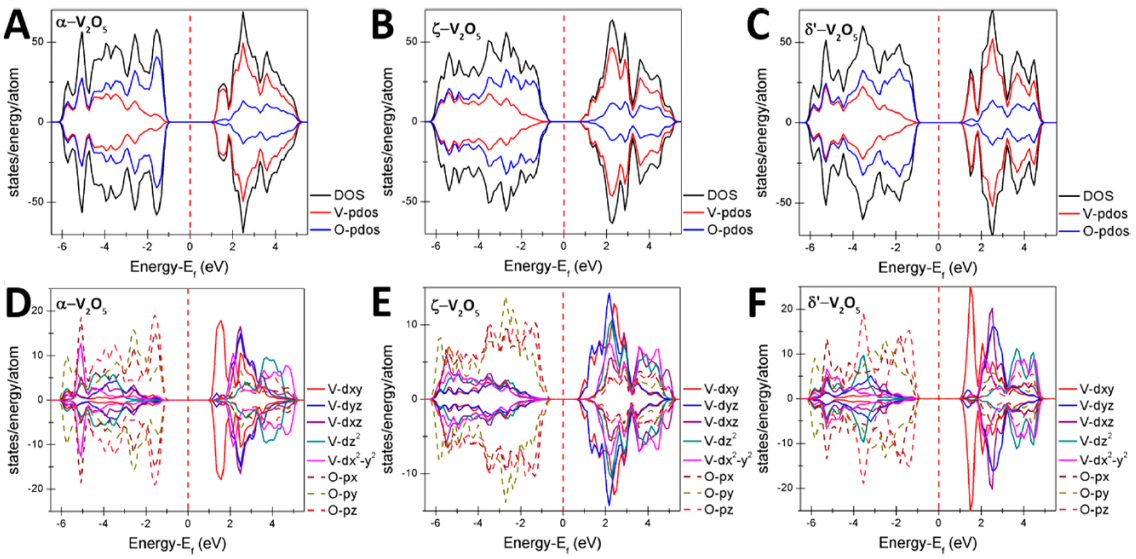

Figure I. 6. (A−C) Total density of states and atom-projected density of states. Vanadium and oxygen orbital-projected density of states for (D) α-V_2O_5, (E) ζ-V_2O_5, and (F) δ′-V_2O_5.

Electronic Structure Differences between V_2O_5 Polymorphs

The varying V−O connectivity profoundly changes the electronic structure of V_2O_5 polymorphs; altering the energy dispersion of conduction band states and varying the band gap provides a means to tune electron transport and further makes available a variety of semiconductors with tunable separations between valence and conduction band edges. The electronic structure of the polymorphs has substantial implications for intercalation chemistry given the oftentimes coupled nature of electron and ion diffusion (observed by the creation of small polarons and the self-trapping of small polarons by Li-ions).[108,118]

In α-V_2O_5, the localization of electrons on V $3d_{xy}$ orbitals and the subsequent structural relaxation of the V−O lattice phonon mode upon lithiation create a small polaron that traps the diffusing Li ions and hampers their facile diffusion.[119] There is a growing

realization that the electronic structure plays an important role in the electronically coupled diffusion of a cation through the lattice.[92,108,120] **Figure I. 6** contrasts the total density of states (DOS) and the atom-projected density of states (PDOS) of several selected polymorphs of V_2O_5, illustrating the substantial implications of altered atomistic connectivity on the electronic structure. In all depicted polymorphs of V_2O_5, the valence band is predominantly derived from O 2p states, whereas the conduction band is primarily vanadium 3d in origin.[121,122] On careful observation, the conduction band can be roughly separated into t_{2g} and e_g states. The lower energy t_{2g} states correspond to V $3d_{xy}$, $3d_{xz}$, and $3d_{yz}$ orbitals engaged in π-overlap with O 2p orbitals, whereas higher energy e_g states have contributions from V $3d_{z2}$ and $3d_{x2-y2}$ engaged in head-on σ-overlap with O 2p orbitals. In α-V_2O_5, owing to the distortion of the vanadium coordination from a perfect octahedron, a nonbonding split-off band V $3d_{xy}$ band is formed below the rest of the conduction band. Early transition metals tend to have narrow 3d bands, as is the case in V_2O_5.[71,73,108] The localization of charge in such narrow bands has a deleterious influence on electronic transport properties and further impedes ion transport through self-trapping of ions by small polarons.[71,118] In sharp contrast, ζ-V_2O_5 crystallizes in a lower symmetry structure with reduced structural dimensionality and has three distinct vanadium-centered polyhedra (two crystallographically inequivalent octahedra and one square pyramid). In ζ-V_2O_5, degenerate V $3d_{xy}$ and V $3d_{yz}$ orbital character is observed at the conduction band edge (**Figure I. 6B**). The broader energy dispersion of bands and the inclusion of the previously split-off states within the conduction band yield a lower band gap polymorph with considerably greater covalent character of V−O bonds; as such, it substantially

mitigates polaronic self-trapping,[71,73] which is evidenced experimentally by the improved Li- as well as Mg-ion diffusion in ζ-V_2O_5[73,92] as compared with α-V_2O_5.[104,123] Unlike α-V_2O_5, which undergoes several phase transitions upon lithiation as a result of gaps in miscibility,[104,108] the rigid 3D tunnel-structured framework is preserved across a wide range of Li- and Mg-ion insertion in ζ-V_2O_5,[73,107] yielding a large solid solution range with minimal volume expansion (<2%).[73,74]

Similar to the α-V_2O_5 structure, the double-layered δ′-V_2O_5 phase (and similar polymorphs such as ε′-V_2O_5 and ρ′-V_2O_5) has a sharp split-off conduction band that is primarily V $3d_{xy}$ in origin (**Figure I. 6C**).[71] The presence of split-off band, despite having two nonequivalent V sites, suggests the possibility of periodic charge ordering when the structure is distorted. As a result of stronger V=O bonding in the double-layered frameworks, δ′-V_2O_5 further shows increased covalency of V−O connectivity, which reduces the extent to which the intercalated cations are bonded to the anionic framework. It is clear from this limited comparison that the electronic structure of V_2O_5 polymorphs is delicately sensitive to the connectivity of V−O polymorphs, allowing for considerable tunability of effective orbital overlap and thus ionic/covalent character.

As detailed in recent work examining the mechanism of Mg-ion diffusion within ζ-V_2O_5,[73] ionic diffusion of the inserted cation and electronic diffusion of the localized electron/phonon (polaron) pair are inextricably coupled.[73] Importantly, the energetic barrier arising from this concerted diffusion is exacerbated when considering the diffusion of divalent cations, which requires the concomitant diffusion of two polarons. Perhaps a more compelling and broad conclusion that emerges is that when designing multivalent-

ion cathode materials, consideration of ionic diffusion alone is insufficient.[72] Additional attention to mitigating small polaron formation and the resulting self-trapping of intercalated cations is of great importance, particularly in early first-row transition metals with narrow 3d bands. Careful selection of metastable polymorphs allows for considerable tunability of electronic structure and by means of the available bonding motifs provides a valuable tool for potentially mitigating such problems. In other words, metastable materials provide opportunities to modulate the electronic structure and relative ionicity/ covalency of cathode materials (in addition to defining different diffusion pathways),[72] which can greatly modify interactions with intercalated cations.

I.5. Elucidating structure—function correlations across polymorphs

When comparing a metastable material to its thermodynamically stable counterpart, it is important to note that the stoichiometry, constituent elements, and generally the formal valence states of the elements that comprise the material remain the same; only the specific ordering and connectivity of the material changes, and thus utilizing metastable polymorphs represents a means to directly alter the arrangement of the atoms of a material in physical space. The altered connectivity can have a pronounced influence on the local bonding, strongly altering the ionicity/covalency of the framework[71] and giving rise to a vastly different electronic structure. Such structures can thus allow for substantial tunability of electronic, magnetic, and optical properties.

A detailed elucidation of chemical bonding across different polymorphs can further delineate structural (and bonding) motifs from the equilibrium structure that are conserved in accessible metastable frameworks, and, conversely, those "free energy

raising" features that represent excursions from the thermodynamic minima that are still accessible. The identification of structural motifs that underpin a certain function furthermore provides design rules for targeted exploration of phase space. The specific role of metastability in altering structure−function relationships is perhaps nowhere more apparent than in metastable vanadium oxide materials; the accessibility of different oxidation states of vanadium and the close stabilities of tetrahedral, square pyramidal, and octahedral environments allows for the stabilization of a variety of structural motifs. In our recent work, we have explored the structure–function relationship between ionic diffusion barriers and crystallographic structure for several polymorphs of V_2O_5 with distinct structural motifs.[74,75] A detailed discussion of different V_2O_5 polymorphs as potential cathode and for metal-insulator-transition will be the focus in **Chapter II-IV**.

As we will discuss in **Chapters II** and **III**, the rigid connectivity of vanadium-centered polyhedra and a diverse range of interstitial sites and diffusion pathways facilitates the diffusion of mono and multivalent cations;[72,73] as another example which is discussed in detail in **Chapter IV**, a subtle rearrangement of the atom positions and occupancies of Cu-ions within a 1D tunnel-structured phase of V_2O_5 underpins large metal—insulator transitions of β'-$Cu_xV_2O_5$.[5]

I.6. Mapping site occupancies, polaronic distortions, and charge delocalization across the metal-insulator transition of nanoscale β′-$Cu_xV_2O_5$

Transition metal oxides span a vast range of electrical conductivity and include examples of insulators, semiconductors, and metals. Single materials capable of abruptly and cleanly transitioning from insulating to metallic states are exceedingly rare and of

great interest for device applications such as neuromorphic circuit elements, electro/thermochromic coatings, and memristors. Ternary vanadium oxide bronzes ($M_xV_2O_5$) are a singularly unique class of oxides where M encompasses a large number of metal intercalants from across the main group and transition metals; monovalent and divalent main-group and transition metal cations; as noted in preceding sections, the V_2O_5 framework can adopt a diverse set of 1D, 2D, and 3D structure types.[107] The insertion of cations within interstitial sites of open-framework V_2O_5 structures results in reduction of the formally d^0 vanadium sites of the host structures; the extent of localization, ordering, and electron correlation resulting from partially filled vanadium 3d states underpin a variety of electronic and magnetic instabilities. Vanadium oxide bronzes exhibit sharply nonlinear electronic phenomena including charge and spin density waves, metal-insulator transitions, spin-gap transitions, and superconductivity, derived in part from the rich redox chemistry of vanadium and the ability to readily localize/delocalize charge density. We have previously reported that β′-$Cu_xV_2O_5$ exhibits a metal-insulator transition around 300 K, but have observed that the metal-insulator transition in single nanowires is extremely sensitive to the copper stoichiometry, *x*.[5] The β/β′ phase is a 1D tunnel structure in which the metal cation, in this case, Cu (I), is arrayed along the tunnel and partially reduces specific V^{5+} sites in the V_2O_5 framework to V^{4+}, yielding potentially charge ordered frameworks. Using first-principles density functional theory calculations, photoemission spectroscopy, variable-temperature single-crystal X-ray diffraction, and electrical transport measurements, in **Chapter IV** of this dissertation, we expand mechanistic understanding of the coupling of lattice and electronic degrees of freedom underpinning

the metal-insulator transition. We find that the melting of this polaronic state because of subtle perturbations in the position of the copper ions along the 1D tunnel results in the delocalization of the electrons across the charge ordered network, ultimately manifesting in metallic behavior. Insights into the structural and electronic properties underpinning this transition obtained during this study will allow for rational tuning of transformation characteristics such as the transition temperature and magnitude (by changing *x*) and help to establish structure-function correlations in this material.

I.7. Edge modification of MoS_2 for enhanced catalysis inspired by first-principles modeling and mapping of electronic structure

In **Chapter V**, we turn our attention to modulation of the electronic structure of 2D layered MoS_2 to enable the design and systematic alteration of the chemical reactivity of its edge sites. The combination of solar energy and water represents the most attractive and fundamentally viable solution to our energy needs. Water splitting, the sum of water oxidation and hydrogen evolution half-reactions, remains a formidable challenge since it requires the concerted transfer of four electrons and four protons.[124-127] The 2H polymorph of MoS_2, a semiconducting transition metal dichalcogenide, has gained prominence as an earth-abundant and inexpensive catalyst for the hydrogen evolution reaction (HER)[128-133] but requires a much greater overpotential as compared to Pt. Specifically, the edges of MoS_2 nanostructures are known to be the active sites for hydrogen evolution reaction. The adsorption of hydrogen is energetically uphill by about +0.08 eV at the edges of MoS_2, whereas Pt catalysts that are more active in reactions involving hydrogen have near null enthalpies of hydrogen adsorption.[134] Several studies of MoS_2 catalysts indicate that only

one in four atoms on edge sites of MoS_2 are active in catalysis, requiring substantial effort to maximize the density of edge sites and implying that a large volume fraction of catalytic particles are essentially catalytically inert.[135] However, modification of edge sites to reduce the enthalpy of hydrogen adsorption has been stymied by the absence of a precise understanding of the atomistic and electronic structure of active sites.[136] **In Chapter V**, first-principles density functional theory calculations along with element-specific X-ray absorption spectroscopy and imaging have been used to probe edge electronic structure, which has further been correlated to catalytic performance.[137] Modeling of excited state spectra allows for assignment of X-ray absorption features to specific structural and bonding motifs. In **Chapter VI**, we have shown the incorporation of dopants such as selenium provide a powerful means to modulate edge electronic structure and reactivity.

I.8. References

(1) Woodley, S. M.; Catlow, R. Crystal Structure Prediction from First Principles. *Nat. Mater.* **2008**, *7*, 937.

(2) Wang, Y.; Lv, J.; Zhu, L.; Ma, Y. Crystal Structure Prediction via Particle-Swarm Optimization. *Phy. Rev. B* **2010**, *82*, 094116.

(3) Oganov, A. R.; Lyakhov, A. O.; Valle, M. How Evolutionary Crystal Structure Prediction Works and Why. *Acc. Chem. Res.* **2011**, *44*, 227-237.

(4) Navrotsky, A. Nanoscale Effects on Thermodynamics and Phase Equilibria in Oxide Systems. *Chem. Phys. Chem.* **2011**, *12*, 2207-2215.

(5) Marley, P. M.; Horrocks, G. A.; Pelcher, K. E.; Banerjee, S. Transformers: The Changing Phases of Low-Dimensional Vanadium Oxide Bronzes. *Chem. Commun.* **2015**, *51*, 5181-5198.

(6) Whittaker, L.; Patridge, C. J.; Banerjee, S. Microscopic and Nanoscale Perspective of the Metal−Insulator Phase Transitions of VO_2: Some New Twists to an Old Tale. *J. Phys. Chem. Lett.* **2011**, *2*, 745-758.

(7) Navrotsky, A.; Mazeina, L.; Majzlan, J. Size-Driven Structural and Thermodynamic Complexity in Iron Oxides. *Science* **2008**, *319*, 1635-1638.

(8) Waitz, T.; Tsuchiya, K.; Antretter, T.; Fischer, F. Phase Transformations of Nanocrystalline Martensitic Materials. *MRS Bull.* **2009**, *34*, 814-821.

(9) Oganov, A. R.; Glass, C. W. Crystal Structure Prediction using ab initio Evolutionary Techniques: Principles and Applications. *J. Chem. Phys.* **2006**, *124*, 244704.

(10) Turnbull, D. Metastable Structures in Metallurgy. *Metall. Trans. A* **1981**, *12*, 695-708.

(11) Angus, J. C.; Hayman, C. C. Low-pressure, Metastable Growth of Diamond and "Diamondlike" Phases. *Science* **1988**, *241*, 913-921.

(12) Angus, J. C.; Wang, Y.; Sunkara, M. Metastable Growth of Diamond and Diamond-like phases. *Annu. Rev. Mater. Sci.* **1991**, *21*, 221-248.

(13) Lukowski, M. A.; Daniel, A. S.; Meng, F.; Forticaux, A.; Li, L.; Jin, S. Enhanced Hydrogen Evolution Catalysis from Chemically Exfoliated Metallic MoS_2 Nanosheets. *J. Am. Chem. Soc.* **2013**, *135*, 10274-10277.

(14) Voiry, D.; Salehi, M.; Silva, R.; Fujita, T.; Chen, M.; Asefa, T.; Shenoy, V. B.; Eda, G.; Chhowalla, M. Conducting MoS_2 Nanosheets as Catalysts for Hydrogen Evolution Reaction. *Nano Lett.* **2013**, *13*, 6222-6227.

(15) Nasr Esfahani, D.; Leenaerts, O.; Sahin, H.; Partoens, B.; Peeters, F. M. Structural Transitions in Monolayer MoS_2 by Lithium Adsorption. *J. Phys. Chem. C* **2015**, *119*, 10602-10609.

(16) Liu, H.; Strobridge, F. C.; Borkiewicz, O. J.; Wiaderek, K. M.; Chapman, K. W.; Chupas, P. J.; Grey, C. P. Capturing Metastable Structures During High-Rate Cycling of $LiFePO_4$ Nanoparticle Electrodes. *Science* **2014**, *344*, 1252817.

(17) Zhao, Y.; De Jesus, L. R.; Stein, P.; Horrocks, G. A.; Banerjee, S.; Xu, B.-X. Modeling of Phase Separation across Interconnected Electrode Particles in Lithium-Ion Batteries. *RSC Adv.* **2017**, *7*, 41254-41264.

(18) Somani, M.; Juntunen, P.; Karjalainen, L.; Misra, R.; Kyröläinen, A. Enhanced Mechanical Properties through Reversion in Metastable Austenitic Stainless Steels. *Metall. Mater. Trans. A* **2009**, *40*, 729-744.

(19) Datta, K.; Delhez, R.; Bronsveld, P.; Beyer, J.; Geijselaers, H. J.; Post, J. A Low-Temperature Study to Examine the Role of ε-Martensite During Strain-Induced Transformations in Metastable Austenitic Stainless Steels. *Acta Mater.* **2009**, *57*, 3321-3326.

(20) Gopalakrishnan, J. Chimie Douce Approaches to the Synthesis of Metastable Oxide Materials. *Chem. Mater.* **1995**, *7*, 1265-1275.

(21) Stein, A.; Keller, S. W.; Mallouk, T. E. Turning Down the Heat: Design and Mechanism in Solid-State Synthesis. *Science* **1993**, *259*, 1558-1564.

(22) Jansen, M. A Concept for Synthesis Planning in Solid-State Chemistry. *Angew. Chem. Int. Ed.* **2002**, *41*, 3746-3766.

(23) Price, S. L. Why Don't We Find More Polymorphs? *Acta Crystallogr., Sect. B: Struct. Sci* **2013**, *69*, 313-328.

(24) Stevanović, V.; Trottier, R.; Musgrave, C.; Therrien, F.; Holder, A.; Graf, P. Predicting Kinetics of Polymorphic Transformations from Structure Mapping and Coordination Analysis. *Phys. Rev. Mater.* **2018**, *2*, 033802.

(25) Lonie, D. C.; Zurek, E. XtalOpt: An Open-Source Evolutionary Algorithm for Crystal Structure Prediction. *Comput. Phys. Commun.* **2011**, *182*, 372-387.

(26) Shamp, A.; Terpstra, T.; Bi, T.; Falls, Z.; Avery, P.; Zurek, E. Decomposition Products of Phosphine under Pressure: PH_2 Stable and Superconducting? *J. Am. Chem. Soc.* **2016**, *138*, 1884-1892.

(27) Zurek, E.; Yao, Y. Theoretical Predictions of Novel Superconducting Phases of $BaGe_3$ Stable at Atmospheric and High Pressures. *Inorg. Chem.* **2015**, *54*, 2875-2884.

(28) Castillo, R.; Baranov, A. I.; Burkhardt, U.; Cardoso-Gil, R.; Schnelle, W.; Bobnar, M.; Schwarz, U. Germanium Dumbbells in a New Superconducting Modification of $BaGe_3$. *Inorg. Chem.* **2016**, *55*, 4498-4503.

(29) Stevanović, V. Sampling Polymorphs of Ionic Solids using Random Superlattices. *Phys. Rev. Lett.* **2016**, *116*, 075503.

(30) Curtarolo, S.; Hart, G. L.; Nardelli, M. B.; Mingo, N.; Sanvito, S.; Levy, O. The High-Throughput Highway to Computational Materials Design. *Nat. Mater.* **2013**, *12*, 191.

(31) Jain, A.; Ong, S. P.; Hautier, G.; Chen, W.; Richards, W. D.; Dacek, S.; Cholia, S.; Gunter, D.; Skinner, D.; Ceder, G. Commentary: The Materials Project: A Materials Genome Approach to Accelerating Materials Innovation. *Appl. Mater.* **2013**, *1*, 011002.

(32) Saal, J. E.; Kirklin, S.; Aykol, M.; Meredig, B.; Wolverton, C. Materials Design and Discovery with High-Throughput Density Functional Theory: The Open Quantum Materials Database (OQMD). *JOM* **2013**, *65*, 1501-1509.

(33) Curtarolo, S.; Setyawan, W.; Wang, S.; Xue, J.; Yang, K.; Taylor, R. H.; Nelson, L. J.; Hart, G. L.; Sanvito, S.; Buongiorno-Nardelli, M. AFLOWLIB. ORG: A Distributed Materials Properties Repository from High-Throughput ab initio Calculations. *Comput. Mater. Sci.* **2012**, *58*, 227-235.

(34) Sun, W.; Dacek, S. T.; Ong, S. P.; Hautier, G.; Jain, A.; Richards, W. D.; Gamst, A. C.; Persson, K. A.; Ceder, G. The Thermodynamic Scale of Inorganic Crystalline Metastability. *Sci. Adv.* **2016**, *2*, e1600225.

(35) Reed, J.; Ceder, G. Role of Electronic Structure in the Susceptibility of Metastable Transition-Metal Oxide Structures to Transformation. *Chem. Rev.* **2004**, *104*, 4513-4534.

(36) O'Hara, A.; Demkov, A. A. Nature of the Metal-Insulator Transition in NbO_2. *Phy. Rev. B* **2015**, *91*, 094305.

(37) Brito, W.; Aguiar, M.; Haule, K.; Kotliar, G. Dynamic Electronic Correlation Effects in NbO_2 as Compared to VO_2. *Phys. Rev. B* **2017**, *96*, 195102.

(38) Caspersen, K. J.; Carter, E. A. Finding Transition States for Crystalline Solid–Solid Phase Transformations. *Proc. Natl. Acad. Sci. U.S.A.* **2005**, *102*, 6738-6743.

(39) Sheppard, D.; Xiao, P.; Chemelewski, W.; Johnson, D. D.; Henkelman, G. A Generalized Solid-State Nudged Elastic Band Method. *J. Chem. Phys.* **2012**, *136*, 074103.

(40) Qian, G.-R.; Dong, X.; Zhou, X.-F.; Tian, Y.; Oganov, A. R.; Wang, H.-T. Variable Cell Nudged Elastic Band Method for Studying Solid–Solid Structural Phase Transitions. *Comput. Phys. Commun.* **2013**, *184*, 2111-2118.

(41) Bajaj, S.; Haverty, M. G.; Arróyave, R.; Shankar, S. Phase Stability in Nanoscale Material Systems: Extension From Bulk Phase Diagrams. *Nanoscale* **2015**, *7*, 9868-9877.

(42) Powell, A. E.; Hodges, J. M.; Schaak, R. E. Preserving Both Anion and Cation Sublattice Features during a Nanocrystal Cation-Exchange Reaction: Synthesis of Metastable Wurtzite-Type CoS and MnS. *J. Am. Chem. Soc.* **2016**, *138*, 471-474.

(43) Saha, D.; Jensen, K. M.; Tyrsted, C.; Bøjesen, E. D.; Mamakhel, A. H.; Dippel, A. C.; Christensen, M.; Iversen, B. B. In Situ Total X-Ray Scattering Study of WO_3 Nanoparticle Formation under Hydrothermal Conditions. *Angew. Chem. Int. Ed.* **2014**, *53*, 3667-3670.

(44) Nayak, A. P.; Bhattacharyya, S.; Zhu, J.; Liu, J.; Wu, X.; Pandey, T.; Jin, C.; Singh, A. K.; Akinwande, D.; Lin, J.-F. Pressure-Induced Semiconducting to Metallic Transition in Multilayered Molybdenum Disulphide. *Nat. Commun.* **2014**, *5*, 3731.

(45) Seddon, J.; Suard, E.; Hayward, M. A. Topotactic Reduction of $YBaCo_2O_5$ and $LaBaCo_2O_5$: Square-Planar Co (I) in an Extended Oxide. *J. Am. Chem. Soc.* **2010**, *132*, 2802-2810.

(46) Schaak, R. E.; Mallouk, T. E. Topochemical Synthesis of Three-Dimensional Perovskites from Lamellar Precursors. *J. Am. Chem. Soc.* **2000**, *122*, 2798-2803.

(47) Bianco, E.; Butler, S.; Jiang, S.; Restrepo, O. D.; Windl, W.; Goldberger, J. E. Stability and Exfoliation of Germanane: A Germanium Graphane Analogue. *ACS Nano* **2013**, *7*, 4414-4421.

(48) Cultrara, N. D.; Wang, Y.; Arguilla, M. Q.; Scudder, M. R.; Jiang, S.; Windl, W.; Bobev, S.; Goldberger, J. E. Synthesis of 1T, 2H, and 6R Germanane Polytypes. *Chem. Mater*. **2018**, *30*, 1335-1343.

(49) Waetzig, G. R.; Horrocks, G. A.; Jude, J. W.; Zuin, L.; Banerjee, S. X-ray Excited Photoluminescence near the Giant Resonance in Solid-Solution $Gd_{1-x}Tb_xOCl$ Nanocrystals and their Retention upon Solvothermal Topotactic Transformation to $Gd_{1-x}Tb_xF_3$. *Nanoscale* **2016**, *8*, 979-986.

(50) Ranade, M.; Navrotsky, A.; Zhang, H.; Banfield, J.; Elder, S.; Zaban, A.; Borse, P.; Kulkarni, S.; Doran, G.; Whitfield, H. Energetics of Nanocrystalline TiO_2. *Proc. Natl. Acad. Sci.* **2002**, *99*, 6476-6481.

(51) Garvie, R. C. The Occurrence of Metastable Tetragonal Zirconia as a Crystallite Size Effect. *J. Phys. Chem.* **1965**, *69*, 1238-1243.

(52) Garvie, R. Stabilization of the Tetragonal Structure in Zirconia Microcrystals. *J. Phys. Chem.* **1978**, *82*, 218-224.

(53) Waetzig, G. R.; Depner, S. W.; Asayesh-Ardakani, H.; Cultrara, N. D.; Shahbazian-Yassar, R.; Banerjee, S. Stabilizing Metastable Tetragonal HfO_2 using a Non-Hydrolytic

Solution-Phase Route: Ligand Exchange as a Means of Controlling Particle Size. *Chem. Sci.* **2016**, *7*, 4930-4939.

(54) Hudak, B. M.; Depner, S. W.; Waetzig, G. R.; Talapatra, A.; Arroyave, R.; Banerjee, S.; Guiton, B. S. Real-Time Atomistic Observation of Structural Phase Transformations in Individual Hafnia Nanorods. *Nat. Commun.* **2017**, *8*, 15316.

(55) Farrow, R. The Stabilization of Metastable Phases by Epitaxy. *J. Vac. Sci. Technol., B* **1983**, *1*, 222-228.

(56) David, L.; Bradford, C.; Tang, X.; Graham, T.; Prior, K.; Cavenett, B. Growth of Zinc Blende MnS and MnS Heterostructures by MBE using ZnS as a Sulfur Source. *J. Cryst. Growth* **2003**, *251*, 591-595.

(57) Quackenbush, N.; Paik, H.; Wahila, M.; Sallis, S.; Holtz, M.; Huang, X.; Ganose, A.; Morgan, B.; Scanlon, D. O.; Gu, Y. Stability of the M2 Phase of Vanadium Dioxide Induced by Coherent Epitaxial Strain. *Phy. Rev. B* **2016**, *94*, 085105.

(58) Park, J. H.; Coy, J. M.; Kasirga, T. S.; Huang, C.; Fei, Z.; Hunter, S.; Cobden, D. H. Measurement of a Solid-State Triple Point at the Metal–Insulator Transition in VO_2. *Nature* **2013**, *500*, 431.

(59) Braham, E. J.; Sellers, D.; Emmons, E.; Villarreal, R.; Asayesh-Ardakani, H.; Fleer, N. A.; Farley, K. E.; Shahbazian-Yassar, R.; Arròyave, R.; Shamberger, P. J. Modulating the Hysteresis of an Electronic Transition: Launching Alternative Transformation Pathways in the Metal–Insulator Transition of Vanadium (IV) Oxide. *Chem. Mater.* **2017**, *30*, 214-224.

(60) Asayesh-Ardakani, H.; Nie, A.; Marley, P. M.; Zhu, Y.; Phillips, P. J.; Singh, S.; Mashayek, F.; Sambandamurthy, G.; Low, K.-b.; Klie, R. F. Atomic Origins of Monoclinic-Tetragonal (Rutile) Phase Transition in Doped VO_2 Nanowires. *Nano Lett.* **2015**, *15*, 7179-7188.

(61) Birgisson, S.; Saha, D.; Iversen, B. B. Formation Mechanisms of Nanocrystalline MnO_2 Polymorphs under Hydrothermal Conditions. *Cryst. Growth Des.* **2018**, *18*, 827-838.

(62) Tuller, H. L.; Bishop, S. R. Point Defects in Oxides: Tailoring Materials Through Defect Engineering. *Annu. Rev. Mater. Res.* **2011**, *41*, 369-398.

(63) Batra, R.; Huan, T. D.; Rossetti Jr, G. A.; Ramprasad, R. Dopants Promoting Ferroelectricity in Hafnia: Insights from a Comprehensive Chemical Space Exploration. *Chem. Mater.* **2017**, *29*, 9102-9109.

(64) Huan, T. D.; Sharma, V.; Rossetti Jr, G. A.; Ramprasad, R. Pathways Towards Ferroelectricity in Hafnia. *Phy. Rev. B* **2014**, *90*, 064111.

(65) Kappera, R.; Voiry, D.; Yalcin, S. E.; Branch, B.; Gupta, G.; Mohite, A. D.; Chhowalla, M. Phase-Engineered Low-Resistance Contacts for Ultrathin MoS_2 Transistors. *Nat. Mater.* **2014**, *13*, 1128.

(66) Wang, Y.; Xiao, J.; Zhu, H.; Li, Y.; Alsaid, Y.; Fong, K. Y.; Zhou, Y.; Wang, S.; Shi, W.; Wang, Y. Structural Phase Transition in Monolayer $MoTe_2$ Driven by Electrostatic Doping. *Nature* **2017**, *550*, 487.

(67) Filinchuk, Y.; Tumanov, N. A.; Ban, V.; Ji, H.; Wei, J.; Swift, M. W.; Nevidomskyy, A. H.; Natelson, D. In Situ Diffraction Study of Catalytic Hydrogenation of VO_2: Stable Phases and Origins of Metallicity. *J. Am. Chem. Soc.* **2014**, *136*, 8100-8109.

(68) Alivio, T. E.; Sellers, D. G.; Asayesh-Ardakani, H.; Braham, E. J.; Horrocks, G. A.; Pelcher, K. E.; Villareal, R.; Zuin, L.; Shamberger, P. J.; Arroyave, R. Postsynthetic Route for Modifying the Metal-Insulator Transition of VO_2 by Interstitial Dopant Incorporation. *Chem. Mater.* **2017**, *29*, 5401-5412.

(69) Flores-Livas, J. A.; Sanna, A.; Drozdov, A. P.; Boeri, L.; Profeta, G.; Eremets, M.; Goedecker, S. Interplay between Structure and Superconductivity: Metastable Phases of Phosphorus under Pressure. *Phys. Rev. Mater.* **2017**, *1*, 024802.

(70) Filonenko, V.; Sundberg, M.; Werner, P.-E.; Zibrov, I. Structure of a High-Pressure Phase of Vanadium Pentoxide, β-V_2O_5. *Acta Crystallogr., Sect. B: Struct. Sci* **2004**, *60*, 375-381.

(71) Tolhurst, T. M.; Leedahl, B.; Andrews, J. L.; Marley, P. M.; Banerjee, S.; Moewes, A. Contrasting 1D Tunnel-Structured and 2D Layered Polymorphs of V_2O_5: Relating Crystal Structure and Bonding to Band Gaps and Electronic Structure. *Phys. Chem. Chem. Phys.* **2016**, *18*, 15798-15806.

(72) De Jesus, L. R.; Andrews, J. L.; Parija, A.; Banerjee, S. Defining Diffusion Pathways in Intercalation Cathode Materials: Some Lessons from V_2O_5 on Directing Cation Traffic. *ACS Energy Lett.* **2018**, *3*, 915-931.

(73) Andrews, J. L.; Mukherjee, A.; Yoo, H. D.; Parija, A.; Marley, P. M.; Fakra, S.; Prendergast, D.; Cabana, J.; Klie, R. F.; Banerjee, S. Reversible Mg-Ion Insertion in a Metastable One-Dimensional Polymorph of V_2O_5. *Chem* **2018**, *4*, 564-585.

(74) Parija, A.; Liang, Y.; Andrews, J. L.; De Jesus, L. R.; Prendergast, D.; Banerjee, S. Topochemically De-Intercalated Phases of V_2O_5 as Cathode Materials for Multivalent Intercalation Batteries: A First-Principles Evaluation. *Chem. Mater.* **2016**, *28*, 5611-5620.

(75) Parija, A.; Prendergast, D.; Banerjee, S. Evaluation of Multivalent Cation Insertion in Single-and Double-Layered Polymorphs of V_2O_5. *ACS Appl. Mater. Interfaces* **2017**, *9*, 23756-23765.

(76) Gutowski, M.; Jaffe, J. E.; Liu, C.-L.; Stoker, M.; Hegde, R. I.; Rai, R. S.; Tobin, P. J. Thermodynamic Stability of High-K Dielectric Metal Oxides ZrO_2 and HfO_2 in Contact with Si and SiO_2. *Appl. Phys. Lett.* **2002**, *80*, 1897-1899.

(77) Jiang, H.; Gomez-Abal, R. I.; Rinke, P.; Scheffler, M. Electronic Band Structure of Zirconia and Hafnia Polymorphs from the GW Perspective. *Phy. Rev. B* **2010**, *81*, 085119.

(78) Zhao, X.; Vanderbilt, D. First-Principles Study of Structural, Vibrational, and Lattice Dielectric Properties of Hafnium Oxide. *Phy. Rev. B* **2002**, *65*, 233106.

(79) Tarascon, J.; Vaughan, G.; Chabre, Y.; Seguin, L.; Anne, M.; Strobel, P.; Amatucci, G. In Situ Structural and Electrochemical Study of $Ni_{1-x}Co_xO_2$ Metastable Oxides Prepared by Soft Chemistry. *J. Solid State Chem.* **1999**, *147*, 410-420.

(80) Orikasa, Y.; Maeda, T.; Koyama, Y.; Murayama, H.; Fukuda, K.; Tanida, H.; Arai, H.; Matsubara, E.; Uchimoto, Y.; Ogumi, Z. Direct Observation of a Metastable Crystal

Phase of Li_xFePO_4 under Electrochemical Phase Transition. *J. Am. Chem. Soc.* **2013**, *135*, 5497-5500.

(81) Liu, C.; Neale, Z. G.; Cao, G. Understanding Electrochemical Potentials of Cathode Materials in Rechargeable Batteries. *Mater. Today* **2016**, *19*, 109-123.

(82) Goodenough, J. B.; Kim, Y. Challenges for Rechargeable Li Batteries. *Chem. Mater.* **2009**, *22*, 587-603.

(83) Wang, J.; Chen-Wiegart, Y.-c. K.; Wang, J. In Operando Tracking Phase Transformation Evolution of Lithium Iron Phosphate with Hard X-ray Microscopy. *Nat. Commun.* **2014**, *5*, 4570.

(84) Love, C. T.; Korovina, A.; Patridge, C. J.; Swider-Lyons, K. E.; Twigg, M. E.; Ramaker, D. E. Review of $LiFePO_4$ Phase Transition Mechanisms and New Observations From X-Ray Absorption Spectroscopy. *J. Electrochem. Soc.* **2013**, *160*, A3153-A3161.

(85) Zhao, J.; Tao, Z.; Liang, J.; Chen, J. Facile Synthesis of Nanoporous γ-MnO_2 Structures and their Application in Rechargeable Li-ion Batteries. *Cryst. Growth Des.* **2008**, *8*, 2799-2805.

(86) Greedan, J. E.; Raju, N.; Wills, A.; Morin, C.; Shaw, S.; Reimers, J. Structure and Magnetism in λ-MnO_2. Geometric Frustration in a Defect Spinel. *Chem. Mater.* **1998**, *10*, 3058-3067.

(87) Capitaine, F.; Gravereau, P.; Delmas, C. A New Variety of $LiMnO_2$ with a Layered Structure. *Solid State Ionics* **1996**, *89*, 197-202.

(88) Kitchaev, D. A.; Peng, H.; Liu, Y.; Sun, J.; Perdew, J. P.; Ceder, G. Energetics of MnO_2 Polymorphs in Density Functional Theory. *Phy. Rev. B* **2016**, *93*, 045132.

(89) Han, S.-D.; Kim, S.; Li, D.; Petkov, V.; Yoo, H. D.; Phillips, P. J.; Wang, H.; Kim, J. J.; More, K. L.; Key, B. Mechanism of Zn Insertion into Nanostructured δ-MnO_2: A Nonaqueous Rechargeable Zn Metal Battery. *Chem. Mater.* **2017**, *29*, 4874-4884.

(90) Lipson, A. L.; Pan, B.; Lapidus, S. H.; Liao, C.; Vaughey, J. T.; Ingram, B. J. Rechargeable Ca-ion Batteries: A New Energy Storage System. *Chem. Mater.* **2015**, *27*, 8442-8447.

(91) Zavalij, P. Y.; Whittingham, M. S. Structural Chemistry of Vanadium Oxides with Open Frameworks. *Acta Crystallogr., Sect. B: Struct. Sci* **1999**, *55*, 627-663.

(92) Horrocks, G. A.; Parija, A.; De Jesus, L. R.; Wangoh, L.; Sallis, S.; Luo, Y.; Andrews, J. L.; Jude, J.; Jaye, C.; Fischer, D. A.; et al. Mitigating Cation Diffusion Limitations and Intercalation-Induced Framework Transitions in a 1D Tunnel-Structured Polymorph of V_2O_5. *Chem. Mater.* **2017**, *29*, 10386-10397.

(93) Pouchard, M. H., P. The System $K_xV_2O_5$ of a Few Novel Families of Vanadium Oxibronzes. *Mater. Res. Bull.* **1967**, *2*, 799–808.

(94) Savariault, J.-M.; Parize, J.-L.; Ballivet-Tkatchendo, D.; Galy, J. τ-$Na_xV_2O_5$ (x= 0.64): A Vanadium Bronze with an Original Intergrowth Structure. *J. Solid State Chem.* **1996**, *122*, 1-6.

(95) Waltersson, K.; Forslund, B. A Refinement of the Crystal Structure of CsV_2O_5. *Acta Crystallogr., Sect. B: Struct. Sci* **1977**, *33*, 789-793.

(96) Waltersson, K.; Forslund, B. On the Crystal Structure of $Cs_xV_3O_7$ (x Approx. 0.35), A New Hexagonal Vanadium Bronze Structure Type. *Acta Crystallogr., Sect. B: Struct. Sci* **1977**, *33*, 775-779.

(97) Oka, Y.; Tamada, O.; Yao, T.; Yamamoto, N. Hydrothermal Synthesis and Crystal Structure of a Novel Barium Vanadium Oxide: $Ba_{0.4}V_3O_8(VO)_{0.4}\cdot nH_2O$. *J. Solid State Chem.* **1995**, *114*, 359-363.

(98) Yamauchi, T.; Ueda, H.; Ueda, Y.; Kikuchi, J. Rich Phase Transitions under Pressure in β-$A_{0.33}V_2O_5$ (A= Ca and Pb). *Phys. C* **2007**, *460*, 532-533.

(99) Marley, P. M.; Singh, S.; Abtew, T. A.; Jaye, C.; Fischer, D. A.; Zhang, P.; Sambandamurthy, G.; Banerjee, S. Electronic Phase Transitions of δ-$Ag_xV_2O_5$ Nanowires: Interplay between Geometric and Electronic Structures. *J. Phys. Chem. C* **2014**, *118*, 21235-21243.

(100) Patridge, C. J.; Wu, T.-L.; Sambandamurthy, G.; Banerjee, S. Colossal Above-Room-Temperature Metal–Insulator Switching of a Wadsley-Type Tunnel Bronze. *Chem. Commun.* **2011**, *47*, 4484-4486.

(101) Permer, L.; Ferey, G. Crystal Structure of β'-$Fe_{0.33}V_2O_5$. *Z. Kristallogr.* **1994**, *209*, 413-417.

(102) Chirayil, T. Z., P. Y.; Whittingham, M. S. Synthesis and Characterization of a New Vanadium Oxide, $TMAV_8O_{20}$. *J. Mater. Chem.* **1997**, *7*, 2193-2195.

(103) Zhang, Y. H., R. C.; Clearfield, A. Hydrothermal Syntheses and Structural Characterization of Layered Vanadium Oxides Incorporating Organic Cations: α-, β-$(H_3N(CH_2)_2NH_3)[V_4O_{10}]$ and α-, β-$(H_2N(C_2H_4)_2NH_2)[V_4O_{10}]$. *Inorg. Chem.* **1996**, *35*, 4950–4956.

(104) Horrocks, G. A.; Likely, M. F.; Velazquez, J. M.; Banerjee, S. Finite Size Effects on the Structural Progression Induced by Lithiation of V_2O_5: A Combined Diffraction and Raman Spectroscopy Study. *J. Mater. Chem. A* **2013**, *1*, 15265-15277.

(105) Cocciantelli, J.; Gravereau, P.; Doumerc, J.; Pouchard, M.; Hagenmuller, P. On the Preparation and Characterization of a New Polymorph of V_2O_5. *J. Solid State Chem.* **1991**, *93*, 497-502.

(106) Zibrov, I. P.; Filonenko, V. P.; Lyapin, S. G.; Sidorov, V. A. The High Pressure Phases β-and δ-V_2O_5: Structure Refinement, Electrical and Optical Properties, Thermal Stability. *High Pressure Res.* **2013**, *33*, 399-408.

(107) Marley, P. M.; Abtew, T. A.; Farley, K. E.; Horrocks, G. A.; Dennis, R. V.; Zhang, P.; Banerjee, S. Emptying and Filling a Tunnel Bronze. *Chem. Sci.* **2015**, *6*, 1712-1718.

(108) De Jesus, L. R.; Horrocks, G. A.; Liang, Y.; Parija, A.; Jaye, C.; Wangoh, L.; Wang, J.; Fischer, D. A.; Piper, L. F.; Prendergast, D. Mapping Polaronic States and Lithiation Gradients in Individual V_2O_5 Nanowires. *Nat. Commun.* **2016**, *7*, 12022.

(109) Enjalbert, R.; Galy, J. A Refinement of the Structure of V_2O_5. *Acta Crystallogr., Sect. C: Cryst. Struct. Commun.* **1986**, *42*, 1467-1469.

(110) Galy, J. Vanadium Pentoxide and Vanadium Oxide Bronzes—Structural Chemistry of Single (S) and Double (D) Layer $M_xV_2O_5$ Phases. *J. Solid State Chem.* **1992**, *100*, 229-245.

(111) Bystrom, A.; Wilhelmi, K.; Brotzen, O. Vanadium Pentoxide-A Compound with Five-Coordinated Vanadium Atoms. *Acta. Chem. Scand.* **1950**, *4*, 1119.

(112) Satto, C.; Sciau, P.; Dooryhee, E.; Galy, J.; Millet, P. The δ⟶ ε⟶ γ LiV_2O_5 "High Temperature" Phase Transitions Evidenced by Synchrotron X-Ray Powder Diffraction Analysis. *J. Solid State Chem.* **1999**, *146*, 103-109.

(113) Marley, P. M.; Banerjee, S. Reversible Interconversion of a Divalent Vanadium Bronze between δ and β Quasi-1D Structures. *Inorg. Chem.* **2012**, *51*, 5264-5269.

(114) Delmas, C.; Cognac-Auradou, H.; Cocciantelli, J.; Menetrier, M.; Doumerc, J. The $Li_xV_2O_5$ System: An Overview of the Structure Modifications Induced by the Lithium Intercalation. *Solid State Ionics* **1994**, *69*, 257-264.

(115) Gershinsky, G.; Yoo, H. D.; Gofer, Y.; Aurbach, D. Electrochemical and Spectroscopic Analysis of Mg^{2+} Intercalation into thin Film Electrodes of Layered Oxides: V_2O_5 and MoO_3. *Langmuir* **2013**, *29*, 10964-10972.

(116) Rong, Z.; Malik, R.; Canepa, P.; Sai Gautam, G.; Liu, M.; Jain, A.; Persson, K.; Ceder, G. Materials Design Rules for Multivalent Ion Mobility in Intercalation Structures. *Chem. Mater.* **2015**, *27*, 6016-6021.

(117) Gautam, G. S.; Canepa, P.; Malik, R.; Liu, M.; Persson, K.; Ceder, G. First-Principles Evaluation of Multi-Valent Cation Insertion into Orthorhombic V_2O_5. *Chem. Commun.* **2015**, *51*, 13619-13622.

(118) Sanchez, C.; Henry, M.; Morineau, R.; Leroy, M. Small Polaron Mobility in α-Li_xO_5. *Phys. Status Solidi.* **1984**, *122*, 175-182.

(119) Maxisch, T.; Zhou, F.; Ceder, G. Ab initio Study of the Migration of Small Polarons in Olivine Li_xFePO_4 and their Association with Lithium Ions and Vacancies. *Phy. Rev. B* **2006**, *73*, 104301.

(120) De Jesus, L. R.; Stein, P.; Andrews, J. L.; Luo, Y.; Xu, B.-X.; Banerjee, S. Striping Modulations and Strain Gradients within Individual Particles of a Cathode Material upon Lithiation. *Mater. Horiz.* **2018**, *5*, 486-498.

(121) Maganas, D.; Roemelt, M.; Hävecker, M.; Trunschke, A.; Knop-Gericke, A.; Schlögl, R.; Neese, F. First-Principles Calculations of the Structure and V L-edge X-ray Absorption Spectra of V_2O_5 using Local Pair Natural Orbital Coupled Cluster Theory and Spin–Orbit Coupled Configuration Interaction Approaches. *Phys. Chem. Chem. Phys.* **2013**, *15*, 7260-7276.

(122) Velazquez, J. M.; Jaye, C.; Fischer, D. A.; Banerjee, S. Near Edge X-Ray Absorption Fine Structure Spectroscopy Studies of Single-Crystalline V_2O_5 Nanowire Arrays. *J. Phys. Chem. C* **2009**, *113*, 7639-7645.

(123) Mukherjee, A.; Sa, N.; Phillips, P. J.; Burrell, A.; Vaughey, J.; Klie, R. F. Direct Investigation of Mg Intercalation into the Orthorhombic V_2O_5 Cathode Using Atomic-Resolution Transmission Electron Microscopy. *Chem. Mater.* **2017**, *29*, 2218-2226.

(124) Lewis, N. S.; Nocera, D. G. Powering the planet: Chemical challenges in solar energy utilization. *Proc. Natl. Acad. Sci. U. S. A.* **2006**, *103*, 15729−15735.

(125) Nocera, D. G. The artificial leaf. *Acc. Chem. Res.* **2012**, *45*, 767−776.

(126) Hisatomi, T.; Kubota, J.; Domen, K. Recent advances in semiconductors for photocatalytic and photoelectrochemical water splitting. *Chem. Soc. Rev.* **2014**, *43*, 7520−7535.

(127) Chen, X.; Shen, S.; Guo, L.; Mao, S. S. Semiconductor-based photocatalytic hydrogen generation. *Chem. Rev.* **2010**, *110*, 6503−6570.

(128) Hinnemann, B.; Moses, P. G.; Bonde, J.; Jørgensen, K. P.; Nielsen, J. H.; Horch, S.; Chorkendorff, I.; Nørskov, J. K. Biomimetic Hydrogen Evolution: MoS_2 Nanoparticles as Catalyst for Hydrogen Evolution. *J. Am. Chem. Soc.* **2005**, *127*, 5308−5309.

(129) Jaramillo, T. F.; Jørgensen, K. P.; Bonde, J.; Nielsen, J. H.; Horch, S.; Chorkendorff, I. Identification of active edge sites for electro chemical H_2 evolution from MoS_2 nanocatalysts. *Science* **2007**, *317*, 100−102.

(130) Li, Y.; Wang, H.; Xie, L.; Liang, Y.; Hong, G.; Dai, H. MoS_2 nanoparticles grown on graphene: an advanced catalyst for the hydrogen evolution reaction. *J. Am. Chem. Soc.* **2011**, *133*, 7296−7299.

(131) Ye, G.; Gong, Y.; Lin, J.; Li, B.; He, Y.; Pantelides, S. T.; Zhou, W.; Vajtai, R.; Ajayan, P. M. Defects engineered monolayer MoS_2 for improved hydrogen evolution reaction. *Nano Lett.* **2016**, *16*, 1097−1103.

(132) Li, H.; Tsai, C.; Koh, A. L.; Cai, L.; Contryman, A. W.; Fragapane, A. H.; Zhao, J.; Han, H. S.; Manoharan, H. C.; AbildPedersen, F.; Nørskov, J. K.; Zheng, X. Activating and optimizing MoS_2 basal planes for hydrogen evolution through the formation of strained sulphur vacancies. *Nat. Mater.* **2016**, *15*, 48−53.

(133) Choi, Y.-H.; Lee, J.; Parija, A.; Cho, J.; Verkhoturov, S. V.; Al-Hashimi, M.; Fang, L.; Banerjee, S. An in Situ Sulfidation Approach for the Integration of MoS_2 Nanosheets on Carbon Fiber Paper and the Modulation of Its Electrocatalytic Activity by Interfacing with $n$$C_{60}$. *ACS Catal.* **2016**, *6*, 6246−6254.

(134) Lauritsen, J. V.; Kibsgaard, J.; Helveg, S.; Topsoe, H.; Clausen, B. S.; Laegsgaard, E.; Besenbacher, F. Size-dependent structure of MoS_2 nanocrystals. *Nat. Nanotechnol.* **2007**, *2*, 53−58.

(135) Kibsgaard, J.; Chen, Z.; Reinecke, B. N.; Jaramillo, T. F. Engineering the surface structure of MoS_2 to preferentially expose active edge sites for electrocatalysis. *Nat. Mater.* **2012**, *11*, 963−969.

(136) Tinoco, M.; Maduro, L.; Masaki, M.; Okunishi, E.; Conesa-Boj, S. Strain-Dependent Edge Structures in MoS_2 Layers. *Nano Lett.* **2017**, *17*, 7021−7026.

(137) Parija, A.; Choi, Y.-H.; Liu, Z.; Andrews, J. L.; De Jesus, L. R.; Fakra, S. C.; Al-Hashimi, M.; Batteas, J. D.; Prendergast, D.; Banerjee, S., Mapping Catalytically Relevant Edge Electronic States of MoS_2. *ACS Cent. Sci.* **2018,** *4* (4), 493-503.

CHAPTER II

TOPOCHEMICALLY DE-INTERCALATED PHASES OF V_2O_5 AS CATHODE MATERIALS FOR MULTIVALENT INTERCALATION BATTERIES: A FIRST-PRINCIPLES EVALUATION*

II.1 Introduction

Rechargeable Mg- and Al-ion batteries based on the reversible intercalation of multivalent cations are of interest primarily because of the high volumetric energy densities theoretically possible with the use of metallic Mg and Al anodes (3832 mAh cm^{-3} for Mg and 8046 mAh cm^{-3} for Al in contrast to the value of ~800 mAh cm^{-3} obtained for Li ions stored in graphite).[1,2] The high volumetric energy density of multivalent intercalation chemistries derives both from the use of a multivalent metal as the anode and from the storage of more charge per ion in the cathode given that most cathode materials are limited by the number of intercalation sites and not the accessibility of the redox couple at the transition metal center.[3,4] Additionally, neither of these metals forms dendrites upon electrodeposition, which could mitigate safety concerns that have plagued current Li-ion technologies.[5] Finally, these metals are many orders of magnitude more accessible and extractable from geological deposits than lithium is. The latter earth abundance and safety characteristics are particularly significant and often used to imply considerable scalability (as compared to conventional Li-ion technologies) if fundamental scientific challenges

*Reprinted with permission from "Topochemically De-Intercalated Phases of V_2O_5 as Cathode Materials for Multivalent Intercalation Batteries: A First-Principles Evaluation" by A. Parija, Y. Liang, J. L. Andrews, L. R. De Jesus, D. Prendergast, S. Banerjee, *Chem. Mater.*, 2016, **28**, 5611-5620.

pertaining to the construction of viable multivalent intercalation cells can be resolved. The development of multivalent-ion insertion chemistries as a means of electrochemical energy storage has been hindered by two primary impediments: (a) the absence of electrolytes with a sufficiently large electrochemical stability window to facilitate high-voltage operation and (b) the sparse repertoire of solids that can reversibly intercalate multivalent cations.[2,6,7] Here, we focus on the second of the two problems and predict on the basis of first-principles calculations that two metastable phases of V_2O_5 that are topochemically accessible in nanostructured form[8–10] should exhibit much enhanced diffusivity of multivalent ions in comparison to the thermodynamically stable orthorhombic (α) polymorph of V_2O_5. The fundamental origins of the reduced diffusion barriers and higher voltages expected for these structures are discussed with regard to the available coordination environments and the metastable nature of these frameworks.

The identification of high-voltage cathode materials that can reversibly store multivalent ions has been challenging; for instance, the inventory of crystalline compounds that demonstrate reversible intercalation of Mg ions is rather sparse, comprising only three members, α-V_2O_5, layered MoO_3, and the Chevrel phase Mo_6S_8.[6,11,12] Several other morphologies of V_2O_5 such as xerogels[13,14] and aerogels[15] with expanded, quasiamorphous, crystal structures incorporating water are known. However, the inclusion of water renders high-voltage operation difficult, and furthermore, the focus of this work is on elucidating fundamental design principles for preparation of cathode materials with well-defined crystal structures.

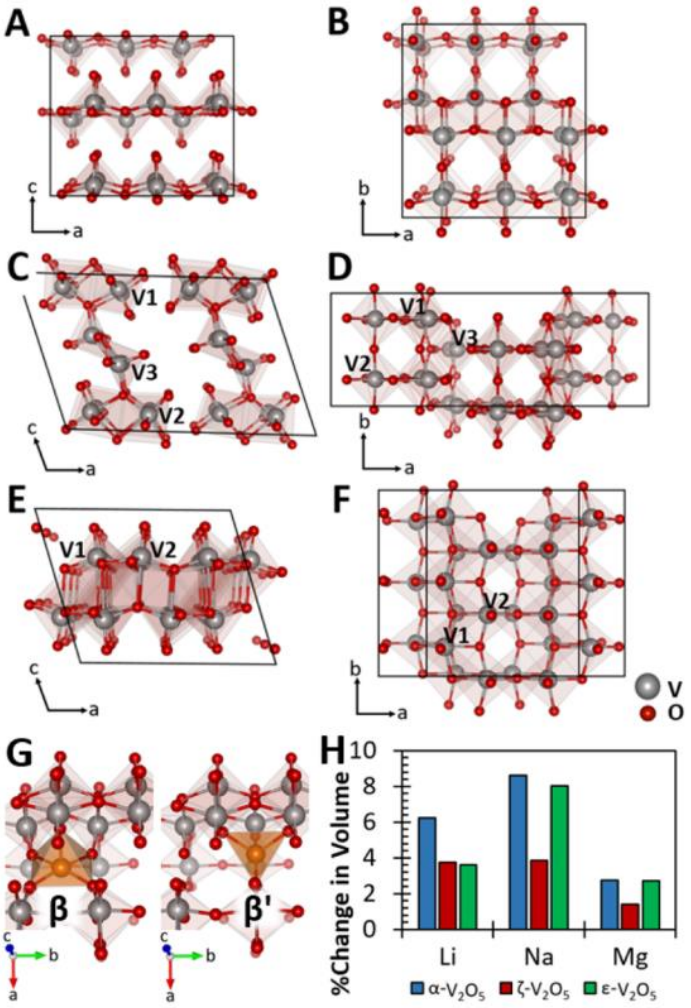

Figure II. 1. Supercell structures of (A and B) α-V_2O_5, (C and D) ζ-V_2O_5, and (E and F) ε-V_2O_5. The gray and red spheres represent vanadium and oxygen atoms, respectively. The left panels depict the crystal structures viewed along the *b* direction, whereas in the right panels, the structures are viewed along their respective crystallographic *c* directions. (G) Two distinct crystallographic sites β and β′ in ζ-V_2O_5. (H) Predicted changes in the unit cell volume of the three V_2O_5 polymorphs upon maximal intercalation of Li, Na, and Mg ions. A final stoichiometry of MV_2O_5 is used as the intercalation limit of all of the ions considered here in α- and ε-V_2O_5. In contrast, $M_{0.33}V_2O_5$ is used for the calculation of the change in volume for ζ-V_2O_5 for Mg and Na ions, whereas $M_{0.66}V_2O_5$ is used for intercalation of Li ions, representing the intercalation limits for this polymorph.

The fundamental challenge with diffusing multivalent cations through a close-packed lattice is that the highly polarizing nature of divalent and trivalent ions gives rise

to strong electrostatic interactions with the anionic framework of the solid, resulting in the rather sluggish diffusion of Mg^{2+} and Al^{3+} ions in most cathode materials. Indeed, this effect is exacerbated in compounds exhibiting poor electronic conductivity where small polarons are stabilized and the lattice is locally distorted, thereby giving rise to further charge localization.[16,17] First principles calculations have proven to be useful in predicting diffusivity of multivalent (and monovalent) cations in crystalline frameworks and can provide a direct comparison of barriers to ion diffusion across different frameworks that can be difficult to deconvolute from experiments given unresolved issues with electrolytes, optimizing electrolyte−electrode interfaces, and the poorly defined geometry of complete electrochemical cells wherein multiple charge diffusion and charge transfer events proceed with disparate kinetics.[4,18–20] Such calculations are used here to explore multivalent cation diffusion in metastable frameworks that can be synthetically accessed by topochemical means.

Computational screening of diffusion barriers in several common oxide frameworks by Ceder and co-workers suggests that the magnitude of the barriers depends strongly on the specific anionic framework and the coordination preference of the diffusing cation and to a much lesser extent on the type of transition metal or the void space in the framework.[1,4,5,21] The layered orthorhombic α-phase of V_2O_5 (**Figure II. 1A,B**) has long attracted attention as a classical layered intercalation host since the first report by Whittingham because of its abundance of interlayer sites that can accommodate intercalating species without substantial structural distortions, the readily accessible vanadium redox couples, and the strongly negative free energy for Li-ion insertion within

this structure.[22–25] As noted above, this compound is one of the three viable materials for reversible intercalation of Mg ions and yields a reasonable voltage in the range of 2.4−2.6 V.[2,6] In addition, α-V_2O_5 has shown promising results for the diffusion of Ca^{2+} and Y^{3+} ions.[11]

A metastable phase of V_2O_5, δ-V_2O_5, derived from the sliding of alternate layers along the crystallographic a direction by half a unit cell length appears to be particularly intriguing as an intercalation host for multivalent cations and has been predicted to have an activation energy barrier for Mg-ion diffusion greatly decreased compared to that of α-V_2O_5 as a result of the quasi-octahedral instead of eight-coordinated interstitial coordination environment available for Mg ions and the relatively smaller changes in coordination accompanying the diffusion of cations.[1,21] The δ-phase of V_2O_5 is ∼13 meV/atom more unstable than the α-phase depicted in **Figure II. 1A** and is readily accessible via direct synthesis and may further be accessible by phase transformation upon insertion of Mg ions.[5,21,22] However, to the best of our knowledge, this is the only metastable structure of V_2O_5 to have been considered thus far. A vast array of intercalated vanadium oxide bronze phases with the formula $M_xV_2O_5$ are known with distinctive low-dimensional layered and tunnel-structured V_2O_5 frameworks ensconcing cations; the specific structure type depends on the stoichiometry, size, charge, and polarizability of the cations.[23,26–28] Intriguingly, in nanostructures, because of the shorter cation diffusion lengths, topochemical leaching of the cations yields metastable V_2O_5 structures with tunnel and layered structures that are very different from the single-layer α phase depicted in **Figure II. 1**. In recent work, we have stabilized a metastable one-dimensional (1D) tunnel-

structured framework, ζ-V_2O_5 depicted in panels C and D of **Figure II. 1**, based on the leaching of Ag ions from β-$Ag_{0.33}V_2O_5$.[9] Although this structure represents a novel metastable phase, it is nevertheless stable upon being annealed to temperatures in excess of 500 °C and can further be intercalated with Li and Mg ions by reaction with n-butyllithium and Mg nanoparticles, respectively.[9] The motivation for examining this structure for multivalent cation diffusion arises from recent electronic structure studies, which indicate that unlike orthorhombic V_2O_5 where the V $3d_{xy}$ level forms a split-off conduction band and mediates stabilization of a polaron upon ion intercalation,[16] the increased symmetry in the vanadium coordination environment results in improved overlap of the V $3d_{xy}$ states with the rest of the conduction band.[17] Such an improved overlap could potentially reduce polaron diffusion barriers and allow for improved multivalent cation mobility. Indeed, another putative metastable phase, ε-V_2O_5, is depicted in panels E and F of **Figure II. 1**, and initial reports suggest stabilization of this phase by extraction of Cu ions from ε-$Cu_xV_2O_5$.[8,10] Although this layered structure is analogous to that of orthorhombic V_2O_5, the expanded galleries in this structure provide a far richer number of coordination sites than in α-V_2O_5. The energies of both these structures are somewhat higher than that of thermodynamically stable α-V_2O_5, but their synthetic accessibility and thermal stability suggest that they may still represent polymorphs trapped by relatively deep kinetic barriers and may be viable candidates for multivalent intercalation batteries. Indeed, in this work, we perform a first-principles evaluation of the mobility of different cations within these metastable polymorphs.

II.2 Theoretical Methods

Initial coordinates of ζ-V_2O_5 were obtained from a Rietveld refinement of powder X-ray diffraction data that we have reported previously.[9] Coordinates of ε-V_2O_5 were optimized after Cu ions were removed from ε-$Cu_xV_2O_5$ because a full structure solution of the topochemically de-intercalated phase is not thus far available.[8,10] To effectively describe the electron exchange correlation, energies were calculated within the generalized gradient approximation (GGA) of Perdew−Burke−Ernzerhof (PBE) implemented within the Vienna *ab initio* simulation package (VASP).[29] Electron−ion interactions were treated with projector-augmented waves (PAW) with a kinetic energy cutoff of 600 eV. A rotationally invariant density functional theory (DFT+U) approach was used to describe the on-site Coulomb interactions[30] upon calculation of structural parameters and electronic structure. A U value of 4.0 eV was used in the calculations as benchmarked previously in the literature.[26] To converge the total energy, the first Brillouin zone was sampled with a Monkhorst−Pack reciprocal space grid of 4 × 4 × 4 k-points for the unit cells and 2 × 2 × 2 k-points for the supercells. A detailed k-point analysis is provided in **Table A1**. All the atomic structures are considered to have been relaxed when each Cartesian force component is no greater than 0.01 eV/Å unless otherwise noted. To calculate the diffusion pathways and energetics of multivalent ions in various phases of V_2O_5, nudged elastic band (NEB) calculations were used as also implemented in VASP. Such calculations have been implemented successfully in the past for similar systems.[1,21] For each structure, a total of seven images were interpolated between the initial and final positions to describe the diffusion of the ions starting with the fully relaxed equilibrium

structure. DFT was used instead of DFT+U for the calculation of diffusion barriers because of the difficulty with the convergence of the metastable image points as previously noted by Liu et al.[4] Furthermore, as Ceder and co-workers have noted, there is no conclusive evidence thus far that the Hubbard parameter improves the accuracy of prediction of cation migration barriers.1,4 The end positions were optimized to a force tolerance of ±0.05 eV $Å^{-1}$, whereas for the forces along the NEB path, the convergence criterion was 0.1 eV $Å^{-1}$. To avoid physically unreasonable interactions, supercells of adequate dimensions were used such that the distance between the images was no less than 7.3 Å.

II.3 Results and Discussion

Thermodynamics of Intercalation. A Comparison of the Structural Parameters of Intercalated Phases, Lattice Expansion, and Calculated Open Circuit Voltages

Orthorhombic α-V_2O_5 crystallizes in a layered structure as depicted in panels A and B of Figure II. 1 with *Pmmn* space group symmetry.[31] The fundamental building blocks of the crystal structure are [VO_5] square pyramids wherein the central vanadium atom forms a double bond with an apical oxygen atom (denoted as the vanadyl oxygen) and four V−O bonds define the base of the square pyramid. The [VO_5] polyhedra further share edges to form a zigzag chain along the a axis and share corner oxygens along the *b* axis giving rise to infinite twodimensional (2D) sheets, which in turn are stacked in a staggered configuration and held together by van der Waals interactions. In contrast to the 2D layered structure of α-V_2O_5, the ζ-phase adopts a 1D tunnel structure as illustrated in panels C and D of Figure II. 1.[9] This metastable polymorph crystallizes with *C*2/*m* space

group symmetry and has three distinct vanadium-centered polyhedra: (a) distorted $V(1)O_6$ octahedra that share edges, (b) distorted $V(2)O_6$ octahedra that are connected via corner sharing, and (c) $V(3)O_5$ square pyramids. These linked chains of polyhedra enclose 1D tunnels along the *b* axis with two distinct sites for intercalating cations as illustrated in Figure II. 1G;[32] smaller monovalent cations such as Li^+ and Cu^+ occupy β′ sites, whereas larger cations reside in β sites that are shifted down the tunnels by approximately half a unit cell (*b*/2) as depicted in Figure II. 1G.[23] Our third polymorph, ε-V_2O_5, again crystallizes with *C2/m* space group symmetry with two distinct vanadium-centered polyhedra. In this structure, distorted $V(1)O_6$ octahedra share edges with a crystallographically inequivalent set of distorted $V(2)O_6$ octahedra as shown in panels E and F of Figure II. 1. These units share corners along the crystallographic *b*- and *a*-axes to form infinite sheets, which in turn are fused at the edges to form a double-layered structure. The double layers are further held together by van der Waals interactions, and the interlayer sites therein are much larger than those of the α- and ζ-polymorphs.[8,10,33] Intercalating cations occupy sites between the single layers of α-V_2O_5, between the double layers of ε-V_2O_5, and along the tunnels of ζ-V_2O_5. **Table A2** contrasts the predicted lattice parameters of relaxed structures obtained from GGA+U (with and without van der Waals corrections) calculations with experimental data for the charged (empty) structures. The calculated structures are in good agreement with experimentally derived parameters. Given the tendency of DFT to underestimate dispersive interactions, the explicit introduction of van der Waals interactions vdW-DF2 results in improved agreement with experiment for the *c*

parameter of α-V_2O_5 (**Table A2**), but such calculations tend to greatly overestimate the open circuit voltage and diffusion barriers and are not discussed further.[26]

Intercalation of cations is inevitably accompanied by a change in volume resulting from (a) the addition of the extra cation and (b) the concomitant reduction of the transition metal cation. A substantial volume change is detrimental to the retention of capacity in an intercalation battery because it can give rise to electromechanical degradation of active electrodes.[4,34] **Figure II. 1H** contrasts changes in the volume of the unit cell of the three V_2O_5 polymorphs upon maximal intercalation of Li, Na, and Mg ions. For the ζ-V_2O_5 polymorph, lattice parameters at the intercalation limit of 0.66 have been calculated for Li-ion intercalation and 0.33 for Mg- and Na-ion intercalation. All the structural calculations have been performed using vdW-DF2 to include van der Waals interactions. The Al-ion-intercalated structures could not be converged under these conditions. Notably, the van der Waals bound layered α- and ε-phases are more strongly distorted by the insertion of ions (and also correspond to an increased limit given the higher number of possible sites) than ζ-V_2O_5 is. The latter structure is only minimally distorted (<4%) for all of the cations considered here as a result of its rigid 1D tunnel structure. The larger ionic radius of Na ions leads to the relatively greater lattice expansion noted upon intercalation within the α- and ε-phases. Interestingly, the volume changes induced upon intercalation of Mg ions are minimal as a result of the smaller ionic radius of Mg ions coupled with its divalent charge, which yields a "hard" intercalant that polarizes the anionic framework without considerable lattice expansion. Notably, the volume change is

within 8% for all of the considered scenarios and thus well within the range of practical strains that can be sustained within active electrodes.

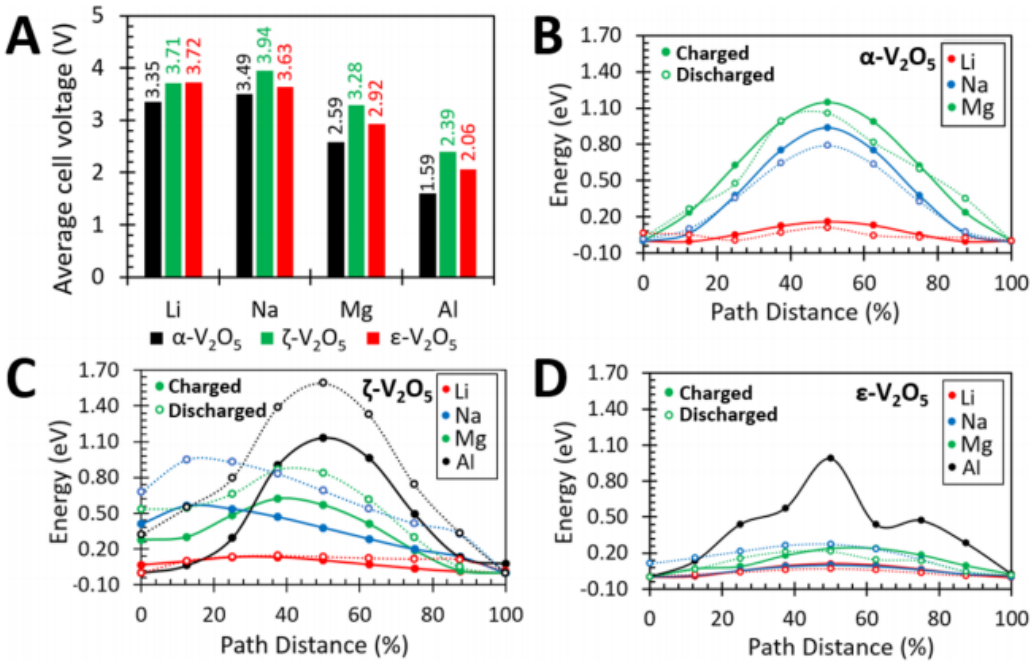

Figure II. 2. (A) Predicted average open circuit voltages of α-, ζ-, and ε-V_2O_5 polymorphs for various intercalating cations. Activation barriers for the diffusion of different cations at both high and low concentrations of the intercalating ions in (B) α-V_2O_5, (C) metastable ζ-V_2O_5, and (D) metastable ε-V_2O_5. The solid lines correspond to low concentrations (charged), whereas dotted lines correspond to high cation concentrations (close to fully discharged).

The fundamental premise of an electrochemical intercalation cell is mass transport driven by a large chemical potential difference between the anode and the cathode with the concomitant flow of electrons. **Figure II. 2A** shows the average open circuit voltage for various ions (Li^+ , Na^+ , Mg^{2+}, and Al^{3+}) in the three polymorphs of V_2O_5 (α-V_2O_5, ζ-V_2O_5, and ε-V_2O_5) calculated using GGA+U.[35,36] The voltages have been deduced for cation stoichiometries $0 < x <$ intercalation limit with intercalation limits being x = 1 for all cations in α- and ε-V_2O_5, 0.66 for Li ions in ζ-V_2O_5, and 0.33 for Na and Mg ions in ζ-

V_2O_5. All the voltages are referenced to their corresponding bulk metal anode (body-centered Li, Na, and Al and hexagonal close-packed Mg). The voltages for intercalation of these metals ions in α-V_2O_5 (3.35 V for Li ions, 3.49 V for Na ions, 2.59 V for Mg ions, and 1.59 V for Al ions) are consistent with the values previously predicted by Gautam et al. and are in reasonable agreement with the GGA +U calculations of Zhou for α-V_2O_5.[26] The calculated voltage ranges are furthermore concordant with experimental observations of approximately 3.2−3.4 V for Li ions, 3.0−3.5 V for Na ions, and 2.2−2.4 V for Mg ions.[6,37,38] Two trends are immediately discernible from **Figure II. 2A**. As in α-V_2O_5, the open circuit voltages monotonically decrease in going from monovalent to divalent to trivalent ions, which parallels the ordering of reduction potentials in the aqueous electrochemical series (−3.04 V vs SHE for Li, −2.71 V for Na, −2.37 V for Mg, and −1.66 V for Al). Next, it is clear that for all of the ions examined here, the metastable ζ- and ε-phases are characterized by appreciably higher voltages compared to that of thermodynamically stable α-V_2O_5. The ζ-phase exhibits a slightly higher open circuit voltage in each case except for Li^+ , where the voltages of the ζ- and ε-phases are nearly identical. Notably, these voltages are substantially higher than those predicted previously for any other V_2O_5 polymorph.[21] The origin of the higher open circuit voltage values predicted for the ζ- and ε-phase polymorphs can be traced to their metastability; α-V_2O_5 is more stable than ζ- and ε-V_2O_5 by 0.17 and 0.21 eV/ V2O5 unit, respectively. As indicated in **Figure A1**, the intercalated phases of α-V_2O_5 are slightly more stable than their intercalated ζ- and ε-phase counterparts. However, the differential in energy between the metastable polymorphs and their discharged phases turns out to be appreciably greater than

the differential for α-V_2O_5. Because the metastable structures are much less stable and thereby lie substantially higher in energy on a potential energy landscape as compared to α-V_2O_5, the chemical potential difference is much greater for these structures, resulting in higher values of the open circuit voltage.

A particularly important factor for battery operation is the stability of the intercalated cathode materials. Hence, **Figure A2** shows the energy (Ehull) of decomposition of MV_2O_5 into its stable constituents.[21] The equations for the decomposition of these materials are provided in the **Appendix A**. A thermodynamically stable structure will have an E^{hull} value of 0 meV, whereas an unstable structure will have a positive E^{hull} value. α-V_2O_5 is the thermodynamic sink in this system and thus has an E^{hull} value of 0. In contrast, ζ-V_2O_5 and ε-V_2O_5 are only 24 and 32 meV higher in energy, respectively. For Li-ion intercalation, α-LiV_2O_5, ζ-$Li_{0.66}V_2O_5$, and ε-LiV_2O_5 are only 45, 23, and 47 meV, respectively, higher in energy than the thermodynamically stable orthorhombic phase γ-LiV_2O_5, indicating α-LiV_2O_5, ζ-$Li_{0.66}V_2O_5$, and ε-LiV_2O_5 phases are metastable but likely accessible at 298 K. Analogously, α-NaV_2O_5, ζ-$Na_{0.33}V_2O_5$, and ε-NaV_2O_5 are also metastable at 298 K, with values of 23, 20, and 47 meV for α-NaV_2O_5, ζ-$Na_{0.33}V_2O_5$, and ε-NaV_2O_5, respectively, higher in energy than the thermodynamically stable phase. α-MgV_2O_5 is 118 meV higher in energy, indicating its instability, whereas ε-MgV_2O_5 has a relatively lower E^{hull} of 83 meV compared to that of α-MgV_2O_5. Surprisingly, ζ-$Mg_{0.33}V_2O_5$ is thermodynamically more stable than its constituents by −17 meV, indicating the ζ-$Mg_{0.33}V_2O_5$ phase is stable at 298 K. α-AlV_2O_5 could not be converged being thermodynamically unstable; in contrast, ε-AlV_2O_5 is rather unstable with

an E^{hull} of 258 meV. However, ζ- $Al_{0.33}V_2O_5$ is only 66 meV higher is energy, indicating its potential stabilization.

Kinetics of Ion Diffusion. A Comparison of Diffusion Barriers and Coordination Environments

The migration of monovalent (Li^+ and Na^+) and multivalent cations (Mg^{2+} and Al^{3+}) has been examined by nudged elastic band calculations for all three polymorphs of V_2O_5 at both low (initial stages) and high (close to fully discharged) concentrations of cations. Because the number of images used for nudged elastic band calculations is quite large, the results obtained are comparable to the computationally more expensive climbing-image nudged elastic band calculations. A comparison of both the methodologies is provided in **Figure A3**, and they indicate very comparable values across the different polymorphs. In the following discussions, the charged state refers to $M_{0.083}V_2O_5$ for all of the polymorphs, whereas the discharged state refers to $M_{0.917}V_2O_5$ in the case of α- and ε-V_2O_5 and $M_{0.33}V_2O_5$ in the case of ζ-V_2O_5, reflecting their respective intercalation limits as discussed above. The discharged state for Li-ion-intercalated ζ-V_2O_5 is ζ-$Li_{0.66}V_2O_5$.

Given the exponential dependence of the diffusivity as a function of the activation energy barrier, a 60 meV change correlates to an approximately 1 order of magnitude change in the diffusion rate. For a compound to be viable as a cathode material at room temperature, the migration barrier should be no greater than ~0.525 eV for a micrometer-sized particle or 0.650 eV for a nanometer-sized particle.[1] The maximal energy required for the hopping of an ion between two low-energy intercalant positions is termed the migration barrier (E_a). Panels B−D of **Figure II. 2** contrast the migration energies for the

diffusion of ions along the crystallographic *b*-axes of α-V_2O_5, ζ-V_2O_5, and ε-V_2O_5, respectively. Migration energies for both the dilute limit (upon insertion of a single cation) shown as a solid line and the high-concentration limit (corresponding to a single cation vacancy) shown as a dotted line are noted in the figure.

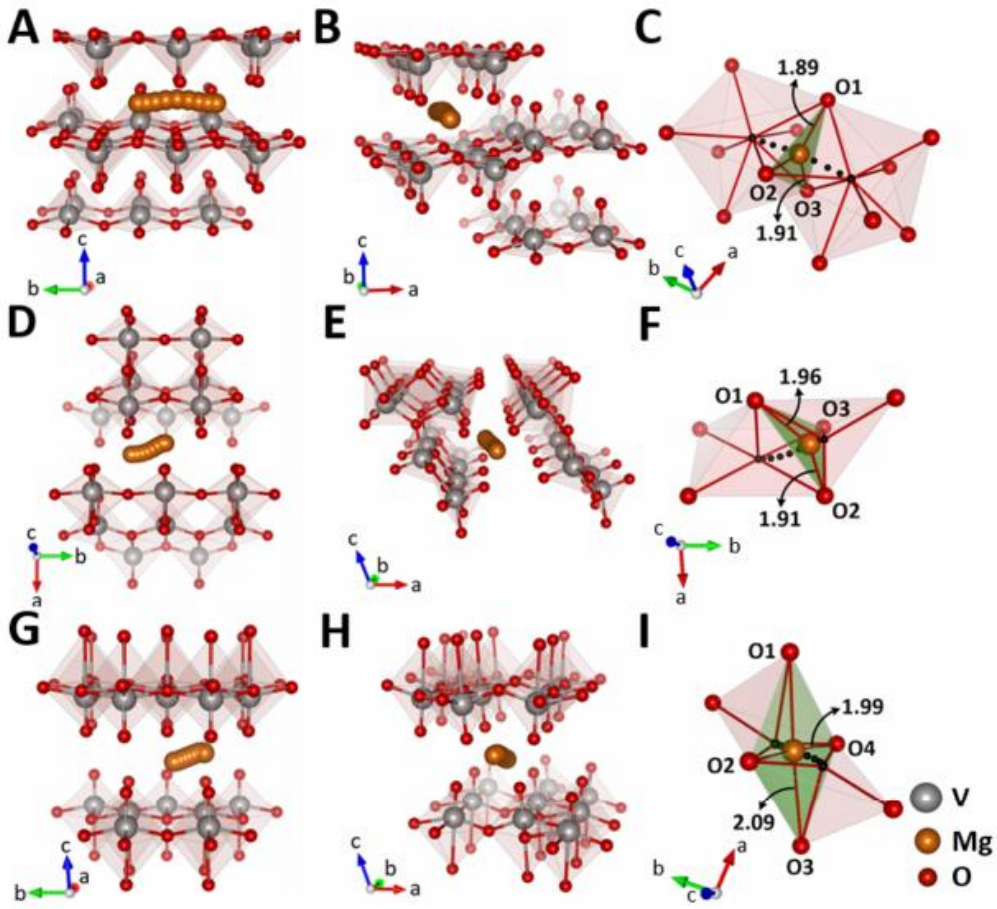

Figure II. 3. Pathways for migration of Mg ions viewed along two different orientations and a view of the oxygen coordination environment at the transition state for (A−C) α-V_2O_5, (D−F) ζ-V_2O_5, and (G−I) ε-V_2O_5.

The two situations correspond to evaluating cation diffusivity near the charged and discharged limits of a multivalent intercalation battery. Because of the strong

thermodynamic instability of certain structures along the ion diffusion pathway, meaningful migration energies are not available for certain combinations of cations within a specific V_2O_5 framework, for instance, Al^{3+} at both low and high concentrations in α-V_2O_5.[26] In each instance, the energy of the lowest-energy initial structure has been set to zero and the path distance has been normalized to 100% along the cation diffusion axis. In Figure 2D, the energies of the end points are unequal for ε-NaV_2O_5; at low concentrations of Na ions, the two end points are equivalent by symmetry and hence of equal energy. However, at high concentrations of Na ions, this equivalence in symmetry is lost, and hence, the end points are inequivalent in energy. **Figure II. 3** depicts the specific diffusion pathways calculated for the diffusion of Mg ions within the three polymorphs. Panels C, F, and I of **Figure II. 3** depict the transition states corresponding to the highest-energy configuration of Mg ions traversing from one low-energy site to another in α-V_2O_5, ζ-V_2O_5, and ε-V_2O_5, respectively.

For the diffusion of Li ions, the migration barriers are well below 0.525 eV (approximately 0.11−0.16 eV in α-V_2O_5, approximately 0.13−0.14 eV in ζ-V_2O_5, and approximately 0.10−0.11 eV in ε-V_2O_5). These activation energy barriers correlate to diffusivities on the order of 2−4 × 10−4 $cm^2\ s^{-1}$. The differences between the different polymorphs are relatively small for Li ions primarily because the monovalent cation does not strongly polarize the anion sublattice, as also illustrated by the relatively small structural distortions induced upon lithiation (**Figure II. 1G**). In contrast, the type of polymorph strongly influences the activation energy barrier for the diffusion of Na ions, which is further consistent with the larger structural distortions induced upon Na-ion

intercalation within the α- and ζ-phases (**Figure II. 1H**). For Na ions, the migration barrier is approximately 0.94−0.96 eV in α-V_2O_5; however, this value significantly decreases to approximately 0.47−0.95 eV in ζ-V_2O_5 and to approximately 0.10−0.25 eV in ε-V_2O_5. These differences can be rationalized in terms of the coordination environment preference of Na ions as discussed in more detail below. Multivalent Mg and Al ions strongly polarize the anion framework; thus, the migration energy barriers are a sensitive function of the specific anion coordination environment (**Figure II. 3**), and the coordination preference of the ions can vary strongly across the different polymorphs. For the diffusion of Mg ions, the migration barrier is approximately 1.15−1.23 eV in α-V_2O_5, consistent with previous calculations by Ceder and co-workers.[5,21] However, this barrier decreases substantially to approximately 0.62−0.86 eV in ζ-V_2O_5 and approximately 0.21−0.24 eV in ε-V_2O_5. The values for Na and Mg ions in the metastable phases are lower than 650 meV, indicating that these materials are indeed candidates for the viable intercalation of multivalent cations and should deliver reasonable high-rate performance. These studies further indicate that the diffusion barriers in these systems are strongly dependent on concentration. In contrast, for trivalent Al ions, the migration barrier remains considerable for the metastable phases of V_2O_5 (approximately 1.13−1.59 eV in ζ-V_2O_5 and approximately 0.99 eV in ε-V_2O_5).

To gain a mechanistic understanding of the origins of the differences in diffusion barriers, we consider in some detail the changes in the anion coordination environment as the cations traverse the path between two low-energy sites. We further examine the modifications to the electronic structure of V_2O_5 induced by cation intercalation. **Figure II. 3** specifically depicts the changes in the local coordination environments of Mg ions.

In α-V_2O_5, diffusion of Mg ions is considered between the layers of V_2O_5 along the crystallographic *b* axis (**Figure II. 3A,B**);[21,26] the staggered 1D row of pendant oxygen atoms renders this a relatively low-energy pathway compared to diffusion along the a direction.[39] As suggested by Ceder and co-workers, the diffusion of Mg ions between the initial and final states requires the Mg ions to squeeze through a shared face as shown in **Figure II. 3C**, which transiently places the Mg ions in an approximately trigonal planar environment.[5,21] In other words, the hopping process of Mg ions in α-V_2O_5 involves a change in coordination from 8 to 3 to 8, with the cations situated in a trigonal planar coordination environment in the transition state (**Figure II. 3C**). The 1.89 Å Mg−O interaction depicted in **Figure II. 3C** suggests a rather strong Mg−O interaction, which defines a rather tight and unfavorable coordination environment for Mg ions in the transition state. The large change in coordination number and the suboptimal coordination of Mg ions in the transition states lead to the large predicted energies of Mg-ion diffusion.

In stark contrast, the metastable ζ-V_2O_5 phase possesses a distinctive 1D open tunnel structure, which defines alternating tetrahedral (β′) and five-coordinated approximately square pyramidal (β) coordination environments along the b axis.[9] As indicated in **Figure II. 3C**, the β sites are energetically more favorable for Mg ions than the β′ sites are (note that the opposite is true for Li ions, where at high concentrations of Li ions, β′ sites are occupied to weaken Li−Li repulsions as indicated by the offset between the lowest-energy points along the diffusion pathway for high- and low-concentration limits in **Figure II. 2C**).[23,40] Hence, the hopping process of Mg ions in ζ-V_2O_5 involves a change in oxygen coordination from 4 (β′) → 3 (transition state) → 5 (β) → 3 (transition

state) → 4 (β′); the energetics of half of the symmetrical pathway is depicted in **Figure II. 2C**. Similar to the α-V_2O_5 phase, the transition state in this metastable phase places Mg ions in a trigonal planar site (**Figure II. 3F**); however, notably, the change in coordination environment is much less acute for this polymorph, and the trigonal planar site is substantially larger. These two factors result in a substantially decreased activation energy barrier for Mg-ion diffusion in this polymorph.

The energetically most favorable intercalation sites in ε-V_2O_5 are quite distinct from the other two phases (**Figure II. 3G−I**). The lowest-energy hopping process involves the diffusion of the Mg ion along the *b* axis. The initial and final intercalated structures involve Mg ions coordinated within quasi-tetrahedral environments. The diffusion pathway links two edge-shared tetrahedra. In complete contrast to the other two phases, the transition state in ε-V_2O_5 consists of a Mg^{2+} ion coordinated within an approximately square planar environment (**Figure II. 3I**). In other words, the Mg ions hop between tetrahedral sites through a square planar transition state with constancy of the overall coordination number from 4 → 4 → 4 along the diffusion path. While the local coordination environment is distorted from tetrahedral to square planar as the Mg ion diffuses through the ε-V_2O_5 lattice, the relatively small change in coordination and the large size of the square planar pocket imply a much lower diffusion barrier. The discussion presented above indicates greatly enhanced mobility of Mg ions in the metastable polymorphs with the following overall ordering of Mg-ion mobilities: α-V_2O_5 < ζ-V_2O_5 < ε-V_2O_5. As suggested by Ceder and co-workers, the suboptimal "frustrated" coordination of Mg ions in the metastable polymorphs likely contributes in large measure to the reduced

diffusion energies because they represent relatively unstable sites.[5,21] The geometry of the transition state clearly also has a substantial role in determining the migration barrier. The transition state in ε-V_2O_5 has a relatively open geometry (Mg−O1 and Mg−O3 distances of 2.09 Å and Mg−O2 and Mg−O4 distances of 1.99 Å), which translates to the smallest diffusion barrier for Mg^{2+} as well as the other ions examined here. In ζ-V_2O_5, the Mg−O distances are as follows: Mg−O1, 1.96 Å; Mg−O2 and Mg−O3, 1.9 Å. They define a slightly more open geometry in the transition state as compared to that in α-V_2O_5 (Mg−O1 and Mg−O2 distances of 1.89 Å and Mg− O3 distance of 1.91 Å). A clear correlation is thus observed between the Mg−O distances in the transition state and the predicted migration barriers. **Figure A4** contrasts the transition states for the high and low cation concentrations. In proximity to the fully discharged limit, we observe lattice distortions that induce a tighter coordination environment around the intercalating cation in the transition state. For instance, in ζ-$Mg_xV_2O_5$, the canting of VO_6 octahedra toward each other shrinks the trigonal planar pocket that needs to be traversed by the intercalating cation, which in turn leads to a higher migration barrier. ε-V_2O_5 shows rather distinctive behavior wherein the migration barrier is reduced at the high-concentration limit because of the activation of a second pathway for cation migration. As shown in **Figure A4**, at low Mg-ion concentrations, the Mg ion hops between adjacent tetrahedral sites via a square planar pocket. With an increasing concentration of Mg ions, the size of the square planar pocket decreases, which in turn results in stabilization of an alternative pathway involving the diffusion of Mg ions from a four-coordinated site to a fivecoordinated site through a distorted trigonal pyramidal pocket as depicted in **Figure A4**. Note that these two pathways

represent the lowest-energy pathways and other possible coordination environments are appeciably higher in energy. **Table A3** illustrates that five-coordinated sites are highly disfavored at low Mg-ion concentrations but only slightly disfavored with respect to four-coordinated sites at high concentrations. Because of the high energy of the pentacoordinated sites, at low concentrations of Mg ions, the 4 → 4 → 4 diffusion pathway is the most energetically favored. However, at high Mg-ion concentrations, the shrinking of the square planar pocket renders this pathway much less favorable, and instead, as a result of the stabilization of a pentacoordinated square pyramidal pocket, a different 4 → 5 → 4 pathway is adopted as illustrated in **Figure A5**. The predicted diffusion barrier is as low as 0.21 eV even at a high concentrations of Mg ions. The introduction of cations within a cathode material inevitably results in a reduction of the oxidation state of the transition metal. In early transition metal oxides, the electrons are added to transition metal nonbonding d orbitals that are of t_{2g} symmetry instead of antibonding e_g orbitals, and thus, the structural distortions are relatively less pronounced. The intercalation of cations within the open-framework V_2O_5 structures is accompanied by a concomitant reduction of a subset of vanadium sites from V^{5+} to V^{4+}; the additional charge is initially localized at these vanadium sites with the specific charge ordering pattern being a function of the size, stoichiometry, and polarizability of the intercalated cation.[23]

Figure II. 4 plots the DFT+U-calculated total and atomprojected density of states for the three V_2O_5 polymorphs upon intercalation of a single Mg ion. The valence band is primarily O 2p in origin, whereas the conduction band states are derived from V 3d states.[23,24,41,42] Orbital-resolved densities of states (DOSs) indicating the relative

contributions of different V 3d orbitals are shown in **Figure A6**. To permit a better understanding of midgap states, a comparison of the total DOS of magnesiated V_2O_5 with pristine V_2O_5 is also provided in **Figure A6**. The intercalation of a Mg ion gives rise to midgap state(s) intermediate in energy between the conduction and valence bands.[24,43]

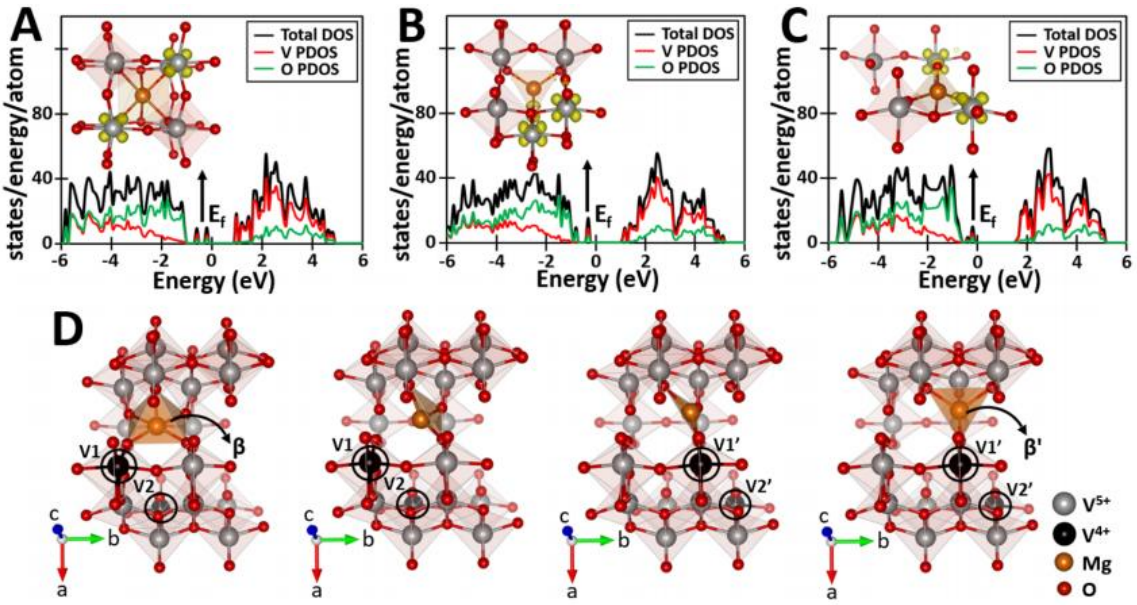

Figure II. 4. Total density of states (DOS) and atom-projected vanadium and oxygen partial density of states (PDOS) calculated for (A) α-V_2O_5, (B) ζ-V_2O_5, and (C) ε-V_2O_5 upon intercalation of a single Mg ion. The insets in these figures depict the differential charge density at vanadium sites suggesting localization of charge on specific vanadium sites. (D) Diffusion of localized charge closely tracks the diffusion of a Mg ion in ζ-V_2O_5. The vanadium atoms that are shaded dark and encircled correspond to a nominal vanadium oxidation state of +4 corresponding to localization of electron density. The intercalated Mg ion is colored orange.

Unlike in β-$Pb_xV_2O_5$, which is characterized by a midgap state derived from interactions between lone-pair Pb $6s^2$ and O 2p orbitals,[23,44] the midgap states upon Mg-ion intercalation result from filling of the lowest-energy nonbonding V 3d states. The specific nature of the midgap state depends on the orbital symmetry and energy positioning

of V 3d orbitals, which in turn is dictated by the structure of vanadium-centered polyhedra. In α-V_2O_5, Mg-ion intercalation results in the addition of electrons to the lowest-lying V $3d_{xy}$ states of two adjacent V atoms, and the midgap states are thus V $3d_{xy}$ in character as indicated by the charge difference plot shown as an inset in **Figure II. 4A**. This plot indicates the increase in charge density on the V_2O_5 framework upon intercalation of Mg ions [see the **Appendix A** for further discussion and a corresponding plot (**Figure A7**) indicating the decrease in charge density along V−O bonds]. In contrast, in ζ-V_2O_5, the midgap states arise from electron localization on hybridized V $3d_{xy}$ and $3d_{yz}$ states derived from two adjacent V atoms, reflecting the better overlap of the V $3d_{xy}$ orbitals that give rise to the bottom of the conduction band with the rest of the conduction band.[17] Notably, **Figure II. 4B** indicates that a single hybrid midgap state is stabilized given the reduced symmetry of this structure as compared to two distinct V $3d_{xy}$ states observed for α-V_2O_5. Finally, in ε-V_2O_5, the midgap state results from localization of electron density in V $3d_{xy}$ states. The stabilization of midgap states and the localization of electron density at specific vanadium sites at low concentrations of Mg-ion intercalation suggest the formation of a small polaron wherein the structure is locally distorted to accommodate the localized charge. As also previously suggested in the literature,[45] the most stable configuration of the small polaron places the localized electron density in the proximity of the intercalated ion. The migration of the polaron will likely further contribute to the diffusion barrier. The specific polaron diffusion energy barriers are known to be sensitive to the Hubbard U values or the extent of electron correlation.[46,47] **Figure A8A** shows the migration of the polaron from V1 to V2, which resides in the proximity of the Li ion in ζ-$Li_{0.083}V_2O_5$. The

polaron migration barrier has been calculated for various values of the U parameter. **Figure A8B** shows the increase in the barrier for the migration of the polaron in ζ-$Li_{0.083}V_2O_5$ with an increasing value of the Hubbard U parameter. This suggests the ability of polaronic distortions to impede cation diffusion. Moreover, the polaronic barrier has been contrasted for α-, ζ-, and ε-$Li_{0.083}V_2O_5$ in **Figure A9**. The figure shows that the polaronic barrier decreases in the following order: ε-$Li_{0.083}V_2O_5$ (∼0.37 eV) > α-$Li_{0.083}V_2O_5$ (∼0.34 eV) > ζ-$Li_{0.083}V_2O_5$ (∼0.24 eV). **Figure II. 4D** illustrates the stepwise diffusion of a Mg ion along the 1D tunnel of ζ-V_2O_5. The diffusion of the Mg ion through the trigonal planar transition state is accompanied by a concomitant motion of the electron density (small polaron hopping) along the V_2O_5 framework. At the transition state, the electron has migrated from positions labeled V1 and V2 to V1′ and V2′. **Figure A10** depicts the motion of the small polaron in α- and ε-V_2O_5. It is important to note that in the case of α-V_2O_5, because all of the vanadium atoms are equivalent by symmetry, the polarons are more localized near the Mg ions. In contrast, in the ζ- and ε-phases, because of the reduction in symmetry, polarons are stabilized on crystallographically inequivalent vanadium atoms that are separated in space, which allows for more facile accommodation of the polaronic structural distortions.

II.4 Conclusions

The limited catalog of compounds that allow for reasonable diffusion of multivalent cations has emerged as a major impediment to the development of rechargeable Mg- and Al-ion batteries. However, the design of multivalent cathodes has thus far been driven almost entirely by empirical considerations inspired by analogies to Li-ion intercalation hosts. In particular, metastable compounds have not been adequately

examined despite the tremendous available range of structural versatility. Here, we have contrasted the thermodynamics and kinetics of insertion of Li^+, Na^+, Mg^{2+}, and Al^{3+} in two synthetically accessible metastable phases of V_2O_5, 1D tunnel structured ζ-V_2O_5 and 2D double-layered ε-V_2O_5, with the thermodynamically stable single-layered α-V_2O_5 phase. The metastability of the ζ- and ε-V_2O_5 polymorphs suggests that open circuit voltages in excess of 3 V (much greater than that of α-V_2O_5) can be derived for Mg- and Na-ion intercalation, reflecting the increased thermodynamic driving force for ion intercalation in these polymorphs that results from their relative instability. Interestingly, the volume change upon insertion of Li, Na, and Mg ions is <8% for all of the polymorphs examined here, which is well within the range for practical electrodes.

A nudged elastic band examination of ion diffusion pathways suggests that migration barriers are substantially diminished for Na- and Mg-ion diffusion in the metastable polymorphs. Specifically, the migration barriers for Mg ions in ζ-V_2O_5 and ε-V_2O_5 are approximately 0.62−0.86 and 0.21−0.24 eV, respectively; for the diffusion of Na ions, the calculated diffusion barriers are approximately 0.47−0.95 and 0.10 eV in ζ-V_2O_5 and ε-V_2O_5, respectively), whereas the diffusivity of these ions is extremely poor in α-V_2O_5. Al-ion diffusion does not appear to be viable at room temperature in any of these polymorphs. The results indicate that topochemically derived metastable polymorphs represent an interesting class of compounds for realizing multivalent cation diffusion because many such compounds place cations in unfavorable coordination environments. For instance, considering Mg-ion intercalation in $Mg_xV_2O_5$, the tetrahedral and square bipyramidal coordination environments accessible to Mg ions are not ideal given that Mg

ions prefer octahedral coordination.[1] In contrast, a thermodynamically stable phase would have optimized the coordination environment for Mg ions. Topochemical ion insertion thus represents a powerful means wherein "frustrated" coordination environments can be enforced. If such an unfavorable initial coordination environment can be coupled to a relatively open transition state, the diffusion barrier can be substantially decreased.

II.5 References

(1) Rong, Z.; Malik, R.; Canepa, P.; Sai Gautam, G.; Liu, M.; Jain, A.; Persson, K.; Ceder, G. Materials Design Rules for Multivalent Ion Mobility in Intercalation Structures. *Chem. Mater.* **2015**, *27*, 6016− 6021.

(2) Yoo, H. D.; Shterenberg, I.; Gofer, Y.; Gershinsky, G.; Pour, N.; Aurbach, D. Mg rechargeable batteries: an on-going challenge. *Energy Environ. Sci*. **2013**, *6*, 2265−2279.

(3) Nitta, N.; Wu, F.; Lee, J. T.; Yushin, G. Li-ion battery materials: present and future. *Mater. Today* **2015**, *18*, 252−264.

(4) Liu, M.; Rong, Z.; Malik, R.; Canepa, P.; Jain, A.; Ceder, G.; Persson, K. A. Spinel compounds as multivalent battery cathodes: a systematic evaluation based on *ab initio* calculations. *Energy Environ. Sci.* **2015**, *8*, 964−974.

(5) Sai Gautam, G.; Canepa, P.; Abdellahi, A.; Urban, A.; Malik, R.; Ceder, G. The Intercalation Phase Diagram of Mg in V_2O_5 from First-Principles. *Chem. Mater.* **2015**, *27*, 3733−3742.

(6) Gershinsky, G.; Yoo, H. D.; Gofer, Y.; Aurbach, D., Electrochemical and spectroscopic analysis of Mg^{2+} intercalation into thin film electrodes of layered oxides: V_2O_5 and MoO_3. *Langmuir* **2013,** *29,* 10964-10972.

(7) Muldoon, J.; Bucur, C. B.; Oliver, A. G.; Sugimoto, T.; Matsui, M.; Kim, H. S.; Allred, G. D.; Zajicek, J.; Kotani, Y., Electrolyte roadblocks to a magnesium rechargeable battery. *Energy Environ. Sci.* **2012,** *5,* 5941-5950.

(8) Galy, J.; Lavaud, D.; Casalot, A.; Hagenmuller, P., Les bronzes oxygénés de vanadium de formule $Cu_xV_2O_5$: I. Structure cristalline des phases $Cu_xV_2O_5$ β et $Cu_xV_2O_5$ ϵ. *J. Solid State Chem.* **1970,** *2,* 531-543.

(9) Marley, P. M.; Abtew, T. A.; Farley, K. E.; Horrocks, G. A.; Dennis, R. V.; Zhang, P.; Banerjee, S., Emptying and filling a tunnel bronze. *Chem. Sci.* **2015,** *6,* 1712-1718.

(10) Monchoux, J.-P.; Dollé, M.; Rozier, P.; Galy, J., Reaction kinetics during synthesis of $Cu_xV_2O_5$ and $Ag_yV_2O_5$ by spark plasma sintering. *Solid State Ionics* **2011,** *182,* 24-31.

(11) Amatucci, G.; Badway, F.; Singhal, A.; Beaudoin, B.; Skandan, G.; Bowmer, T.; Plitz, I.; Pereira, N.; Chapman, T.; Jaworski, R., Investigation of Yttrium and polyvalent ion intercalation into nanocrystalline Vanadium Oxide. *J. Electrochem. Soc.* **2001,** *148,* A940-A950.

(12) Aurbach, D.; Lu, Z.; Schechter, A.; Gofer, Y.; Gizbar, H.; Turgeman, R.; Cohen, Y.; Moshkovich, M.; Levi, E., Prototype systems for rechargeable magnesium batteries. *Nature* **2000,** *407,* 724-727.

(13) Tepavcevic, S.; Liu, Y.; Zhou, D.; Lai, B.; Maser, J.; Zuo, X.; Chan, H.; Král, P.; Johnson, C. S.; Stamenkovic, V., Nanostructured Layered Cathode for Rechargeable Mg-Ion Batteries. *ACS Nano* **2015,** *9,* 8194-8205.

(14) Gautam, G. S.; Canepa, P.; Richards, W. D.; Malik, R.; Ceder, G., Role of structural H_2O in intercalation electrodes: the case of Mg in nano-crystalline Xerogel-V_2O_5. *Nano Lett.* **2016**.

(15) Le, D.; Passerini, S.; Coustier, F.; Guo, J.; Soderstrom, T.; Owens, B.; Smyrl, W., Intercalation of polyvalent cations into V_2O_5 aerogels. *Chem. Mater.* **1998,** *10,* 682-684.

(16) De Jesus, L. R.; Horrocks, G. A.; Liang, Y.; Parija, A.; Jaye, C.; Wangoh, L.; Wang, J.; Fischer, D. A.; Piper, L. F. J.; Prendergast, D.; Banerjee, S. Mapping polaronic states and lithiation gradients in individual V_2O_5 nanowires *Nat. Commun.* **2016,** *7***,** 12022.

(17) Tolhurst, T. M.; Leedahl, B.; Andrews, J. L.; Marley, P. M.; Banerjee, S.; Moewes, A., Contrasting 1D tunnel-structured and 2D layered polymorphs of V_2O_5 relating crystal structure and bonding to band gaps and electronic structure. *Phys. Chem. Chem. Phys.* **2016,** *18,* 15798-15806.

(18) Kang, K.; Ceder, G., Factors that affect Li mobility in layered lithium transition metal oxides. *Phys. Rev. B* **2006,** *74,* 094105.

(19) Meng, Y. S.; Arroyo-de Dompablo, M. E., Recent advances in first principles computational research of cathode materials for lithium-ion batteries. *Acc. Chem. Res.* **2012,** *46,* 1171-1180.

(20) Van der Ven, A.; Bhattacharya, J.; Belak, A. A., Understanding Li diffusion in Li-intercalation compounds. *Acc. Chem. Res.* **2012,** *46,* 1216-1225.

(21) Gautam, G. S.; Canepa, P.; Malik, R.; Liu, M.; Persson, K.; Ceder, G., First-principles evaluation of multi-valent cation insertion into orthorhombic V_2O_5. *Chem. Commun.* **2015,** *51,* 13619-13622.

(22) Chernova, N. A.; Roppolo, M.; Dillon, A. C.; Whittingham, M. S., Layered vanadium and molybdenum oxides: batteries and electrochromics. *J. Mater. Chem.* **2009,** *19,* 2526-2552.

(23) Marley, P. M.; Horrocks, G. A.; Pelcher, K. E.; Banerjee, S., Transformers: the changing phases of low-dimensional vanadium oxide bronzes. *Chem. Commun.* **2015,** *51,* 5181-5198.

(24) Scanlon, D. O.; Walsh, A.; Morgan, B. J.; Watson, G. W., An ab initio Study of Reduction of V_2O_5 through the Formation of Oxygen Vacancies and Li Intercalation. *J. Phys. Chem. C* **2008,** *112,* 9903-9911.

(25) Whittingham, M. S., The role of ternary phases in cathode reactions. *J. Electrochem. Soc.* **1976,** *123,* 315-320.

(26) Zhou, B.; Shi, H.; Cao, R.; Zhang, X.; Jiang, Z., Theoretical study on the initial stage of a magnesium battery based on a V_2O_5 cathode. *Phys. Chem. Chem. Phys.* **2014,** *16,* 18578-18585.

(27) Galy, J., Vanadium pentoxide and vanadium oxide bronzes—structural chemistry of single (S) and double (D) layer $M_xV_2O_5$ phases. *J. Solid State Chem.* **1992,** *100,* 229-245.

(28) Withers, R. L.; Millet, P.; Tabira, Y., The inherent displacive structural flexibility of $M_xV_2O_5$ framework structures. *Z. Kristallogr.* **2000,** *215,* 357.

(29) Perdew, J. P.; Burke, K.; Ernzerhof, M., Generalized gradient approximation made simple. *Phys. Rev. Lett.* **1996,** *77,* 3865.

(30) Dudarev, S.; Botton, G.; Savrasov, S.; Humphreys, C.; Sutton, A., Electron-energy-loss spectra and the structural stability of nickel oxide: An LSDA+ U study. *Phys. Rev. B* **1998,** *57,* 1505.

(31) Bystrom, A.; Wilhelmi, K.; Brotzen, O., Vanadium pentoxide-a compound with five-coordinated vanadium atoms. *Acta. Chem. Scand.* **1950,** *4*, 1119.

(32) Patridge, C. J.; Jaye, C.; Zhang, H.; Marschilok, A. C.; Fischer, D. A.; Takeuchi, E. S.; Banerjee, S., Synthesis, Structural Characterization, and Electronic Structure of Single-Crystalline $Cu_xV_2O_5$ Nanowires. *Inorg. Chem.* **2009,** *48,* 3145-3152.

(33) Tepavcevic, S.; Xiong, H.; Stamenkovic, V. R.; Zuo, X.; Balasubramanian, M.; Prakapenka, V. B.; Johnson, C. S.; Rajh, T., Nanostructured bilayered vanadium oxide electrodes for rechargeable sodium-ion batteries. *ACS Nano* **2011,** *6,* 530-538.

(34) Chan, C. K.; Peng, H.; Liu, G.; McIlwrath, K.; Zhang, X. F.; Huggins, R. A.; Cui, Y., High-performance lithium battery anodes using silicon nanowires. *Nat. Nanotechnol.* **2008,** *3,* 31-35.

(35) Aydinol, M.; Ceder, G., First-Principles Prediction of Insertion Potentials in Li-Mn Oxides for Secondary Li Batteries. *J. Electrochem. Soc.* **1997,** *144,* 3832-3835.

(36) Meng, Y. S.; Arroyo-de Dompablo, M. E., First principles computational materials design for energy storage materials in lithium ion batteries. *Energy Environ. Sci.* **2009,** *2,* 589-609.

(37) Delmas, C.; Cognac-Auradou, H.; Cocciantelli, J.; Menetrier, M.; Doumerc, J., The $Li_xV_2O_5$ system: an overview of the structure modifications induced by the lithium intercalation. *Solid State Ionics* **1994,** *69,* 257-264.

(38) Ali, G.; Lee, J. H.; Oh, S. H.; Cho, B. W.; Nam, K.-W.; Chung, K. Y., Investigation of the Na Intercalation Mechanism into Nanosized V_2O_5/C Composite Cathode Material for Na-Ion Batteries. *ACS Appl. Mater. Interfaces* **2016,** *8,* 6032-6039.

(39) Ma, W.; Zhou, B.; Wang, J.; Zhang, X.; Jiang, Z., Effect of oxygen vacancy on Li-ion diffusion in a V_2O_5 cathode: a first-principles study. *J. Phys. D: Appl. Phys.* **2013,** *46,* 105306.

(40) Yamauchi, T.; Ueda, Y., Superconducting β (β′)-vanadium bronzes under pressure. *Phys. Rev. B* **2008,** *77,* 104529.

(41) Velazquez, J. M.; Jaye, C.; Fischer, D. A.; Banerjee, S., Near edge X-ray absorption fine structure spectroscopy studies of single-crystalline V_2O_5 nanowire arrays. *J. Phys. Chem. C* **2009,** *113,* 7639-7645.

(42) Maganas, D.; Roemelt, M.; Hävecker, M.; Trunschke, A.; Knop-Gericke, A.; Schlögl, R.; Neese, F., First principles calculations of the structure and V L-edge X-ray absorption spectra of V_2O_5 using local pair natural orbital coupled cluster theory and spin–orbit coupled configuration interaction approaches. *Phys. Chem. Chem. Phys.* **2013,** *15,* 7260-7276.

(43) Wu, Q.-H.; Thißen, A.; Jaegermann, W., Photoelectron spectroscopic study of Li intercalation into V_2O_5 thin films. *Surf. Sci.* **2005,** *578,* 203-212.

(44) Wangoh, L.; Marley, P.; Quackenbush, N.; Sallis, S.; Fischer, D.; Woicik, J.; Banerjee, S.; Piper, L., Electron lone pair distortion facilitated metal-insulator transition in β-$Pb_{0.33}V_2O_5$ nanowires. *Appl. Phys. Lett.* **2014,** *104,* 182108.

(45) Carrasco, J., Role of van der Waals Forces in Thermodynamics and Kinetics of Layered Transition Metal Oxide Electrodes: Alkali and Alkaline-Earth Ion Insertion into V_2O_5. *J. Phys. Chem. C* **2014,** *118,* 19599-19607.

(46) Maxisch, T.; Zhou, F.; Ceder, G., Ab initio study of the migration of small polarons in olivine Li_xFePO_4 and their association with lithium ions and vacancies. *Phys. Rev. B* **2006,** *73,* 104301.

(47) Garcia-Lastra, J.; Myrdal, J.; Christensen, R.; Thygesen, K.; Vegge, T., DFT+ U study of polaronic conduction in Li_2O_2 and Li_2CO_3: implications for Li–Air batteries. *J. Phys. Chem. C* **2013,** *117,* 5568-5577.

CHAPTER III

EVALUATION OF MULTIVALENT CATION INSERTION IN SINGLE- AND DOUBLE LAYERED POLYMORPHS OF V_2O_5*

III.1 Introduction

Over the last two decades, rechargeable Li-ion batteries have emerged as the pre-eminent technology for electrochemical energy storage and have underpinned the explosive worldwide growth of portable consumer electronics.[1–3] However, the need for vehicle electrification and grid-level storage has now outpaced the capabilities of Li-ion batteries. Rechargeable batteries based on multivalent ions have emerged as potential alternatives but still lag far behind in terms of technology development. Indeed, many fundamental material issues relevant to such systems remain to be resolved.[4–6] Multivalent metal anodes offer high-energy densities, improved safety, and are thought to be less susceptible to material scarcity considerations.[7,8] The theoretical volumetric energy densities for such anodes are 3832 mAh cm^{-3} for Mg, 2073 mAh cm^{-3} for Ca, and 8046 mAh cm^{-3} for Al, which compare rather favorably to the energy density of the safer graphite intercalation anode for Li, ca. 800 mAh cm^{-3}.[4,5] Apart from the potential benefits derived from using high-capacity metallic Mg, Ca, or Al anodes, an enhancement of the volumetric capacity is expected from the availability of multiple electrons per unit cation intercalated at the cathode.[1,9] The primary limitation of most cathodes is the number

*Reprinted with permission from "Evaluation of Multivalent Cation Insertion in Single-and Double-Layered Polymorphs of V_2O_5." by A. Parija, D. Prendergast, S. Banerjee, *ACS Appl. Mater. Inter.* 2017, **9**, 23756-23765.

of intercalation sites rather than the accessibility of redox couples at transition metal centers. If the number of intercalation sites that can accommodate cations is held constant, the inserted multivalent ions will reduce the cathode more as compared to monovalent cations, yielding a higher capacity. Despite the perceived benefits, the development of viable multivalent intercalation batteries has been hindered by the limited number of viable cathode materials. The polarizing nature of multivalent cations distorts the anionic sublattice and gives rise to large diffusion barriers in many intercalation hosts.[10–13]

α-V_2O_5, first compositionally isolated in 1868, is the thermodynamically most stable phase of V_2O_5[14] and has garnered much attention as a potential cathode material since the early work of Whittingham and co-workers.[15] Layered α-V_2O_5 has shown Mg-ion capacities of >150 mAh g^{-1} over a potential range of 2.2−3.0 V.[16] A fundamental challenge with diffusing Mg-ions within this structure is that it involves drastic changes of the local coordination number from 8 → 3 → 8, requires Mg-ions to hop through a narrow trigonal planar transition state, and involves relatively stable eight-coordinated sites, from which the Mg-ions can be difficult to eject.[8,16–19] Carrasco has examined the intercalation of a variety of alkali and alkaline-earth cations in this polymorph using density functional theory (DFT) calculations taking into account dispersive interactions, and, indeed, diffusion barriers for Ca and Sr-ions are predicted to be substantially higher as compared to the values deduced for Mg-ions.[20] The rich phase diagram of binary and ternary vanadium oxides provides access to a diverse range of open frameworks, allowing for large tunability of intercalation pathways and energetics.[4,21–24] This rich compositional and phase space renders these compounds particularly of interest for exploration of the

correlation between specific structural motifs and the thermodynamics and kinetics of multivalent cation intercalation. In this article, we explore the role of specific structural characteristics accessible in metastable V_2O_5 polymorphs: single versus condensed double layers, planar versus puckered layers, and varying stacking sequences of double layers. The metastable polymorphs are accessible via the topochemical elimination of cations from ternary vanadium oxide bronzes with the formula $M_xV_2O_5$; the specific V_2O_5 frameworks adopted within these compounds depend on the size, stoichiometry (x), and charge of the M cation.[21,23,25] Indeed, in recent work, we have demonstrated stabilization of a one-dimensional tunnel-structured ζ-phase of V_2O_5.[22] A double-layered polymorph, the ε-phase of V_2O_5, has been synthesized by topochemical deintercalation of Cu from ε-$Cu_xV_2O_5$.[22,26,27] In our previous work, we predicted, based on DFT calculations, that these novel metastable phases will show low diffusion barriers for Mg-ion diffusion and are further characterized by a high open-circuit voltage (OCV).[17] The ζ-V_2O_5 structure enforces rather unfavorable tetrahedral and square-pyramidal local coordination environments for Mg-ions, whereas in ε-V_2O_5, the Mg-ions reside within tetrahedral sites. A combination of frustrated coordination, energetically similar sites, and relatively capacious transition states gives rise to a low diffusion barrier for both these polymorphs. As other examples of metastable intercalation hosts, Hwang et al. reported increased Li-ion diffusion in MoS_2 by increasing the interlayer spacing.[28] Similarly, bilayered V_2O_5 showed increased Na-ion diffusion as a result of an increase in interlayer spacing.[29]

In this study, we have attempted to address this problem and have specifically contrasted cation diffusion mechanisms in several related single- and double-layered

phases of V_2O_5 to elucidate structure−function correlations. The specific bonding motifs within the layers as well as their sequence of stacking defines the diffusion pathways for cations and thereby the magnitudes of the diffusion barriers. The electrochemical parameters that are influenced by the diffusion barriers include the charging rate, the ability to access the full theoretical capacity, and cyclability. Other characteristics that are of no less importance include the voltage and volume change upon intercalation. In order to rationally design these vitally important electrochemical metrics, we have used first-principles DFT to correlate specific structural motifs to the predicted OCV (a thermodynamic quantity) and the diffusion barrier (a measure of the kinetics of cation diffusion and a function of the specific diffusion pathways adopted in the single- and double layered polymorphs). The polymorphs examined here are particularly promising as Ca-ion intercalation hosts. The intercalation of Ca-ions is much less studied as compared to that of Mg-ions;[20] studies have focused largely on Prussian blue structure types, such as manganese hexacyanoferrate, although reversible capacities remain low.[30,31] Ca-ions have a lower reduction potential than Mg-ions and are more abundant in the Earth's crust.[7] The thermodynamics and kinetics of intercalating both Ca- and Mg-ions is contrasted with that of Na- and Li ions in each case here.

Figure III. 1 demonstrates the crystallographic relationships between the different phases. In all subsequent discussions, we have represented intercalated $M_xV_2O_5$ as γ/δ/ρ and the empty metastable V_2O_5 polymorphs as γ′/δ′/ρ′. The first phase under consideration is single-layered γ′-V_2O_5, which can be conceptualized as being derived from the topochemical deintercalation of Li from γ-$Li_xV_2O_5$ ($1 < x < 2$).[32] Li-ion insertion within

α-V_2O_5 beyond a stoichiometry of ca. 1.0 Li per formula units results in a pronounced rearrangement of the two-dimensional (2D) layers of V_2O_5, leading to an alternating up and down pattern of [VO_5] square pyramids within γ-$Li_xV_2O_5$, which has the effect of increasing the number of possible coordination sites.[3,33] This framework (γ′-V_2O_5) is preserved upon electrochemical delithiation and thus this structure is synthetically accessible.[34]

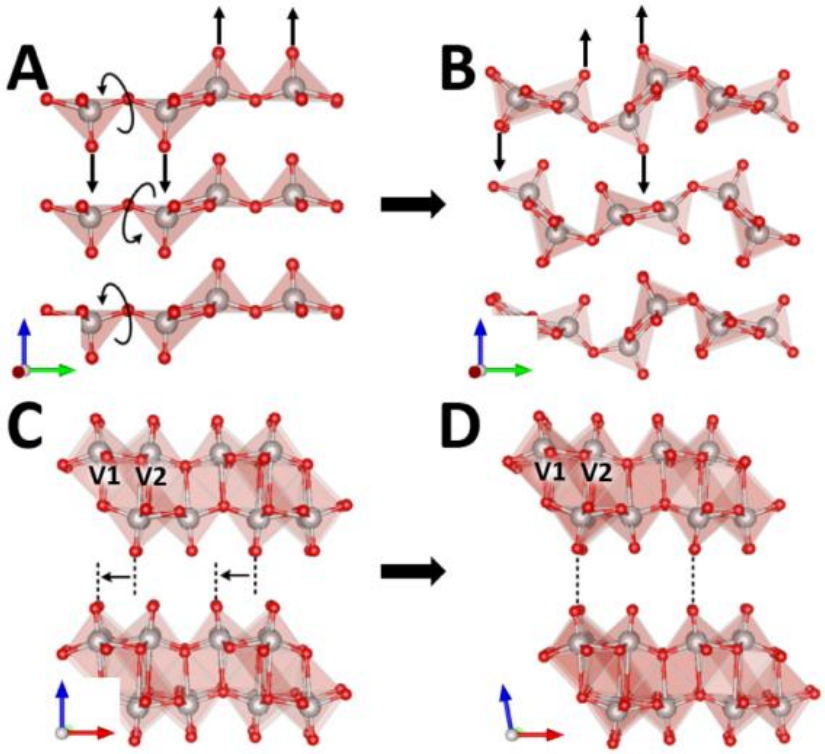

Figure III. 1. Supercell structures of (A) α-V_2O_5, (B) γ′-V_2O_5, (C) δ′-V_2O_5, and (D) ρ′-V_2O_5. The gray and the red spheres represent vanadium and oxygen atoms, respectively. α-V_2O_5 is transformed to γ′-V_2O_5 by rotation of two [V_2O_5] pyramids (A, B), whereas δ′-V_2O_5 can be transformed to ρ′-V_2O_5 by sliding of alternate [V_2O_5] double layers (C, D).

Multivalent cation insertion in undistorted (α) and distorted (γ′) single-layered phases are contrasted to cation insertion in a pair of double layered 2D δ′-V_2O_5 and ρ′-

V_2O_5 structures (**Figure III. 1C,D**). The δ-$M_xV_2O_5$ structure is commonly encountered for different transition metal intercalants and involves cations situated between condensed V_4O_{10} double layers.[21] Some examples of the parent structure include δ-$K_{0.5}V_2O_5$ and δ-$Sr_{0.5}V_2O_5$ (note that the double-layered δ′ polymorph is distinct from the single-layered δ-phase previously considered by Ceder[24] and also that the structures have been stabilized without hydration of intercalated cations in previous work by our group and others).[21,35–38] The ρ′-phase differs from the δ′-phase in terms of the stacking sequence of the V_4O_{10} layers and can be generated by sliding of two alternate layers with respect to each other as indicated in **Figure III. 1C,D**.[23,39,40]

III.2 Theoretical Methods

Ground-state electronic calculations were performed using DFT[41,42] as implemented in the Vienna *ab initio* simulation package (VASP).[43] Electronic exchange and correlation effects were included using the Perdew−Burke−Ernzerhof (PBE) formulation of the generalized gradient approximation (GGA) to the exchange-correlation potential.[44] In calculations of the thermodynamic parameters such as the hull energies, OCVs, and lattice parameters, we employed the DFT+U formalism of Anisimov et al.,[45] wherein strong on-site Coulomb interactions of the vanadium 3d-electrons are approximated using a Hubbard model, with a specific on-site potential of U = 4.0 eV.[46] All the lattice parameter calculations were performed using the vdW-DF2 functionals developed by Langreth and Lundqvist among others,[47–50] to explicitly account for van der Waals' interactions. Calculations were further performed using the optB86b-vdW functional, which has shown promising improvements over the vdW-DF2 functional for

layered compounds.[51] The vdW-DF2 method was not employed in the calculation of hull energies, OCV, and the diffusion barrier because these methods are known to overestimate these parameters.[24,52] Electron−ion interactions were incorporated using the projector augmented wave formalism. Electronic structure was described within a plane-wave basis with a kinetic energy cutoff of 600 eV. In the total energy calculations, a Monkhorst-packed reciprocal space grid of 4 × 4 × 4 k-points for the unit cells and 2 × 2 × 2 k-points for the supercells was used for numerical sampling of the first Brillouin zone. Because the structures of the V_2O_5 systems discussed here are vastly different with significantly different total energies, it is assumed that the contribution of vibrational degrees of freedom to the total energy is negligible. It is worth noting that thermodynamically metastable phases of V_2O_5 are synthetically accessible in nanostructured form upon topochemical deintercalation and represent kinetically trapped species. In these structures, the barrier to the most thermodynamically stable phase cannot be overcome at room temperature.[21] Full phonon calculations to evaluate the potential energy landscapes have not been performed, given the large unit cells considered here.

The nudged elastic band (NEB) method as implemented in VASP was used to calculate the diffusion barriers of the mono/multivalent ions in various polymorphs of V_2O_5. As demonstrated in our previous work, the difference between NEB and climbing-image NEB (CI-NEB) methods is insignificant for these systems.[17] CI-NEB, being more computationally expensive, was not used in this case. A total of seven images were interpolated between the initial and the final relaxed structures in each case. As previously discussed by Liu et al., DFT was used instead of DFT+U because of the difficulty in

stabilizing metastable image points with the latter approach.[9] It is notable that Ceder and co-workers have reported that no significant improvements in the diffusion barriers were found upon using DFT+U calculations.[4,9] The initial and the final images were optimized until the Cartesian components of the forces were below ±0.05 eV $Å^{-1}$; the forces along the NEB pathway were optimized to values below 0.1 eV $Å^{-1}$. To avoid spurious interactions, the supercells used were larger than 9.1 Å in each case.

III.3 Results and Discussion

Thermodynamic Aspects of Multivalent Cation Intercalation

Lattice Parameters and Volume Expansion

α-V_2O_5 is a layered structure built from [VO_5] square pyramidal units sharing edges on one side and corners on the other side to form zigzag linear sheets along the crystallographic a axis (**Figure III. 1A**).[53] These sheets are held together by van der Waals' interactions to form a layered compound with a space group symmetry of *Pmmn*. Electrochemical lithiation of this phase up to a Li content $1 < x < 2$ of $Li_xV_2O_5$ stabilizes the γ-phase, which can be deintercalated electrochemically to obtain the distorted γ′-V_2O_5 polymorph.[32] γ′-V_2O_5 is also a layered structure and crystallizes in the *Pnma* space group (**Figure III. 1B**). However, in α-V_2O_5 the apical oxygen atoms of pairs of adjacent [VO_5] units alternate in opposite directions along the c axis, whereas in γ′-V_2O_5, the apical oxygen atoms from each [VO_5] unit alternate in opposite directions along the c axis (delineated by arrows in **Figure III. 1B**). This configuration can be conceptualized as arising from the rotation of two [VO_5] square pyramidal units by 180° with respect to each other, along their shared corner oxygen atom. Furthermore, the apical V=O bonds are

oriented directly along the c axis in α-V_2O_5, whereas in γ′-V_2O_5 they are slightly skewed (**Figure A11** in Appendix A). The second set of polymorphs shown in panels C and D of **Figure III. 1** are δ′- V_2O_5 and ρ′-V_2O_5, respectively. These polymorphs differ from α-V_2O_5 and γ′-V_2O_5 in having double-layered condensed V_4O_{10} sheets arrayed along the c axis (**Figure A11**). The δ′-V_2O_5 polymorph crystallizes with a space group symmetry of *C2/m* and has two distinct [V(1)O_6] and [V(2)O_6] octahedral units, which share edges along the a and b axes to form infinite sheets. The lamellar sheets of δ′-V_2O_5 and ρ′-V_2O_5 are similar in terms of their local structure but have a substantially altered stacking sequence along the a axis (**Figure A11**), which changes the space group symmetry of the ρ′-phase to *Cmcm*. **Figure III. 1C,D** illustrates that the double-layered sheets are congruently stacked on top of each other with apical oxygen atoms of two different sheets facing each other in ρ′-V_2O_5, whereas in δ′-V_2O_5 these sheets are shifted by 1.9 Å along the a axis. **Table A4** provides the calculated lattice parameters for the empty metastable polymorphs.

Cation intercalation in the host lattice brings about a distortion of the lattice because the host has to make space for the extra volume of the intercalated cation. Furthermore, the reduction of the transition metal center accompanying cation insertion typically weakens metal−ligand bonds and results in an expansion of the host framework. The insertion of multivalent cations oftentimes leads to lattice contraction. The volumetric change induced by cation insertion represents an important practical consideration because large volume changes can result in electromechanical degradation and loss of capacity. **Figure III. 2A** contrasts the percentage volume of the unit cells at maximal

intercalation for α-V_2O_5, γ′-V_2O_5, δ′-V_2O_5, and ρ′-V_2O_5. For α-V_2O_5, γ′-V_2O_5, and δ′-V_2O_5, the final stoichiometry for the intercalated lattice is MV_2O_5, whereas for ρ′-V_2O_5, it is $M_{0.5}V_2O_5$. All of the calculations have been performed using the vdW-DF2 functional to account for the influence of van der Waals' interactions,[50] which clearly play an important role for these layered structures.

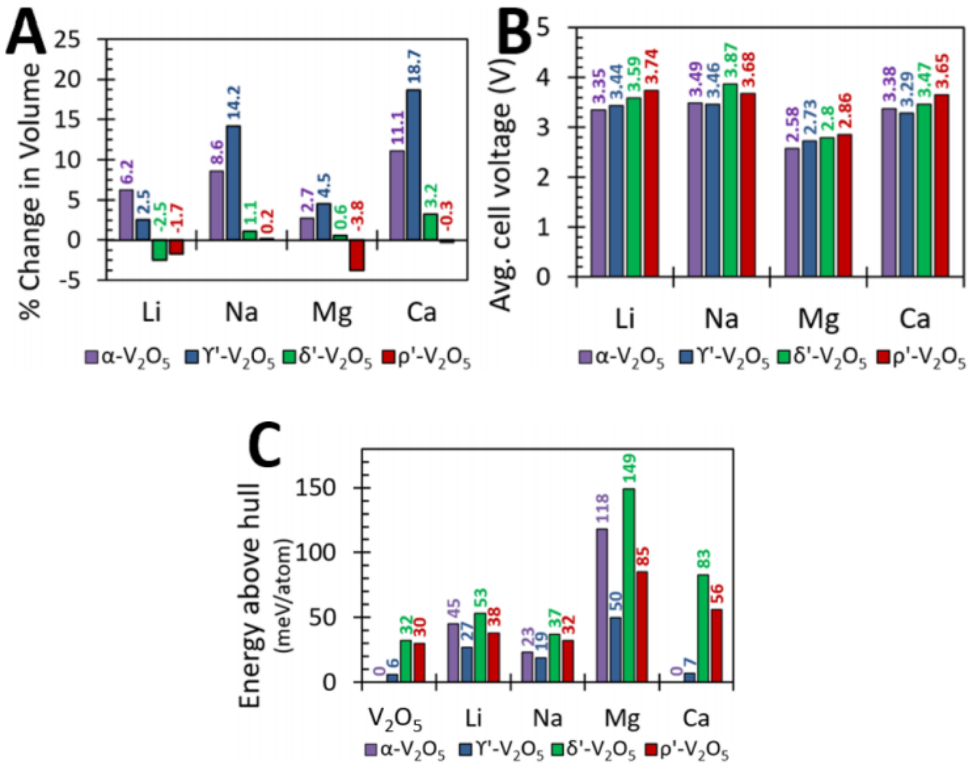

Figure III. 2. (A) Volume expansion of the different polymorphs of V_2O_5 after intercalation with Li, Na, Mg, and Ca cations up to their respective stoichiometric limit. For γ′-V_2O_5 and δ′-V_2O_5, the final stoichiometry for the intercalated lattice is MV_2O_5, whereas for ρ′-V_2O_5, it is $M_{0.5}V_2O_5$. (B) Predicted average OCV for the different V_2O_5 polymorphs at both low and high concentrations of various intercalating cations. (C) The energy above-hull (E^{hull}), which predicts the stability of the polymorphs with respect to their stable constituents in meV/atom. An E^{hull} value of 0 meV/atom represents the polymorph, which is the ground state of the system. The equations for these calculations are listed in the Appendix A.

A recent insightful study suggests that the optB86b-vdW functional can better account for dispersive interactions as compared with the vdWDF2 functional.[51] However, in the case of γ′-V_2O_5, the use of the optB86b-vdW functional yields lattice constants substantially lower than experimentally determined values (**Table A5**). In general, the vdW-DF2 functional (**Tables A4 and A5**) slightly overestimates the lattice parameters in comparison to PBE+U and optB86b-vdW. In this work, the discrepancy between vdWDF2 and the experimentally determined lattice parameters is consideration, all of the putative cathode materials, with the exception of α-V_2O_5 and γ′-V_2O_5 with intercalated Na- and Caions have a volume change of less than 7%, suggesting that these structures represent viable cathode materials from an electromechanical perspective.

OCV

The chemical potential difference between the cathode and the anode material provides a direct measure of the expected OCV.

The OCV is a thermodynamic quantity that can be calculated as

$$\emptyset(x) = \frac{\mu^{\text{cathode}}(x) - \mu^{\text{anode}}}{Ze} \quad \ldots \qquad \text{(III.1)}$$

where $\mu^{\text{cathode}}(x)$ is defined as the energy difference between the metallated cathode and the pure cathode, μ^{anode} is defined as the free energy per atom of the metallic anode (body-centered cubic Li and Na, hexagonal close-packed (hcp) Mg, and face centered cubic Ca), *e* represents the electronic charge, and *Z* is the charge of the cation.[54,46] The average OCVs for mono- and multivalent ions (Li, Na, Mg, and Ca) in various polymorphs of V_2O_5 (γ′-V_2O_5, δ′-V_2O_5, and ρ′-V_2O_5) have been calculated using GGA+U and are plotted in **Figure III. 2B**.[55,56] The cation concentration used for the calculation of OCV is $0 < x < 1$ for γ′-

V_2O_5 and δ′-V_2O_5, and $0 < x < 0.5$ for ρ′-V_2O_5. Bulk metallic anodes (body-centered Li and Na; hcp Mg and Ca) are used as references for the calculation of voltages. The average OCV values calculated for metal ions in α-V_2O_5 (3.35 V for Li-ions, 3.49 V for Na-ions, 2.58 V for Mg-ions, and 3.38 V for Caions)[17] agree well with the experimentally observed values of approximately 3.2−3.4 V for Li-ions, 3.0−3.5 V for Na-ions, 2.2−2.4 V for Mg-ions, and 2.8−3.2 V for Ca-ions.[16,57–59] Predicted values for γ′-V_2O_5 (3.44 V for Li-ions, 3.46 V for Na ions, 2.73 V for Mg-ions, and 3.29 V for Ca-ions), δ′-V_2O_5 (3.59 V for Li-ions, 3.87 V for Na-ions, 2.8 V for Mg-ions, and 3.47 V for Ca-ions), and ρ′-V_2O_5 (3.74 V for Li-ions, 3.68 V for Na-ions, 2.86 V for Mg-ions, and 3.65 V for Ca-ions) follow the same trend as the standard reduction potentials in the aqueous electrochemical series (−3.04 V vs standard hydrogen electrode for Li, −2.71 V for Na, −2.37 V for Mg, and −2.87 V for Ca).[60] Notably, a key benefit of using the metastable phases is that their OCV values are invariably larger than those of α-V_2O_5 for each of the ions considered. The reason for the higher OCV values deduced for the metastable phases is the relative instability of the metastable polymorphs in comparison to α-V_2O_5, which is the thermodynamic sink in this system. As shown in **Figure A12**, the metastable phases γ′-V_2O_5, δ′-V_2O_5, and ρ′-V_2O_5 are 6, 32, and 30 meV per V_2O_5 unit higher in energy as compared with α-V_2O_5. The intercalated phases of α-V_2O_5 are more stable than the intercalated phases of metastable V_2O_5. However, the difference in energy between the cation intercalated metastable polymorphs and the empty (discharged) metastable polymorphs is higher in each instance in comparison to the same differential in energy for α-V_2O_5. This provides as much as a 390 meV higher voltage for the metastable

polymorphs. The double-layered δ′-V_2O_5 and ρ′-V_2O_5 phases furthermore show a higher OCV value as compared to that of the γ′-phase.

Energy above the Hull

The stability of the cathode material and its ability to retain its crystal structure (and not be transformed to an entirely different polymorph or decomposed to other compounds) is an important practical consideration for an intercalation battery. Hence, **Figure III. 2C** shows the calculated energies of decomposition (E^{hull}) of each of the polymorphs to their stable constituents. A cathode material with an E^{hull} value of zero is considered to be thermodynamically stable, whereas a positive E^{hull} value infers relative instability. The equations for the decomposition of the cathodes are provided in the Appendix A. To be a truly thermodynamic estimate, E^{hull} should reflect the free energy difference including finite temperature effects in both enthalpy and entropy. Our assumption, also used by others,[9,24] is that the free energy difference might be less dependent on entropy that might be common to both phases. If E^{hull} is within k_BT of the thermodynamic minimum, we might expect the phase to be accessible, as posited by Ceder and co-workers.[9,24] As noted above, α-V_2O_5 is the lowest-energy state with an E^{hull} value of zero. In comparison, γ′-V_2O_5, δ′-V_2O_5, and ρ′-V_2O_5 are 6, 32, and 30 meV higher in energy, respectively, which suggests that these structures should indeed be accessible (albeit metastable) at 298 K. Similarly, α-LiV_2O_5, γ-LiV_2O_5, δ-LiV_2O_5, and ρ-$Li_{0.5}V_2O_5$ are 45, 27, 53, and 38 meV higher in energy as compared to the ground state, suggesting that these systems are again metastable but accessible at room temperature. Analogously, α-NaV_2O_5, γ-NaV_2O_5, δ-NaV_2O_5, and ρ-$Na_{0.5}V_2O_5$ are also metastable and have similar

values of 23, 19, 37, and 32 meV, respectively, well within the range that can be accessed at 298 K. In contrast, the calculated E^{hull} values for α-MgV_2O_5 and δ-MgV_2O_5 are 118 and 149 meV, respectively, indicating that the fully intercalated polymorphs would be highly unstable and thus unsuitable as cathode materials. However, two of the other polymorphs, γ-MgV_2O_5 and ρ-$Mg_{0.5}V_2O_5$, are at 50 and 85 meV, relatively less unstable, and combined with their reasonable OCV values, represent potentially viable candidates for Mg-ion intercalation cathodes. Interestingly, the slight change in stacking sequence from δ-MgV_2O_5 to ρ-$Mg_{0.5}V_2O_5$ increases the stability of the Mg-ion intercalated phase by 64 meV by altering the local coordination environment (which will be discussed in some detail below). With regard to the Ca-ion intercalated materials, γ-CaV_2O_5, δ-CaV_2O_5, and ρ-$Ca_{0.5}V_2O_5$ are only 7, 83, and 56 meV, respectively, higher in energy than the thermodynamic stable phase α-CaV_2O_5. Indeed, all three of these polymorphs thus represent viable candidates for Ca-ion batteries from a thermodynamic perspective.

Kinetic Aspects of Multivalent Cation Diffusion

Migration Energy Barriers

The preceding section unveiled several potential candidates for multivalent intercalation cathodes that are thermodynamically accessible at room temperature, yield high OCVs, and show minimal volume expansion upon cation intercalation. However, thermodynamics represents a necessary but insufficient criterion for a cathode material; an optimal cathode material must also be able to diffuse multivalent cations at a reasonable rate. Energy barriers to the diffusion of monovalent (Li and Na) and divalent cations (Mg and Ca) have been evaluated using the NEB approach.[17] The migration energy barrier (E_b)

is defined as the energy required for an intercalating cation to hop between two low energy sites, across a transition state whose geometry typically determines the magnitude of the barrier. In other words, it represents the peak of the energy profile of the system as the cation diffuses from one stable site to another. If a cation has to diffuse across sites that are spaced far apart in energy (for instance, if the sites have vastly different coordination environments), the activation energy barrier will inevitably be high. If the sites are relatively similar in terms of the local coordination geometry and energy, a relatively lower activation energy barrier is possible depending on the availability of a low energy diffusion pathway.

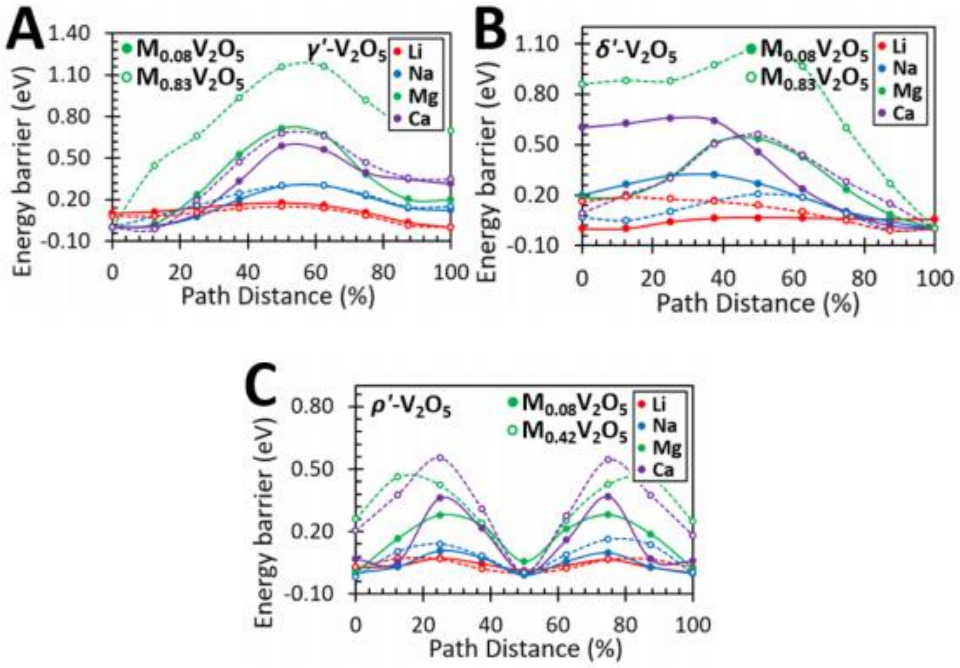

Figure III. 3. Activation barriers of (A) γ′-V_2O_5, (B) δ′-V_2O_5, and (C) ρ′-V_2O_5 at both low and high concentrations of metal ions. The dashed line represents the low-concentration (charged) limit, whereas the solid line represents the high-concentration (discharged) limit.

As a point of calibration, a 60 meV change in barrier height is enough to change the diffusivity of the intercalants by 1 order of magnitude. For a micrometer sized particle to be used as a viable cathode material at room temperature, the energy barrier should be no greater than 0.525 eV; for a nanometer-sized particle, for room-temperature operation, the barrier should be no greater than 0.650 eV.[4] **Figure III. 3** shows the migration energy barriers calculated for Li, Na, Mg, and Ca ions in γ′-V_2O_5, δ′-V_2O_5, and ρ′-V_2O_5. The charged state refers to $M_{0.083}V_2O_5$ in all of the polymorphs of V_2O_5, whereas the discharged state refers to $M_{0.83}V_2O_5$ in γ′-V_2O_5 and δ′-V_2O_5 and $M_{0.42}V_2O_5$ in the ρ′-V_2O_5 polymorph; these approximations to the discharged limit are necessarily one cation short of their respective full intercalation limits (the introduction of a cation vacancy facilitates calculation of the diffusion barrier at high cation concentrations). The lowest energy configuration is set to zero, and the path distance for the migration of the cations is normalized to 100%. In **Figure III. 3A,B**, for γ′-V_2O_5 and δ′-V_2O_5, the end points are unequal in energy because the initial (zero) state represents a tetrahedral site, whereas the end (100% path length) point reflects a square pyramidal site. In other words, the migration barriers for these polymorphs represent hopping of the cations between two crystallographically inequivalent sites, a second hop in each case would bring the cation to a crystallographically equivalent position to the initial site. The diffusion barriers depicted in **Figure III. 3** correspond to the diffusion of cations along the lowest-energy pathways between accessible coordination environments. **Table A6** provides a complete listing of the energies for occupation of different possible coordination environments in these polymorphs, and **Figure A13** depicts the viable coordination sites. These

considerations suggest that the diffusion from tetrahedral → square pyramidal → tetrahedral sites represents the lowest energy pathway in the δ′- and γ′- polymorphs.

In the case of Li-ions, the diffusion barriers are quite low (0.15−0.18 eV for γ′-V_2O_5, 0.07−0.19 eV for δ′-V_2O_5, and 0.07 eV for ρ′-V_2O_5), which corresponds to diffusivity values in the range of 2−4 × 10−4 cm^2 s^{-1} (at 298 K assuming an attempt frequency of 3 × 1013 Hz and an average hopping distance of 4.0 Å, as derived from previous work by Zhou et al).[46] These values are comparable or better than the diffusion barriers of 0.11−0.16 eV deduced for Li-ions in α-V_2O_5.[17] As the smallest cation, Li-ion diffusion perturbs the V_2O_5 frameworks by the least amount (**Figure III. 2A**), and the diffusion of this ion is also relatively less sensitive to the spatial confinement imposed at the transition state (the motion of larger Na- and Ca-ions is much more circumscribed by the transition state geometry). Interestingly, for γ′-V_2O_5, the diffusion barrier decreases from 0.18 to 0.15 eV as the Li-ion concentration is increased from 0.08 to 2.0 Li-ions per formula unit of V_2O_5. The diffusion pathway involves migration of a Li-ion from a square pyramidal site to a tetrahedral site. At a lower Li-ion concentration, the square pyramidal site is 0.10 eV higher in energy than the tetrahedral site and this difference remains comparable at a higher Li-ion concentration (0.09 eV). This in turn leads to a lower diffusion barrier at higher Li-ion concentrations. The larger size of Na-ions leads to a greater lattice distortion (**Figure III. 2A**) and makes for a tighter squeeze through the transition states, which results in higher diffusion barriers as compared to those of Li-ions. In α-V_2O_5, the diffusion barrier is 0.94−0.96 eV for Na-ions.[17] It is greatly decreased to 0.30 eV in γ′-V_2O_5, despite retention of the single-layered structure. The migration barrier

for Na-ions is further decreased in the double-layered polymorphs of V_2O_5 (ca. 0.22−0.32 in δ′-V_2O_5 and ca. 0.12−0.18 eV in ρ′-V_2O_5). The reason for the decrease in the diffusion barrier is discussed with reference to the changes in the local coordination environment and transition state geometry below. Multivalent Mg- and Ca-ions have a greater ability to polarize the oxygen coordination environment and hence give rise to relatively higher diffusion barriers. Indeed, this makes multivalent diffusion exceedingly sensitive to the specific details of the coordination environment. Barriers to Mg-ion diffusion are 1.15−1.23 eV in α-V_2O_5,[17] decreased somewhat to 0.71−1.16 eV in γ′-V_2O_5, further decreased to ca. 0.54−1.07 eV in δ′-V_2O_5, and reach a rather desirable range of 0.28−0.46 eV in ρ′-V_2O_5. Similarly, for Ca-ion diffusion, the barrier height is ca. 1.76−1.86 eV in α-V_2O_5, which is in good agreement with a previous calculation by Carrasco,[20] which suggests that this material will not be viable as a Ca-ion insertion cathode. However, the diffusion barrier is greatly reduced to ca. 0.59−0.68 eV in γ′-V_2O_5, ca. 0.56−0.65 eV in δ′-V_2O_5 and ca. 0.37−0.55 eV in ρ′-V_2O_5. All three metastable polymorphs thus represent attractive and viable candidates for Ca-ion batteries. The migration barriers for Na-ions in all three metastable polymorphs and for Mg-ions in ρ′-V_2O_5 are further within the range of the 650 meV value, suggesting their viability as cathode materials. **Figure A14** shows that a threshold value of 0.05 eV $Å^{-1}$ instead of 0.1 eV $Å^{-1}$ does not substantially alter the diffusion barriers.

Coordination Environment and Transition State Geometry

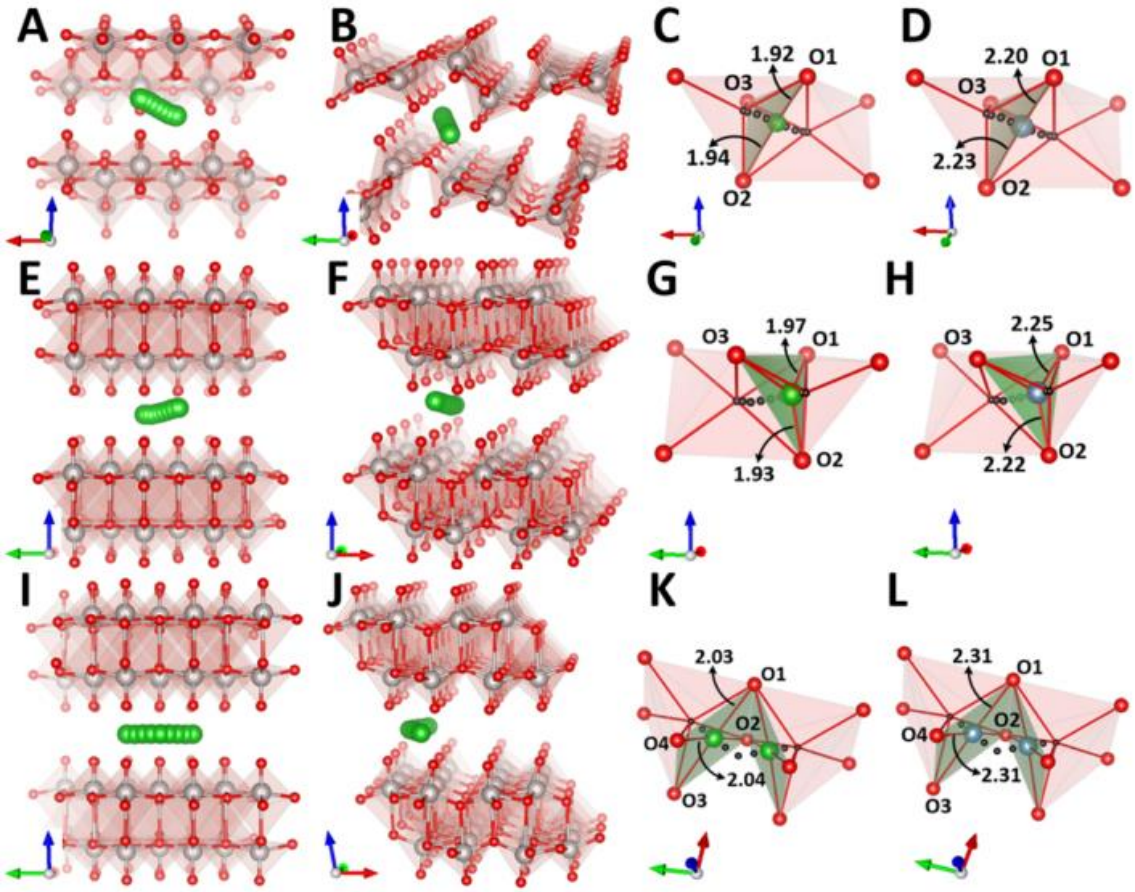

Figure III. 4. Left panels indicate migration pathways for the Mg ions at two different orientations (A, B) γ′−V_2O_5, (E, F) δ′−V_2O_5, and (I, J) ρ′−V_2O_5. The Ca-ions follow essentially the same pathway for all of these polymorphs. The right panels depict the transition states and the oxygen coordination environment for Mg-ions in (C) γ′−V_2O_5, (G) δ′−V_2O_5, and (K) ρ′−V_2O_5. The transition state geometries and oxygen coordination environments of Ca-ions are shown in (D) for γ′−V_2O_5, (H) for δ′−V_2O_5, and (L) for ρ′−V_2O_5. The gray, red, green, and light blue spheres represent vanadium, oxygen, magnesium, and calcium atoms, respectively.

To develop systematic design principles, it is necessary to correlate the calculated diffusion barriers to finer details of the local coordination environment. **Figure III. 3** clearly shows that subtle structural differences between the single- and double-layered polymorphs can greatly modify the diffusion barriers. The diffusion pathways (along two

different orientations) and the oxygen coordination environments for Mg- and Ca-ions along these pathways are shown in **Figure III. 4** for all three metastable polymorphs of V_2O_5 considered here. It is worth reviewing the cation diffusion pathways adopted by Mg-ions in the thermodynamically stable α-V_2O_5 polymorph. As extensively discussed in the literature, the diffusion of cations in α-V_2O_5 involves a change in the oxygen coordination number from $8 \rightarrow 3 \rightarrow 8$, with the transition state involving a trigonal planar geometry.[8,24] As a result of the strong cation-oxygen bond in the transition state and large change in oxygen coordination that must be accommodated during the cation diffusion process (the eight- and three coordinated sites are spaced far apart in energy), the migration energy barriers are high.

Despite also being a single-layered phase, the distorted γ′-V_2O_5 polymorph is characterized by a somewhat lower barrier for Na-, Mg-, and Ca-ion diffusion (**Figure III. 3**). **Figure III. 4A−D** illustrates that the two low-energy sites occupied by Ca- and Mg-ions in γ′-V_2O_5 are a four-coordinated tetrahedral and a five-coordinated approximately square pyramidal site; the ions must pass through a trigonal planar transition state in traversing from one site to another. As indicated by the offset between the two end points in **Figure III. 3A**, the quasi-square-pyramidal site is more stable for Na-, Mg-, and Ca-ions, whereas the tetrahedral site is more stable for Li-ions owing to their smaller radii. These two sites share a trigonal planar face, and the diffusion process involves the cations transiently being coordinated to three oxygens in the transition state. Regarding the case of Mg-ion diffusion, the area spanned by the trigonal planar transition state (Mg−O bond length is 1.92 and 1.94 Å in γ′-V_2O_5 as compared to 1.89 and 1.91 Å in α-V_2O_5, **Figure**

III. 4C) is slightly larger than that of α-V_2O_5, contributing to a lower barrier for Mg-ion diffusion. It is worth noting that unlike the 8 → 3 → 8 progression in α-V_2O_5, the sequence of coordination environment changes in γ-V_2O_5 is much more modest and follows 5 (intermediate site) → 3 (transition state) → 4 (intermediate site) → 3 (transition state) → 5 (intermediate site), always placing the Mg-ion within an undesirable "frustrated" coordination site. The energetics for half of the pathway is depicted in **Figure III. 3A**. The stable quasi-square-pyramidal and tetrahedral sites are closer in energy in this polymorph (**Figure III. 3A**) as compared to the energy differential between the eight and three-coordinated sites in α-V_2O_5, which reduces the barrier to Mg-ion diffusion. Similarly, Ca-ion diffusion follows the same progression. However, the Ca-ion is much more stabilized at the tetrahedral site as compared to the Mg-ion and thus the five- and four-coordinated intermediate states are closer in energy, yielding a relatively smaller diffusion barrier. Ca-ions are moreover less polarizing, and Ca−O bond distances are longer at the transition state for γ′-V_2O_5 (2.20 and 2.23 Å in γ′-V_2O_5 *vs* 2.18 and 2.25 Å in α-V_2O_5, **Figure III. 4D**). Another important point reflected in **Figures III. 3A and A15A−D** is that the migration barrier is dependent on the concentration of cations. At higher cation concentrations, the trigonal site is further decreased in size and this along with cation−cation repulsion increases the diffusion barrier.

The next class of polymorphs have cations sandwiched between double-layered V_4O_{10} slabs. Similar to γ′-V_2O_5, the metastable polymorph δ′-V_2O_5 has two energetically viable intermediate sites, a four-coordinated tetrahedral site and a fivecoordinated square pyramidal site (**Figure III. 4E−H**). Mg- and Ca ions diffuse preferentially along the *b*

axis, and again, both divalent cations exhibit a preference for the square pyramidal instead of tetrahedral geometry. The two intermediate sites again share a trigonal planar face setting up the following sequence of hops for the diffusing cation: 5 (intermediate site) → 3 (transition state) → 4 (intermediate site) → 3 (transition state) → 5 (intermediate site). Because the energy differential between the five- and four-coordinated sites is somewhat the same in this phase as compared to that of γ′-V_2O_5, the lowering of the diffusion barrier (0.54−1.07 eV in comparison to 0.71− 1.16 eV in γ′-V_2O_5) is due to the distortion of the O1−O2−O3 trigonal planar pocket (**Figure III. 4G**). Regarding δ′-V_2O_5, there is a 1.2% increase in the area of O1−O2−O3 trigonal planar pocket to accommodate the motion of the Mg-ion from its stable square-pyramidal site across the transition state. In contrast, the analogous increase in the area of the O1−O2−O3 trigonal planar pocket is 5.4% for the γ′-V_2O_5 phase. This significant decrease in distortion of the double-layered phase reduces the diffusion barrier for δ′-V_2O_5 as compared to that for γ′-V_2O_5. In the case of Ca-ion insertion within this phase, at low concentrations, the tetrahedral position is substantially higher in energy in comparison to the square-pyramidal site (note that Ca-ions have a strong preference for eightfold coordination; **Figure III. 4H** indicates that the transition state is closer to the tetrahedral site in geometry). In other words, it is not the narrow trigonal planar site but the approach to the tetrahedral site that is energetically expensive in this polymorph. This differential leads to a relatively large barrier for diffusion at low concentrations. However, at higher Ca-ion concentrations, the energy differential between the tetrahedral and the square-pyramidal site is reduced, and the transition state lies between the two intermediates on the trigonal planar face. This causes the barrier to

decrease from 0.65 to 0.56 eV. Overall, the diffusion barriers are lower in δ′-V_2O_5 as compared to those in γ′-V_2O_5 for Li, Na, Mg, and Ca-ions owing to the rigid (more difficult to distort) double-layered V_2O_5 framework and slightly larger trigonal planar pockets.

ρ′-V_2O_5 has a different stacking sequence of the double layered slabs. The shift in stacking along the *a* axis gives rise to a completely altered oxygen coordination environment for cation intercalation. The hopping of Mg- and Ca-ions along the *b* axis of this structure is illustrated in **Figure III. 4I,J**. The lowest energy site for both multivalent cations is a six-coordinated trigonal prism (**Figure III. 4K,L**). Taking half of the diffusion path into consideration, two adjacent trigonal prismatic sites share a square planar face. The diffusion of a Mg-ion involves the following sequence of coordination environments: 6 (intermediate site) → 4 (transition state) → 6 (intermediate site) → 4 (transition state) → 6 (intermediate site). Because the transition state has a square planar geometry with relatively large Mg−O separations (calculated Mg−O1 = Mg−O3 = 2.03 Å and Mg−O2 = Mg−O4 = 2.04 Å), the diffusion barrier is as low as 0.28−0.46 eV, which makes this material rather attractive as a Mg-ion intercalation compound. At the discharged limit, the Mg−O separations (**Figure A15I,J**) slightly decrease reflecting a somewhat higher barrier. Similarly, Ca-ions traverse a similar pathway with an identical sequence of coordination changes. The Ca−O separations at the transition state depicted in **Figure III. 4L** are the largest among all of the polymorphs discussed and hence this polymorph is characterized by the smallest diffusion barrier of 0.37−0.55 eV. The ability to access a square planar instead of a spatially more confined trigonal planar transition state geometry is clearly

critical to the reduced diffusion barriers predicted for this polymorph and is indeed similar to ε-V_2O_5.[17]

Based on the above analysis, Ca-ion diffusion is deduced to be relatively facile in all three metastable polymorphs. Mg-ion diffusion is also viable in ρ′-V_2O_5 and to a limited extent (perhaps at smaller particle sizes) for γ′ and δ′-V_2O_5. The predicted multivalent-ion mobility approximately follows the order: α-V_2O_5 < γ′-V_2O_5 < δ′-V_2O_5 < ρ′-V_2O_5. The two important factors dictating this trend are the change in the cation coordination number (and the resulting differential in energy between intermediate states) and the specific geometry of the transition state. Minimal change in cation coordination between the intermediate site and the transition state and the expanded geometry at the transition state are thus seen to be necessary conditions for the rational design of optimal cathodes.

III.4 Conclusions

The scarce options for multivalent-ion insertion cathodes has been a major impediment to the development of multivalent rechargeable batteries. The use of metastable phases brings some specific benefits with respect to thermodynamically stable polymorphs in terms of a higher chemical potential difference (giving rise to a larger OCV) and in providing access to unusual coordination environments not readily available for thermodynamically stable polymorphs. Here, we have contrasted the role of puckering, number of layers, and the specific stacking sequence of layers for V_2O_5 by contrasting three metastable polymorphs (**Figures III. 1 and A11**) with the thermodynamically stable α-phase of V_2O_5 both in terms of thermodynamic parameters and the diffusion barriers.

Specifically, a distorted single-layered γ′-V_2O_5 phase and double-layered δ′-V_2O_5 and ρ′-V_2O_5 phases constituted from V_4O_{10} slabs are compared. The metastable polymorphs yield reasonable OCVs of 2.73− 2.86 V for Mg-ion insertion and attractive voltages ranging from 3.29 to 3.65 V for Ca-ion insertion. The volume expansion upon cation intercalation is less than 7% for all of the polymorphs examined here with the exception of Na and Ca ion intercalation in γ′-V_2O_5, evidencing the practicality of these polymorphs for use as cathodes.

The diffusivities of the cation in these metastable polymorphs have been calculated using NEB simulations. The diffusion barriers for the metastable polymorphs are substantially lower than those of the thermodynamically stable α-V_2O_5 phase. For Mg-ion diffusion, the barriers are ca. 0.71−1.16 eV in γ′-V_2O_5, ca. 0.54−1.07 eV in δ′-V_2O_5, and ca. 0.28−0.46 eV in ρ′-V_2O_5. For Ca-ion diffusion, the calculated barriers are ca. 0.59−0.68 eV in γ′−V_2O_5, ca. 0.56−0.65 eV in δ′-V_2O_5, and ca. 0.37−0.55 eV in ρ′-V_2O_5. The calculated values of the diffusion barriers along with the calculated specific diffusion pathways provide valuable insight into the structural characteristics that promote the diffusion of multivalent cations. The double-layered metastable phases, δ′-V_2O_5 and ρ′-V_2O_5, have lower diffusion barriers in comparison to single-layered γ′-V_2O_5, owing to the greater rigidity of the double-layered polymorphs, which renders them less susceptible to distortion by the polarizing multivalent cations. All three metastable phases exhibit lower diffusion barriers for Ca- and Mg-ion diffusion as compared to those of α-V_2O_5 as a result of (a) their ability to enforce frustrated coordination environments and (b) the relatively small changes in coordination geometry (and thus smaller variations in energy) across the

diffusion pathway. A comparison of the similarly structured δ′-V_2O_5 and ρ′-V_2O_5 frameworks suggest that a small change of stacking sequence can bring about a substantial alteration of the local coordination environments and by providing a more spacious transition state open up a lower energy diffusion pathway. A more accurate treatment of dispersive interactions across all calculated parameters would further improve the search for viable metastable compounds.[51] Surface diffusion phenomena are expected to assume particular importance if the proposed metastable materials are prepared and exfoliated to few-layered structures. A full elucidation of surface effects will require consideration of the cathode−electrolyte interface and cation diffusion on multiple surfaces of the same material and will be the focus of future work.

III.5 References

(1) Nitta, N.; Wu, F.; Lee, J. T.; Yushin, G. Li-Ion Battery Materials: Present and Future. *Mater. Today* **2015**, *18*, 252−264.

(2) Tran, M.; Banister, D.; Bishop, J. D.; McCulloch, M. D. Realizing the Electric-Vehicle Revolution. *Nat. Clim. Change* **2012**, *2*, 328−333.

(3) Whittingham, M. S. Lithium Batteries and Cathode Materials. *Chem. Rev.* **2004**, *104*, 4271−4302.

(4) Rong, Z.; Malik, R.; Canepa, P.; Sai Gautam, G.; Liu, M.; Jain, A.; Persson, K.; Ceder, G. Materials Design Rules for Multivalent Ion Mobility in Intercalation Structures. *Chem. Mater.* **2015**, *27*, 6016−6021.

(5) Yoo, H. D.; Shterenberg, I.; Gofer, Y.; Gershinsky, G.; Pour, N.; Aurbach, D. Mg Rechargeable Batteries: An On-Going Challenge. *Energy Environ. Sci.* **2013**, *6*, 2265−2279.

(6) Cheng, Y.; Chang, H. J.; Dong, H.; Choi, D.; Sprenkle, V. L.; Liu, J.; Yao, Y.; Li, G. Rechargeable Mg−Li Hybrid Batteries: Status and Challenges. *J. Mater. Res.* **2016**, *31*, 3125−3141.

(7) Muldoon, J.; Bucur, C. B.; Gregory, T. Quest for Nonaqueous Multivalent Secondary Batteries: Magnesium and Beyond. *Chem. Rev.* **2014**, *114*, 11683−11720.

(8) Sai Gautam, G.; Canepa, P.; Abdellahi, A.; Urban, A.; Malik, R.; Ceder, G. The Intercalation Phase Diagram of Mg in V_2O_5 from First Principles. *Chem. Mater.* **2015**, *27*, 3733−3742.

(9) Liu, M.; Rong, Z.; Malik, R.; Canepa, P.; Jain, A.; Ceder, G.; Persson, K. A. Spinel Compounds as Multivalent Battery Cathodes: A Systematic Evaluation Based on Ab Initio Calculations. *Energy Environ. Sci.* **2015**, *8*, 964−974.

(10) Canepa, P.; Sai Gautam, G.; Hannah, D. C.; Malik, R.; Liu, M.; Gallagher, K. G.; Persson, K. A.; Ceder, G. Odyssey of Multivalent Cathode Materials: Open Questions and Future Challenges. *Chem. Rev.* **2017**, *117*, 4287−4341.

(11) Muldoon, J.; Bucur, C. B.; Gregory, T. Fervent Hype behind Magnesium Batteries: An Open Call to Synthetic Chemists-Electrolytes and Cathodes Needed. *Angew. Chem., Int. Ed.* **2017**. 10.1002/ anie.201700673.

(12) Ling, C.; Suto, K. Thermodynamic Origin of Irreversible Magnesium Trapping in Chevrel Phase Mo_6S_8: Importance of Magnesium and Vacancy Ordering. *Chem. Mater.* **2017**, *29*, 3731− 3739.

(13) Fan, X.; Gaddam, R. R.; Kumar, N. A.; Zhao, X. S. A Hybrid Mg^{2+}/Li^{+} Battery Based on Interlayer-Expanded MoS_2/Graphene Cathode. *Adv. Energy Mater.* **2017**, *7*, No. 1700317.

(14) Roscoe, H. E. XXXVI.–Researches on Vanadium. *J. Chem. Soc.* **1868**, *21*, 322−350.

(15) Whittingham, M. S. The Role of Ternary Phases in Cathode Reactions. *J. Electrochem. Soc.* **1976**, *123*, 315−320.

(16) Gershinsky, G.; Yoo, H. D.; Gofer, Y.; Aurbach, D. Electrochemical and Spectroscopic Analysis of Mg^{2+} Intercalation into Thin Film Electrodes of Layered Oxides: V_2O_5 and MoO_3. *Langmuir* **2013**, *29*, 10964−10972.

(17) Parija, A.; Liang, Y.; Andrews, J. L.; De Jesus, L. R.; Prendergast, D.; Banerjee, S. Topochemically De-Intercalated Phases of V_2O_5 as Cathode Materials for Multivalent Intercalation Batteries: A First Principles Evaluation. *Chem. Mater.* **2016**, *28*, 5611−5620.

(18) Imamura, D.; Miyayama, M.; Hibino, M.; Kudo, T. Mg Intercalation Properties into V_2O_5 Gel/Carbon Composites under High-Rate Condition. *J. Electrochem. Soc.* **2003**, *150*, A753−A758.

(19) Tepavcevic, S.; Liu, Y.; Zhou, D.; Lai, B.; Maser, J.; Zuo, X.; Chan, H.; Kral, P.; Johnson, C. S.; Stamenkovic, V.; et al.́ Nanostructured Layered Cathode for Rechargeable Mg-Ion Batteries. *ACS Nano* **2015**, *9*, 8194−8205.

(20) Carrasco, J. Role of van der Waals Forces in Thermodynamics and Kinetics of Layered Transition Metal Oxide Electrodes: Alkali and Alkaline-Earth Ion Insertion into V_2O_5. *J. Phys. Chem. C* **2014**, *118*, 19599−19607.

(21) Marley, P. M.; Horrocks, G. A.; Pelcher, K. E.; Banerjee, S. Transformers: the Changing Phases of Low-Dimensional Vanadium Oxide Bronzes. *Chem. Commun.* **2015**, *51*, 5181−5198.

(22) Marley, P. M.; Abtew, T. A.; Farley, K. E.; Horrocks, G. A.; Dennis, R. V.; Zhang, P.; Banerjee, S. Emptying and Filling a Tunnel Bronze. *Chem. Sci.* **2015**, *6*, 1712−1718.

(23) Galy, J. Vanadium Pentoxide and Vanadium Oxide Bronzes–Structural Chemistry of Single (S) and Double (D) Layer $M_xV_2O_5$ Phases. *J. Solid State Chem.* **1992**, *100*, 229−245.

(24) Gautam, G. S.; Canepa, P.; Malik, R.; Liu, M.; Persson, K.; Ceder, G. First-Principles Evaluation of Multi-Valent Cation Insertion into Orthorhombic V_2O_5. *Chem. Commun.* **2015**, *51*, 13619−13622.

(25) Withers, R. L.; Millet, P.; Tabira, Y. The Inherent Displacive Structural Flexibility of $M_xV_2O_5$ Framework Structures. *Z. Kristallogr. - Cryst. Mater.* **2000**, *215*, 357−363.

(26) Monchoux, J.-P.; Dolle, M.; Rozier, P.; Galy, J. Reaction Kinetics′ During Synthesis of $Cu_xV_2O_5$ and $Ag_yV_2O_5$ by Spark Plasma Sintering. *Solid State Ionics* **2011**, *182*, 24−31.

(27) Galy, J.; Lavaud, D.; Casalot, A.; Hagenmuller, P. Les Bronzes Oxygené s de Vanadium de Formule $Cu'_xV_2O_5$: I. Structure Cristalline Des Phases $Cu_xV_2O_5$ β et $Cu_xV_2O_5$ ϵ. *J. Solid State Chem.* **1970**, *2*, 531−543.

(28) Hwang, H.; Kim, H.; Cho, J. MoS_2 Nanoplates Consisting of Disordered Graphene-like Layers for High Rate Lithium Battery Anode Materials. *Nano Lett.* **2011**, *11*, 4826−4830.

(29) Su, D.; Wang, G. Single-Crystalline Bilayered V_2O_5 Nanobelts for High-Capacity Sodium-Ion Batteries. *ACS Nano* **2013**, *7*, 11218−11226.

(30) Tojo, T.; Sugiura, Y.; Inada, R.; Sakurai, Y. Reversible Calcium Ion Batteries Using a Dehydrated Prussian Blue Analogue Cathode. *Electrochim. Acta* **2016**, *207*, 22−27. (31) Ponrouch, A.; Frontera, C.; Barde, F.; Palacín, M. Towards a′ Calcium-Based Rechargeable Battery. *Nat. Mater.* **2016**, *15*, 169−172.

(32) Wang, W.; Wang, H.; Liu, S.; Huang, J. Synthesis of γ-LiV_2O_5 Nanorods as a High-Performance Cathode for Li Ion Battery. *J. Solid State Electrochem.* **2012**, *16*, 2555−2561.

(33) Galy, J.; Satto, C.; Sciau, P.; Millet, P. Atomic Modeling of the δ ⇔ ε LiV_2O_5 Phase Transition and Simulation of the XRD Powder Pattern Evolution. *J. Solid State Chem.* **1999**, *146*, 129−136.

(34) Dai, J.; Li, S. F.; Gao, Z.; Siow, K. S. Novel Method for Synthesis of γ-Lithium Vanadium Oxide as Cathode Materials in Lithium Ion Batteries. *Chem. Mater.* **1999**, *11*, 3086−3090.

(35) Patridge, C. J.; Wu, T.-L.; Jaye, C.; Ravel, B.; Takeuchi, E. S.; Fischer, D. A.; Sambandamurthy, G.; Banerjee, S. Synthesis, Spectroscopic Characterization, and Observation of Massive Metal−Insulator Transitions in Nanowires of a Nonstoichiometric Vanadium Oxide Bronze. *Nano Lett.* **2010**, *10*, 2448−2453.

(36) Oka, Y.; Yao, T.; Yamamoto, N. Layered Structures of Hydrated Vanadium Oxides. Part 4.–Single-Crystal Structure and Phase Conversion of the Unhydrated Potassium Intercalate $K_{0.5}V_2O_5$. *J. Mater. Chem.* **1995**, *5*, 1423−1426.

(37) Yao, T.; Oka, Y.; Yamamoto, N. Layered Structures of Hydrated Vanadium Oxides. Part 5.–Single-Crystal Structure of $Rb_{0.5}V_2O_5$ and Phase Changes of Rubidium Intercalate. *J. Mater. Chem.* **1996**, *6*, 1195−1198.

(38) Andrews, J. L.; De Jesus, L. R.; Tolhurst, T. M.; Marley, P. M.; Moewes, A.; Banerjee, S. Intercalation-Induced Exfoliation and Thickness-Modulated Electronic Structure of a Layered Ternary Vanadium Oxide. *Chem. Mater.* **2017**, *29*, 3285−3294.

(39) Marley, P. M.; Singh, S.; Abtew, T. A.; Jaye, C.; Fischer, D. A.; Zhang, P.; Sambandamurthy, G.; Banerjee, S. Electronic Phase Transitions of δ-$Ag_xV_2O_5$ Nanowires: Interplay between Geometric and Electronic Structures. *J. Phys. Chem. C* **2014**, *118*, 21235−21243.

(40) Savariault, J.-M.; Galy, J. Synthesis and Structural Investigation of a New Potassium Vanadium Oxide Bronze: ϱ-$K_{0.50}V_2O_5$. *J. Solid State Chem.* **1992**, *101*, 119−127.

(41) Hohenberg, P.; Kohn, W. Inhomogeneous Electron Gas. *Phys. Rev.* **1964**, *136*, B864−B871.

(42) Kohn, W.; Sham, L. J. Self-Consistent Equations Including Exchange and Correlation Effects. *Phys. Rev.* **1965**, *140*, A1133− A1138.

(43) Kresse, G.; Furthmüller, J. Efficiency of Ab-Initio Total Energy Calculations for Metals and Semiconductors using a Plane-Wave Basis Set. *Comput. Mater. Sci.* **1996**, *6*, 15−50.

(44) Perdew, J. P.; Burke, K.; Ernzerhof, M. Generalized Gradient Approximation Made Simple. *Phys. Rev. Lett.* **1996**, *77*, 3865−3868.

(45) Anisimov, V. I.; Aryasetiawan, F.; Lichtenstein, A. First Principles Calculations of the Electronic Structure and Spectra of Strongly Correlated Systems: The LDA+U Method. *J. Phys. Condens. Matter* **1997**, *9*, 767−808.

(46) Zhou, B.; Shi, H.; Cao, R.; Zhang, X.; Jiang, Z. Theoretical Study on the Initial Stage of a Magnesium Battery Based on a V_2O_5 Cathode. *Phys. Chem. Chem. Phys.* **2014**, *16*, 18578−18585.

(47) Klimes, J.; Bowler, D. R.; Michaelides, A. Van der Waals Density ˇ Functionals Applied to Solids. *Phys. Rev. B* **2011**, *83*, No. 195131.

(48) Roman-Pe´ rez, G.; Soler, J. M. Efficient Implementation of a Van´ der Waals Density Functional: Application to Double-Wall Carbon Nanotubes. *Phys. Rev. Lett.* **2009**, *103*, No. 096102.

(49) Dion, M.; Rydberg, H.; Schrö der, E.; Langreth, D. C.; Lundqvist, B. I. Van der Waals Density Functional for General Geometries. *Phys. Rev. Lett.* **2004**, *92*, No. 246401.

(50) Lee, K.; Murray, É . D.; Kong, L.; Lundqvist, B. I.; Langreth, D. C. Higher-Accuracy Van der Waals Density Functional. *Phys. Rev. B* **2010**, *82*, No. 081101.

(51) Lozano, A.; Escribano, B.; Akhmatskaya, E.; Carrasco, J. Assessment of Van der Waals Inclusive Density Functional Theory Methods for Layered Electroactive Materials. *Phys. Chem. Chem. Phys.* **2017**, *19*, 10133−10139.

(52) Kulish, V. V.; Manzhos, S. Comparison of Li, Na, Mg and Al-Ion Insertion in Vanadium Pentoxides and Vanadium Dioxides. *RSC Adv.* **2017**, *7*, 18643−18649.

(53) Byström, A.; Wilhelmi, K.-A.; Brotzen, O. Vanadium Pentoxide A Compound with Five-Coordinated Vanadium Atoms. *Acta. Chem. Scand.* **1950**, *4*, 1119−1130.

(54) Van der Ven, A.; Bhattacharya, J.; Belak, A. A. Understanding Li Diffusion in Li-Intercalation Compounds. *Acc. Chem. Res.* **2013**, *46*, 1216−1225.

(55) Aydinol, M. K. First-Principles Prediction of Insertion Potentials in Li-Mn Oxides for Secondary Li Batteries. *J. Electrochem. Soc.* **1997**, *144*, 3832−3835.

(56) Meng, Y. S.; Arroyo-de Dompablo, M. E. First Principles Computational Materials Design for Energy Storage Materials in Lithium Ion Batteries. *Energy Environ. Sci.* **2009**, *2*, 589−609.

(57) Amatucci, G.; Badway, F.; Singhal, A.; Beaudoin, B.; Skandan, G.; Bowmer, T.; Plitz, I.; Pereira, N.; Chapman, T.; Jaworski, R. Investigation of Yttrium and Polyvalent Ion Intercalation into Nanocrystalline Vanadium Oxide. *J. Electrochem. Soc.* **2001**, *148*, A940−A950.

(58) Delmas, C.; Cognac-Auradou, H.; Cocciantelli, J.; Menetrier, M.; Doumerc, J. The $Li_xV_2O_5$ System: An Overview of the Structure Modifications Induced by the Lithium Intercalation. *Solid State Ionics* **1994**, *69*, 257−264.

(59) Ali, G.; Lee, J. H.; Oh, S. H.; Cho, B. W.; Nam, K.-W.; Chung, K. Y. Investigation of the Na Intercalation Mechanism into Nanosized V_2O_5/C Composite Cathode Material for Na-Ion Batteries. *ACS Appl. Mater. Interfaces* **2016**, *8*, 6032−6039.

(60) Fuhr, J.; Wiese, W. In *CRC Handbook of Chemistry and Physics*; Lide, D. R., Ed.; CRC Press: Boca Raton, FL, **2011**.

CHAPTER IV

POLARON OSCILLATION AND CATION SHUTTLING UNDERPIN THE METAL-INSULATOR TRANSITION OF β′-$Cu_xV_2O_5$

IV.1. Introduction

Complementary metal–oxide–semiconductor (CMOS) field-effect transistors (FETs) constructed from silicon have long been the workhorse of computing architectures, and their scaling to ever smaller dimensions has underpinned a far-reaching revolution in computational power, capacity, and cost.[1-4] However, the use of silicon circuitry is fundamentally constrained by the Fermi-Dirac electron distribution of electron energies, which establishes a 60 mV/decade limit to the steepness of switching characteristics upon application of a gate voltage at room temperature.[1] The shallow slopes of electrostatically modulated transistors lead to wasted power consumption and are the genesis of "dark silicon", the necessary practice of leaving large swathes of logic circuitry on a chip inoperative at any given time in order to prevent circuit overheating. To mitigate this challenge, which has upended Moore's scaling, the utilization of steep-slope switches have been proposed,[5-7] wherein a small change in voltage induces a large modulation of current. Electron-correlated transition metal oxides exhibiting pronounced metal-to-insulator transitions (MIT) are excellent candidates for such steep-slope transistors and further provide a means of emulating the spiking behavior of biological neural circuitry within neuromorphic architectures.[8] These materials can be classified along a Mott—

Peierls' continuum corresponding to varying extents of electronic and structural contributions to their electronic instabilities.[3,9]

VO_2 is perhaps the most famous example of an electron correlated material and undergoes several orders of magnitude switching of conductance in relatively close proximity to room temperature (67°C).[10-12] An abruptly discontinuous five orders of magnitude change in resistivity is manifested in this material in response to temperature, voltage, or photoexcitation; however, the electronic transition is accompanied by a large energy-dissipative structural distortion; recent estimates suggest[13] that phonons contribute to ca. 2/3 of the total entropy change at the phase transition. Consequently, much attention has focused on the search for materials exhibiting large conductance switching but with a substantially decreased magnitude of lattice distortions and greater tunability of the transformation temperature. Here, we identify a coupled polaron oscillation and cation shuttling mechanism as the origin of thermally triggered and voltage-driven metal—insulator transitions in a family of 1D tunnel-structured materials, β'-$Cu_xV_2O_5$ where *x* represents the variable stoichiometry of Cu-ions. Such a mechanism points to an entirely distinctive approach to the design of materials exhibiting programmable electronic instabilities as required for neuromorphic electronics.

Ternary vanadium oxides ($M_xV_2O_5$) represent a diverse palette of compounds spanning different structural motifs (derived from multiple polymorphs of V_2O_5 characterized by varying V—O connectivities); cations (M) drawn from across the s- and p-block as well as transition metals; and widely variable stoichiometries (*x*).[14-17] Such compounds can be conceptualized as formally d^0 V_2O_5 systems that are reduced as a result

of the insertion of metal cations to mixed-valence d^1/d^0 V_2O_5 frameworks with varying extents of electron localization. Emergent electron correlation along such frameworks can be sensitively tuned as a function of structure and composition, and underpins the manifestation of phenomena such as memristive switching,[18] low-temperature spin-gaps,[19] pressure-induced superconductivity,[20] and metal-insulator transitions.[14,21-26] β'-$Cu_xV_2O_5$ is characterized by pronounced metal—insulator transitions whose critical transition temperature and magnitude have been found to depend sensitively on the Cu stoichiometry.[14,24-26] However, the fundamental mechanisms underpinning such transitions remain to be determined. Here, we use a combination of high-resolution structure refinement from variable-temperature single-crystal and powder X-ray diffraction; variable-temperature extended X-ray absorption fine structure spectroscopy (EXAFS) studies of local structure; angle-integrated photoemission spectroscopy, resonant inelastic X-ray scattering (RIXS), and hard X-ray photoemission spectroscopy (HAXPES) studies of electronic structure; density functional theory (DFT) modeling of electronic structure; and single-nanowire measurements of transport phenomena to unravel the mechanistic origins of metal-insulator transitions in β'-$Cu_xV_2O_5$. Polaron oscillation, underpinned by the real-space shuttling of Cu-ions between two adjacent sites underpins the metal-insulator transition of this material. *Ab initio* molecular dynamics (MD) and nudged elastic band (NEB) calculations demonstrate that polaron oscillation and cation shuttling can be directly correlated with the observed electronic transformations. The distinctive polaron oscillation—cation-shuttling mechanism underpinning metal-insulator transitions unraveled in this work unveils novel descriptors for obtaining tunable

transformation characteristics based on the coupling of ionics, crystal structure, and electronic band structure.

IV.2. Results and Discussion

Structural Underpinnings of the Electronic Phase Transition of β'-$Cu_xV_2O_5$

Figure IV. 1A shows the electrical resistance of an individual β′-$Cu_xV_2O_5$ (x ~ 0.50 nanowire arrayed between four electrodes measured as a function of temperature. A pronounced insulator—metal transition transition is observed at 190K; differential resistance plots in **Figure IV. 1B** further indicate field-driven melting of the insulating state. The insulating state can be melted with the passage of a small current bias. Indeed, a small current of 4 μA triggers the insulator-metal transition, even at 135K, which is well within the insulating regime. **Figure IV. 1C** indicates the remarkable current-driven transition induced within another individual nanowire device; each successive increase in current depresses the insulator—metal transition to a lower temperatures; the transition is altogether suppressed at a current of 1 μA. A linear relationship is observed between the thermal activation energy and $\sqrt{I}$. **Figure A16** exhibits optical microscopy images of individual nanowire devices with scanning electron microscopy (SEM) images and energy dispersive X-ray (EDX) spectra plotted alongside. **Figure A17** illustrates approximate measurements of Cu stoichiometry within individual nanowires from EDX experiments.

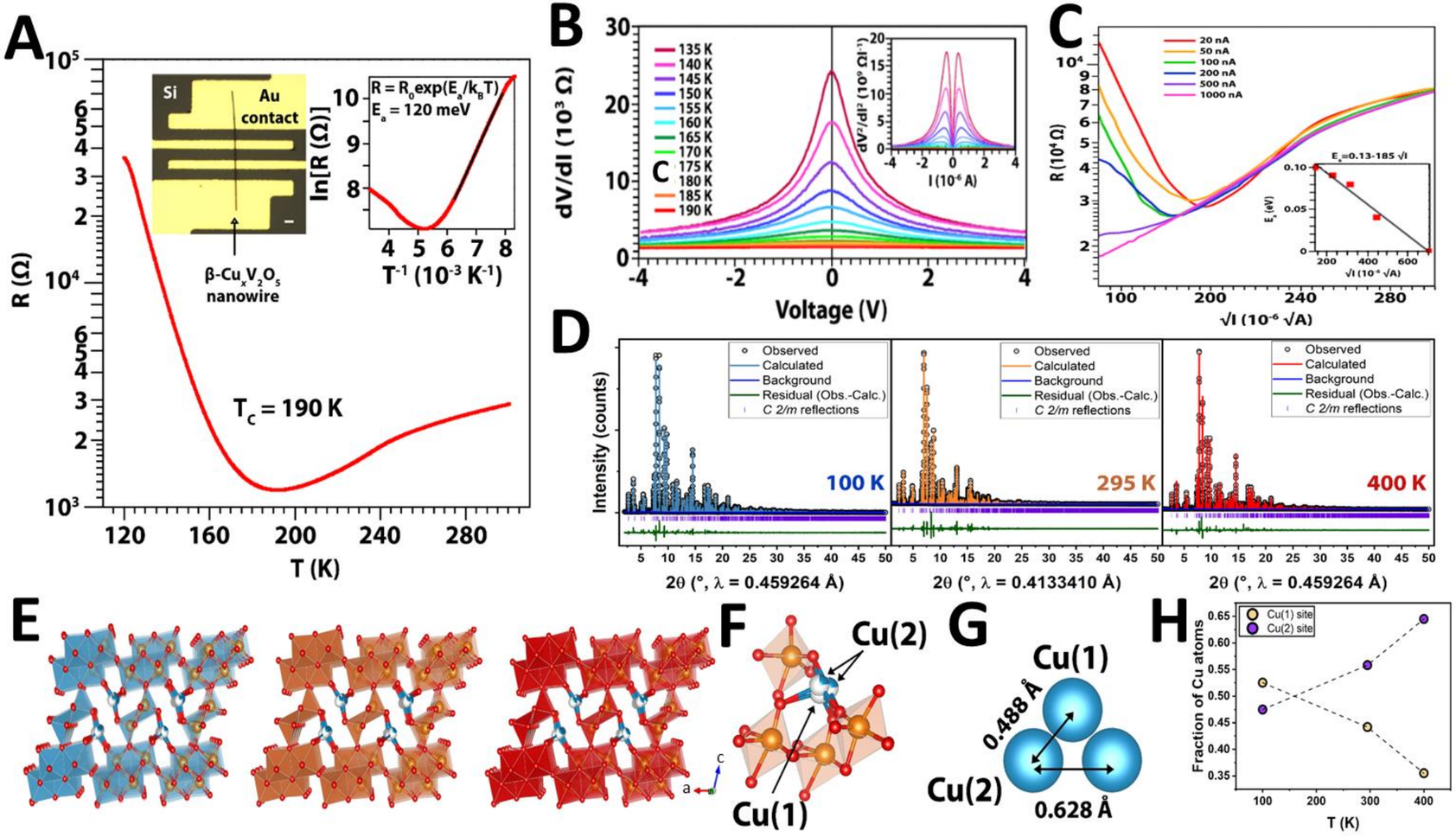

Figure IV. 1. Electronic Phase Transition and its Structural Underpinnings. (A) Resistance versus temperature curve measured for an individual nanowire of β'-$Cu_xV_2O_5$. An optical micrograph of the device is shown in the inset. The scale bar is 5 μm. The right inset indicates an exponential fit with a thermal activation energy of 120 meV for the insulating phase. **(B)** Differential resistance plots illustrating a voltage-driven metal-insulator transition. The second derivative curve of the differential resistance plot is shown in the inset. **(C)** Resistance versus temperature plots measured under current bias for an individual nanowire of β'-$Cu_xV_2O_5$ (x ~ 0.50). The insulator to metal transition (increasing temperature) is initiated at successively lower temperatures with increasing current bias. A linear relationship (inset) between thermal activation energy and √I is observed, which is suggestive of successful field-assisted melting of charge-ordered states across the metal-insulator transition. **(D)** High-resolution synchrotron X-ray diffraction data (grey circles) collected for β'-$Cu_{0.55}V_2O_5$ below (100K), in the vicinity of (295K), and well above (400K) the phase transition. Rietveld refinement of the diffraction data is plotted as light blue (100K), orange (295K), and red (400K) solid lines. The structure solutions obtained from Rietveld refinement of the patterns in **(D)** are shown in **(E)**. Further details of the refinement are included in the Supporting Information **(Tables A7-A12)**. **(F)** Copper is split between two sites within the tunnels (a central site, Cu(1) and a second site, Cu(2), reflected across the mirror plane). **(G)** Illustration of the two closely spaced the Cu(1) and Cu(2) sites. **(H)** With increasing temperature, a greater fraction of the Cu-ions shift their average position from the Cu(1) to the Cu(2) site.

Figures A16 and **A17** indicate that the transformation temperature (T_c) of the insulator—metal transition varies strongly as a function of the copper stoichiometry from 229K for $x \sim 0.46$ to 171K for $x \sim 0.50$ and 131K for $x \sim 0.62$ in β'-$Cu_xV_2O_5$.[24,26] The general trend that emerges from these experiments is that T_c is decreased with increasing copper content. Given the importance of Cu stoichiometry in determining the onset of the metal-insulator transition, a synthetic approach has been devised for preparing nanowires and single crystals with precisely defined Cu stoichiometry. Bulk β′-$Cu_xV_2O_5$ powders with precisely controlled Cu stoichiometry ($0.35<x<0.65$) are first synthesized by traditional solid-state methods, as described in the Methods section. Such powders are next treated hydrothermally for 24 h to obtain single-crystalline β′-$Cu_xV_2O_5$ nanowires. **Figure A18** displays SEM images of the nanowires, whereas **Figure A19** shows X-ray photoemission spectroscopy (XPS) characterization of the prepared materials. With increasing Cu content, a monotonic increase of the $V^{4+}/(V^{4+}+V^{5+})$ intensity ratio is observed, corresponding to proportionately increasing reduction of the V_2O_5 framework.[27-29] The transformation to a mixed-valence $3d^0/3d^1$ framework with increasing Cu-intercalation is further evidenced by V L-edge X-ray absorption near-edge structure (XANES) spectroscopy measurements, which show a darkening of the transition to unoccupied $3d_{xy}$ states; these states that reside at the bottom of the conduction band are diminished in intensity as they become filled by electrons donated from Cu-ions to V atoms within the framework, reflecting reduction of the V_2O_5 framework **(Figure A20)**.[27-30]

The absence of high-quality materials and dearth of measurements mapping changes in crystal structure and electronic band structure across the phase transformation have thus far confounded mechanistic understanding of the origins of the observed electronic instabilities in ternary vanadium oxide bronzes. Several theories have been proposed such as superstructure ordering of Cu-ions in the low-temperature insulating phase,[26] melting of charge ordering on the vanadium ladder,[25] anharmonic oscillations within the material, and puckering of the V_2O_5 framework.[21,24] High-resolution synchrotron powder X-ray diffraction measurements have been performed for β′-$Cu_xV_2O_5$ (x = 0.55) nanowires across the phase transformation (**Figures IV. 1D—H**). The material retains its characteristic *C 2/m* monoclinic symmetry across the phase transformation with retention of the 1D tunnel structure. However, the most striking finding is that with increasing temperature, a pronounced redistribution of the average position of Cu-ions between two distinct crystallographic sites is observed. In the β′-$Cu_{0.55}V_2O_5$ material, the two sites are occupied nearly equally at 100K (0.52:0.48). However, upon heating to 400K, the Cu-ions appear to have an increased occupancy at Cu(2) sites (0.65:0.35) indicating facile shuttling of Cu-ions between these two sites (**Figures IV. 1G** and **H**).

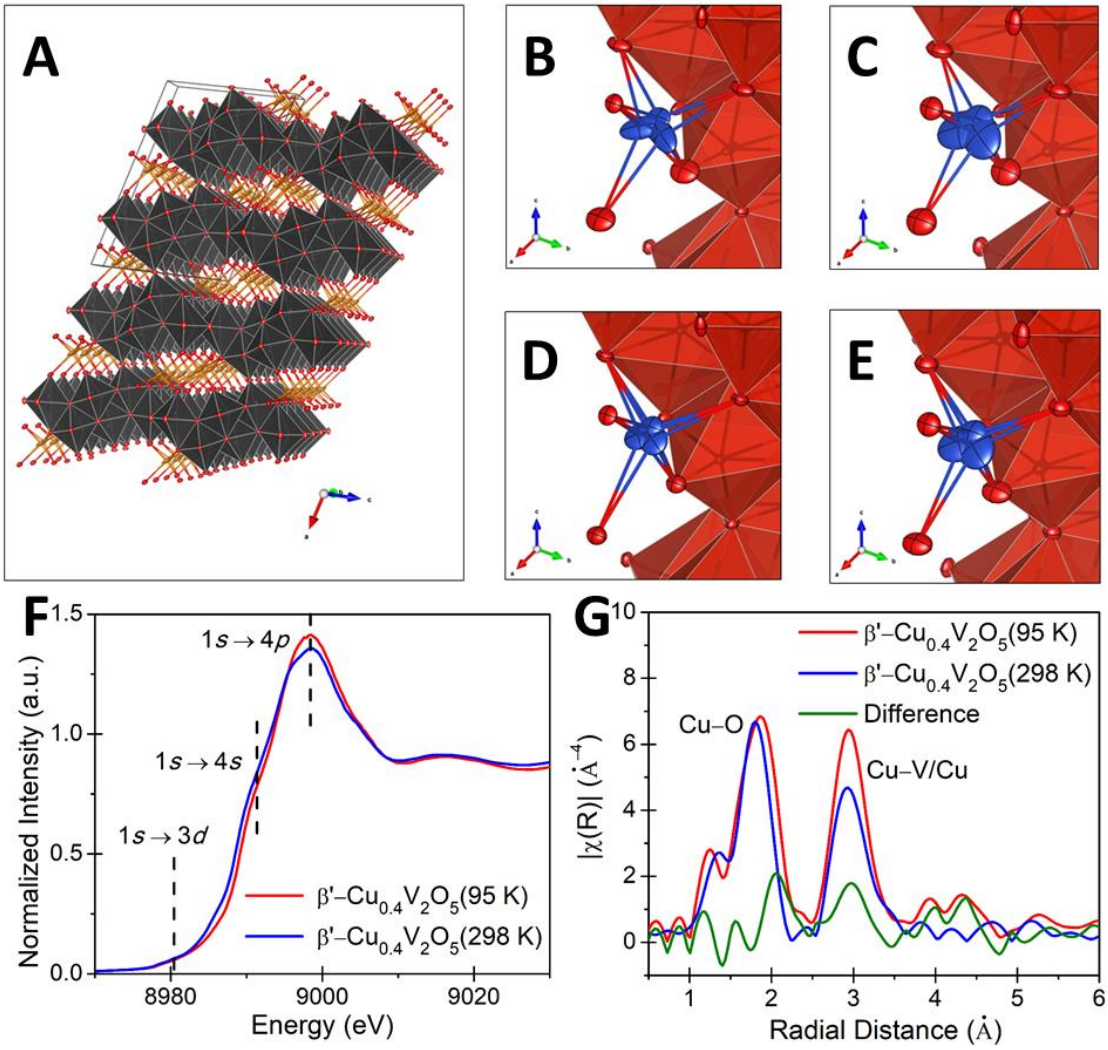

Figure IV. 2. Structural Transformations of β'-$Cu_xV_2O_5$. (A) Crystal structure of β'-$Cu_{0.53}V_2O_5$, showing Cu split-side disorder along tunnels of V_2O_5 polyhedra. Key: Cu = gold, O = red, V = black. **B-E)** Refined structures of β'-$Cu_xV_2O_5$ derived from single crystal diffraction. Thermal ellipsoids are shown at 90% probability. Key: Cu = blue, O = red, V = black. Cu polyhedra are omitted to show split-site disorder and thermal ellipsoids. Refined structures of **(B)** β'-$Cu_{0.37}V_2O_5$ at 110K; **(C)** β'-$Cu_{0.37}V_2O_5$ at 250K; **(D)** β'-$Cu_{0.64}V_2O_5$ at 110K; and **(E)** β'-$Cu_{0.64}V_2O_5$ at 250K. **(F)** Comparison of Cu K-edge XANES spectra of β'-$Cu_{0.4}V_2O_5$ at 95 and 298K. (**G**) k^3-weighted Fourier transforms of the Cu K-edge EXAFS spectra collected at 95 (red curve) and 298K (blue curve). The green curve shows the difference spectra between the red and blue curves. A phase correction term of ca. 0.3Å has been added to the R-space data.

In order to obtain a more detailed perspective of the subtle thermally driven alterations of Cu sites, single crystals of β'-$Cu_xV_2O_5$ have been grown from the melt as described in the Methods section and single-crystal X-ray diffraction has been performed for β'-$Cu_xV_2O_5$ crystals with x = 0.37 and 0.64. **Figure IV. 2A** displays the extended crystal structure of the monoclinic β'-$Cu_{0.64}V_2O_5$ structure. Stacked layers of distorted V_2O_5 polyhedra give rise to a 1D tunnel-like structure that hosts rows of Cu-ions. The Cu-ions in this structure exhibit static-site disorder, whereby any given Cu-ion resides in one of two symmetry-inequivalent sites that are reflected across a mirror plane in the unit cell, thereby constituting the triangular clusters of potential Cu interstitial sites depicted in **Figure IV.** Single-crystal X-ray diffraction performed on high-quality crystals has allowed the refinement of anisotropic displacement parameters and occupancies of these two Cu sites as a function of temperature. **Figure IV. 2B** depicts the anisotropic displacement of Cu-ions in β'-$Cu_{0.37}V_2O_5$ at 110K, whereas **Figure IV. 2C** depicts the displacement within the same crystal at 250K. At both high and low temperatures, the atomic displacement is relatively constrained along the *z*-direction; however, in the high-temperature structure, a significant increase of the lateral displacement is observed along the *xy* plane, reflecting greater thermal motion and increased spatial overlap between the possible Cu positions. At 110K, the refined Cu occupancy in this structure shows an approximately even distribution of Cu between the sites, with the central Cu on a special position (with the crystallographic label Cu(1)) showing a refined occupancy of 0.097 per V_2O_5 and the secondary atoms (represented in the asymmetric unit as Cu(2)) having a refined occupancy of 0.273 per V_2O_5. The relative relationship between Cu occupancy in

these two sites does not change significantly at higher temperature; at 250K, the occupancies of Cu(1) and Cu(2) are refined as 0.092 and 0.279 per V_2O_5, respectively. However, at higher Cu content, the relationship between the two Cu positions in the V_2O_5 framework is observed to change. **Figure IV. 2D** depicts the Cu thermal ellipsoids in a crystal of β'-$Cu_{0.64}V_2O_5$ at 110K, whereas **Figure IV. 2E** depicts the structure of the same crystal determined at 250K. Whilst the overall thermal displacement increases (as before) at 250K, compared to the $Cu_{0.37}V_2O_5$ structure, there is much less lateral distortion of ellipsoids, and at a higher total occupancy the overall dimensional confinement of Cu to either the Cu(1) or Cu(2) position appears to be increased. Indeed, the relative occupancy of Cu-ions is shifted towards the central Cu(1) site when compared to $Cu_{0.37}V_2O_5$: At 110K, the refined occupancy of the Cu(1) position in β'-$Cu_{0.64}V_2O_5$ is 0.239 per V_2O_5, whereas that of the Cu(2) position is 0.406 per V_2O_5. At 250K, a significant portion of the Cu occupancy distribution is shifted towards the secondary site. At the higher temperature, the occupancy of the Cu(1) site is reduced to 0.121 per V_2O_5, whereas that of the Cu(2) site correspondingly increases to 0.523 per V_2O_5. Whereas at 250K, the Cu(1) site accounts for approximately 19% of the total Cu occupancy, at 110K Cu-ions appear to increasingly favor the Cu(1) site and it instead accounts for 37% of the total occupancy. The relative occupancies observed as a function of temperature and Cu stoichiometry are summarized in **Table A13**.

To further illuminate the subtle changes in the local coordination environment of Cu-ions in β'-$Cu_{0.4}V_2O_5$, Cu K-edge X-ray absorption near-edge spectroscopy (XANES) and extended X-ray absorption fine-structure spectroscopy (EXAFS) measurements have

been performed across the metal—insulator transition (**Figure IV. 2F, G**). Three prominent spectral regions are plotted in **Figure IV. 2F**; the pre-edge region at ca. 8980.4 eV involves dipole-forbidden transitions from Cu 1*s* core states → Cu 3*d* states hybridized with O 2*p* states; the rising-edge at ca. 8991.2 eV represents transitions from Cu 1*s* → Cu 4*s* states hybridized with O2*p* states, and finally the white line absorption at ca. 8998.4 eV is attributed to dipole-allowed Cu 1*s* → Cu 4*p* transitions.[31,32] Subtle differences are observed in XANES features acquired for β'-$Cu_{0.4}V_2O_5$ at 95 and 298K (**Figures IV. 2F**, **A21)** and derive from alterations of the local symmetry of the intercalated Cu-ions.[33,34] Notably, the increase in intensity of the Cu 1*s* → Cu 4*s* transition at 298K in comparison to 95K suggests a change of the oxygen-coordination environment around the Cu-atom.

Temperature-variant EXAFS spectroscopy has further been used to examine the local structure across the insulator—metal transition.[35] **Figures IV. 2G** and **A21** plot Cu K-edge EXAFS spectra of β'-$Cu_{0.40}V_2O_5$ at 95 and 298 K. The oscillation function $\chi(k)$ is most strongly modified in the *k*-range of 8—13 $Å^{-1}$ (**Fig. A21**); concomitant changes in the Fourier transform functions plotted in real space are shown in **Figure IV. 2G**. Two features in the Fourier transform curve are most notably modified with increasing temperature; the first feature corresponds to Cu–O bond distance at ~1.9Å, whereas the second corresponds to overlapping Cu–V/Cu bond distances at ~3.0Å. Fourier transform plots of EXAFS spectra measured for β'-$Cu_{0.40}V_2O_5$ (**Figure IV. 2G**) indicate pronounced broadening of the first (Cu-O) feature with increasing temperature; furthermore, the intensity of the Cu–V/Cu feature is decreased with increasing temperature. Two additional correlations are observed at ca. 2.0Å and 3.0 Å in the 95K Fourier transform spectrum and

are most clearly discernible in the difference plot (green). Fitted R-space and *k*-space EXAFS spectra are shown in **Figures A21C–F**; fitting parameters related to the major scattering paths are provided in **Table A14**. The primary scattering paths used to reproduce the experimental spectra between 1.1—3.1 Å are the Cu–O nearest-neighbor-shell at ca. 1.9Å and the Cu–V/Cu shell at ca. 3.0Å. The results further demonstrate that Cu-ions diffuse between the two proximate sites and are increasingly disordered cross the sites as a function of increasing temperature, thereby modifying the local coordination environment of Cu-ions and their interactions with the V_2O_5 lattice. The electronic structure implications of these modified Cu occupancies are discussed below with reference to DFT calculations (**Figure IV. 3**).

In order to understand the scattering paths involved in the broadening of the Cu–O peak and increase in intensity of the Cu–V/Cu peak with decrease in temperature, we have calculated the difference in intensity of the fitted Fourier transform spectra at 95K and 298K (**Figure A22**). This difference spectra is further split into components originating from the Cu-ion positioned at the Cu(1) (red) and Cu(2) (black) sites. For clarity, the Cu(1) component is shown on a negative intensity scale. The diffusion of Cu-ions from the Cu(1) to the Cu(2) site modifies the peaks at 1.95Å and 3.0Å (black curve), whereas the features at ca. 1.85Å and 2.7Å show the most pronounced changes (red curve) upon diffusion to the Cu(1)-site. The difference between the Cu(2)-component and Cu(1)-component reproduces the experimental difference spectra. Thus, the features at 1.9Å and 3.0Å serve as measures of the Cu-ion occupancies at the two crystallographically inequivalent sites. The crystallography and EXAFS data suggest a pronounced

temperature-induced cation shuttling mechanism underpins the metal-insulator transitions of β'-$Cu_xV_2O_5$.

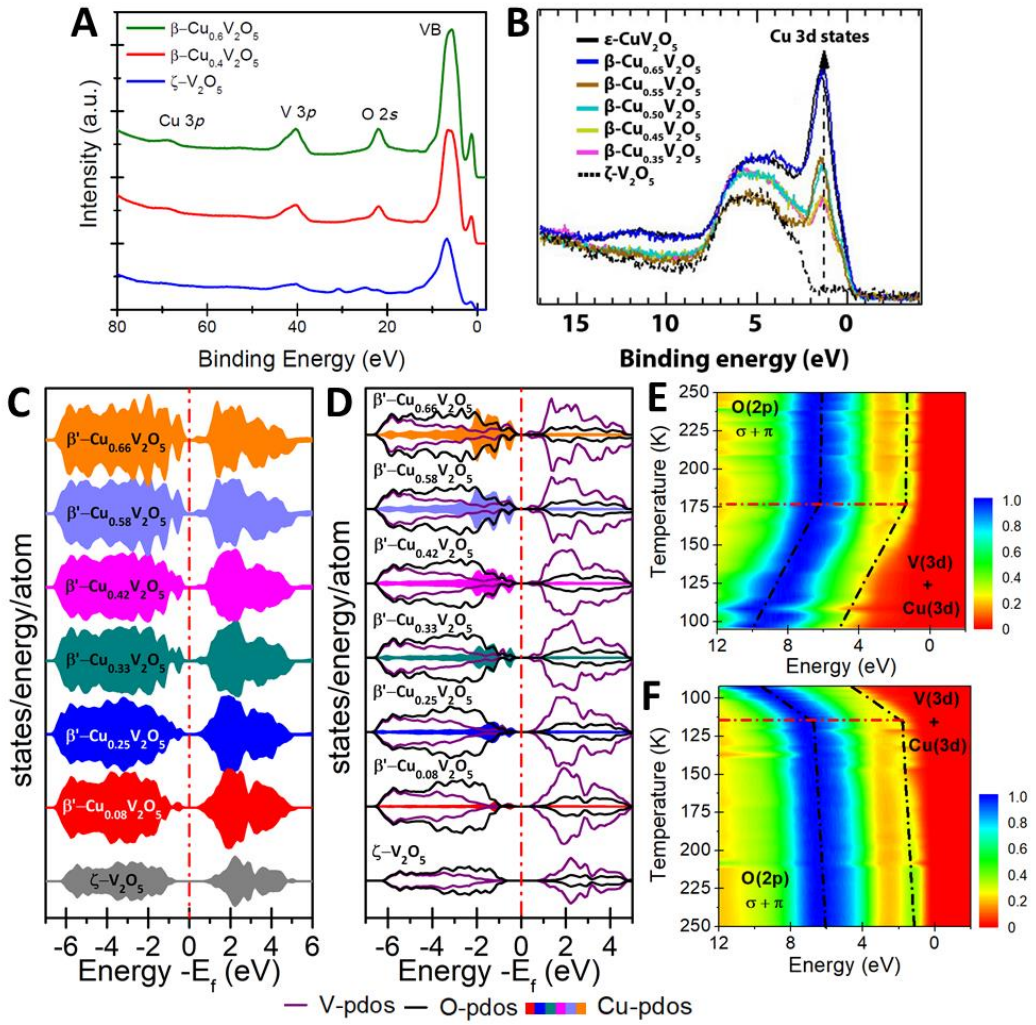

Figure IV. 3. (A) Cu 3p, V 3p, O 2s core level and valence band XPS spectra for ζ-V_2O_5, β'-$Cu_{0.40}V_2O_5$, and β'-$Cu_{0.60}V_2O_5$. **(B)** Valence band HAXPES data acquired for ζ-V_2O_5 and β'-$Cu_xV_2O_5$ where x=0.35, 0.45, 0.50, 0.55, and 0.65. A Cu 3d-derived 'midgap' state is observed in all the cuprated samples and is positioned at the upper edge of the valence band; the intensity of this feature increases monotonically with Cu content. **(C)** DFT+U calculated total density of states; and **(D)** atom-projected density of states for β'-$Cu_xV_2O_5$ as a function of Cu stoichiometry; **(E, F)** temperature-dependent angle-integrated valence band photoemission spectra for β'-$Cu_{0.4}V_2O_5$, illustrating a discontinuous opening of the energy gap opening at ca. 177K during heating in **(E)** and at ca. 115K during cooling in **(F)**

Mapping Electronic Structure across the Metal—Insulator Transitions of β'-$Cu_xV_2O_5$

Figures IV. 3C and **D** plot the calculated total density of states (DOS) and the atom-projected density of states (PDOS) of β'-$Cu_xV_2O_5$ as a function of increasing Cu content (*x*) within the 1D tunnels of ζ-V_2O_5. ζ-V_2O_5, a synthetically accessible metastable polymorph of V_2O_5,[36,37] is a semiconductor with the Fermi level positioned just above the valence band.[38] The valence band predominately comprises O 2*p* states, whereas the conduction band is mostly V 3*d* in origin. The conduction band is further split into a t_{2g} manifold derived from V $3d_{xy}$, $3d_{yz}$, and $3d_{xz}$ states undergoing π-type interactions with O 2*p* states and higher energy e_g^* states derived from V $3d_{z2}$ and $3d_{x2-y2}$ states interacting through σ interactions with O 2*p* states.[17,27,28] As a result of the significant distortion of the vanadium coordination environment away from octahedral geometry and the presence of vanadium-centered square pyramidal coordination environments, the t_{2g} manifold is further split into a set of nondegenerate states positioning V $3d_{xy}$ and $3d_{yz}$ orbitals at the bottom-edge of the conduction band (**Fig. IV. 3D**). Li-ion insertion within this structure is known to fill these states; the filled V 3*d* states are situated at the top of the valence band.[27,28] The localization of electrons within these states and the associated lattice distortion results in the stabilization of a small polaron (which is particularly prominent in α-V_2O_5 given its distinctive split-off V $3d_{xy}$ conduction band feature).[28] With increasing Cu-ion insertion within the ζ-V_2O_5 framework, filled states begin to appear just below the Fermi level at the top-edge of the valence band (**Figure IV. 3C**). These filled polaronic states are derived predominantly from Cu 3*d* states hybridized with V 3*d* and O 2*p* states

(**Figure IV. 3D**). The increase in the Cu-ion concentration further distorts the vanadium coordination environment away from octahedral symmetry, which in turn increases the energy dispersion of band-edge V 3*d* states. The increased population of midgap states effectively decreases the band gap of the material (from ca. 1.45 eV in ζ-V_2O_5 to ca. 0.27 eV in β'-$Cu_{0.66}V_2O_5$). In contrast to the weakly localized polaronic states in β'-$Li_xV_2O_5$, the polaronic states in β'-$Cu_xV_2O_5$ are considerably stronger in intensity owing to hybridization with Cu 3*d* states.[27,28,39]

The occupied density of states (DOS) and the binding energies of the core levels of ζ-V_2O_5 and β'-$Cu_xV_2O_5$ have been experimentally probed by X-ray photoemission spectroscopy (XPS). **Figure IV. 3A** plots the valence band (0—10 eV below the Fermi level) and the core levels of β'-$Cu_xV_2O_5$ as a function of the Cu stoichiometry.[27,39] **Figure IV. 3A** shows that an increase in the intensity of the Cu 3*p* band at ca. 70 eV as well as an increase in intensity of the valence band peak at ca. 1.1 eV is observed with increasing Cu-ion concentration from $x = 0$ to $x = 0.4$ to $x = 0.6$. Hard X-ray photoemission spectroscopy (HAXPES) data in **Figure IV. 3B** provide increased bulk sensitivity in comparison to the surface-sensitive soft XPS. A broad feature observed between binding energies of 0 and 8 eV common to ζ-V_2O_5 and the β'-$Cu_xV_2O_5$ series is ascribed to O 2*p* states based on DFT+U calculations. A prominent feature centered at ca. 1.1 eV below the Fermi level is absent for ζ-V_2O_5 but monotonically increases with Cu stoichiometry in β'-$Cu_xV_2O_5$ ($0.35 < x < 0.65$); based on the DFT+U calculations in **Figures IV. 3C** and **D**, this feature can be attributed to Cu 3*d* states hybridized with occupied (polaronic) V 3*d* states. **Figure IV. 3B** thereby provides direct evidence for the role of Cu-ions in

diminishing the bandgap of the material, which furthermore underpins the dependence of the metal-insulator transformation temperature on the Cu concentration.

Figures IV. 3E and **F** plot temperature-variant angle-integrated valence band photoemission spectra measurements for β'-$Cu_{0.40}V_2O_5$ upon heating and cooling, respectively. Analogous spectra for ζ-V_2O_5 and β'-$Cu_{0.60}V_2O_5$ are displayed in **Figure A23**. Spectral features ascribed to the "midgap" hybrid Cu 3*d*—V *3d*—O 2*p* and the O 2*p* states have been delineated by black dashed lines. During the heating cycle, an abrupt change in the spectrum is observed at 177K, denoting a discontinuous electronic transition. Specifically, an energy gap between the midgap and O 2*p* region (valence band) is seen to merge at high temperatures. Upon cooling (**Fig. IV. 3F**), a discontinuous transition and reversion of the spectrum is observed at ca. 115K, consistent with hysteresis observed in single-nanowire transport measurements.[14] In stark contrast, no such discontinuities are observed in corresponding spectra acquired for ζ-V_2O_5, devoid of Cu-ions, in the temperature range between 80K and 250K (**Figure A23C**, **A23D**). Similar hysteretic discontinuities albeit at lower temperature are observed in angle-integrated valence band photoemission spectra acquired for β'-$Cu_{0.60}V_2O_5$. At this Cu stoichiometry, the transition temperature is depressed to 124K and 108K during the heating and the cooling cycles, respectively (**Figures A23A** and **A23B**). The decrease in transition temperature with increasing Cu content noted in transport measurements can thus be ascribed to the reduced effective bandgap as also deduced from the DFT+U calculations.

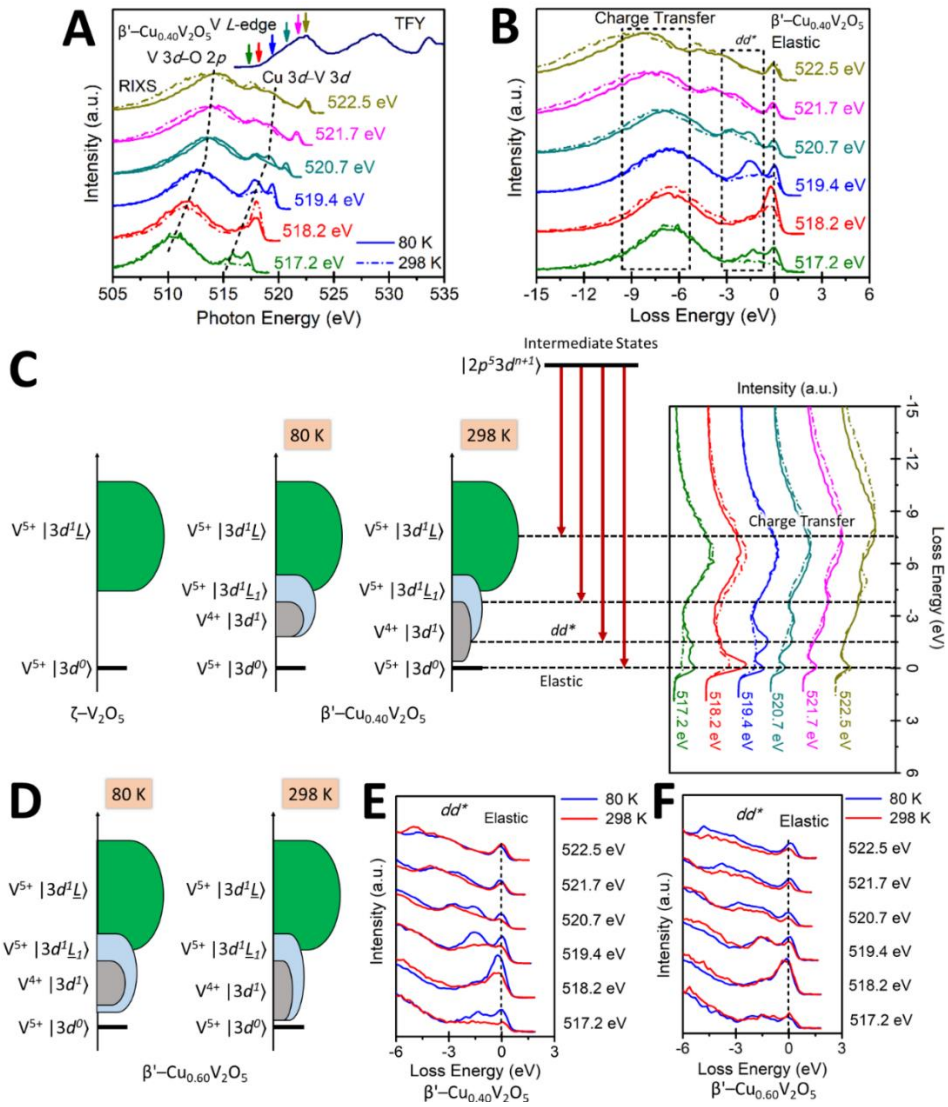

Figure IV. 4. (A) RIXS spectra, normalized to the maximum of the CT peak, at the V L_3-edge for β'-$Cu_{0.40}V_2O_5$ nanowires and the corresponding XAS (TFY) spectra is shown as dark blue curve. The RIXS excitation energy is increased from the absorption onset to the main V L_2-edge, which is shown as colored arrows on the XAS peak and the normalized RIXS spectra for the corresponding excitation energies follow the same color pattern as the arrows, **(B)** the normalized V L_3-edge RIXS spectra displayed on the loss energy scale. Schematic representation of V 2p → 3d → 2p excitations based on a single impurity Anderson model for ζ–V_2O_5 and β′–$Cu_{0.40}V_2O_5$ is shown in **(C)** and for β′–$Cu_{0.60}V_2O_5$ is shown in **(D)**, $\underline{L}$ represents an electron transferred from the oxygen 2p valence band to V 3d states through p–d hybridization and $\underline{L}_1$ represents an electron transferred from the hybridized Cu 3d – O 2p valence band to V 3d states through p–d hybridization, the spectrum shown in this panel is same as panel **(B)** for β′–$Cu_{0.40}V_2O_5$. Variable-temperature normalized V L_3-edge RIXS spectra displayed on the loss energy scale for **(E)** β'-$Cu_{0.40}V_2O_5$ and **(F)** β'-$Cu_{0.60}V_2O_5$. The spectra are plotted in the range -6 to 3 eV emphasizing on the d—d* transition.

Resonant inelastic X-ray scattering (RIXS) measurements have further been acquired for β'-$Cu_{0.40}V_2O_5$ and β'-$Cu_{0.60}V_2O_5$ nanowires. In a typical RIXS process, the incident photon energy is held close to the absorption threshold (e.g., at the transition metal L-edge). This results in the formation of electron-hole pair near the Fermi level. RIXS processes are able to probe low-energy excitations, such as local crystal-field excitations (d–d* transitions) and O 2p–V 3d charge-transfer (CT) excitations.[39] **Figure IV. 4A** displays the RIXS spectra, normalized to the maximum of the CT peak, at the V L_3-edge for β'-$Cu_{0.40}V_2O_5$ nanowires alongside the corresponding XANES spectrum. RIXS excitation energies are denoted by colored arrows. The normalized V L_3-edge RIXS spectra have further been plotted on the energy loss scale in **Figure IV. 4B**. The low-energy loss features are easily discernible when the material is excited at the absorption threshold because the interfering fluorescence features are generally weak. When excited at 517.2 eV corresponding to the absorption onset, a broad feature emerges around ~511 eV on the emission scale and ca. -6 eV on the loss-energy scale. Based on the DFT+U calculations noted above (**Fig. IV. 3D**), this feature is ascribed to charge transfer excitations between V 3*d*—O 2*p* hybrid states analogous to assignments for V_2O_5, β–$Sr_{0.17}V_2O_5$, and α'/β–$Na_xV_2O_5$.[39-43] Spectral features at -3 to -4 eV on the energy-loss scale (**Figure IV. 4B**) are thought to originate from hybrid O 2*p*–Cu 3*d*–V 3*d* filled "polaronic" bands, as discussed above and predicted from the DFT+U calculations (**Figure IV. 3D**). A sharp feature at ca. 516 eV in the emission spectrum and at ca. -1.5 eV on the loss-energy scale is observed and is most pronounced upon excitation at 519.4 eV (**Figures IV. 4A** and **4B**). In accordance with previous literature, this feature can be ascribed to *d*—

d* transitions.[39,41-44] Temperature-variant spectra plotted in **Figure IV. 4** reveal that the d—d* feature is relatively reduced in intensity at 298K ($T > T_{MIT}$) in comparison to 80K ($T < T_{MIT}$), reflective of greater delocalization of electrons at higher temperature.

Figure IV. 4C, D sketches the V $2p \rightarrow 3d \rightarrow 2p$ RIXS processes as per a single impurity Anderson model (AIM).[45,46] According to the model, the V-ion in ζ–V_2O_5 is in a +5 oxidation state and has a $3d^0$ configuration. Since RIXS probes charge neutral excitations, the only charge neutral oscillations possible in AIM are from the full O $2p$ band to the V $3d^0$ states. As a result of neutral charge fluctuations, it leads to the formation of V^{5+} $|3d^1\underline{L}\rangle$ band (green states in **Figure IV. 4C, D**; wherein $\underline{L}$ represents an electron transferred from the oxygen $2p$ valence band to the V $3d$ band through p–d hybridization), observed as charge-transfer excitations at ca. 6 eV on the loss-energy scale (**Figure IV. 4C, D**). In contrast to ζ–V_2O_5, β′–$Cu_xV_2O_5$ has additional Cu $3d$ states which hybridize with O $2p$ states. Neutral charge fluctuations in these states leads to the formation of V^{5+} $|3d^1\underline{L}_1\rangle$ band (light blue states in **Figure IV. 4C, D** wherein $\underline{L}_1$ represents an electron transferred from the hybrid Cu $3d$–O $2p$ valence band to the V $3d$ state through p–d hybridization), observed as extended charge-transfer excitations between approximately -3 to -4 eV on the loss energy scale. In addition, when Cu-ions are intercalated within the V_2O_5 lattice, specific vanadium sites are reduced from a nominal +5 to +4 oxidation state, thereby yielding a mixed $3d^1/3d^0$ system. Consequently, additional V^{4+} $|3d^1\rangle$ states (**Figure IV. 4C, D**) corresponding to d—d* transitions appear below the CT bands at ca. -1.5 eV on the loss-energy scale.

In the case of β′–$Cu_{0.4}V_2O_5$, the intensity of the *d*—*d** feature is diminished at higher temperature (298 K) (blue and cyan spectra in **Figure IV. 4A, 4B, and 4E**). As sketched in **Figure IV. 4C**, the V^{4+} $|3d^1\rangle$ band is more delocalized and has a higher energy dispersion at 298K as compared to 80K. The diminution in the intensity of the *d*—*d** feature can be understood by considering that the X-ray absorption cross-section is dependent on the coupling of the initial and the final state.[47,48] Since, the initial 2*p* eigenstate on the V-atom is localized, the most intense peak will be obtained for a final state that is also localized, which indeed is the situation at 80K wherein Cu-ions are predominantly situated in one of the two crystallographic sites; the polaronic states, are thus localized allowing strong coupling between initial and final states. However, as a result of Cu diffusion between the Cu(1) and the Cu(2) sites and increased disorder at 298 K, the final polaronic states are delocalized at high temperature, which leads to weaker coupling and a substantially broadened *d*—*d* * feature (**Figure IV. 4C, D**).

RIXS spectra acquired for β'-$Cu_{0.60}V_2O_5$ nanowires exhibit analogous CT excitations at ca. 511 eV on the emission scale and ca. -6 eV on the loss-energy scale (**Figure A24**). Besides the CT excitations, a $V^{5+}|3d^1\underline{L}_1\rangle$ band between -3 to -4 eV (**Figure IV. 4F and A24**) is again observed and ascribed to the mixing of V^{5+} $3d^1$ states with the hybridized Cu $3d^{10}$–O 2*p* states. However, the RIXS features are broader at this stoichiometry owing to the higher intercalation of Cu-ions in the sample and increased availability of Cu $3d^{10}$ states. The *d*—*d** feature is observed at ca. -1.5 eV on the loss-energy scale (**Figure IV. 4F** and **Figure A24**). With increasing Cu-ion intercalation, there is a relatively greater abundance and delocalization of V^{4+} $3d^1$ states, which makes the *d*—

*d** feature broader. Indeed, as delineated by the PDOS calculation in **Figure IV. 3D** and RIXS spectra in **Figure IV. 4F and A24**, the Cu $3d^{10}$ states almost entirely close the gap yielding a poor metal. Consequently, the metal—insulator transition likely derives from delocalization of polarons trapped at specific defect sites. Consistent with this picture, a broadening of the $V^{5+}|3d^1\underline{L}_1\rangle$ band of the RIXS spectrum between -2 to -4 eV is observed in **Figure IV. 4D**. Relatively weak coupling between the localized initial state (V 2*p* eigenstate) and the delocalized final states ($V^{5+}|3d^1\underline{L}_1\rangle$) leads to a diminished intensity of the features at 298K (**Figure IV. 4D, 4F and A24**).[47,48] The probes of electronic structure thus allow an orbital-specific delineation of electronic structure changes underpinning the metal—insulator transition and underscore the critical role of polaronic states.

Interplay of Structural Distortions and Electronic Structure Changes

Molecular dynamics simulations have been used to examine the migration of Cu-ions between the Cu(1) (symmetric) and the Cu(2) (asymmetric) sites in β'-$Cu_xV_2O_5$. Snapshots of the MD trajectory for the diffusion of one of the Cu-ions between these sites in β'-$Cu_{0.33}V_2O_5$ are shown in **Figures IV. 5A–C.** The total density of states (DOS) and the PDOS for the V atoms delineated V9 and V10 are shown in **Figures IV. 5D–F**. At 2.00 ps (**Figure IV. 5A**), the Cu-ion is in relatively closer proximity to the V10 atom with an approximate bond distance of 3.29Å, whereas the Cu1–V9 bond length is 3.56Å. Analyzing the corresponding DOS and PDOS in **Figure IV. 5D** reveals a bandgap of ca. 0.56 eV for this configuration.

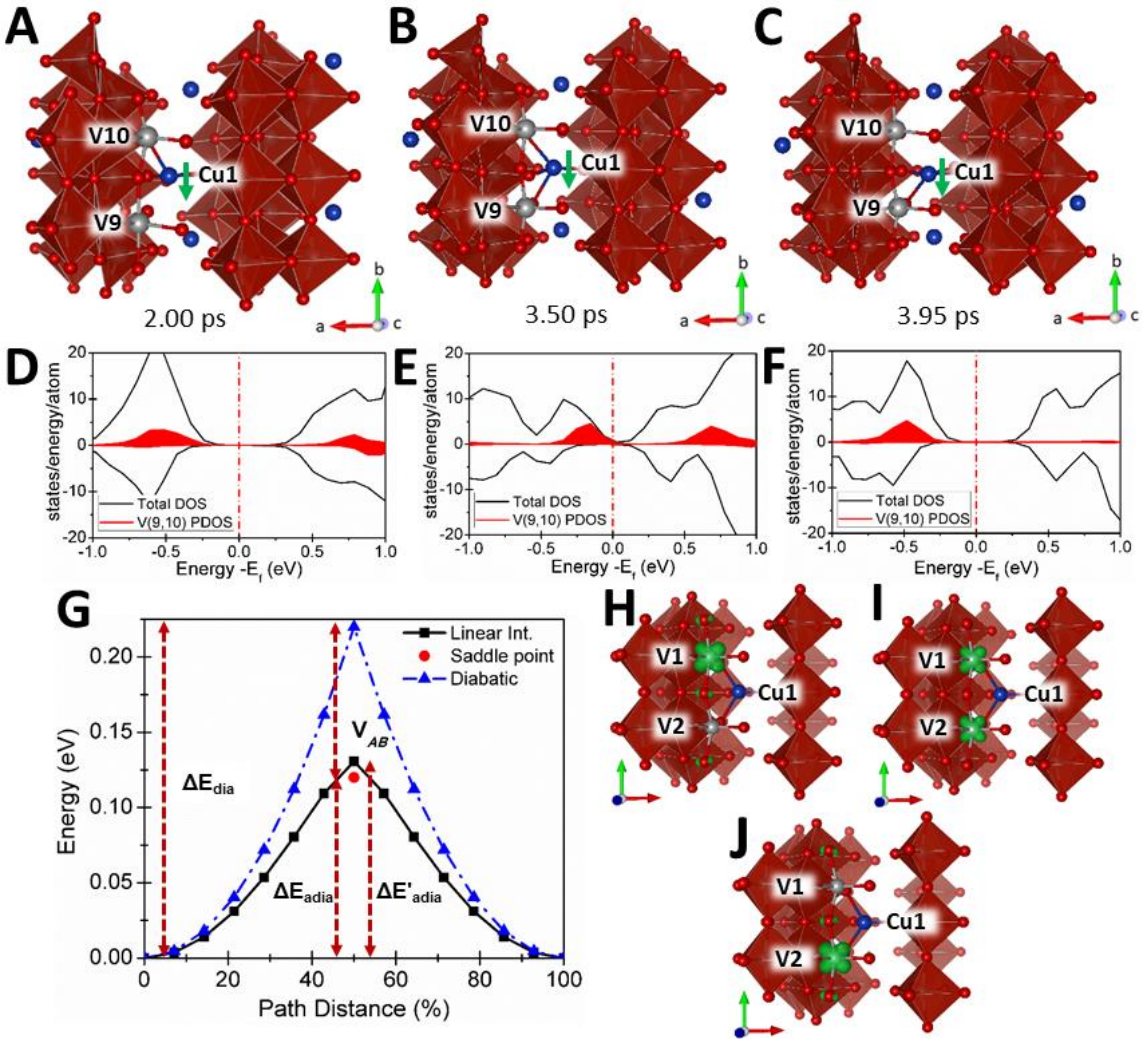

Figure IV. 5. The migration of Cu-ions between the Cu(1) and the Cu(2) sites of β'-$Cu_{0.33}V_2O_5$ have been studied using MD calculations. A snapshot of the MD trajectory for diffusion of one of the Cu-ions when it is in the Cu(2) site is illustrated in **(A)**, to the Cu(1) site in **(B)**, and back again to the Cu(2) site in **(C)**. The corresponding total DOS and PDOS for atoms labeled V9 and V10 are plotted in **(D-F)**, respectively. **(G)** Adiabatic and non-adiabatic diffusion barriers for the concomitant diffusion of polarons from V1 to V2 sites and the Cu-ion in β-$Cu_{0.08}V_2O_5$ are depicted, wherein **(H)** is the initial state, **(I)** is the transition state, and **(J)** is the final state. The dashed blue line in **(G)** shows the harmonic energy curves and its intersection represents the non-adiabatic energy barrier (ΔE_{dia}). The black line in **(G)** shows the adiabatic energy barrier, which is calculated along a reaction path defined by linear interpolation of the initial and final states. The red circle in **(G)** represents the relaxed saddle point geometry as calculated by nudged elastic band (NEB) theory.

In contrast at 3.50 ps (**Fig. IV. 5B**), the Cu-ion is positioned almost equidistant to the V9 and V10 atoms with Cu–V10 and Cu–V9 bond lengths of 3.63 and 3.56Å, respectively. Interestingly, analyzing the DOS in **Figure IV. 5E** reveals that bandgap of the material is almost entirely closed (ca. 0.05 eV), reflecting transformation to a metallic state for this configuration. The corresponding PDOS in **Figure IV. 5E** reveals that a significant contribution to the decrease in the bandgap arises from the Cu-ion being equidistant to the two V atoms. At 3.95 ps (**Figure IV. 5C**), the Cu-ions is again positioned in the asymmetric site; however, in contrast to the configuration at 2.00 ps. (**Figure IV. 5A**), the Cu–V10 bond length (4.02Å) is longer than the Cu-V9 (3.69Å) bond length. **Figure IV. 5F** illustrates the electronic structure consequences of this configuration, which results in a bandgap of 0.46 eV. Analogous MD simulations, snapshots of diffusion trajectories, and the corresponding PDOS for β'-$Cu_{0.41}V_2O_5$, are shown in **Figure A25** of the Supporting Information. The MD simulations depict the trajectory of Cu-ions and illustrate that thermally induced diffusion between the sites brings about metallization.

Figure IV. 5G illustrates that the approximate adiabatic activation energy barrier ($\Delta E'_{adia}$) calculated using linearly interpolated ionic positions is 0.13 eV. In contrast, the diffusion barrier (ΔE_{adia}) calculated using the relaxed geometry of the transition state is slightly lower at 0.12 eV. These values are in close agreement with the diffusion barrier calculated for polaron diffusion in β-$Li_{0.08}V_2O_5$.[27] Substituting the value of V_{AB} and ΔE_{dia} in Eq. **(1) (Theoretical methods section)** gives the value of ΔE_{dia} to be 0.22 eV. Consequently, adiabatic polaron transfer is energetically more favorable than diabatic polaron hopping by 0.1 eV. These results make a compelling case that the diffusion of the

Cu-ion is vital as the electronic diffusion of polaron is strongly coupled to the structural distortion of the Cu-ion and the subsequent structural distortion of the V_2O_5 lattice. In summary, at higher temperatures the shuttling of the Cu-ions between the Cu(1) (symmetric) and the Cu(2) (asymmetric) sites is facile, and readily enables the diffusion of coupled polarons. The electronic structure implications of the Cu shuttling and polaron diffusion is a decrease in the bandgap of the material, bringing about a transformation to a metallic phase.

IV.3. Conclusions

In conclusion, metal—insulator transitions are triggered in β′-$Cu_xV_2O_5$ by temperature, voltage, or current; the transition temperature is found to depend sensitively on the Cu-ion stoichiometry (x). Structural distortions of β′-$Cu_xV_2O_5$ across the thermal metal—insulator transition have been monitored using synchrotron powder X-ray diffraction, single-crystal X-ray diffraction, and EXAFS spectroscopy. Cu-ions exhibit split site disorder between two proximate crystallographic sites; crystallographic studies indicate increased disorder and shuttling of Cu-ions between the two sites at higher temperatures. The evolution of electronic structure with temperature has been examined by HAXPES, angle-integrated photoemission spectroscopy, and RIXS and the results have been interpreted with the aid of first-principles DFT calculations. These results evidence the clear stabilization of polarons comprising electrons trapped on the V_2O_5 framework; increasing polaron delocalization is observed at higher temperatures concurrent with Cu-ion shuttling and corresponds to polaron oscillation between two vanadium sites. MD simulations and NEB calculations demonstrate that the shuttling of

the Cu-ions between the two sites is facile, and readily enables the adiabatic diffusion of coupled polarons. The electronic structure implication of thermally driven Cu shuttling and polaron diffusion is a decrease in the bandgap of the material, thereby stabilizing a metallic phase. The results provide mechanistic insights into the close interplay of structural and electronic properties in underpinning metal—insulator transitions of a strongly correlated system. The utilization of cation diffusion and polaron shuttling paves the way to the use of ionic vectors with subtle structural distortions for obtaining conductance switching with minimal energy dissipation such as required for neuromorphic computing and sensing.

IV.4. Methods

Preparation of β/β′-$Cu_xV_2O_5$ and of ε-$Cu_xV_2O_5$ (Standard) Nanowires

The $Cu_xV_2O_5$ nanomaterials described in this work were prepared through two distinctive approaches. In the first approach, (β′/ε)-$Cu_xV_2O_5$ powders were synthesized using a high-temperature solid-state reaction. Briefly, Cu metal powder (Alfa Aesar, 99.99%) and V_2O_5 powder (Beantown Chemical, 99.5%) were mixed in stoichiometric amounts (x in $Cu_xV_2O_5$ ranging from $0.35<x<0.65$ and $x = 1.0$) and ball-milled (Spex mill, acrylic beads) for 30 min. The intimately mixed powders were next sealed in a quartz ampoule under vacuum. The ampoules were further heated in a muffle furnace at 550°C for 72 h. The contents of the ampoules were then removed and ground using a mortar and pestle prior to again sealing within a quartz ampoule under vacuum. The remixed powder was further annealed within a muffle furnace at 550°C for 7 days to obtain phase-pure samples. Black or purple/black polycrystalline powders were obtained depending on the

Cu stoichiometry. Phase-pure powders of β′-$Cu_xV_2O_5$ (x = 0.35, 0.45, 0.55, 0.65) were then treated hydrothermally to obtain 1D nanowires. In a typical reaction, 300 mg of β′-$Cu_xV_2O_5$ powders were added to a 23 mL polytetrafluoroethylene cup, which was placed within a steel autoclave (Parr Instruments). Subsequently, 15 mL of deionized water (18 $M\Omega \cdot cm^{-1}$) and 1 mL of 2-propanol were added to the reaction vessel. The sealed autoclave was heated to 210°C for 24 h and then allowed to cool to room temperature. The obtained black/purple powders were removed from suspension by filtration, washed with copious amounts of water and 2-propanol, and allowed to dry in air overnight.

In an alternative approach, β′-$Cu_xV_2O_5$ nanowires were synthesized according to a previously reported method.[14] Briefly, CuO and V_2O_5 were ground together in a mortar and pestle and were subsequently ball-milled as above to obtain an intimately mixed reaction mixture. Next, the milled materials were added to an alumina crucible and heated in ambient air within a muffle furnace at 550°C for 48 h. The powders were removed from the crucible, re-ground using a mortar and pestle, and treated under the same conditions for an additional 72 h. Next, 300 mg of the resulting α-CuV_2O_6 powder was added to a polytetrafluoroethylene cup, which was placed within a stainless-steel autoclave. Subsequently, 14 mL of deionized water (18 $M\Omega \cdot cm^{-1}$) and 2 mL of 2-propanol were added to the vessel. The autoclave was sealed and heated to 210°C for 7 days. The product was recovered by vacuum filtration and washed with copious amounts of deionized water and 2-propanol.

Large diffraction-quality single crystals of β'-$Cu_xV_2O_5$ were grown by mixing precursor Cu metal and α-V_2O_5 powders in a ball mill at targeted stoichiometries (0.35:1,

0.50:1, and 0.65:1, respectively), melting the solid mixture at 800ºC under an argon atmosphere in alumina crucibles, and cooling at a rate of 2ºC/h through the melting point (~690ºC). The resultant large black β'-$Cu_xV_2O_5$ crystals exhibited high luster and were needle- or plate-like with well-defined faces.

Powder Diffraction and Rietveld Refinement of β′-$Cu_xV_2O_5$ Nanowires

High-resolution synchrotron powder diffraction data were collected at beamline 11-BM of the Advanced Photon Source (APS), Argonne National Laboratory using an average wavelength of 0.436303Å (specific wavelengths for each pattern are indicated in the corresponding figure captions and tables). Discrete detectors covering an angular range from -6 to 16 2θ were scanned with data points collected every 0.001° at a scan speed of 0.01°·s^{-1}. Rietveld refinements were performed using the EXPGUI user interface of GSAS I.[49] Atomic positions, profile terms, lattice parameters and fractional copper occupancies were refined from high-resolution synchrotron diffraction data. All crystal structure renditions were prepared using the Vesta III software package.[50]

Single-Crystal X-Ray Diffraction

Diffraction data was collected on a BRUKER Quest X-ray diffractometer utilizing the APEX3 software suite,[51] with X-Ray radiation generated from a Mo-Iμs X-ray tube (K_α = 0.71073Å). Crystals were placed in a cold nitrogen stream (Oxford) maintained at either 110 or 250K. Following unit cell determination, extended data collection was performed using omega and phi scans. Data reduction, integration of frames, merging, and scaling were performed with the program APEX3, and absorption correction was performed utilizing the program SADABS.[52] Structures were solved using intrinsic

phasing, and least-squares refinement for all structures was carried out on F^2. Structural refinement and the calculation of derived results were performed using the SHELXTL package of computer programs and ShelXle.[53,54]

XANES and EXAFS Measurements

Cu K-edge X-ray absorption near-edge structure (XANES) and EXAFS spectra were collected at the Advanced Light Source (ALS) bending-magnet beamline 10.3.2 (2.4–17 keV). The storage ring is operated at 500 mA and 1.9 GeV. A custom made liquid nitrogen cryo-stage was used to collect the data at 95K, whereas spectra at 298K were measured by stopping the flow of liquid nitrogen. Spectra were collected in fluorescence mode in the energy rage 8880–9280 eV and 8880–9980eV (up to $k \approx 16.0 Å^{-1}$) by continuously scanning the Si (111) monochromator. Cu foil was used as a calibration standard. LabVIEW custom software was used to perform deadtime correction, glitch removal, energy calibration, pre-edge subtraction, and post-edge normalization.[55] The Athena suite of programs in the IFEFFIT package was used for further processing of the data. Multishell least-squares parameter fitting of the Cu K-edge EXAFS data was performed using ARTEMIS module of IFEFFIT software package.[56] The photoelectron mean free path, scattering amplitude, and phase functions were calculated using the FEFF6 program.[57] Crystallographic data obtained from high-resolution synchrotron powder X-ray diffraction has been used to build models of the Cu site with the Cu-ion positioned at both Cu(1) and Cu(2) sites. Physical constraints have been placed on the coordination numbers (based on the structure refined from XRD) to reduce the correlation between the best-fit parameters and improve the quality of the refinement.

Scanning Electron Microscopy

SEM images and energy dispersive X-ray spectra (EDX) were collected using a JEOL JSM-7500F FE-instrument equipped with an Oxford EDX elemental characterization system. Following device measurements, Si substrates containing single-nanowire devices constructed using photolithographic techniques were affixed to carbon tape and SEM images and EDX spectra were collected for regions of the individual nanowires.

Single-Nanowire Transport Measurements

Standard photolithographic techniques were employed to isolate individual nanowires of single-crystalline β′-$Cu_xV_2O_5$ and construct device architectures. Briefly, prior to device fabrication, a Si/SiO_2 substrate comprising a Si wafer passivated with a SiO_2 oxide layer with a thickness of 300 nm was thoroughly cleaned by ultrasonication in acetone, methanol, and deionized water. β′-$Cu_xV_2O_5$ nanowire samples were dispersed in 2-propanol with the aid of ultrasonication. This dispersion was drop-cast onto the cleaned Si/SiO_2 substrate. Individual nanowires were identified by optical microscopy and multi-terminal devices were fabricated using standard photolithographic techniques. Typically, fabricated devices had a channel length of 2 μm between the source and drain. Finally, Cr/Au layers (5 nm/70 nm) were deposited using an electron-beam evaporator. All transport measurements were performed in a two-terminal DC configuration using a liquid nitrogen cryostat using Lakeshore 330 temperature controller, SR 7265 lock-in amplifiers, and a Keithley 2400 SourceMeter under high vacuum. For resistance *versus* temperature measurements (**Figure IV. 1A-C, A16**).

X-ray Emission and Absorption Spectroscopy

RIXS spectra were collected at the ultrahigh efficiency iRIXS endstation of Beamline 8.0.1.1 of the Advanced Light Source. The beamline undulator and spherical grating monochromator supply a linearly polarized photon beam. The linear polarization of the incident beam is parallel to the scattering plane. RIXS spectra were acquired at specific excitation energies; the excitation energy value was first calibrated, and then the emission energy was calibrated based on the elastic feature. The XAS data shown in this work are collected in total fluorescence yield mode. All the data have been normalized to the beam flux measured by a clean gold mesh upstream of the endstation. To collect the RIXS spectra at 80K the samples were cooled using liquid N_2, whereas spectra at 298K were measured by stopping the flow of liquid N_2. X-ray absorption spectroscopy (XAS) measurements were acquired at RE/IXS beamline (10lD-2) of the Canadian Light Source (CLS). All measurements were performed using the impurity diffraction grating, which has a resolving power $\Delta E/E$ of 700 in the measured energy range (508—565 eV). The utilized REIXS endstation is equipped with a microchannel plate detector (MCP) and a silicon drift detector (SDD). Partial fluorescence yield spectra were obtained by averaging spectra across a 100-channel width centered on either the V L- or O K-edge emission lines. Prior to measurement, powder samples were dispersed and affixed to copper tape. XES spectra plotted on an energy loss scale were adjusted to 0 by subtracting the excitation energy from the spectra.

HAXPES and XPS Measurements

HAXPES measurements were performed at the I09 Surface and Interface Structural Analysis beamline of the Diamond Light Source. The beamline has two canted undulators that enable access to photon energies spanning the range from 100 eV to 20 keV. Photoelectron spectra were energy resolved and measured using a VG Scienta EW40000 high-energy analyzer with a 30° acceptance angle. Measurements were performed at $h\upsilon$ of 6 keV with an overall energy resolution of better than 250 meV. XPS measurements were performed using a Phi VersaProbe 5000 laboratory instrument outfitted with a monochromated Al Kα source and a hemispherical analyzer with an overall resolution of 450 meV. All samples were measured with both XPS and HAXPES. For HAXPES, the samples were rastered to avoid possible beam damage. The (HA)XPS spectra were energy calibrated to O 1s and V 2p core-levels of reference ζ-V_2O_5 (energy aligned to the Fermi level of a gold foil) in order to account for any shifts due to charging.

Angle-Integrated Photoemission Spectroscopy Measurements

High-resolution angle-integrated photoemission spectroscopy were performed using μARPES end station at the MAESTRO facility at beamline 7.0.2 of the Advanced Light Source (ALS). This end station is equipped with a hemispherical VG Sienta R4000 analyzer. The synchrotron beam is estimated to have a lateral size of around 30—50 μm. Powder samples of β'-$Cu_xV_2O_5$ nanowires were loaded onto the sample holder and placed within the ultra-high vacuum chamber. For ARPES and XPS measurements, a 15 μm field-of-view circular aperture in the electron beam path was used to select an area of interest in the sample. The end station has a total energy resolution of ca. 20 meV. Photon energies

of 100 eV were used to acquire the Cu 3*p*, V 3*p*, O 2*s* core-level data, and a photon energy of 30 eV to collect the valence-band spectra. The chamber was equipped with a custom-designed heating stage to facilitate temperature-variant experiments. The temperature was varied between a temperature range of 80–298K across heating and cooling cycles.

Theoretical Methods

Initial coordinates of β'-$Cu_xV_2O_5$ were obtained from refinement of powder and single-crystal X-ray diffraction data. Electronic structure calculations were performed using DFT[58] as implemented in Vienna ab initio simulation package (VASP).[59,60] Electron exchange-correlation interactions were implemented by using generalized gradient approximation (GGA) of Perdew–Burke–Ernzerhof (PBE) functionals.[61] The projector-augmented wave (PAW) formalism with a kinetic energy cutoff of 600 eV was used to describe the electron–ion interactions.[62] On-site Coulomb interactions was included by using the rotationally invariant density functional theory (DFT+*U*) formalism of Dudarev *et al.*[63] For vanadium and copper atoms, on-site coulomb interaction parameters of U = 3.0 and 7.0 eV, respectively, were used. The U value for vanadium was determined by comparing the bandgap calculated for ζ-V_2O_5 (**Figure A26A**) and its experimental bandgap measured in our earlier work.[38] The band-gap of β'-$Cu_{0.10}V_2O_5$ was then calculated at different values of U for both V and Cu-atoms (**Figure A26B**) and compared to **Figure IV. 3A and 3B** in order to deduce U parameters for both Cu and V atoms. A Γ-point centered Monkhorst−Pack reciprocal grid of 4×4×4 k-points was used for first Brillouin zone sampling in the density-of-states calculation; a 2×2×2 k-points reciprocal

grid was used for relaxation of the structures. The structures were considered to be relaxed when each Cartesian force component was less the 0.03 eV/Å unless otherwise noted.

The diffusion of the Cu-ions and the concomitant diffusion of polarons were calculated by employing the NEB formalism as implemented in VASP. DFT+*U* calculations were employed to examine the energetics and migration energy barriers associated with diffusion pathways. The linearly interpolated midpoint of the initial and final structures were relaxed to find the geometry and energy of the transition state. The end points were relaxed until each Cartesian force component was less the 0.001 eV/Å, whereas for the forces along the NEB path, the convergence criterion was 0.05 eV/Å. In order to discard spurious interactions between the images, the supercell was built such that the distance between the images was no less than 7.3 Å.

Cu-ion diffusion and the associated polaron diffusion on the vanadium centers have further been modeled using nudged elastic band (NEB) calculations. The Cu-ion and its associated polaron at site V1 represents the initial ground-state configuration (labeled as **0** in **Figure IV. 5G**). The final state of the system is related to the initial state by symmetry (labeled as **100** in **Figure IV. 5G**). Hence, once the polaron is obtained on the initial ground state geometry, a simple translational operation can be performed to obtain the coordinates of the final state. **Figure IV. 5G** plots the diffusion-energy barrier *versus* the reaction coordinate for the diffusion of the polaron and the Cu-ion from the initial to the final state. Three different scenarios have been considered for polaron diffusion. In the first case, as shown by the dashed blue line, change in energy as a function of change in ionic position keeping the polaron localized either on site **0** or site **100** is described by

harmonic potential energy wells centered at sites **0** and **100**. The intersection of these harmonic potentials yields the non-adiabatic activation energy barrier (ΔE_{dia}). In this figure, we have plotted the harmonic potential energy wells using the calculated value of ΔE_{dia}:[64]

$$\Delta E_{dia} = \Delta E_{adia} + V_{AB} \quad \ldots(IV.1)$$

where ΔE_{adia} is the adiabatic activation energy and V_{AB} is the electron coupling matrix element. According to the Mulliken-Hush formalism within the Marcus theory,[65] the parameter V_{AB} was estimated as follows:

$$V_{AB} = \frac{1}{2} \Delta E_{12} \quad \ldots(IV.2)$$

where ΔE_{12} is the energy difference between the highest occupied state and the lowest unoccupied state of the adiabatic transition state. It should be noted that since we are using ground state theory (DFT) to calculate the energy of the unoccupied state, the value of V_{AB} calculated here is approximate, but nevertheless illustrates the adiabaticity of polaron transfer. **Figure A26** shows the total DOS and the PDOS of the relaxed transition state geometry for atoms V1 and V2. The electron coupling matrix (V_{AB}) has been calculated to be 0.1 eV using the value of ΔE_{12} (0.2 eV) which is determined from **Figure A26B**.

In the second scenario, the approximate adiabatic activation energy barrier has been calculated by linearly interpolating the ion positions between states **0** and **100**. Energies for the self-consistent charge densities on the Born-Oppenheimer surface correspond to these approximate ionic positions. The difference in energy calculated for the states **0** and **50**, the linearly interpolated transition state, gives the value of approximate adiabatic activation energy barrier, denoted as $\Delta E'_{adia}$. Finally, in the third scenario, the

linearly interpolated transition state is further relaxed using the NEB method to provide a refined transition state geometry and with that the refined approximation of the adiabatic activation energy barrier, denoted as ΔE_{adia}.

Spin-polarized *ab initio* molecular dynamics (AIMD) calculations were performed for the simulation of polaron hopping events and Cu-ion diffusion. DFT+*U* was employed for the simulation of polaron hopping and Cu-ion diffusion. A 1×2×1 supercell of β'-$Cu_xV_2O_5$ with *x* values of 0.33 and 0.42 were used. A Γ-point centered Monkhorst−Pack reciprocal grid of 2×2×2 k-points was used for first Brillouin zone sampling. The simulations employed a microcanonical ensemble (*NVE*) for 2 ps to thermally equilibrate the model followed by a molecular dynamics run for 20 ps. The Nose–Hoover thermostat was used to control the temperature.[66] A time step of 5 fs was used to add the equations of motion. The simulations were performed at 700K in order to decrease the computational effort and increase the probability of polaron hopping events and Cu-ion diffusion in the simulated time interval.

IV.5. References

(1) Ionescu, A. M.; Riel, H. Tunnel Field-Effect Transistors as Energy-Efficient Electronic Switches. *Nature* **2011**, *479*, 329.

(2) Salahuddin, S.; Ni, K.; Datta, S. The Era of Hyper-Scaling in Electronics. *Nat. Electron.* **2018**, *1*, 442-450.

(3) Pickett, M. D.; Medeiros-Ribeiro, G.; Williams, R. S. A Scalable Neuristor Built with Mott Memristors. *Nat. Mater.* **2013**, *12*, 114.

(4) Zhou, Y.; Ramanathan, S. Correlated Electron Materials and Field Effect Transistors for Logic: A Review. *Crit. Rev. Solid State Mater. Sci.* **2013**, *38*, 286-317.

(5) Sarkar, D.; Xie, X.; Liu, W.; Cao, W.; Kang, J.; Gong, Y.; Kraemer, S.; Ajayan, P. M.; Banerjee, K. A Subthermionic Tunnel Field-Effect Transistor with an Atomically Thin Channel. *Nature* **2015**, *526*, 91.

(6) Salahuddin, S.; Datta, S. Use of Negative Capacitance to Provide Voltage Amplification for Low Power Nanoscale Devices. *Nano Lett.* **2008**, *8*, 405-410.

(7) Shukla, N.; Thathachary, A. V.; Agrawal, A.; Paik, H.; Aziz, A.; Schlom, D. G.; Gupta, S. K.; Engel-Herbert, R.; Datta, S. A Steep-Slope Transistor Based on Abrupt Electronic Phase Transition. *Nat. Commun.* **2015**, *6*, 7812.

(8) Imada, M.; Fujimori, A.; Tokura, Y. Metal-Insulator Transitions. *Rev. Mod. Phys.* **1998**, *70*, 1039.

(9) Kumar, S.; Strachan, J. P.; Williams, R. S. Chaotic Dynamics in Nanoscale NbO_2 Mott Memristors for Analogue Computing. *Nature* **2017**, *548*, 318.

(10) Qazilbash, M. M.; Brehm, M.; Chae, B.-G.; Ho, P.-C.; Andreev, G. O.; Kim, B.-J.; Yun, S. J.; Balatsky, A.; Maple, M.; Keilmann, F. Mott Transition in VO_2 Revealed by Infrared Spectroscopy and Nano-Imaging. *Science* **2007**, *318*, 1750-1753.

(11) Cao, J.; Ertekin, E.; Srinivasan, V.; Fan, W.; Huang, S.; Zheng, H.; Yim, J.; Khanal, D.; Ogletree, D.; Grossman, J. Strain Engineering and One-Dimensional Organization of Metal–Insulator Domains in Single-Crystal Vanadium Dioxide Beams. *Nat. Nanotech.* **2009**, *4*, 732.

(12) Zimmers, A.; Aigouy, L.; Mortier, M.; Sharoni, A.; Wang, S.; West, K.; Ramirez, J.; Schuller, I. K. Role of Thermal Heating on the Voltage Induced Insulator-Metal Transition in VO_2. *Phys. Rev. Lett.* **2013**, *110*, 056601.

(13) Budai, J. D.; Hong, J.; Manley, M. E.; Specht, E. D.; Li, C. W.; Tischler, J. Z.; Abernathy, D. L.; Said, A. H.; Leu, B. M.; Boatner, L. A. Metallization of Vanadium Dioxide Driven by Large Phonon Entropy. *Nature* **2014**, *515*, 535.

(14) Patridge, C. J.; Wu, T.-L.; Sambandamurthy, G.; Banerjee, S. Colossal Above-Room-Temperature Metal–Insulator Switching of a Wadsley-Type Tunnel Bronze. *Chem. Commun.* **2011**, *47*, 4484-4486.

(15) Andrews, J. L.; De Jesus, L. R.; Tolhurst, T. M.; Marley, P. M.; Moewes, A.; Banerjee, S. Intercalation-Induced Exfoliation and Thickness-Modulated Electronic Structure of a Layered Ternary Vanadium Oxide. *Chem. Mater.* **2017**, *29*, 3285-3294.

(16) Zavalij, P. Y.; Whittingham, M. S. Structural Chemistry of Vanadium Oxides with Open Frameworks. *Acta Crystallogr., Sect. B: Struct. Sci* **1999**, *55*, 627-663.

(17) Parija, A.; Waetzig, G. R.; Andrews, J. L.; Banerjee, S. Traversing Energy Landscapes Away from Equilibrium: Strategies for Accessing and Utilizing Metastable Phase Space. *J. Phys. Chem. C* **2018**, *122*, 25709-25728.

(18) Andrews, J. L.; Singh, S.; Kilcoyne, C.; Shamberger, P. J.; Sambandamurthy, G.; Banerjee, S. Memristive Response of a New Class of Hydrated Vanadium Oxide Intercalation Compounds. *MRS Commun.* **2017**, *7*, 634-641.

(19) Ueda, Y. Vanadate Family as Spin-Gap Systems. *Chem. Mater.* **1998**, *10*, 2653-2664.

(20) Ueda, Y.; Isobe, M.; Yamauchi, T. Superconductivity under High Pressure in β (β′)-Vanadium Bronzes. *J. Phys. Chem. Solids* **2002**, *63*, 951-955.

(21) Marley, P. M.; Singh, S.; Abtew, T. A.; Jaye, C.; Fischer, D. A.; Zhang, P.; Sambandamurthy, G.; Banerjee, S. Electronic Phase Transitions of δ-$Ag_xV_2O_5$ Nanowires: Interplay between Geometric and Electronic Structures. *J. Phys. Chem. C* **2014**, *118*, 21235-21243.

(22) Marley, P. M.; Stabile, A. A.; Kwan, C. P.; Singh, S.; Zhang, P.; Sambandamurthy, G.; Banerjee, S. Charge Disproportionation and Voltage-Induced Metal–Insulator Transitions Evidenced in β-$Pb_xV_2O_5$ Nanowires. *Adv. Funct. Mater.* **2013**, *23*, 153-160.

(23) Patridge, C. J.; Wu, T.-L.; Jaye, C.; Ravel, B.; Takeuchi, E. S.; Fischer, D. A.; Sambandamurthy, G.; Banerjee, S. Synthesis, Spectroscopic Characterization, and Observation of Massive Metal-Insulator Transitions in Nanowires of a Nonstoichiometric Vanadium Oxide Bronze. *Nano Lett.* **2010**, *10*, 2448-2453.

(24) Onoda, M.; Sato, T. Polaronic Nonmetal–Correlated Metal Crossover System β′-$Cu_xV_2O_5$ with Anharmonic Copper Oscillation and Thermoelectric Conversion Performance. *J. Phys. Soc. Japan* **2017**, *86*, 124801.

(25) Yamaura, J.-I.; Yamauchi, T.; Isobe, M.; Yamada, H.; Ueda, Y. Observation of Structural Change with Possible Charge Disproportionation in Copper Vanadium Oxide Bronze β′-$Cu_{0.65}V_2O_5$. *J. Phys. Soc. Japan* **2004**, *73*, 914-920.

(26) Yamada, H.; Ueda, Y. Structural and Electric Properties of β′-$Cu_xV_2O_5$. *J. Phys. Soc. Japan* **2000**, *69*, 1437-1442.

(27) Horrocks, G. A.; Parija, A.; De Jesus, L. R.; Wangoh, L.; Sallis, S.; Luo, Y.; Andrews, J. L.; Jude, J.; Jaye, C.; Fischer, D. A.; Prendergast, D.; Piper, L. F. J.; Banerjee, S. Mitigating Cation Diffusion Limitations and Intercalation-Induced Framework Transitions in a 1D Tunnel-Structured Polymorph of V_2O_5. *Chem. Mater.* **2017**, *29*, 10386-10397.

(28) De Jesus, L. R.; Horrocks, G. A.; Liang, Y.; Parija, A.; Jaye, C.; Wangoh, L.; Wang, J.; Fischer, D. A.; Piper, L. F.; Prendergast, D. Mapping Polaronic States and Lithiation Gradients in Individual V_2O_5 Nanowires. *Nat. Commun.* **2016**, *7*, 12022.

(29) Parija, A.; Liang, Y.; Andrews, J. L.; De Jesus, L. R.; Prendergast, D.; Banerjee, S. Topochemically De-Intercalated Phases of V_2O_5 as Cathode Materials for Multivalent Intercalation Batteries: A First-Principles Evaluation. *Chem. Mater.* **2016**, *28*, 5611-5620.

(30) Andrews, J. L.; Cho, J.; Wangoh, L.; Suwandaratne, N.; Sheng, A.; Chauhan, S.; Nieto, K.; Mohr, A.; Kadassery, K. J.; Popeil, M. R.; Thakur, P. K.; Sfeir, M.; Lacy, D. C.; Lee, T.-L.; Zhang, P.; Watson, D. F.; Piper, L. F. J.; Banerjee, S. Hole Extraction by Design in Photocatalytic Architectures Interfacing CdSe Quantum Dots with Topochemically Stabilized Tin Vanadium Oxide. *J. Am. Chem. Soc.* **2018**, *140*, 17163-17174.

(31) Staniuk, M.; Zindel, D.; Van Beek, W.; Hirsch, O.; Kränzlin, N.; Niederberger, M.; Koziej, D. Matching the Organic and Inorganic Counterparts during Nucleation and Growth of Copper-Based Nanoparticles–*in situ* Spectroscopic Studies. *CrystEngComm.* **2015**, *17*, 6962-6971.

(32) Kumar, P.; Nagarajan, R.; Sarangi, R. Quantitative X-ray Absorption and Emission Spectroscopies: Electronic Structure Elucidation of Cu_2S and CuS. *J. Mater. Chem. C* **2013**, *1*, 2448-2454.

(33) Gross, S.; Bauer, M. EXAFS as Powerful Analytical Tool for the Investigation of Organic–Inorganic Hybrid Materials. *Adv. Funct. Mater.* **2010**, *20*, 4026-4047.

(34) Guillerm, V.; Gross, S.; Serre, C.; Devic, T.; Bauer, M.; Férey, G. A Zirconium Methacrylate Oxocluster as Precursor for the Low-Temperature Synthesis of Porous Zirconium (IV) Dicarboxylates. *Chem. Commun.* **2010**, *46*, 767-769.

(35) Yao, T.; Zhang, X.; Sun, Z.; Liu, S.; Huang, Y.; Xie, Y.; Wu, C.; Yuan, X.; Zhang, W.; Wu, Z. Understanding the Nature of the Kinetic Process in a VO_2 Metal-Insulator Transition. *Phys. Rev. Lett.* **2010**, *105*, 226405.

(36) Marley, P. M.; Abtew, T. A.; Farley, K. E.; Horrocks, G. A.; Dennis, R. V.; Zhang, P.; Banerjee, S. Emptying and Filling a Tunnel Bronze. *Chem. Sci.* **2015**, *6*, 1712-1718.

(37) Andrews, J. L.; Mukherjee, A.; Yoo, H. D.; Parija, A.; Marley, P. M.; Fakra, S.; Prendergast, D.; Cabana, J.; Klie, R. F.; Banerjee, S. Reversible Mg-Ion Insertion in a Metastable One-Dimensional Polymorph of V_2O_5. *Chem* **2018**, *4*, 564-585.

(38) Tolhurst, T. M.; Leedahl, B.; Andrews, J. L.; Marley, P. M.; Banerjee, S.; Moewes, A. Contrasting 1D Tunnel-Structured and 2D Layered Polymorphs of V_2O_5: Relating Crystal Structure and Bonding to Band Gaps and Electronic Structure. *Phys. Chem. Chem. Phys.* **2016**, *18*, 15798-15806.

(39) Chen, B.; Laverock, J.; Newby Jr, D.; Su, T.-Y.; Smith, K. E.; Wu, W.; Doerrer, L. H.; Quackenbush, N. F.; Sallis, S.; Piper, L. F. Electronic Structure of β-$Na_xV_2O_5$ (x≈

0.33) Polycrystalline Films: Growth, Spectroscopy, and Theory. *J. Phys. Chem. C* **2014**, *118*, 1081-1094.

(40) Khyzhun, O. Y.; Strunskus, T.; Grünert, W.; Wöll, C. Valence Band Electronic Structure of V_2O_5 as Determined by Resonant Soft X-ray Emission Spectroscopy. *J. Electron Spectrosc. Relat. Phenom.* **2005**, *149*, 45-50.

(41) Schmitt, T.; Duda, L.-C.; Matsubara, M.; Augustsson, A.; Trif, F.; Guo, J.-H.; Gridneva, L.; Uozumi, T.; Kotani, A.; Nordgren, J. Resonant Soft X-ray Emission Spectroscopy of Doped and Undoped Vanadium Oxides. *J. Alloys Compd.* **2004**, *362*, 143-150.

(42) Zhang, G.; Callcott, T. Resolving *dd* Transitions in NaV_2O_5 using Angle-Resolved Resonant Inelastic X-ray Scattering at the V L-edge. *Phys. Rev. B* **2006**, *73*, 125102.

(43) Laverock, J.; Preston, A.; Chen, B.; McNulty, J.; Smith, K.; Piper, L.; Glans, P.-A.; Guo, J.-H.; Marin, C.; Janod, E. Orbital Anisotropy and Low-Energy Excitations of the Quasi-One-Dimensional Conductor β-$Sr_{0.17}V_2O_5$. *Phys. Rev. B* **2011**, *84*, 155103.

(44) Duda, L.-C.; Schmitt, T.; Nordgren, J.; Kuiper, P.; Dhalenne, G.; Revcolevschi, A. Low-Energy Excitations in Resonant Inelastic X-Ray Scattering of α'-NaV_2O_5. *Phys. Rev. Lett.* **2004**, *93*, 169701.

(45) Kotani, A. Resonant Inelastic X-ray Scattering in d and f Electron Systems. *Eur. Phys. J. B* **2005**, *47*, 3-27.

(46) Bisogni, V.; Catalano, S.; Green, R. J.; Gibert, M.; Scherwitzl, R.; Huang, Y.; Strocov, V. N.; Zubko, P.; Balandeh, S.; Triscone, J.-M. Ground-State Oxygen Holes and

the Metal–Insulator Transition in the Negative Charge-Transfer Rare-Earth Nickelates. *Nat. Commun.* **2016**, *7*, 13017.

(47) Prendergast, D.; Galli, G. X-ray Absorption Spectra of Water from First Principles Calculations. *Phys. Rev. Lett.* **2006**, *96*, 215502.

(48) Parija, A.; Choi, Y.-H.; Liu, Z.; Andrews, J. L.; De Jesus, L. R.; Fakra, S. C.; Al-Hashimi, M.; Batteas, J. D.; Prendergast, D.; Banerjee, S. Mapping Catalytically Relevant Edge Electronic States of MoS_2. *ACS Cent. Sci.* **2018**, *4*, 493-503.

(49) Toby, B. H. EXPGUI, A Graphical User Interface for GSAS. *J. Appl. Cryst.* **2001**, *34*, 210-213.

(50) Momma, K.; Izumi, F. VESTA 3 for Three-Dimensional Visualization of Crystal, Volumetric and Morphology Data. *J. Appl. Cryst.* **2011**, *44*, 1272-1276.

(51) APEX2. *Program for Data Collection on Area Detectors*, BRUKER AXS Inc., 5465 East Cheryl Parkway, Madison, WI 53711–55373 USA.

(52) SADABS; Sheldrick, G. M. *Program for Absorption Correction of Area Detector Frames*, BRUKER AXS Inc., 5465 East Cheryl Parkway, Madison, WI 53711–55373 USA.

(53) Sheldrick, G. M. A Short History of SHELX. *Acta Crystallogr., A, Found. Crystallogr.* **2008**, *64*, 112-122.

(54) Hübschle, C. B.; Sheldrick, G. M.; Dittrich, B. ShelXle: A Qt Graphical User Interface for SHELXL. *J. Appl. Cryst.* **2011**, *44*, 1281-1284.

(55) Kelly, S.; Hesterberg, D.; Ravel, B. Analysis of Soils and Minerals Using X-ray Absorption Spectroscopy. In. *Methods of Soil Analysis Part 5–Mineralogical Methods*,

Ulery, A. L., Drees, L. R., Eds.; Soil Science Society of America: Madison, WI, 2008; pp 2367–2464.

(56) Ravel, B.; Newville, M. ATHENA, ARTEMIS, HEPHAESTUS: Data Analysis for X-ray Absorption Spectroscopy using IFEFFIT. *J. Synchrotron Rad.* **2005**, *12*, 537-541.

(57) Zabinsky, S.; Rehr, J.; Ankudinov, A.; Albers, R.; Eller, M. Multiple-Scattering Calculations of X-ray-Absorption Spectra. *Phys. Rev. B* **1995**, *52*, 2995.

(58) Kohn, W.; Sham, L. J. Self-Consistent Equations Including Exchange and Correlation Effects. *Phys. Rev.* **1965**, *140*, A1133-A1138.

(59) Kresse, G.; Hafner, J. Ab Initio Molecular Dynamics for Liquid Metals. *Phys. Rev. B* **1993**, *47*, 558.

(60) Kresse, G.; Furthmüller, J. Efficiency of *Ab-Initio* Total Energy Calculations for Metals and Semiconductors Using a Plane-Wave Basis Set. *Comput. Mater. Sci.* **1996**, *6*, 15-50.

(61) Perdew, J. P.; Burke, K.; Ernzerhof, M. Generalized Gradient Approximation Made Simple. *Phys. Rev. Lett.* **1996**, *77*, 3865.

(62) Kresse, G.; Joubert, D. From Ultrasoft Pseudopotentials to the Projector Augmented-Wave Method. *Phys. Rev. B* **1999**, *59*, 1758−1775.

(63) Dudarev, S.; Botton, G.; Savrasov, S.; Humphreys, C.; Sutton, A. Electron-Energy-Loss Spectra and the Structural Stability of Nickel Oxide: An LSDA+U Study. *Phys. Rev. B* **1998**, *57*, 1505−1509.

(64) Adelstein, N.; Neaton, J. B.; Asta, M.; De Jonghe, L. C. Density Functional Theory based Calculation of Small-Polaron Mobility in Hematite. *Phys. Rev. B* **2014**, *89*, 245115.

(65) Reimers, J.; Hush, N. Electronic Properties of Transition-Metal Complexes Determined from Electroabsorption (Stark) Spectroscopy. 2. Mononuclear Complexes of Ruthenium (II). *J. Phys. Chem.* **1991**, *95*, 9773-9781.

(66) Nosé, S. A Unified Formulation of the Constant Temperature Molecular Dynamics Methods. *J. Chem. Phys.* **1984**, *81*, 511-519.

CHAPTER V

MAPPING CATALYTICALLY RELEVANT EDGE ELECTRONIC STATES OF MoS_2*

V.1 Introduction

The combination of solar energy and water represents the most attractive and fundamentally viable solution to our energy needs if methods can be developed to effectively split water into hydrogen and oxygen.[1–3] Water splitting, the sum of water oxidation and hydrogen evolution half-reactions, remains a formidable challenge since it requires the concerted transfer of four electrons and four protons.[4] Catalysts that can mediate both of the half-reactions at low overpotentials are imperative to avoid squandering valuable free energy harvested using a semiconductor in a photoelectrochemical cell, or provided directly in the form of current in a water electrolyzer. Platinum group metals are known to effectively catalyze the production of H_2 at low overpotentials; however, their high cost and low crustal abundance has focused attention on the design of more earth-abundant alternatives.[5,6] The 2H polymorph of MoS_2, a semiconducting hexagonally close packed transition metal dichalcogenide, has gained prominence as a catalyst for both the hydrogen evolution reaction (HER)[7–12] as well as for hydro-desulfurization (HDS)[13–16] of sulfur-rich hydrocarbon fuels. Recent reports suggest that it can also electrocatalytically mediate the conversion of higher order lithium polysulfides to solid lower polysulfides.[17] The current understanding from both

*Reprinted with permission from "Mapping Catalytically Relevant Edge Electronic States of MoS_2" by A. Parija, Y.-H. Choi, Z. Liu, J. L. Andrews, L. R. De Jesus, S. C. Fakra, M. Al-Hashimi, J. D. Batteas, D. Prendergast, S. Banerjee, *ACS Cent. Sci.* **2018,** *4*, 493-503.

theoretical[7,18,19] and experimental[8,20–22] approaches is that the catalytic activity of MoS_2 is derived primarily from specific edge sites that are metallic, whereas, in contrast, the basal planes exhibit substantially lower catalytic activity.[23] On the basis of calculations by Tsai and co-workers, the free energy of hydrogen adsorption on the basal plane of MoS_2 is 1.92 eV, which is substantially greater than the 0.06 eV value for the Mo edges of MoS_2.[24] Furthermore, Voiry and co-workers have demonstrated that the catalytic activity of 2H-MoS_2 is greatly reduced by partially oxidizing the MoS_2 edges, whereas the electrocatalytic performance of the basal plane of 2H-MoS_2 can be somewhat improved by interfacing with carbon nanotubes.[25] Consequently, considerable effort has been invested in increasing the edge density of MoS_2 through precise control of mesoscale structures.[26,27] Despite these advances, the enthalpy of hydrogen adsorption, which is correlated with the overpotential, remains considerably higher for MoS_2 edge sites as compared to Pt.[8,26] As such, a more detailed understanding of the geometric and electronic structure of these sites is required to afford the requisite control to precisely design MoS_2 materials that can function as effective catalysts for water splitting.

Despite considerable research, the precise atomistic structure of the active sites and structure−function correlations of catalytic activity remain unclear in this system,[28] hindering the development of a rational means of modulating the edge reactivity of MoS_2. While scanning tunneling spectroscopy and hyperspectral nano-photoluminescence imaging allow for localized measurements of electronic structure,[29,30] they do not provide an element-specific understanding of specific states mediating catalytic activity. Moreover, these methods have specific length-scale resolution, and probe states without

distinct localization or chemical specificity near the band edges that can be rather challenging to interpret theoretically. In this article, we demonstrate that sulfur K- and L-edge X-ray absorption near edge structure (XANES) spectroscopy and imaging serve as sensitive element-specific probes of edge electronic structure. Scanning transmission X-ray microscopy (STXM) measurements at the sulfur $L_{2,3}$-edge of exfoliated MoS_2 samples, an ultrasoft-X-ray elemental edge that has rarely been explored, provide detailed insight into the spatial localization of electronic states based on their distinctive spectroscopic signatures. First-principles density functional theory (DFT) calculations, using the excited electron and core-hole X-ray absorption spectroscopy (XCH-XAS) approach,[31] allow for an orbital-specific description of the origin of the edge electronic states. Remarkably, distinctive spectroscopic signatures are seen as pre-edge absorption features in both S $L_{2,3}$- and K-edge spectra, for specific edge corrugation motifs, and a direct correlation is observed between the density of such sites and the measured electrocatalytic activity. This study thus reveals a direct correspondence between a measured spectroscopic signature (corresponding to a specific symmetry and electronic structure) and macroscopic function, specifically, the electrocatalytic activity of MoS_2, thereby providing a rational means of catalyst design. In other words, a direct correlation between localized chemical bonding motifs and ultimate macroscopic functionality is revealed. Drawing such a correlation is enabling for rational design in terms of parameters such as composition, nano/atomic scale morphology, defect structure, and defect composition/concentration.

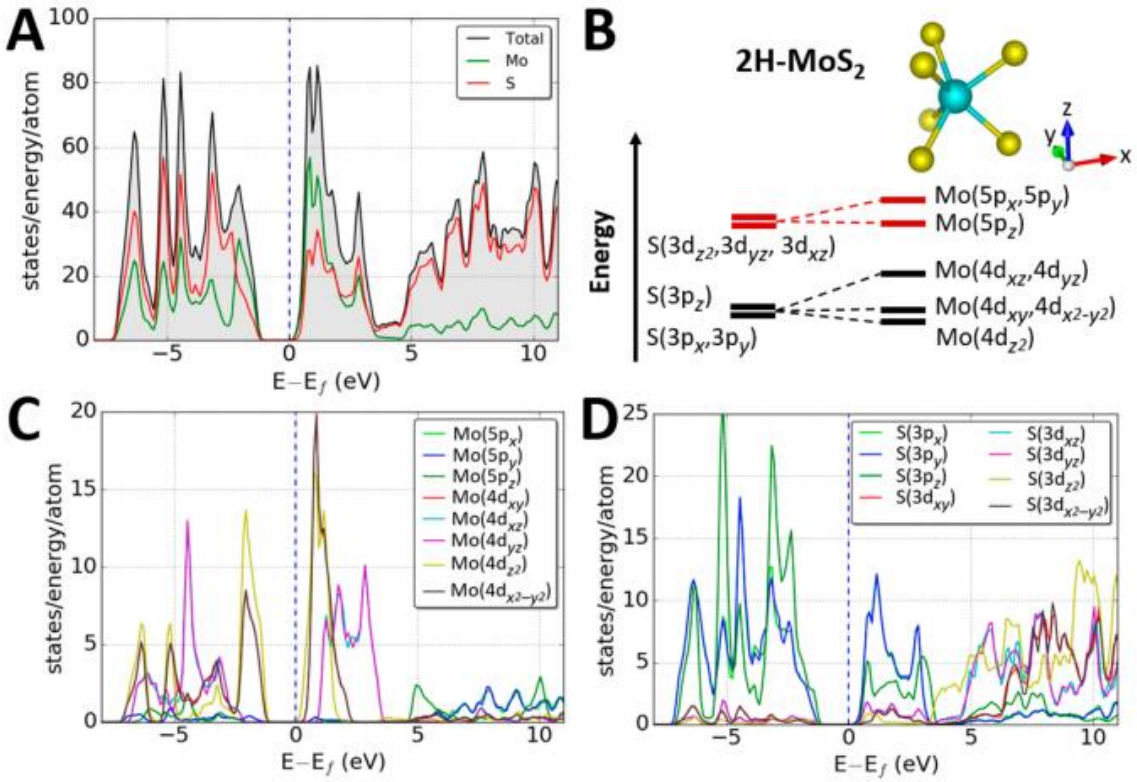

Figure V. 1. Calculated density of states for a monolayer of 2H-MoS_2. (A) Total density of states and atom-projected density of states plots delineating Mo and S contributions; (B) orbital approximation of the energy levels of the molybdenum and sulfur states and their primary hybridization interactions; the inset depicts the trigonal prismatic local coordination environment of Mo; Mo atoms are depicted as blue spheres, whereas S atoms are depicted as yellow spheres. Orbital-projected density of states for (C) Mo and (D) S atoms in 2H-MoS_2.

V.2 Results and Discussion

There is increasing realization of the paramount importance of electronic structure in mediating the electrocatalytic activity of MoS_2 given the need for interfacial charge transfer as well as both electron and proton diffusion.[11,32] A monolayer of 2H-MoS_2 is a semiconductor with a band gap of ca. 1.74 eV with the Fermi level situated just below the conduction band edge.[33] **Figure V. 1** plots the combined density of states (DOS) as well

as atom- and orbital-projected densities of states (PDOS) calculated for a 2H-MoS_2 monolayer. The valence and conduction band edges are dominated by hybrid Mo−S states with the orbital-specific interactions schematically illustrated in **Figure V. 1B**. Above ca. 4.2 eV, the extent of hybridization is diminished, and the states are predominantly of S character. However, in proximity to the Fermi level, the conduction band edge has hybrid Mo−S character and is split by crystal field splitting effects characteristic of the trigonal prismatic local coordination environment (D_{3h}) of Mo atoms into three distinct envelopes; the lower energy A1′ state has contributions from Mo $4d_{z2}$ states hybridized with S 3p states, the intermediate energy E′ states comprise $4d_{xy}$ and $4d_{x2-y2}$ Mo states hybridized with S 3p states, and the high energy E″ states comprise contributions of Mo $4d_{xz}$ and $4d_{yz}$ origin hybridized with S 3p states (**Figure V. 1C,D**). The unoccupied density of states above ca. 4.2 eV comprises S 3d states split as per the following energy progression owing to hybridization with Mo 5p orbitals $3d_{z2} < 3d_{xz} = 3d_{yz} < 3d_{xy} = 3d_{x2-y2}$ (**Figure V. 1B**). **Figure A28** (Appendix A) plots the calculated excited-state density of states for all the S and Mo atoms (including the excited S atom) in 2H-MoS_2. The projected density of states for the specific excited sulfur atom is provided in **Figure A29** (Appendix A). In this calculation, a core−hole is created in the MoS_2 supercell by removing an electron from the 2p orbital of a S atom, and the extra electron is then accounted for in the occupied states.[34–36]

In order to directly probe the electronic structure of MoS_2, specifically the unoccupied density of states, scanning transmission X-ray microscopy (STXM) has been used to image a few-layered 2H-MoS_2 samples prepared by exfoliation of a single-crystal

MoS_2 sample, as depicted in **Figure V. 2**. STXM provides a hyperspectral map of element-specific X-ray absorption (at the S $L_{2,3}$-edge in this case) with a pixel size of 30 nm × 30 nm and is obtained by raster scanning a finely focused and highly monochromatic incident soft X-ray beam across the sample.[37–40] As a first approximation, STXM provides a spatially localized view of the atom-projected density of states; the strong hybridization of S 3p and Mo 4d states at the conduction band edge can thus be directly probed at the S $L_{2,3}$-edge. **Figure V. 2A** illustrates an integrated STXM image of a ca. 45 nm thick (corresponding to about 60 layers assuming a layer thickness of 0.8 nm)[41] 2H-MoS_2 sample laying on a silicon nitride window, with **Figure V. 2B** showing the corresponding topographic atomic force microscopy (AFM) image and cross-sectional profile for this exfoliated flake. **Figure V. 2D** plots the integrated sulfur $L_{2,3}$-edge X-ray absorption spectrum measured across the flake. The sulfur L-edge comprises two spectral envelopes labeled as such in **Figure V. 2D**; a pre-edge region involving transitions from S $2p_{3/2}$ + $2p_{1/2}$ states → S 3p (ca. 162−165 eV, hybridized with Mo 4d states) and a much more intense primary absorption edge corresponding to S $2p_{3/2}$ + $2p_{1/2}$ → S 4d (ca. 167−180 eV, hybridized with Mo 5p states) transitions. Notably, the selection rules for X-ray absorption spectroscopy (change of angular momentum quantum number $\Delta l = \pm 1$; no change of spin) explain the much diminished intensity of the pre-edge absorption feature as compared to the primary absorption. The former feature is symmetry forbidden but observed as a result of the local breaking of symmetry[42] as well as hybridization of S 3p and Mo 4d states; in contrast, the p−d whiteline absorption is symmetry allowed.

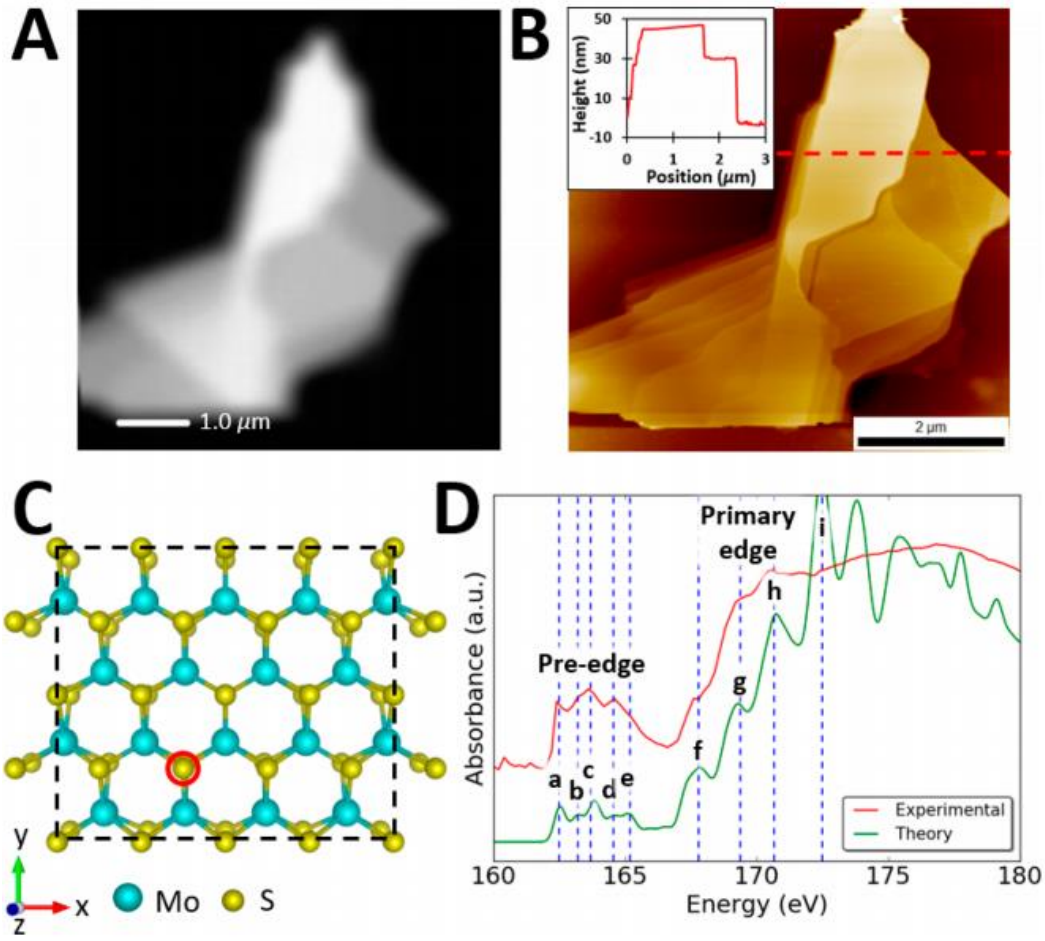

Figure V. 2. STXM mapping of few-layered 2H-MoS_2. (A) Integrated STXM image (brighter regions correspond to higher absorption) and (B) AFM image for a ca. 45 nm thick 2H-MoS_2 sheet; the inset depicts the cross-sectional topographical profile; (C) supercell of 2H-MoS_2 used to model S $L_{2,3}$-edge X-ray absorption near-edge spectra; the excited sulfur atom is delineated by a red circle. (D) Comparison of experimental and calculated sulfur L-edge XANES spectra of 2H-MoS_2. Final state assignments of the spectral features a–i are detailed in **Figure A32** and **Table A15** (Appendix A).

Figure V. 2D shows a theoretical S-$L_{2,3}$-edge spectrum modeled using the XCH-XAS method[31] for the monolayer 2H-MoS_2 supercell depicted in **Figure V. 2C** along with the experimental spectrum. It is worth noting that in van der Waals' solid such as MoS_2, the calculated spectra for monolayer MoS_2 and bulk MoS_2 are closely concordant (as

illustrated in **Figure A30** of the Appendix A) since element-specific XAS methods probe local structure, and the layers of multilayered samples are 3.22 Å apart. The simulated spectrum shows good agreement with the experimental spectrum and provides insight into the specific transitions and final states involved at this edge. Owing to atomic core-level spin−orbit coupling, the electrons can be excited from either $2p_{3/2}$ or $2p_{1/2}$ core levels of sulfur atoms, which results in splitting of the absorption features. Assuming the probability of excitation from a $2p_{1/2}$ core level is half of that from the $2p_{3/2}$ core level, which assumes the ground state population ratio of four $2p_{3/2}$ *vs* two $2p_{1/2}$ electrons, the total spectrum is modeled by using the following equation:

$$I_{total}(E) = I_0(E) + \frac{1}{2} I_0(E - \Delta S) + c \ \ldots \text{(V.1)}$$

where $I_{total}(E)$ is the total intensity of the simulated spectrum, $I_0(E)$ is the intensity due to excitations from the $2p_{3/2}$ core level, E is the energy, ΔS is the spin−orbit coupling constant (which is 1.2 eV for sulfur),[43] and *c* is the constant added to the overall spectrum (158.7 eV in our case). **Figure A31A** (Appendix A) schematically depicts excitations from $2p_{3/2}$ and $2p_{1/2}$ core levels to unoccupied electronic states. The total intensity of the simulated spectrum with the distinctive contributions from $2p_{3/2}$ and $2p_{1/2}$ core levels is shown in **Figure A31B** (Appendix A).

Isosurfaces representing the square of the wave functions, corresponding to the charge density distribution of final states giving rise to the absorption features a−i in the sulfur $L_{2,3}$-edge XANES spectrum, have been plotted in **Figure A32** (Appendix A). Visualizing these isosurfaces and analyzing their orbital character facilitates chemically meaningful assignment of the spectral features. Also, as discernible from comparison with

the atom-projected density of states in **Figure V. 1C,D**, the absorption features labeled a, c, and e in the pre-edge region correspond to transitions to final states that comprise S 3p character hybridized with Mo 4d states. For instance, in **Figure A32B-a** (Supporting Information), the lowest energy pre-edge absorption labeled a at 162.4 eV is attributed to an excited state with Mo 4d character, localized on three Mo atoms, which is furthermore hybridized with S 3p states localized on the excited sulfur atom. A quantitative analysis of the orbital projected density of states reveals that this absorption feature has 16.6% Mo $4d_{xy}$, 26.0% Mo $4d_{z2}$, and 16.5% Mo $4d_{x2-y2}$ character as the major contributors, as listed in **Table A15** (Supporting Information). The percentage contribution of the excited S atom (red circle in **Figure V. 2C**) to the total DOS is shown in parentheses in **Table A15** (Supporting Information). In contrast, the pre-edge feature c at 163.5 eV (**Figure A32B-c**) has primarily Mo 4d character delocalized across all the Mo atoms in the supercell with relatively little hybridization with S 3p states. The pre-edge feature labeled e at 164.8 eV (**Figure A32B-e**) is again attributed to excited Mo 4d states, delocalized across all molybdenum atoms in the supercell, which are further hybridized with S 3p states. The excited state corresponding to this absorption feature has 22.0% Mo $4d_{xz}$, 22.0% M $4d_{yz}$, 17.7% S $3p_x$, and 17.7% S $3p_y$ character.

The next set of absorption features, f–i, arises from dipoleallowed excitations of the S 2p core level electrons to states with substantial S 4d character. For instance, the feature f at 167.5 eV (**Figure A32B-f**, Appendix A) corresponds to an excited state with S 4d character, localized on two adjacent S atoms and is predominantly antibonding in

nature. **Table A15** specifies that this excited state has 23.7% S $4d_{xz}$, 23.2% S $4d_{yz}$, and 19.5% S $4d_{z2}$ character with some hybridization with Mo 5p states.

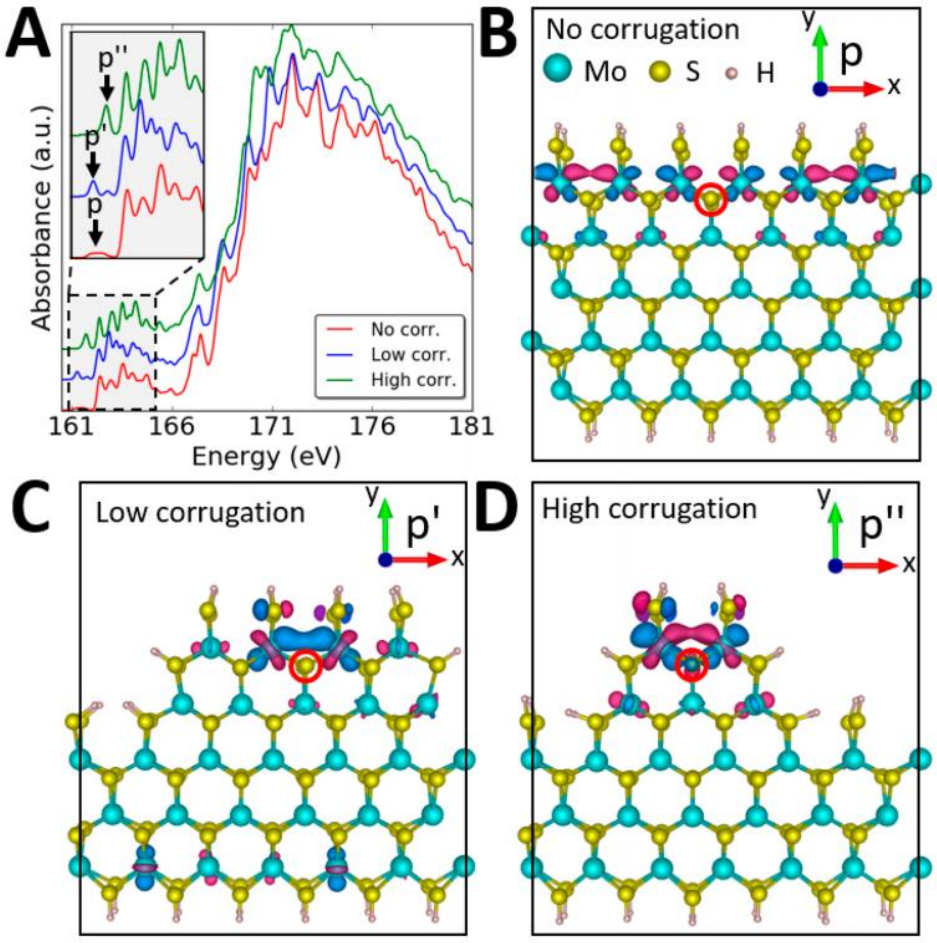

Figure V. 3. Influence of edge corrugation on S $L_{2,3}$-edge X-ray absorption spectra. (A) Comparison of simulated S $L_{2,3}$-edge X-ray absorption spectra for various degrees of edge corrugation. The inset shows an expanded view of the pre-edge region. With increasing extent of corrugation as depicted in panels (B), (C), and (D), the absorption feature delineated by an arrow increases in intensity. The orbital character for the emergent absorption feature demarcated with an arrow in (A) is shown for MoS_2 with (B) an intact edge; (C) partial edge corrugation; and (D) substantial edge corrugation. Mo atoms are depicted as light blue spheres and S atoms as yellow spheres. Opposite phases of the wave functions are represented as violet and dark blue lobes. In panels (B), (C), and (D), the excited sulfur atoms are delineated by red circles.

Similarly, the state that gives rise to the absorption feature g at 168.8 eV (**Figure A32B-g**) is highly localized on two S atoms and has S 4d character; a detailed analysis of the state confirms that it is 14% S $4d_{xz}$ and 17.8% S $4d_{z2}$ in nature. The orbital contributions to each of the absorption features can thus be visualized, and quantitative contributions from specific orbitals can be parsed as depicted in **Figure A32** and **Table A15** (Appendix A), respectively. Given the strong contributions from Mo 4d states and their apparent delocalization at the conduction band edge (**Figures V. 1** and **A28; Table A15**), we have examined the evolution of S $L_{2,3}$- edge XANES spectra with increasing edge corrugation as realistically expected in high-edge-density nanotextured MoS_2 samples such as typically used for catalytic studies.[44] **Figure V. 3** depicts S $L_{2,3}$-edge XANES spectra for a continuous 2H-MoS_2 nanoribbon with three distinct degrees of corrugation: (i) **Figure V. 3B** depicts the case of a MoS_2 nanoribbon with continuous thiol-terminated edges and no explicit corrugation; (ii) **Figure V. 3C** depicts a broken edge with a continuous strip of four and five sulfur-coordinated Mo atoms as the edge and edge-proximate layers, respectively; finally, (iii) **Figure V. 3D** depicts a highly corrugated edge where just two Mo-centered polyhedra constitute the edge and four neighboring Mo centered polyhedra define the edge-proximal layer. Edge corrugation is believed to play a particularly important role in mediating the electrocatalytic hydrogen evolution reaction.44 Simulated sulfur $L_{2,3}$-edge XANES spectra for these three configurations are plotted in **Figure V. 3A**. Weaker dipole forbidden transitions corresponding to S $2p_{3/2}$ + $2p_{1/2}$ states → S 3p (hybridized with Mo 4d states) and more intense dipole-allowed transitions corresponding to S $2p_{3/2}$ + $2p_{1/2}$ → S 4d (hybridized with Mo 5p states) are again observed. However, the

calculations suggest some intriguing differences in the spectral signatures of the three configurations at the lower edge of the conduction band in the spectral energy range from 161.3–161.7 eV, i.e., at the absorption onset, just below the pre-edge region. These features are marked in **Figure V. 3A** as p, p′, and p″ for the three edge configurations; the predicted intensity scales with increasing corrugation as p < p′ < p″. The final state corresponding to the absorption feature denoted p at 161.4 eV (red curve in **Figure V. 3A**) for an uncorrugated MoS_2 nanoribbon can be attributed to a delocalized state, spanning all of the edge Mo atoms, with predominantly Mo 4d character. **Table A16** (Appendix A) suggests that the state comprises 20.0% Mo $4d_{xy}$, 13.1% Mo $4d_{z2}$, 12.4% Mo $4d_{x2-y2}$, and 30.1% S $3p_y$ orbitals as the major contributors. Adjacent molybdenum atom pairs appear to interact through bonding interactions. In contrast, the more intense feature p′ at 161.3 eV (blue curve in **Figure V. 3A**) predicted for the MoS_2 monolayer with a corrugated edge is associated with excited states of Mo 4d character that are now localized on a single pair of Mo atoms at the edge and are hybridized to 3p states of the edge S atoms (**Figure V. 3C**). Similarly, the feature p″ at 161.7 eV (green curve in **Figure V. 3A**) predicted for highly corrugated MoS_2 is again Mo 4d in nature and is strongly localized on the two edge Mo atoms and hybridized with the 3p states of the four edge sulfur atoms (Figure 3D). **Table A16** suggests that this state has 20.7% Mo $4d_{xy}$, 25.1% Mo $4d_{z2}$, 16.1% Mo $4d_{x2-y2}$, and 22.4% S $3p_y$ character. The expected intensity differences can be rationalized considering that the X-ray absorption cross-section is dependent on the coupling between the initial state (2p eigenstate of the S atom) and the final state.[31] Since the initial 2p eigenstate is localized on an excited S atom, overlap with the final state will be the greatest

if the final state is also localized. Consequently, delocalization of the final state across an extended array of Mo atoms, as expected for uncorrugated MoS_2 sheets (**Figure V. 3B**), will result in relatively weak coupling and thus low intensity of the corresponding edge feature, p; indeed, this feature is indistinguishable in S $L_{2,3}$-edge spectra acquired for an exfoliated few-layered MoS_2 sample shown in **Figure V. 2**. In contrast, extensive localization, as indicated for the highly corrugated edge configuration illustrated in **Figure V. 3D**, is expected to yield a low-energy spectral feature, p″, of much greater intensity. Indeed, this analysis reveals that corrugated edge sites such as depicted in **Figure V. 3C,D** that are thought to be catalytically active[44] have spectroscopically distinguishable signatures in the $S_{2,3}$ L-edge X-ray absorption spectra. According to a study by Liu and co-workers,[45] the dilute adsorption of hydrogen on metal chalcogenide surfaces has a negligible effect on its total electronic structure (DOS). However, the primary consequence of hydrogen adsorption is the population of states at or near the lowest unoccupied state, i.e., the conduction band minimum for semiconductors or the Fermi level for metals. Consequently, one strategy to increase the activity of a catalytic site (reflected in a decrease of its overpotential) in a semiconducting catalyst would be to decrease the energy of the conduction band minimum. In the case of MoS_2, the creation of edge defects has this very effect. **Figure A33** (Appendix A) indicates that the upon the inclusion of edges in a semi-infinite MoS_2 strip, "mid gap" states start to appear in the band gap and the conduction band minimum is lowered by 1.2 eV in comparison to monolayer 2H-MoS_2. The catalytic reactivity of the edges of MoS_2 catalysts is thus a direct reflection of this modified electronic structure.

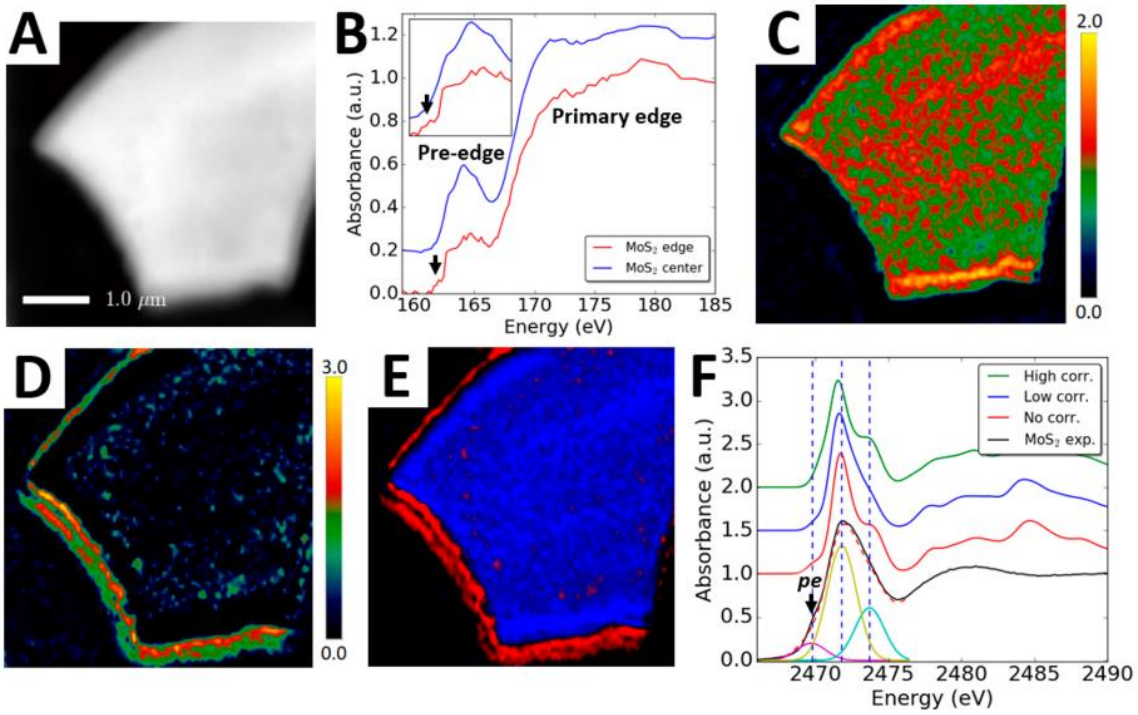

Figure V.4. Mapping edge spectral signatures across a high-edge-density nanostructured MoS_2 sample. (A) Integrated S $L_{2,3}$-edge STXM image acquired for a high-edge-density MoS_2 nanosheet; (B) two spectral components that contribute to the overall integrated spectrum as derived from singular variable decomposition of the hyperspectral data based on region of interest analysis; (C) intensity map for the spectral contribution shown in the blue spectrum of panel (B) (corresponding to uncorrugated MoS_2); (D) intensity map for the spectral contribution shown in the red spectrum of panel (B) (corresponding to edge electronic states). In (C) and (D), the color bars to the right depict the relative intensity of the spectrum at each pixel. (E) False color map showing the relative spatial localization of the two spectral features; the color at each pixel represents the majority spectral contribution (red or blue as delineated by the plots in (B)). (F) Comparison of experimental S K-edge XANES spectrum (black) acquired for a high-edge-density MoS_2 nanosheet compared to spectra calculated for the three configurations with varying edge corrugation depicted in **Figure V. 3B−D**. Three distinct features are deconvoluted centered at 2469.8, 2471.8, and 2473.7 eV. The lowest energy pre-edge feature is delineated as "pe" using an arrow.

As the mechanically exfoliated MoS_2 depicted in **Figure V. 2** exhibited a low concentration of edge sites and barely discernible spectroscopic signatures of edge states, we have further examined a high-edge-density nanotextured MoS_2 sample prepared by

calcination of $(NH_4)_2MoS_4$ solution on carbon fiber paper at 300 °C that is known to exhibit excellent electrocatalytic activity.[27] Extensive previous structural characterization of this sample suggests a mixture of amorphous and crystalline phases with incipient crystalline MoS_2 nuclei characterized by a high density of edge sites embedded within an amorphous matrix.[27,46,47] **Figure V. 4A** depicts the integrated S $L_{2,3}$-edge STXM image acquired for the sample transferred onto a silicon nitride grid. The edges and the center of the lamellar sheet are clearly discernible from the background. Singular value decomposition based on region-of-interest analysis allows for identification of two distinct spectral components as shown in **Figure V. 4B**. Both spectra show distinctive dipole-forbidden pre-edge and more intense dipole-allowed primary edge features as also observed (and assigned in **Figure A32** and **Table A15**) for the mechanically exfoliated few-layered MoS_2 sheet in **Figure V. 2**. Upon comparing the blue and the red spectra in **Figure V. 4B**, a low-energy feature is clearly distinguishable in the range between 161.4 and 162.4 eV (centered at ca. 161.9 eV) and is delineated by an arrow. On the basis of predictions of the energy positioning of spectral features derived from corrugated edge states in **Figure V. 3** and **Table A16**, this feature likely has an origin in localized edge electronic states. Indeed, spatial mapping of the two spectral components depicted in **Figures V. 4C−E** clearly indicates that the red spectral component, which has the additional edge spectroscopic signatures, is indeed strongly localized at the edges of the sheets as well as within specific domains within the interior, whereas the blue spectroscopic component is predominant within the interior of the sheet. **Figure V. 4E** depicts the relative spatial localization of the components and demarcates the clear

segregation of the spectral signatures corresponding to distinctive electronic structures of edge corrugated and uncorrugated MoS_2 in real space.

Considering that S $L_{2,3}$-edge XANES spectra serve as an excellent probe of S 3p–Mo 4d hybridization, S K-edge XANES spectra have furthermore been acquired for the highedge density MoS_2 sample, as plotted in **Figure V. 4F**, in order to serve as an additional independent probe of the S 3p states. Spectral simulations have been performed using the XCH-XAS method to facilitate spectral assignments. Two sets of absorption features can be distinguished corresponding to (i) dipolar transitions from S 1s core states to S 3p states hybridized with Mo 4d states in the energy range between ca. 2468−2476 eV and (ii) less intense dipole-forbidden transitions from S 1s core states to S 4d states in the energy range above 2476 eV, observed due to breaking of symmetry and p–d hybridization. **Figure A34** (Appendix A) depicts the final state assignments of the spectral features observed in S Kedge XANES spectra of monolayer 2H-MoS_2.

Interestingly, three discrete spectral components can be resolved in the experimental S K-edge XANES spectrum centered at 2469.8, 2471.8, and 2473.7 eV (**Figure V. 4F**). A distinctive pre-edge feature (denoted as pe) is observed at 2469.8 eV as demarcated by an arrow. As per **Figure A34**, such a spectral feature is not characteristic or expected for monolayer 2H-MoS_2. In order to delve into the origin of this feature, S K edge X-ray absorption spectra have been further modeled for the three distinctive edge corrugation modes considered in **Figure V. 3B−D** and are plotted alongside the experimental spectrum in **Figure V. 4F**. Indeed, a pre-edge feature is seen to emerge with increasing extent of corrugation. **Figure A35** depicts the final states giving rise to pre-

edge features in the calculated spectra for the three corrugation motifs. Similar to observations of the S $L_{2,3}$-edge XANES spectra, increasing corrugation brings about localization of the S 3p–Mo 4d states, and such a localized hybrid state yields a more intense pre-edge absorption. The independent identification of spectral signatures assigned to defective edge electronic structure in both S $L_{2,3}$- and S K-edge XANES spectra, the distinctive localization of such spectral features at nanostructured edges evidenced in S $L_{2,3}$-edge STXM imaging, and their much increased abundance in a high-edge-density sample thus lend strong credence to the distinctive chemical bonding and electronic character of the edge states of MoS_2. Indeed, the abundance of edge states has been extensively correlated to the catalytic activity of MoS_2.[8,26,29,44]

The high-edge-density nanostructured MoS_2 sample exhibiting distinct spectral signatures of edge corrugation (**Figure V. 4**) has been evaluated for its efficacy as an electrocatalyst. A three electrode system is assembled with high-edge-density MoS_2 on carbon fiber paper as the working electrode, SCE as the reference electrode, and a Pt plate as the counter electrode; a 0.5 M aqueous solution of H_2SO_4 is used as the electrolyte. While previous studies have provided an important caveat regarding the use of Pt as a counter-electrode,[48] **Figure A36** of the Supporting Information illustrates that no discernible difference in electrocatalytic activity is observed within the limits of experimental error when a glassy carbon electrode is used instead of Pt as the counter electrode. The electrocatalytic activity of this sample is contrasted to bulk 2H-MoS_2 which has micron-sized crystalline domains and a substantially reduced edge density.

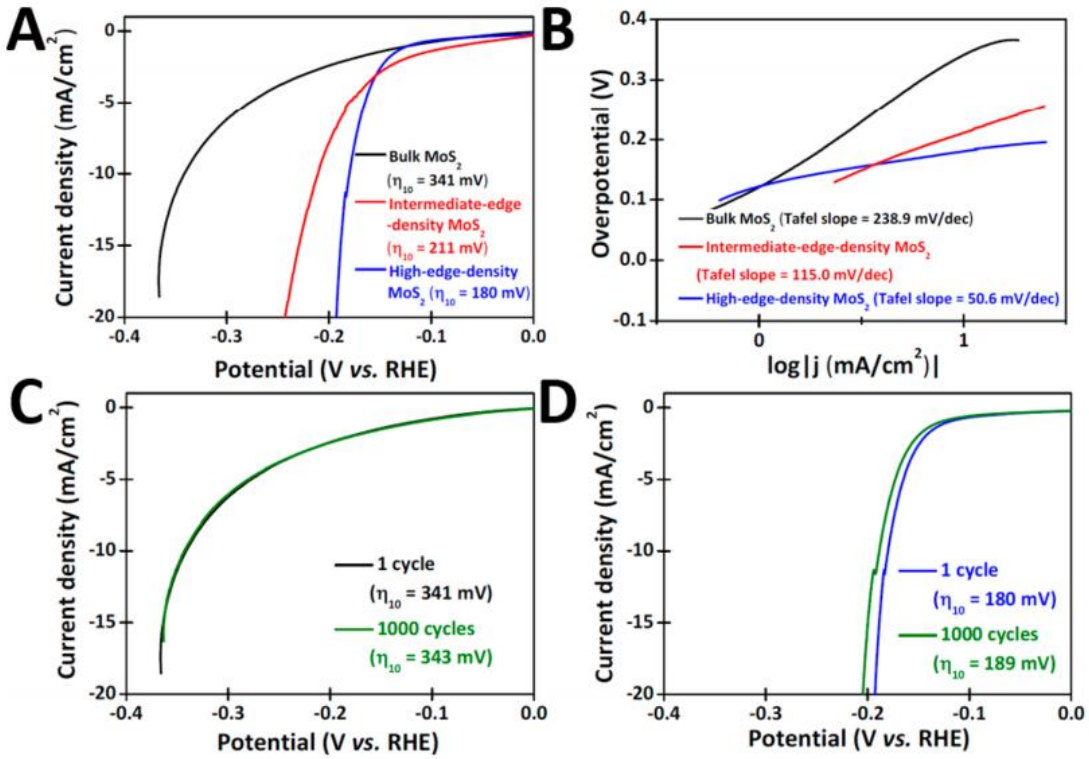

Figure V. 5. Contrasting electrocatalytic activity of bulk 2H-MoS_2, intermediate-edge-density nanostructured MoS_2, and high-edge-density nanostructured MoS_2. (A) Polarization curves and (B) Tafel plots contrasted for bulk 2H-MoS_2, intermediate-edge-density MoS_2, and high-edgedensity MoS_2 integrated onto carbon fiber paper. The overpotentials (η_{10}), required to reach a current density of 10 mA/cm^2 as well as the Tafel slope values are noted. The overpotentials have been corrected for internal resistance losses. Electrocatalytic testing has been performed in a 0.5 M aqueous solution of H_2SO_4 using a three-electrode system. (C) and (D) polarization curves of bulk 2H-MoS_2 and high-edge-density MoS_2 before and after scanning across 1000 cyclic voltammetry cycles between −0.2 and 0.2 V versus RHE at a scan rate of 100 mV/s.

Figure V. 5A,B contrasts the polarization curves and Tafel slopes for bulk 2H-MoS_2, intermediate-edge-density MoS_2, and high-edge-density MoS_2 integrated onto carbon fiber paper. The edge density is controlled by choice of annealing temperature; a higher annealing temperature results in sintering of incipient MoS_2 domains reducing the edge density as larger crystalline sheets are stabilized.[27] The exchange current density (a

measure of the rate of electrochemical reaction at equilibrium)[49] for high-edge-density MoS_2 is far greater at a given overpotential as compared to bulk 2H-MoS_2. The overpotential (η_{10}), required to reach a current density of 10 mA cm^{-2} for bulk MoS_2 (341 mV) is reduced for intermediate-edge-density MoS_2 (211 mV), and furthermore reduced for the high-edge density MoS_2 sample (180 mV). Remarkably, the Tafel slope for the high-edge density MoS_2 sample (50.6 mV/dec) is substantially lower in comparison to the corresponding value for intermediate-edge-density MoS_2 (115.0 mV/dec) as well as for bulk MoS_2 (238.9 mV/dec). The substantial enhancement of the electrocataytic activity can be correlated to increased edge density, and thus suggests that the localized edge electronic states, with energies at the edge of the conduction band comprising localized Mo 4d–S 3p states, play a key role in catalysis. In fact, the excellent catalytic activity of cubane-like $[Mo_3S_4]^{4+}$ units reported in the literature is likely related to the realization of a similar electronic structure motif characterized by such localized states.[50]

To further investigate the long-term stability of the samples, cyclic voltammetry measurements have been performed over 1000 cycles in a 0.5 M aqueous solution of H_2SO_4 between a potential range of −0.2 and 0.2 V versus RHE at a scan rate of 100 mV/s. **Figure V. 5C,D** suggests excellent retention of the electrocatalytic activity with only marginal degradation of the samples. The increase in η_{10} after 1000 cycles for high-edge-density MoS_2 is less than ca. 5 mV.

V. 3 Experimental Section

Electronic Structure Calculations and Modeling of XAS Signatures

First-principles calculations were performed using density functional theory, as implemented within the Vienna ab initio simulation package (VASP).[51−53] The projector augmented wave (PAW) formalism was used to model electron−ion interactions. A kinetic energy cutoff of 600 eV was used for plane wave basis restriction. Electronic exchange and correlation effects were included using the generalized gradient approximation based on the Perdew− Burke−Ernzerhof functional (GGA-PBE).[54] For geometry optimization, the supercells of MoS_2 were relaxed until the Cartesian components of the forces were below ±0.05 eV $Å^{-1}$.

The PWscf code in the Quantum ESPRESSO package was used to calculate the excited state density of states (DOS) and projected density of states (PDOS) and to simulate X-ray absorption spectra. The Shirley optimal basis set was used to facilitate efficient sampling of the Brillouin zone.[55,56] For DOS and PDOS calculations, a uniform Γ-centered 4 × 4 × 4 Monkhorst−Pack k-point grid was used.[57] A uniform k-point grid of 2 × 2 × 2 was used to perform structural relaxations and simulate S K- and $L_{2,3}$-edge XANES spectra. The spectral simulation uses the XCH-XAS approach wherein an electron is removed from the inner shell (1s for S K-edge or 2p for S Ledge) of an excited sulfur atom within a MoS_2 supercell to account for excited state core−hole interactions.[31] The inclusion of the core−hole perturbation is not explicit but is instead accounted for using a modified sulfur quasipotential with one less electron in the 1s orbital for the S K-edge or 2p orbital for the S L-edge. The excited electron is included in the occupied

electronic structure, and the entire electronic system is relaxed to its ground state within DFT. A 4 × 4 × 4 supercell was used for the calculations of the electronic properties of the 2H-MoS_2 monolayer. A vacuum separation of 10 Å was used along the *z* direction to eliminate interactions between the slabs. For the calculation of edge corrugation effects, nanoribbons of MoS_2 extended periodically in the x-direction were used with thiol-terminated edges. A vacuum separation of 10 Å was inserted along the *y*-direction to eliminate interactions between the edges of MoS_2 nanoribbons in adjacent cells. The selected supercell was large enough to eliminate spurious interactions arising from coupling between core−hole images. A broadening of 0.2 eV was applied to spectral simulations in order to reproduce instrumental broadening observed in experimental spectra.

Material Synthesis

Synthesis of Few-Layered 2H-MoS_2

Few-layered MoS_2 nanosheets were deposited onto silicon nitride surfaces using mechanical exfoliation.[58] First, silicon nitride windows (Norcada, thickness 50 μm) were cleaned by using UV/ozone for 10 min to yield hydrophilic surfaces. The windows were then rinsed with deionized water and ethanol and dried under flowing nitrogen. Adhesive tape (Scotch Brand) was applied onto a MoS_2 crystal (SPI Supplies). After peeling, the tape was reapplied to the silicon nitride windows. The tape-MoS_2-window samples were annealed at 80 °C for 2 min to release any trapped gas at the MoS_2-substrate interface and improve the deposition efficiency.[59] After the samples were cooled to room temperature, the tape was peeled from the substrate, leaving MoS_2 flakes on the silicon nitride windows.

Synthesis of Nanostructured Intermediate-Edge Density and High-Edge-Density MoS_2

Nanostructured MoS_2 was synthesized using a previously described procedure starting from an amorphous MoS2 precursor.[27] Briefly, 0.25 g of ammonium thiomolybdate, $(NH_4)_2MoS_4$ (Sigma-Aldrich, 99.97% purity), was added to 20 mL of anhydrous dimethylformamide (DMF) under an argon atmosphere to obtain a 1.25 wt % solution. Next, after ultrasonication for 20 min, a 100 μL cm^{-2} solution was drop cast onto a carbon fiber paper substrate (Toray Paper 120). The substrate was then purged under an argon flow of 50 sccm for 20 min at room temperature and then calcined within a tube furnace at temperatures of 300 and 400 °C to obtain high-edge-density and intermediate-edge-density MoS_2, respectively. A ramp rate of 40 °C min^{-1} was used for calcination; the furnace was held at 300 °C/400 °C for 5 min before allowing the substrate to cool to room temperature. For STXM measurements, the sample was ultrasonicated in ethanol for 5 min, and the supernatant was drop cast onto silicon nitride windows (Norcada). Bulk MoS_2 powder with a particle size of ca. 2 μm was purchased from Sigma-Aldrich (99% purity) and used without further purification.

Atomic Force Microscopy, XAS, and STXM Measurements of MoS_2

The few-layered MoS_2 samples were examined by AFM using an Agilent 5500 AFM in a dry nitrogen environment. MicroMasch (CSC37/ALBS) silicon tips with a nominal spring constant of 1 N/m and a radius of curvature of ca. 12 nm were used to image the samples. AFM images were collected in contact mode at an applied load of 1 nN under a nitrogen atmosphere. Scanning probe image processing (SPIP) software was used to process the images and render topographical images.

STXM measurements were acquired at the S $L_{2,3}$-edge at beamline 10-ID1 of the Canadian Light Source (CLS) and at the 11.0.2 beamline of the Advance Light Source (ALS). The measurements used right circularly polarized light generated by an elliptically polarized undulator. A diffraction-limited spatial resolution of ca. 30 nm was obtained by using a 25 nm outermost-zone zone plate. Spectral stacks were acquired using a 500 line mm^{-1} plane grating monochromator (PGM). The incident photon flux (I_0) count rate was optimized to ca. 17 MHz as read by the STXM detector at 160 eV within a hole located in proximity of the sample of interest. The S L-edge stacks were collected in the energy range from 155 to 200 eV with energy steps of 0.2 eV in the region of interest and with energy steps 1 eV in the continuum region beyond the specific elemental edges; a dwell time of 1 ms was used for each spectral section. All STXM data were analyzed and processed using aXis2000 from McMaster University (http://unicorn. mcmaster.ca/aXis2000.html). STXM maps for spectral components were derived based on singular value decomposition of the image stack (performed in aXis2000) by using as a reference the total integrated spectrum.

Sulfur K-edge X-ray absorption near-edge structure (XANES) spectra were collected at the Advanced Light Source (ALS) bending magnet beamline 10.3.2. S K-edge XANES spectra were recorded in fluorescence mode in the energy range 2450□2510 eV by continuously scanning a Si (111) monochromator (Quick XAS mode) from 20 eV below to 40 eV above the white line absorption. For XANES analysis, a suite of custom LabVIEW programs at the beamline was used to perform deadtime correction, energy

calibration, glitch removal, pre-edge subtraction, and postedge normalization. The Athena suite of programs in the IFEFFIT package was used to analyze the XANES spectra.[60]

Evaluation of Electrocatalytic Activity

A three electrode cell was constructed and cycled using a potentiostat (Bio-Logic, SP-200) with the MoS_2 active layer on carbon fiber paper as the working electrode. A 0.5 M aqueous solution of H_2SO_4 purged with N_2 gas was used as the electrolyte. A saturated calomel electrode (SCE) and a Pt plate were used as the reference and counter electrodes, respectively. Alternatively, glassy carbon was also used as a counter electrode to contrast with the Pt plate. The measurement of the polarization curves and the Tafel slope were recorded using both Pt and glassy carbon as counter electrodes. The expression $E_{RHE} = E_{SCE} + 0.279$ V was used to convert the potential measured versus SCE (E_{SCE}) to the potential versus the reversible hydrogen electrode (RHE, E_{RHE}).[12,27] Linear sweep voltammetry (LSV) was performed in the range between 0.1 and −0.4 V vs. RHE at a scan rate of 10 mV/s. Corrections were implemented to account for ohmic potential (iR) losses, where i is the current and R is the series resistance of the electrochemical cell, based on electrochemical impedance spectroscopy (EIS) measurements. A frequency range of 200 kHz to 50 mHz was used for the EIS measurements with an AC amplitude of 25 mV.

V.4. Conclusions

The electrocatalytic activity of MoS_2 has long been correlated to the abundance of edge sites. However, specific aspects of edge structure and their role in mediating catalysis remains unclear, thereby hampering the development of rational strategies for edge modification. In this article, using element specific X-ray absorption spectroscopy to

probe electronic structure in conjunction with first-principles DFT modeling of X-ray absorption spectra, we have shown that localization of Mo 4d–S 3p states at specific edge corrugations gives rise to distinctive edge electronic states. These edge states are spectroscopically distinguishable, independently, in both the S $L_{2,3}$- and K-edge XANES spectra. STXM imaging at the S $L_{2,3}$- edge indicates a pronounced abundance of such edge electronic states at the peripheries of high-edge density nanostructured MoS_2 samples; in contrast, such states were not observed for mechanically exfoliated MoS_2 flakes with large crystalline domains and a low abundance of edge sites. The presence of edge corrugation serves to disrupt extended delocalization of Mo 4d states and yields low-energy hybrid states at the edge of the conduction band. These states were found to correlate with substantially enhanced electrocatalytic activity, in terms of a lower Tafel slope and a higher exchange current density. Future work will focus on the rational design of schema for modulating the energy positioning and occupancies of these edge electronic states.

V.5. References

(1) Lewis, N. S.; Nocera, D. G. Powering the planet: Chemical challenges in solar energy utilization. *Proc. Natl. Acad. Sci. U. S. A.* **2006**, *103*, 15729−15735.

(2) Nocera, D. G. The artificial leaf. *Acc. Chem. Res.* **2012**, *45*, 767−776.

(3) Hisatomi, T.; Kubota, J.; Domen, K. Recent advances in semiconductors for photocatalytic and photoelectrochemical water splitting. *Chem. Soc. Rev.* **2014**, *43*, 7520−7535.

(4) Chen, X.; Shen, S.; Guo, L.; Mao, S. S. Semiconductor-based photocatalytic hydrogen generation. *Chem. Rev.* **2010**, *110*, 6503−6570.

(5) Bockris, J.; Ammar, I.; Huq, A. The mechanism of the hydrogen evolution reaction on platinum, silver and tungsten surfaces in acid solutions. *J. Phys. Chem.* **1957**, *61*, 879−886.

(6) Parsons, R. Hydrogen evolution on platinum electrodes. The heats of activation for the component reactions. *Trans. Faraday Soc.* **1960**, *56*, 1340−1350.

(7) Hinnemann, B.; Moses, P. G.; Bonde, J.; Jørgensen, K. P.; Nielsen, J. H.; Horch, S.; Chorkendorff, I.; Nørskov, J. K. Biomimetic Hydrogen Evolution: MoS_2 Nanoparticles as Catalyst for Hydrogen Evolution. *J. Am. Chem. Soc.* **2005**, *127*, 5308−5309.

(8) Jaramillo, T. F.; Jørgensen, K. P.; Bonde, J.; Nielsen, J. H.; Horch, S.; Chorkendorff, I. Identification of active edge sites for electro chemical H_2 evolution from MoS_2 nanocatalysts. *Science* **2007**, *317*, 100−102.

(9) Li, Y.; Wang, H.; Xie, L.; Liang, Y.; Hong, G.; Dai, H. MoS_2 nanoparticles grown on graphene: an advanced catalyst for the hydrogen evolution reaction. *J. Am. Chem. Soc.* **2011**, *133*, 7296−7299.

(10) Ye, G.; Gong, Y.; Lin, J.; Li, B.; He, Y.; Pantelides, S. T.; Zhou, W.; Vajtai, R.; Ajayan, P. M. Defects engineered monolayer MoS_2 for improved hydrogen evolution reaction. *Nano Lett.* **2016**, *16*, 1097−1103.

(11) Li, H.; Tsai, C.; Koh, A. L.; Cai, L.; Contryman, A. W.; Fragapane, A. H.; Zhao, J.; Han, H. S.; Manoharan, H. C.; AbildPedersen, F.; Nørskov, J. K.; Zheng, X. Activating and optimizing MoS_2 basal planes for hydrogen evolution through the formation of strained sulphur vacancies. *Nat. Mater.* **2016**, *15*, 48−53.

(12) Choi, Y.-H.; Lee, J.; Parija, A.; Cho, J.; Verkhoturov, S. V.; Al-Hashimi, M.; Fang, L.; Banerjee, S. An in Situ Sulfidation Approach for the Integration of MoS_2 Nanosheets

on Carbon Fiber Paper and the Modulation of Its Electrocatalytic Activity by Interfacing with nC$_{60}$. *ACS Catal.* **2016**, *6*, 6246−6254.

(13) Gutierrez, O. Y.; Singh, S.; Schachtl, E.; Kim, J.; Kondratieva, E.;́ Hein, J.; Lercher, J. A. Effects of the Support on the Performance and Promotion of (Ni)MoS_2 Catalysts for Simultaneous Hydrodenitrogenation and Hydrodesulfurization. *ACS Catal.* **2014**, *4*, 1487−1499.

(14) Rangarajan, S.; Mavrikakis, M. On the Preferred Active Sites of Promoted MoS_2 for Hydrodesulfurization with Minimal Organonitrogen Inhibition. *ACS Catal.* **2017**, *7*, 501−509.

(15) Bremmer, G. M.; van Haandel, L.; Hensen, E. J. M.; Frenken, J. W. M.; Kooyman, P. J. Instability of $NiMoS_2$ and $CoMoS_2$ Hydrodesulfurization Catalysts at Ambient Conditions: A Quasi in Situ High-Resolution Transmission Electron Microscopy and X-ray Photoelectron Spectroscopy Study. *J. Phys. Chem. C* **2016**, *120*, 19204−19211.

(16) Zhou, W.; Liu, M.; Zhou, Y.; Wei, Q.; Zhang, Q.; Ding, S.; Zhang, Y.; Yu, T.; You, Q. 4,6-Dimethyldibenzothiophene Hydrodesulfurization on Nickel-Modified USY-Supported NiMoS Catalysts: Effects of Modification Method. *Energy Fuels* **2017**, *31*, 7445−7455.

(17) Babu, G.; Masurkar, N.; Al Salem, H.; Arava, L. M. R. Transition Metal Dichalcogenide Atomic Layers for Lithium Polysulfides Electrocatalysis. *J. Am. Chem. Soc.* **2017**, *139*, 171−178.

(18) Tsai, C.; Abild-Pedersen, F.; Nørskov, J. K. Tuning the MoS_2 edge-site activity for hydrogen evolution via support interactions. *Nano Lett.* **2014**, *14*, 1381−1387.

(19) Fan, X.-L.; Yang, Y.; Xiao, P.; Lau, W.-M. Site-specific catalytic activity in exfoliated MoS_2 single-layer polytypes for hydrogen evolution: basal plane and edges. *J. Mater. Chem. A* **2014**, *2*, 20545− 20551.

(20) Xiao, W.; Liu, P.; Zhang, J.; Song, W.; Feng, Y. P.; Gao, D.; Ding, J. Dual-Functional N Dopants in Edges and Basal Plane of MoS_2 Nanosheets Toward Efficient and Durable Hydrogen Evolution. *Adv. Energy Mater.* **2017**, *7*, 1602086.

(21) Bollinger, M.; Lauritsen, J.; Jacobsen, K. W.; Nørskov, J. K.; Helveg, S.; Besenbacher, F. One-dimensional metallic edge states in MoS_2. *Phys. Rev. Lett.* **2001**, *87*, 196803.

(22) Yang, Y.; Fei, H.; Ruan, G.; Xiang, C.; Tour, J. M. Edge-oriented MoS_2 nanoporous films as flexible electrodes for hydrogen evolution reactions and supercapacitor devices. *Adv. Mater.* **2014**, *26*, 8163−8168.

(23) Lauritsen, J. V.; Kibsgaard, J.; Helveg, S.; Topsoe, H.; Clausen, B. S.; Laegsgaard, E.; Besenbacher, F. Size-dependent structure of MoS_2 nanocrystals. *Nat. Nanotechnol.* **2007**, *2*, 53−58.

(24) Tsai, C.; Chan, K.; Abild-Pedersen, F.; Nørskov, J. K. Active edge sites in $MoSe_2$ and WSe_2 catalysts for the hydrogen evolution reaction: a density functional study. *Phys. Chem. Chem. Phys.* **2014**, *16*, 13156−13164.

(25) Voiry, D.; Salehi, M.; Silva, R.; Fujita, T.; Chen, M.; Asefa, T.; Shenoy, V. B.; Eda, G.; Chhowalla, M. Conducting MoS_2 nanosheets as catalysts for hydrogen evolution reaction. *Nano Lett.* **2013**, *13*, 6222−6227.

(26) Kibsgaard, J.; Chen, Z.; Reinecke, B. N.; Jaramillo, T. F. Engineering the surface structure of MoS_2 to preferentially expose active edge sites for electrocatalysis. *Nat. Mater.* **2012**, *11*, 963−969.

(27) Choi, Y.-H.; Cho, J.; Lunsford, A. M.; Al-Hashimi, M.; Fang, L.; Banerjee, S. Mapping the electrocatalytic activity of MoS_2 across its amorphous to crystalline transition. *J. Mater. Chem. A* **2017**, *5*, 5129−5141.

(28) Tinoco, M.; Maduro, L.; Masaki, M.; Okunishi, E.; Conesa-Boj, S. Strain-Dependent Edge Structures in MoS_2 Layers. *Nano Lett.* **2017**, *17*, 7021−7026.

(29) Lauritsen, J.; Nyberg, M.; Nørskov, J. K.; Clausen, B.; Topsøe, H.; Lægsgaard, E.; Besenbacher, F. Hydrodesulfurization reaction pathways on MoS_2 nanoclusters revealed by scanning tunneling microscopy. *J. Catal.* **2004**, *224*, 94−106.

(30) Bao, W.; Borys, N. J.; Ko, C.; Suh, J.; Fan, W.; Thron, A.; Zhang, Y.; Buyanin, A.; Zhang, J.; Cabrini, S.; Ashby, P. D.; Weber-Bargioni, A.; Tongay, S.; Aloni, S.; Ogletree, D. F.; Wu, J.; Salmeron, M. B.; Schuck, P. J. Visualizing nanoscale excitonic relaxation properties of disordered edges and grain boundaries in monolayer molybdenum disulfide. *Nat. Commun.* **2015**, *6*, 7993.

(31) Prendergast, D.; Galli, G. X-Ray Absorption Spectra of Water from First Principles Calculations. *Phys. Rev. Lett.* **2006**, *96*, 215502.

(32) Li, T.; Galli, G. Electronic Properties of MoS_2 Nanoparticles. *J. Phys. Chem. C* **2007**, *111*, 16192−16196.

(33) Mak, K. F.; Lee, C.; Hone, J.; Shan, J.; Heinz, T. F. Atomically thin MoS_2: a new direct-gap semiconductor. *Phys. Rev. Lett.* **2010**, *105*, 136805.

(34) Lukowski, M. A.; Daniel, A. S.; Meng, F.; Forticaux, A.; Li, L.; Jin, S. Enhanced hydrogen evolution catalysis from chemically exfoliated metallic MoS_2 nanosheets. *J. Am. Chem. Soc.* **2013**, *135*, 10274−10277.

(35) Lebegue, S.; Eriksson, O. Electronic structure of two dimensional crystals from ab initio theory. *Phys. Rev. B: Condens. Matter Mater. Phys.* **2009**, *79*, 115409.

(36) Eknapakul, T.; King, P. D. C.; Asakawa, M.; Buaphet, P.; He, R. H.; Mo, S. K.; Takagi, H.; Shen, K. M.; Baumberger, F.; Sasagawa, T.; Jungthawan, S.; Meevasana, W. Electronic Structure of a Quasi Freestanding MoS_2 Monolayer. *Nano Lett.* **2014**, *14*, 1312−1316.

(37) Ade, H.; Hitchcock, A. P. NEXAFS microscopy and resonant scattering: Composition and orientation probed in real and reciprocal space. *Polymer* **2008**, *49*, 643−675.

(38) Lim, J.; Li, Y.; Alsem, D. H.; So, H.; Lee, S. C.; Bai, P.; Cogswell, D. A.; Liu, X.; Jin, N.; Yu, Y.-s.; Salmon, N. J.; Shapiro, D. A.; Bazant, M. Z.; Tyliszczak, T.; Chueh, W. C. Origin and hysteresis of lithium compositional spatiodynamics within battery primary particles. *Science* **2016**, *353*, 566−571.

(39) De Jesus, L. R.; Horrocks, G. A.; Liang, Y.; Parija, A.; Jaye, C.; Wangoh, L.; Wang, J.; Fischer, D. A.; Piper, L. F.; Prendergast, D.; Banerjee, S. Mapping polaronic states and lithiation gradients in individual V_2O_5 nanowires. *Nat. Commun.* **2016**, *7*, 12022.

(40) Collins, B. A.; Ade, H. Quantitative compositional analysis of organic thin films using transmission NEXAFS spectroscopy in an X-ray microscope. *J. Electron Spectrosc. Relat. Phenom.* **2012**, *185*, 119−128.

(41) Lee, C.; Yan, H.; Brus, L. E.; Heinz, T. F.; Hone, J.; Ryu, S. Anomalous Lattice Vibrations of Single- and Few-Layer MoS_2. *ACS Nano* **2010**, *4*, 2695−2700.

(42) Yamamoto, T. Assignment of pre-edge peaks in K-edge X-ray absorption spectra of 3d transition metal compounds: electric dipole or quadrupole? *X-Ray Spectrom.* **2008**, *37*, 572−584.

(43) Han, S.; Kwon, H.; Kim, S. K.; Ryu, S.; Yun, W. S.; Kim, D.; Hwang, J.; Kang, J.-S.; Baik, J.; Shin, H.; Hong, S. C. Band-gap transition induced by interlayer van der Waals interaction in MoS_2. *Phys. Rev. B: Condens. Matter Mater. Phys.* **2011**, *84*, 045409.

(44) Benck, J. D.; Hellstern, T. R.; Kibsgaard, J.; Chakthranont, P.; Jaramillo, T. F. Catalyzing the hydrogen evolution reaction (HER) with molybdenum sulfide nanomaterials. *ACS Catal.* **2014**, *4*, 3957− 3971.

(45) Liu, Y.; Wu, J.; Hackenberg, K. P.; Zhang, J.; Wang, Y. M.; Yang, Y.; Keyshar, K.; Gu, J.; Ogitsu, T.; Vajtai, R.; Lou, J.; Ajayan, P. M.; Wood, B. C.; Yakobson, B. I. Self-optimizing, highly surface-active layered metal dichalcogenide catalysts for hydrogen evolution. *Nat. Energy* **2017**, *2*, 17127.

(46) Li, H.; Zhang, Q.; Yap, C. C. R.; Tay, B. K.; Edwin, T. H. T.; Olivier, A.; Baillargeat, D. From bulk to monolayer MoS_2: evolution of Raman scattering. *Adv. Funct. Mater.* **2012**, 22, 1385−1390.

(47) Lee, C.; Yan, H.; Brus, L. E.; Heinz, T. F.; Hone, J.; Ryu, S. Anomalous lattice vibrations of single-and few-layer MoS_2. *ACS Nano* **2010**, *4*, 2695−2700.

(48) Chen, R.; Yang, C.; Cai, W.; Wang, H.-Y.; Miao, J.; Zhang, L.; Chen, S.; Liu, B. Use of Platinum as the Counter Electrode to Study the Activity of Nonprecious Metal Catalysts for the Hydrogen Evolution Reaction. *ACS Energy Letters* **2017**, *2*, 1070−1075.

(49) Bose, R.; Balasingam, S. K.; Shin, S.; Jin, Z.; Kwon, D. H.; Jun, Y.; Min, Y.-S. Importance of hydrophilic pretreatment in the hydrothermal growth of amorphous molybdenum sulfide for hydrogen evolution catalysis. *Langmuir* **2015**, *31*, 5220−5227.

(50) Merki, D.; Hu, X. Recent developments of molybdenum and tungsten sulfides as hydrogen evolution catalysts. *Energy Environ. Sci.* **2011**, *4*, 3878−3888.

(51) Kresse, G.; Furthmüller, J. Efficiency of ab-initio total energy calculations for metals and semiconductors using a plane-wave basis set. *Comput. Mater. Sci.* **1996**, *6*, 15−50.

(52) Hohenberg, P.; Kohn, W. Inhomogeneous electron gas. *Phys. Rev.* **1964**, *136*, B864.

(53) Kohn, W.; Sham, L. J. Self-consistent equations including exchange and correlation effects. *Phys. Rev.* **1965**, *140*, A1133.

(54) Perdew, J. P.; Burke, K.; Ernzerhof, M. Generalized gradient approximation made simple. *Phys. Rev. Lett.* **1996**, *77*, 3865.

(55) Prendergast, D.; Louie, S. G. Bloch-state-based interpolation: An efficient generalization of the Shirley approach to interpolating electronic structure. *Phys. Rev. B: Condens. Matter Mater. Phys.* **2009**, *80*, 235126.

(56) Shirley, E. L. Optimal basis sets for detailed Brillouin-zone integrations. *Phys. Rev. B: Condens. Matter Mater. Phys.* **1996**, *54*, 16464.

(57) Monkhorst, H. J.; Pack, J. D. Special points for Brillouin-zone integrations. *Phys. Rev. B* **1976**, *13*, 5188.

(58) Novoselov, K. S.; Geim, A. K.; Morozov, S. V.; Jiang, D.; Zhang, Y.; Dubonos, S. V.; Grigorieva, I. V.; Firsov, A. A. Electric field effect in atomically thin carbon films. *Science* **2004**, *306*, 666−669.

(59) Huang, Y.; Sutter, E.; Shi, N. N.; Zheng, J.; Yang, T.; Englund, D.; Gao, H.-J.; Sutter, P. Reliable exfoliation of large-area high-quality flakes of graphene and other two-dimensional materials. *ACS Nano* **2015**, *9*, 10612−10620.

(60) Ravel, B.; Newville, M. ATHENA and ARTEMIS: interactive graphical data analysis using IFEFFIT. *Phys. Scr.* **2005**, *2005*, 1007.

CHAPTER VI

MODIFICATION OF MoS_2 THROUGH Se INCORPORATION AND INTERFACIAL HYBRIDIZATION: ELUCIDATING THE MECHANISTIC ORIGINS OF BIFUNCTIONAL ELECTROCATALYTIC FUNCTION

VI.1 Introduction

As a limitless energy source, solar energy represents the most attractive and fundamentally viable solution to our energy needs.[1] Two distinct avenues to harness solar energy include (a) photovoltaic devices that achieve the direct conversion of solar energy to electricity[2-4] and (b) the production of solar fuels wherein energy is stored within chemical bonds; the subsequent combustion of such solar fuels within fuel cells converts the stored chemical energy to electricity.[5-7] Hydrogen has emerged as perhaps the most important energy storage vector of this century and has the potential to supplant fossil fuels in mobility applications. Much of worldwide hydrogen production is currently derived from methane steam reformation with hydrogen generation from water splitting representing a relatively small component.[8] Electrocatalytic water splitting represents a promising, scalable, and sustainable route to hydrogen production but continues to be plagued by the high cost, limited durability, and emerging materials criticality of electrocatalysts amongst other constraints.[9-11] Platinum-group metals and alloys are able to generate H_2 from water at low overpotentials;[12-14] whereas, iridium and ruthenium oxides are the foremost candidates for catalyzing oxygen evolution from water.[15,16] However, in light of the high cost and the low-crustal abundance of these elements, much

attention has focused on the design of earth-abundant alternatives. Molybdenum sulfides,[17-19] carbides,[20-22] and phosphides,[23,24] have gained increasing prominence as viable catalysts for the hydrogen evolution reaction (HER). Similarly, transition-metal sulfides, oxides, and layered double hydroxides such as Co_3S_4,[25,26] Co_3O_4,[27,28] and NiS_x[29,30] have emerged as earth-abundant alternatives for the oxygen evolution reaction (OER). Despite the identification of promising earth-abundant electrocatalysts, their dynamic overpotentials in OER and the HER remain much too high for deployment at scale within water electrolyzers.[15,31] Much attention has therefore focused on designing modification schemes to reduce overpotentials, obtain high current densities at electrolyzer operating voltages, expand operational windows, and increase the longevity of earth-abundant electrocatalysts. Here, we explore selenium substitution on the anion sublattice and interfacial hybridization with MoO_3 as means of modifying the electrocatalytic activity of MoS_2. We furthermore demonstrate bifunctional reactivity of $MoS_{2-x}Se_x/MoO_3$ towards both HER and OER.

The edges of 2D layered dichalcogenide nanostructures are known to be the active sites for HER.[6,18,32] The rate determining step in HER involves stabilization of the intermediate adsorbed H* state, whose Gibbs free energy ΔG_{H*} serves as a primary descriptor of HER activity and is directly correlated to the overpotential. However, modification of edge sites to reduce the enthalpy of hydrogen adsorption has been stymied by the absence of a precise understanding of the atomistic and electronic structure of active sites. Our previous work has examined interfacial hybridization of MoS_2 with C_{60}, which yields a reduced overpotential for HER[17] posited to be a result of interfacial charge

transfer. Other effective approaches involve interfacing MoS_2 nanosheets with graphitic fibers, graphene, and carbon nanotubes; the conjugated graphitic frameworks provide additional conduction pathways for electron (and potentially proton) transport between the current collectors and the MoS_2 edge-sites.[7,33-35] An alternative approach has focused on hybridization of MoS_2 with II-VI semiconductors, which yields Type-II heterostructures with thermodynamic offsets that result in electron transfer from photoexcited quantum dots to MoS_2. Such heterostructures have enabled effective photosensitization and photocatalytic HER production for MoS_2/CdSe and MoS_2/CdS. In this article, we examine the interfacial modification of MoS_2 with an OER catalyst, MoO_3, to form an efficient bifunctional catalytic system. Since, both MoS_2 and MoO_3 are plagued by high overpotentials in HER and OER reactions, respectively, alloying of MoS_2 with Se has been further examined as a means of reducing the overpotential. A facile two-step hydrothermal synthetic method has been used to prepare $MoS_{2-x}Se_x/MoO_3$ heterostructures. These heterostructures show a combination of low overpotential, high current, high turnover frequency, and durability for both HER and OER. Raman spectroscopy, X-ray photoemission spectroscopy (XPS), and element-specific X-ray absorption near edge structure (XANES) spectroscopy along with electronic structure calculations suggest that an increased valance band maximum (VBM), decreased conduction band minimum (CBM), and decreased bandgap in $MoS_{2-x}Se_x/MoO_3$ heterostructures results in superior HER and OER performance. The findings provide a valuable illustration of the use of interfacial modification as a means of catalyst design based on electronic structure considerations.

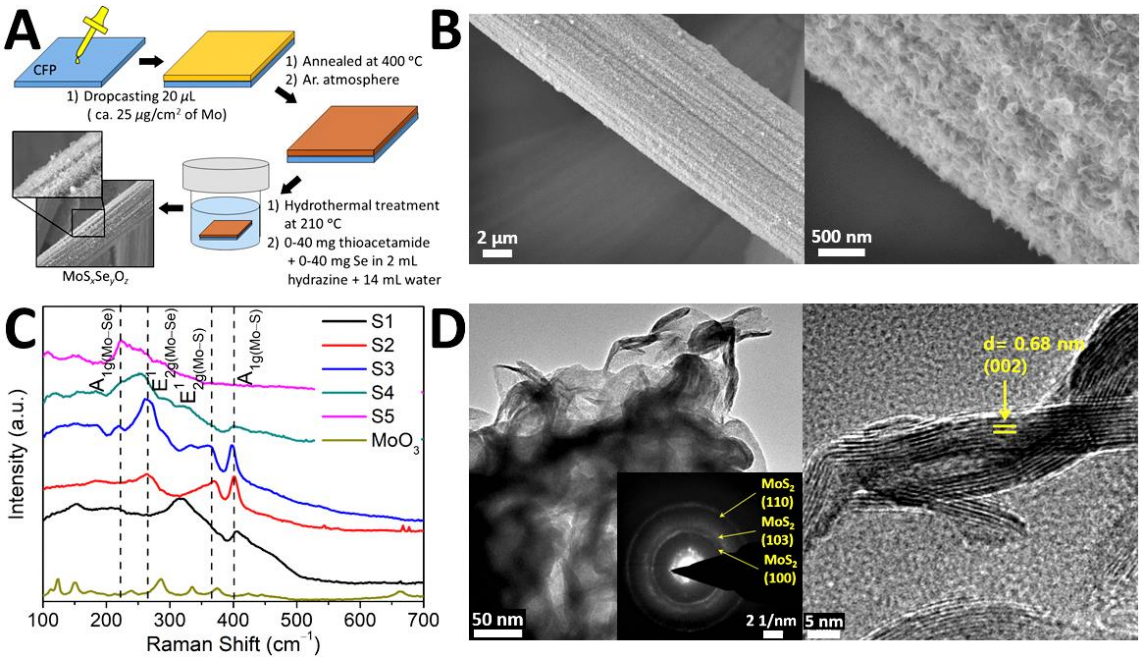

Figure VI. 1. (A) Illustration of the step-wise synthetic process comprising drop-casting, thermal annealing, and hydrothermal sulfidation/selenization used to grow $MoS_{2-x}Se_x/MoO_3$ nanosheets on CFP. (B) SEM image of sample S3 (Se:S=0.48) showing the homogeneous distribution of the nanosheets on CFP. (C) Raman spectra (514.5 nm laser excitation) acquired for $MoS_{2-x}Se_x/MoO_3$ samples with increasing concentration of selenium. (D) Low-magnification and HRTEM images of sample S2 (Se:S=0.62) illustrating the layered structure of $MoS_2/MoSe_2$. The left inset shows a SAED pattern of the chalcogenide layers.

VI.2 Results and Discussion

A sol—gel process followed by thermal annealing and hydrothermal sulfidation/selenization has been used to prepare $MoS_{2-x}Se_x/MoO_3$ heterostructures with tunable amounts of Se incorporation, which are further integrated onto carbon fiber paper (CFP) substrates. The stepwise synthetic process comprising drop-casting of the gel onto the CFP substrates, annealing under an Ar ambient to induce crystallization, and hydrothermal sulfurization/selenization is shown in **Figure VI. 1A**. In the first step, the reaction of molybdenum powder with hydrogen peroxide yields a gel as per:

$$4Mo(s) + 10H_2O_2\ (aq.) + 8H_2O \leftrightarrow 4MoO_3.2H_2O_2.4H_2O\ (gel) + 8H_3O^+ \ldots(VI.1)$$[36]

In the second step, 10 µL of the gel is drop-cast onto the CFP substrate, which is then annealed at 400°C in a flowing argon environment to form MoO_3. Next, the annealed samples are hydrothermally sulfided and/or selenized by immersion of the MoO_3@CFP samples within a solution of thioacetamide and selenium in hydrazine and water. The relative amounts of S and Se precursors determines the relative stoichiometries of the two chalcogenides in the $MoS_{2-x}Se_x/MoO_3$ heterostructures.

Scanning electron microscopy (SEM) and transmission electron microscopy (TEM) images of the $MoS_{2-x}Se_x/MoO_3$ heterostructures are shown in **Figure VI. 1**. The SEM images in **Figures VI. 1B** and **A37** show that the Samples S1—S5 (with intended Se concentrations ranging from x of 0 to 2.0 in $MoS_{2-x}Se_x$) maintain a similar 3D open network framework of the carbon fibers with varying Se content. High-magnification SEM images (**Figs. VI. 1B** and **A37**) show a dense forest of vertically aligned micron-sized $MoS_2/MoSe_2$ platelets adhered to the CFP. The 3D open network with vertically aligned arrays of $MoS_2/MoSe_2$ platelets that expose their reactive edge sites provides a large surface area for electrolyte interactions as is necessary for electrocatalysis. **Figures VI. 1B** and **A37** indicate that the nanosheets increase in size with increasing Se incorporation. However, Sample S5 (**Fig. A37E**) does not show characteristic lattice fringes of $MoS_2/MoSe_2$ in electron microscopy evaluation indicating that selenization is difficult to achieve without initial sulfidation. Clear lattice fringes of $MoS_{2-x}Se_x$ are observed in the TEM image shown in **Figure VI. 1D**. The interlayer spacing between the lattice fringes is ca. 0.68 nm, which corresponds to the separation between the (002) planes

of MoS_2 or $MoSe_2$ (JCPDS: 75-1539 for 2H-MoS_2 and JCPDS: 87-2419 for 2H-$MoSe_2$). Selected area diffraction (SAED) patterns shown in the inset of **Figure VI. 1D** exhibit clear diffuse rings attesting to the polycrystalline nature of the layered $MoS_{2-x}Se_x$ materials. The diffraction rings can be indexed to the (100), (103), (110) planes of 2H-MoS_2 or $MoSe_2$. **Figure A38** shows energy-dispersive X-ray (EDX) spectra acquired for the samples alongside their corresponding SEM images. The Se:S atomic ratio increases from 0 to 0.29 to 0.48 to 0.62 to 1 in going from sample S1 to S5.

Raman spectroscopy measurements have further been performed to probe the local structure of the five samples with varying Se incorporation as shown in **Figure VI. 1C**. Raman bands at ca. 402 and 380 cm^{-1} correspond to out-of-plane $A_{1g(Mo-S)}$ and in-plane $E^1_{2g(Mo-S)}$ vibrational modes, respectively, whereas Raman bands at ca. 230 cm^{-1} and 274 cm^{-1} correspond to out-of-plane $A_{1g(Mo-Se)}$ and in-plane $E^1_{2g(Mo-Se)}$ vibrational modes, respectively.[37-39] With increasing Se incorporation, the intensity of low-frequency Mo–Se bands (200–290 cm^{-1}) increases relative to the high-frequency Mo–S modes (350–400 cm^{-1}).[40] Indeed, low-frequency modes are not detectable for sample S1, which is devoid of any selenium. Similarly no high-frequency modes are observed for sample S5, which is devoid of sulfur. Characteristic Raman modes of MoO_3 are not detected for samples S1-S5 suggesting that the thickness of the chalcogenide layers exceeds the Raman probe depth. The $A_{1g(Mo-Se)}$ and the $A_{1g(Mo-S)}$ Raman modes for the Samples S2, S3, and S4 are slightly red shifted (by ca. 5 cm^{-1}) in comparison to samples devoid of either selenium (S1) or sulfur (S5) suggesting stabilization of MoS_2/$MoSe_2$ domains.[37]

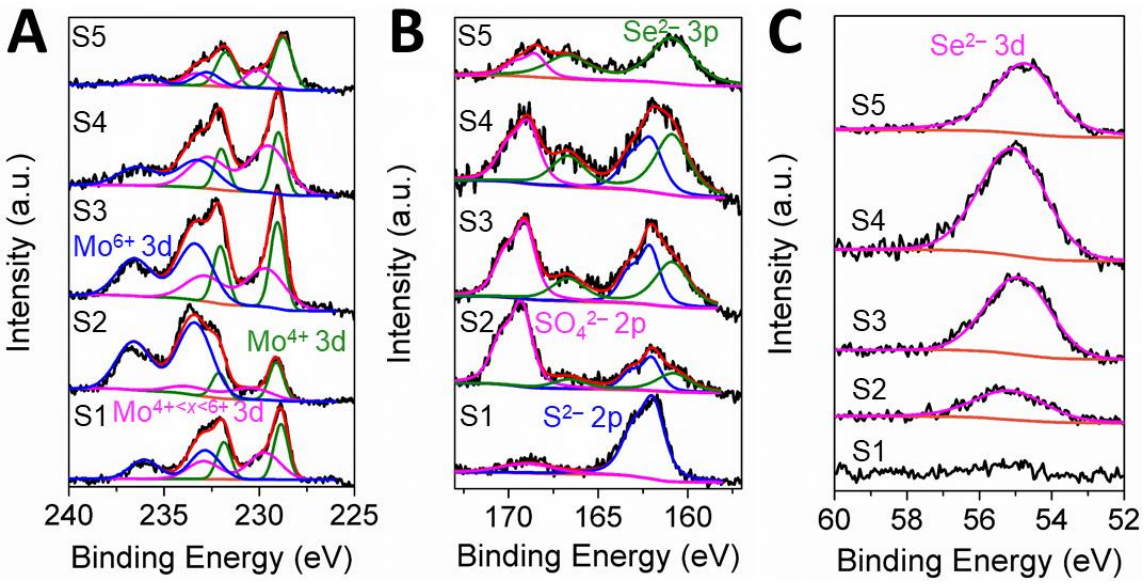

Figure VI. 2. XPS spectra indicating (A) Mo 3d, (B) S 2p, and (C) Se 3d binding energies for samples S1-S5 incorporating increasing amounts of selenium.

X-ray photoemission spectroscopy (XPS) has been performed to examine the oxidation states of molybdenum and chalcogen atoms in the five samples. Three primary peaks are observed for Mo 3d core levels in **Figure VI. 2A**. Peaks at 228.9 eV ($3d_{5/2}$)/ 232.1 eV ($3d_{3/2}$) are ascribed to tetravalent Mo in the hexagonal 2H-phase of MoS_2/$MoSe_2$;[40-42] peaks at 232.9 eV ($3d_{5/2}$)/ 236.1 eV ($3d_{3/2}$) derive from hexavalent Mo in MoO_3;[43-45] and the peaks at 229.7 eV ($3d_{5/2}$)/ 232.9 eV ($3d_{3/2}$) correspond to an intermediate oxidation state $+4 < x < +6$ reflective of Mo atoms at the interface between the chalcogenide and oxide layers (formally oxysulfides or oxyselenides).[43,46] Two peaks observed for each of these features correspond to the spin-orbit splitting of Mo $3d_{5/2}$ and Mo $3d_{3/2}$ levels. When comparing the Mo $3d_{5/2}$ peaks (green) corresponding to MoS_2 for sample S1-S5 (**Figure VI. 2A** and **Table A17**), the position of the peak is shifted to higher energy for S2 in comparison to S1. The peak gradually shifts to lower energies with a

further increase in the Se content from S2 to S5. Hence, changing the relative concentrations of Mo, S, Se, and the hybridization with the underlying MoO_3 lattice alters the energy positioning of the d-states of Mo; the d-band electronic structure is well known to strongly modify electrocatalytic function.[18]

High-resolution S/Se 2p core level XPS spectra are shown in **Figure VI. 2B**. Three primary set of peaks are observed. Doublets in the range of 160.8-160.9 eV[41] correspond to Se 3p core levels, doublets in the range of 161.9-162.1 eV corresponds to S^{2-}-ions in MoS_2.[17,40,47] and doublets in the range of 168.5-169.3 eV in the range of 168.5-169.3 eV derive from high oxidation state of sulfur such as sulfates.[48,49] The spin-orbit splitting between Se $3p_{3/2}$ and Se $3p_{1/2}$ peaks is 5.8 eV, and between S $2p_{3/2}$ and S $2p_{1/2}$ peaks is 1.2 eV. **Figure VI. 2B**, shows that the relative amount of Se increases and the amount of S is decreased in going from sample 1 to 5, which is in accordance with the precursor ratios used in in the hydrothermal step. High-resolution Se 3d XPS spectra are shown in **Figure VI. 2C**. The Se $3d_{5/2}$ peaks for sample S2-S5 are in the range of 54.5-54.9 eV,[40-42] which is characteristic of Se^{2-} species in $MoSe_2$. The spin-orbit-splitting between the Se $3d_{5/2}$ and Se $3d_{3/2}$ peaks is 5.8 eV (**Table A17**).

The conduction band of MoS_2 is defined by the hybridization of Mo 4d states with S 2p and 3d states; the extent of delocalization of Mo 4d states determines the energy positioning of the states. Indeed, corrugated edge sites of MoS_2 are particularly reactive owing to the emergence of localized states at the bottom of the conduction band, which are observed as distinctive pre-edge features in S L- and K-edge XANES spectra.[18] The

evolution of S K-edge and Mo L_3-edge XANES spectra across has been examined Samples S1—S5 as a function of increasing selenium concentration.

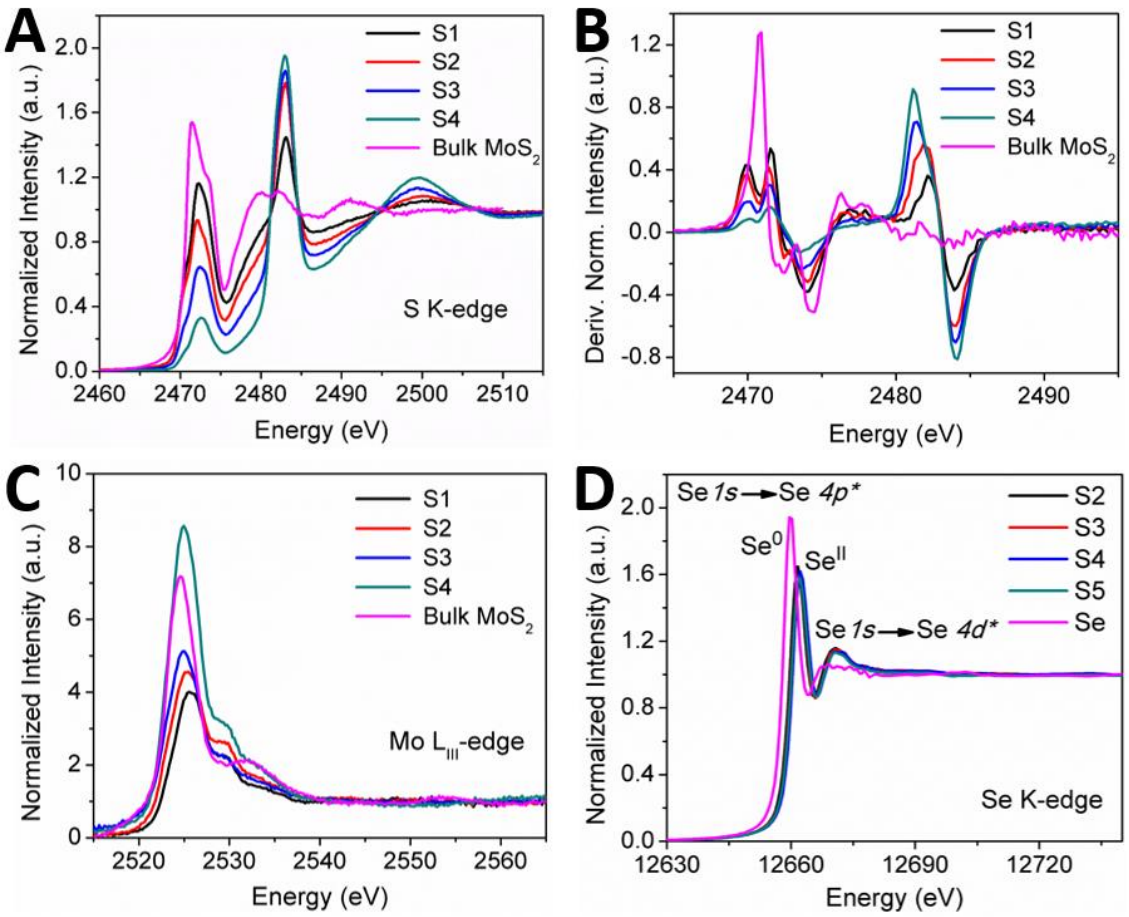

Figure VI. 3. The X-ray absorption near edge spectra (A) at S K-edge, (B) the derivative of the normalized intensity of the S K-edge spectra shown in (A), (C) at Mo L_3-edge, (D) and at Se K-edge of the $MoS_{2-x}Se_x/MoO_3$ samples

Three sets of absorptions are observed in the S K-edge spectra (**Fig. VI. 3A**): (1) dipolar transitions from the S 1s core levels to hybridized S 3p–Mo 4d excited states of S^{2-} species (derived from MoS_2) in the energy range between 2467—2476 eV; (2) dipolar transitions from S 1s core levels to hybridized S 3p–Mo 4d excited levels of oxidized sulfur species in the energy range between 2479—2487 eV; (3) weaker dipole–forbidden transitions

from S 1s core levels to S 3d states above 2487 eV. It is immediately apparent from **Figures VI. 3A** and **B** that oxidized sulfur species[50] (with a maximum absorption centered around ca. 2483 eV) are increased in intensity with an increase of the selenium concentration. The derivative of the normalized intensity of the S K-edge spectrum versus energy is plotted in **Figure VI. 3B**. The absorption features corresponding to the oxidized sulfur species are red-shifted (**Figure VI. 3A**) with increasing Se concentration suggesting more reduced sulfur species, which in turn reflects alteration of the extent of ionicity/covalency of Mo—S bonds upon Se incorporation. **Figures VI. 3A** and **B** furthermore demonstrate that the feature at 2472.3 eV in S K-edge spectra of samples S1-S5 is blue-shifted by ca. 0.7 eV in comparison to bulk-MoS_2 (**Figure VI. 3A and 3B**), suggesting relatively more electropositive sulfur atoms as compared to MoS_2. This observation can be rationalized based on a DFT study[44] that demonstrated interfacial electron transfer from MoS_2 to MoO_3, which increases the formal oxidation state of the sulfur ligands. In other words, the S K-edge XANES spectra indicate that sulfur atoms in MoS_2/MoO_3 are more electropositive than MoS_2 with the oxidized sulfur species somewhat reduced upon Se incorporation.

Based on eXcited Core Hole-X-Ray Absorption Spectroscopy (XCH-XAS) DFT calculations, the 2470 eV pre-edge absorption feature observed in S K-edge XANES spectra of MoS_2 has been ascribed to derive from the increasing corrugation of the MoS_2 edges, which results in the localization of the hybridized S 3p–Mo 4d states.[18] The emergence of such states are thought to be directly correlated with improved

electrocatalytic activity. As we will discuss later, this maybe one of the reason for increased HER activity in all the samples.

Figure VI. 3C plots the evolution of Mo L_3-edge XANES spectra as a function of Se concentration. Two sets of absorption peaks can be identified: (1) dipolar transitions from the Mo $2p_{3/2}$ core levels to hybridized S 3p–Mo 4d excited states of tetravalent molybdenum species in the energy range between ca. 2520—2528 eV, (2) weaker dipole–forbidden transitions from Mo $2p_{3/2}$ core levels to hybridized Mo 5p–S 3d excited states above 2530 eV.[18,51] A high-energy shoulder emerges in the ca. 2528-2530 eV range for Samples S1—S4, which can be ascribed to dipole-allowed transitions from Mo $2p_{3/2}$ core levels to hybridized S 3p–Mo 4d excited levels of hexavalent molybdenum species;[52] notably this feature is absent in the Mo L_3-edge spectrum of bulk MoS_2. Analogous to the S K-edge XANES spectra, the primary absorption at ca. 2520-2528 eV for Samples S1-S4 is blue-shifted in comparison to bulk MoS_2, indicating the presence of more electropositive molybdenum as a result of interfacial hybridization with MoO_3.[44] Furthermore, the peak positions of the primary absorption follows the trend bulk MoS_2 (2524.5 eV) < S4 < S3 < S2 < S1 (2525.6 eV), spanning a range of 1.1 eV, which denotes considerable modulation of electron density on molybdenum sites with increasing Se incorporation.

Figure VI. 3D displays Se K-edge XANES spectra acquired for Samples S1—S5. Two sets of absorption peaks can be identified: (1) dipolar transitions from the Se 1s core levels to Se 4p—Mo 4d excited states of Se^{2-} species in the energy range between ca. 12,653-12,666 eV, and (2) less intense dipole–forbidden transitions from Se 1s core levels

to Se 4d—Mo 4d states above ca. 12,666 eV. The absorption feature centered at xx eV for samples S2—S5 is ca. 2.1 eV higher in energy as compared to elemental Se, which suggests a –2 oxidation state for Se.[53,54] These results corroborate the substitutional incorporation of Se within MoS_2. Taken together, element-specific XANES measurements at the S and Se K-edges and the Mo L_3-edge indicate that interfacing MoS_2 with MoO_3 results in hole doping of the former; which can be counteracted by Se incorporation, enabling modulation of carrier density across a broad range within these heterostructures.

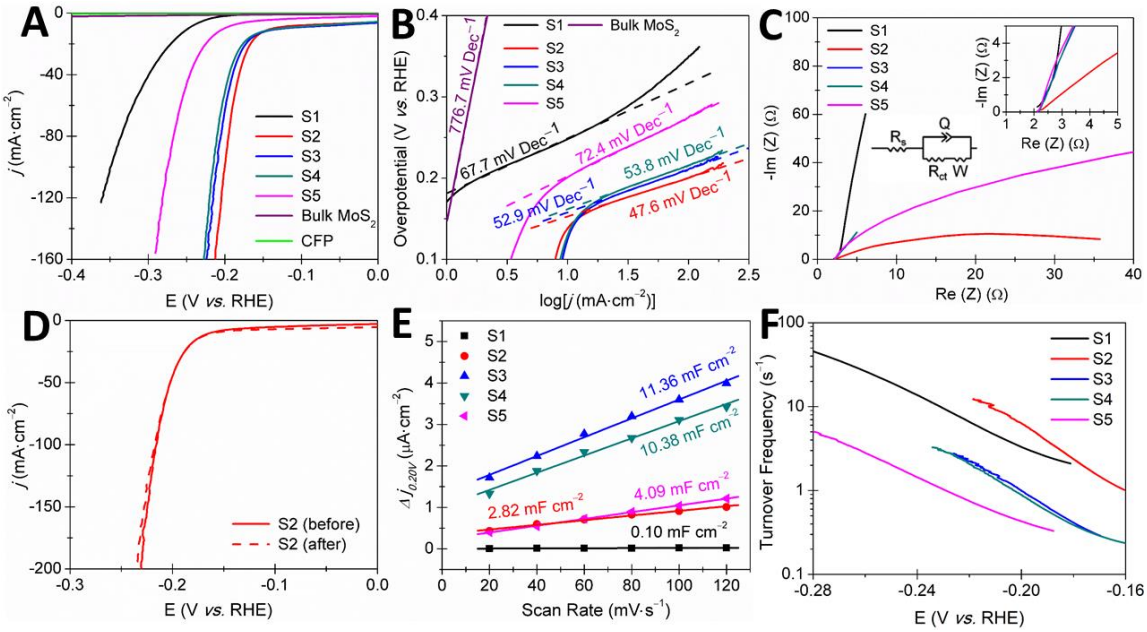

Figure VI. 4. (A) Polarization curve, (B) Tafel plots, and (C) Nyquist plots measured for samples S1-S5 with increasing Se incorporation. (D) Polarization curve for the best performing catalyst S2 before and after scanning across 1000 cycles. (E) Double-layer capacitances (C_{dl}) and (F) turnover frequencies measured for Samples S1-S5 with increasing Se incorporation. HER experiments have been performed in a 0.5M aqueous solution of H_2SO_4 using a three-electrode system. All results shown here have been iR corrected. Linear scanning voltammetry data has been acquired at a scan rate of 5 $mV \cdot s^{-1}$.

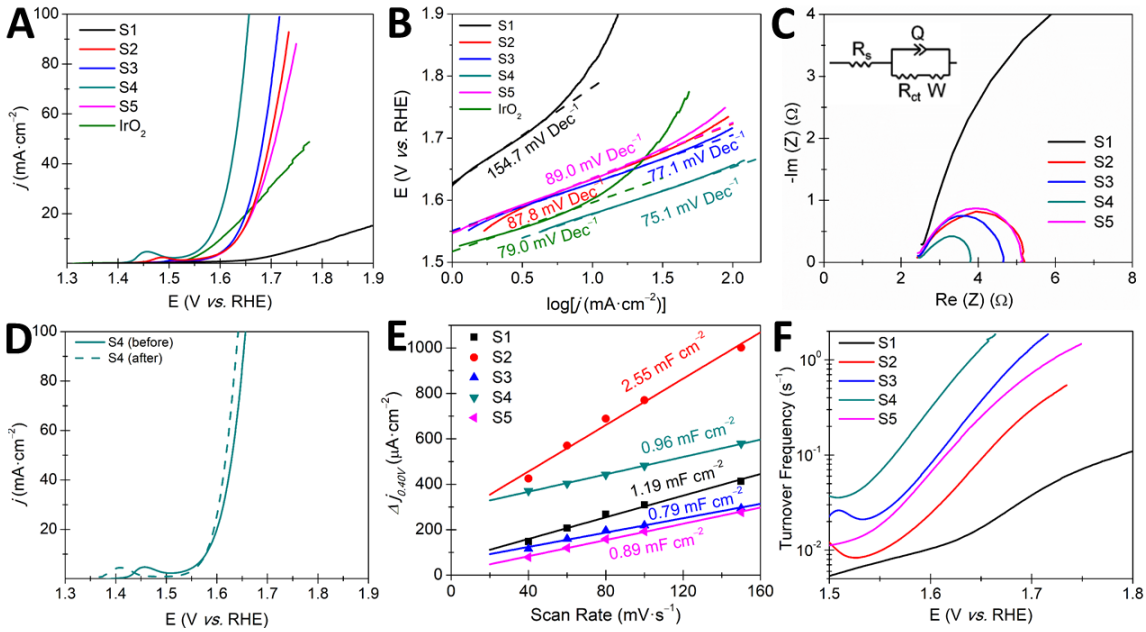

Figure VI. 5. (A) Polarization curve, (B) Tafel plots, and (C) Nyquist plots measured for Samples S1-S5 with increasing Se incorporation. (D) Polarization curve for the best performing catalyst, Sample S4, before and after scanning across 1000 cycles. (E) C_{dl} and (F) TOF measured for Samples S1-S5. OER experiments have been performed in a 1.0M aqueous solution of KOH using a three-electrode system. All results shown here have been iR corrected. Linear scanning voltammetry data has been acquired at a scan rate of 5 $mV \cdot s^{-1}$.

Correlating Composition and Electronic Structure to Electrocatalytic Function

The electrocatalytic performance of Samples S1-S5 on CFP has been contrasted to that of bulk 2H-MoS_2 using a three-electrode setup with a 0.5M aqueous solution of H_2SO_4 as the electrolyte. **Figure VI. 4A** plots the polarization curves corrected for *iR* losses. The polarization curve measured for bare CFP shows that it is catalytically inert towards HER. Remarkably, Samples S1-S5 all outperform bulk 2H-MoS_2 in terms of the overpotential for hydrogen evolution. Samples S1-S5 catalyze HER at relatively low overpotentials (10 mA/cm^2) of ca. 0.12—0.25 V (**Figure VI. 4A**) with Tafel slopes in the range of. 47.6–67.7 mV/dec (**Figure VI. 4B**). The low Tafel slopes of samples S1-S5 attest to the

operation of the Volmer−Heyrovsky mechanism, wherein proton-reduction and hydrogen-desorption are simultaneously the rate-determining steps.[7,34] Sample S2 with ca. xx at.% Se incorporation is the best performing HER catalyst with a current density of 10 mA/cm^2 (η_{10}) achieved at an overpotential of 0.12 V with a Tafel slope of 47.6 mV/dec. Indeed, Samples S2, S3, and S4 show relatively similar Tafel slopes (47.6—53.8 mV/dec) and overpotentials (0.12—0.13 V), and are markedly more active as compared to Samples S1 (Tafel slope of 67.7 mV/dec, overpotential of 0.25 V) and S5 (Tafel slope of 72.4 mV/dec, overpotential of 0.2 V). Notably, the HER performance of the Se-incorporated samples is substantially improved over previously reported values for high-edge-density nanostructured MoS_2.[41,42] A primary conclusion that can be derived from these measurements is that the alloyed $MoS_{2-x}Se_x$ are considerably better HER catalysts as compared to the binary chalcogenides MoS_2 and $MoSe_2$. Furthermore interfacial hybridization with MoO_3 appears to substantially enhance catalytic activity.

The mechanism of HER in these samples has further been investigated using electrochemical impedance spectroscopy (EIS) measurements. These measurements have been performed at potentials between 10 mV to -400 mV by sweeping the frequency from 200 kHz to 100 mHz with an ac amplitude of 10 mV. **Figure VI. 4C** displays Nyquist plots measured for Samples S1—S5. The plots have been fitted using an equivalent circuit model comprising the following elements: an ohmic resistance (R_s), a charge-transfer resistance (R_{ct}), constant phase element (Q), and a Warburg constant (W). The value of R_{ct} serves as a good descriptor for the kinetics of electrocatalytic HER; in general, the lower the value of R_{ct}, faster is the reaction rate.[33,34] The measured trend in R_{ct} values tracks

closely with the trends observed for the Tafel slope and overpotential values. Sample S2 exhibits the lowest R_{ct} value of 35.9 Ω and is two orders of magnitude lower than the value deduced for binary chalcogenide MoS_2. In other words, Se incorporation greatly accelerates the kinetics of H_2 production. **Figure VI. 4D** shows data from CV sweeps for 1000 cycles between a potential range of -0.2 and 0.2 V measured for Sample S2. The polarization curves before and after 1000 CV cycles are most nearly superimposable confirming no degradation of the catalyst even upon prolonged catalytic operation. These results attest to the stability of the chalcogenide/oxide interface.

The mechanistic basis for differences in HER activity with Se incorporation has been further explored by measuring the double-layer capacitance (C_{dl}) (**Figure A39**) of Samples S1—S5 across a non-Faradaic potential window.[17,47,55] CV data have been acquired at scan rates ranging from 20—120 mV/s in the potential range of 0.1—0.3 V *vs*. RHE where the measured current is derived from charging of the double layer and not proton reduction. The differential between cathodic and anodic currents (Δj at 0.20 V) has been plotted *versus* the scan rate in **Figure VI. 4E**; the corresponding C_{dl} values are furthermore noted in this panel. The C_{dl} values measured for Samples S1—S5 span the range between 0.10—11.36 mF/cm^2, which is ca. 1000× higher than the value for flat crystalline MoS_2 (ca. 66.7 μF/cm^2).[17] Electrochemically active surface areas (ECSA) have been determined by dividing the C_{dl} values by the capacitance of an atomically smooth MoS_2 surface. The high ECSA of these samples are derived from their nanoplatelet morphologies, which are characterized by a high density of exposed edge sites (**Figs. VI. 1** and **A37**). Notably, Sample S2 is the best performing HER catalyst despite having half

the ECSA of Samples S3 and S4, suggesting that Se incorporation at xx at.% gives rise to highly reactive sites as a result of its distinctive atomistic structure and electronic band structure characteristics.[42]

One measure of catalytic activity of electrocatalysts is provided by the turnover frequency (TOF), which is defined as the number of product molecules evolved per unit site per unit time.[17,19,56] The TOF can be calculated as:

$$\text{TOF} = JN_A/CFn(ECSA) \qquad \ldots(\text{VI.2})^{17,23,57}$$

where J is the current density, N_A is Avogadro's number, C represents the number of electrons consumed during the electrocatalytic process (which is 2 for HER and 4 for OER), F is Faraday's constant, n is the number of active sites (ca. 1.164×10^{15} cm^{-2}) for a flat surface of single-crystalline MoS_2,[17] and the ECSA is determined as discussed above. This calculation makes the simplified assumption that all Mo-sites are catalytically active. Figure 4F plots the TOF per active site for Samples S1—S5 in the potential range between -0.1 to -0.3 *vs.* RHE for HER. Sample S2 exhibits the highest TOF (6.2 H_2/s per active site at –0.2 V), which further attests to the creation of particularly potent sites with high intrinsic activity as a result of Se incorporation and MoO_3 hybridization in this sample. Consistent with this picture, **Figures VI. 3A** and **B** demonstrate that this sample has the highest intensity of all the selenized samples of the 2470 pre-edge feature associated with active corrugated edge sites.[18] In comparison, Samples S3 and S4 have relatively low TOF values (1.0 and 0.9 H_2/s per active site, respectively); nevertheless, the high density of electroactive sites in these samples underpins the low overpotential and Tafel slope observed in **Figure VI. 4**. Sample S1, MoS_2 without Se incorporation, exhibits a relatively

higher TOF (3.3 H_2/s per active site) but has a substantially lower ECSA, resulting in relatively poor overpotential and Tafel slope metrics.

The electrocatalytic activity of Samples S1—S5 towards OER has similarly been measured and contrasted to that of the canonical OER catalyst IrO_2 using a three-electrode setup with a 1M aqueous solution of KOH as the electrolyte. **Figure VI. 5A** plots the polarization curves corrected for *iR* losses, which demonstrates that the selenized materials S2—S5 exhibit substantially enhanced electrocatalytic activity as compared to MoS_2. Samples S2—S5 exhibit low η_{10} overpotentials of ca. 0.28–0.33 V (**Fig. VI. 5A**) and low Tafel slopes of ca. 75.1–89.0 mV/dec (**Fig. VI. 5B**). Sample S4 with a nominal Se concentration of 0.62 Se:S atomic ratio is the best performing OER catalyst with η_{10} of 0.28 V and a Tafel slope of 75.1 mV/dec. Sample S3 exhibits comparable electrocatalytic function with an η_{10} of 0.33 V and a Tafel slope of 77.1 mV/dec. In comparison, the canonical precious metal OER catalyst IrO_2 fares slightly worse with a η_{10} of 0.30 V and Tafel slope of 79.0 mV/dec.

EIS measurements have been performed in a 1.0M aqueous solution of KOH in the potential window between 200 to 600 mV by sweeping the frequency from 200 kHz to 100 mHz with an ac amplitude of 10 mV. The corresponding Nyquist plots are depicted in **Figure VI. 5C**. Notably, Samples S3 and S4 exhibit two of the lowest R_{ct} values, corresponding to the fastest kinetics for O_2 production. **Figure VI. 5D** illustrates excellent retention of the electrocatalytic activity of Sample S4 with a <0.01 V shift of η_{10} after prolonged cycling over 1000 cycles in a 1.0M aqueous solution of KOH, further attesting to the robustness of the chalcogenide/oxide interfaces in these samples. **Figure A40** plots

CV data collected at various scan rates (40—150 mV/s) in the non-Faradaic potential window of 0.3—0.5 V *vs.* RHE. **Figure VI. 5E** plots the differential between anodic and cathodic currents (Δj at 0.40 V) *versus* the scan rate. The C_{dl} values deduced from this data under OER conditions range from 0.79—2.55 mF/cm^2. The ECSA values are comparable across the sample set, and as a result, the deduced TOF values are concordant with the relative efficiencies measured for Tafel slopes and the η_{10} overpotential. **Figure VI. 5F** plots the TOF measured in the potential window between 1.3 to 1.9 eV *vs.* RHE for OER. Sample S4 exhibits a high TOF of 1.3 O_2/s per active site at 1.65 V. Samples S3 and S5 exhibit somewhat lower TOFs of 0.4 and 0.3 O_2/s per active site at 1.65 V, respectively. Owing to a high ECSA, the TOF of sample S2 is somewhat better than that of Sample S1 despite having a low Tafel slope and low η_{10} overpotential. Notably, despite having a rather similar C_{dl} value, and thus ECSA, as Samples S3 and S5, Sample S4 is the best performing OER catalyst. Once again, these measurements suggest that an optimal Se concentration yields the crystal structure and electronic band structure characteristics necessary for electrocatalytic function.

The electrocatalytic activity of a semiconductor is strongly dependent on the energy positioning of its conduction and valence band edges.[58-62] The dilute adsorption of substituents on the metal chalcogenide surface does not significantly alter the overall electronic structure.[63] However, the adsorption of hydrogen atoms is strongly dependent on the unoccupied states available at the bottom of the conduction band; in contrast, the adsorption of O*/OH*/OOH* is strongly dependent on the population of occupied states at the top of the valence band.[64] As such, one strategy to enhance catalytic activity towards

HER is to shift the conduction band minimum (CBM) down in energy, and for OER, is to raise the level of valence band maximum (VBM).[65] **Figure VI. 6A** illustrates the charge transfer from H 1s states of adsorbed H atoms ($H_{ads.}$) to the empty states available at the bottom of the conduction band edge of MoS_2. These interactions mediate electrocatalytic HER. Consequently, decreasing the energy of the CBM will stabilize adsorbate-substrate hybrid states, resulting in improved surface reactivity. In turn, during OER, the relevant interaction is between the top of the valence band edge of MoS_2 or MoS_2 and O 2p states of intermediate oxygen species ($O_{ads.}$). Hence, pushing the VBM up in energy will more readily stabilize adsorbates resulting in enhanced surface reactivity.

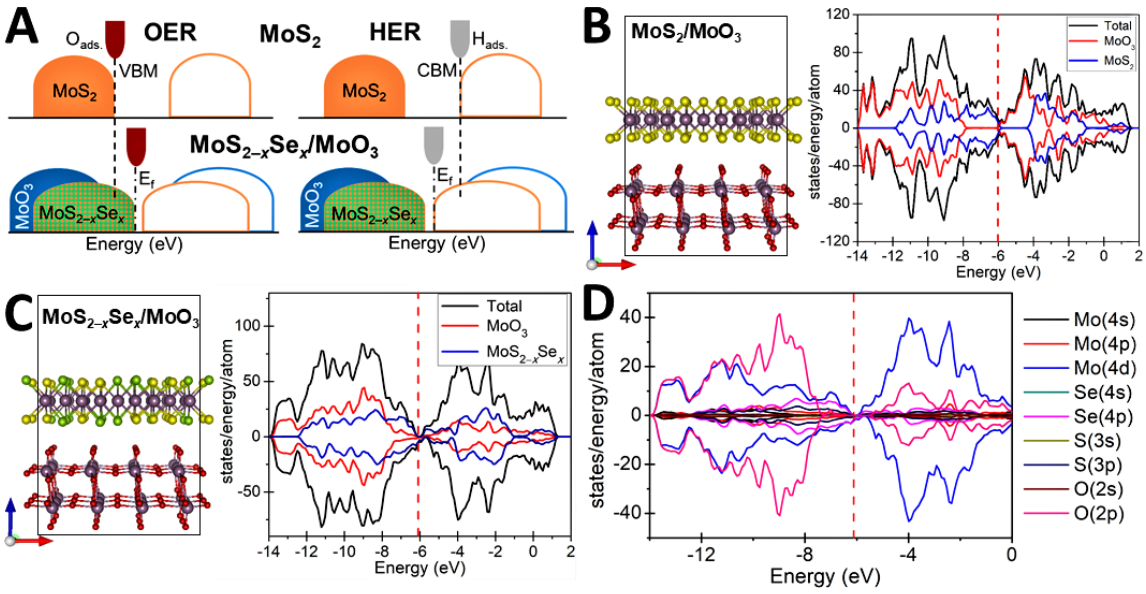

Figure VI. 6. (A) Schematic density of states (DOS) illustrating the interaction between O 2p and H 1s adsorbate states with 2H-MoS_2 and $MoS_{2-x}Se_x/MoO_3$ during OER and HER process, respectively. The supercell geometry and the corresponding DOS and PDOS for MoS_2/MoO_3 and $MoS_{2-x}Se_x/MoO_3$ are represented in (B) and (C) respectively. The atom-projected PDOS for $MoS_{2-x}Se_x/MoO_3$ is represented in (D). All energies are referenced to the vacuum level and the Fermi level is indicated by red dashed line. The molybdenum, selenium, sulfur, and oxygen atoms are represented as violet, green, yellow, and red spheres respectively.

Based on the XPS and XANES spectroscopy studies presented in **Figures VI. 2** and **3**, interfacial hybridization of MoS_2 with MoO_3 results in interfacial electron transfer from MoS_2 to MoO_3. As shown in the density of states (DOS) calculations of **Figure VI. 6B**, interfacing MoO_3 with MoS_2 reduces the CBM in comparison to MoS_2 alone (**Figure A41**), which facilitates enhanced hydrogen adsorption at the interface. Indeed, Sample S1 prepared by sulfidation of MoO_3 corresponding to MoS_2/MoO_3 shows significantly improved HER activity as compared to MoS_2. However, since the VBM remains unmodified upon MoO_3 hybridization, Sample S1 is only modestly active in OER (**Fig. VI. 5**). Incorporation of Se atoms on the anion lattice of MoS_2 raises the VBM (**Figs. VI. 6A** and **D**) owing to the emergence of higher lying Mo 4d–Se 4p hybridized states. As per Fajan's formalism, heavier chalcogenides show increased hybridization and more covalent bonds in lattices incorporating transition metals;[66,67] as such, the VBM of MoS_2 derived primarily from Mo 4d–S 3p hybridized states is situated lower in energy as compared to the VBM of $MoSe_2$ primarily derived from Mo 4d–Se 4p hybridized states. The higher lying VBM of $MoS_{2-x}Se_x/MoO_3$ decreases the overall overpotential required for adsorption of reactive oxygen intermediates. The Se-projected PDOS in **Figure VI. 6D** illustrates that the VBM of $MoS_{2-x}Se_x/MoO_3$ heterostructures is primarily Mo 4d–Se 4p in origin. As such, the $MoS_{2-x}Se_x/MoO_3$ samples S2—S4 show excellent performance in both HER and OER. **Figure A42** plots the DOS of MoS_2/MoO_3 (O-bonded) and $MoS_{2-x}Se_x/MoO_3$ (O-bonded) heterostructures. These materials are again characterized by a decreased bandgap with a reduced CBM as a result of low-lying Mo 4d—O2p states and an increased VBM as a result of high-lying Mo 4d–Se 4p-derived states. In other words,

the distinctive electronic structure of these alloyed heterostructures derived from Se incorporation and MoO_3 hybridization underpins their excellent performance as bifunctional electrocatalysts in both HER and OER. The superior performance of Sample S2 towards HER within this set can be ascribed to its combination of a high density of catalytically active edge electronic states delineated in **Figures VI. 3A** and **B** and an accessible MoO_3 interface that facilitates hydrogen adsorption. In contrast, the superior performance of Sample S4 in OER stems from the high concentration of Se, which results in a high density of Se-derived states at the VBM, facilitating adsorption of oxygen intermediates.

VI.3. Experimental Section

Synthesis

The dissolution of Mo metal in an aqueous solution of H_2O_2 results in the formation of peroxo-polymolybdates as per:

$$2Mo\ (s) + 10H_2O_2\ (aq.) \leftrightarrow [Mo_2(O)_3(O_2)_4(H_2O)_2]^{2-}\ (aq.) + 2H_3O^+\ (aq.) + 5H_2O \quad \ldots (VI.3)$$ [36]

In acidic solution (pH<3), the dimeric species polymerize to form a tetraperoxtetramolybdate complex:

$$2[Mo_2(O)_3(O_2)_4(H_2O)_2]^{2-}\ (aq.) + 2H_3O^+\ (aq.) \leftrightarrow [Mo_4(O)_9(O_2)_4]^{2-}\ (aq.) + 4H_2O_2\ (aq.) + 3H_2O \quad \ldots (VI.4)$$ [36]

A further decrease in the pH stabilizes $[Mo_4(O)_9(O_2)_4]^{2-}$, which reacts with water to form $[Mo_4(O)_{12}(O_2)_2]^{2-}$; which is further hydrated to form $[Mo_4(O)_{12}(O_2)_2(H_2O)_4]_n^{4n\ -1}$. A

molybdic acid peroxide sol($H_{4n}[Mo_4(O)_{12}(O_2)_2(H_2O)_4]_n$) is synthesized, which is annealed to obtain crystalline MoO_3.

A method previously described in the literature was used to prepare the molybdic acid sol, which was subsequently hydrated to form the gel.[36,68] Briefly, 1 g of Mo powder (Sigma-Aldrich, purity ≥99.5%) was reacted with 7 mL of 30% (w/w) aqueous H_2O_2 (Sigma-Aldrich, purity 29.0-32.0 % w/w in water) in a 150 mL beaker cooled using an ice water bath. An orange-red solution was obtained by stirring the reaction mixture for 4—5 min. The obtained solution was then diluted by adding deionized water (ρ= 18.2MΩ/cm) until the total volume of the solution was 20 mL. A10 µL aliquot of this mixture was spread across a 1 cm^2 area of the carbon fiber paper (CFP) (Toray Paper 120). The sol-gel deposited CFP was dried in air and then annealed at 400°C under a flowing Ar atmosphere. The annealed samples were hydrothermally sulfided and selenized by adding the MoO_3@CFP samples to a solution of thioacetamide (Sigma-Aldrich, purity ≥99.0%) and selenium (Sigma-Aldrich, purity ≥99.5%) in 2 mL of hydrazine (Sigma-Aldrich, purity ≥ 98.0%) and 14 mL water. The amounts of thioacetamide in samples S1, S2, S3, S4, and S5 were 40, 35, 30, 25, and 0 mg, respectively, whereas the amounts of selenium added to the reaction mixtures were 0, 5, 10, 15, and 40 mg, respectively. The MoO_3@CFP samples were placed within hydrothermal vessels and annealed at a temperature of 210°C for 12 h. The samples were then removed from the hydrothermal vessels, washed with deionized water, and dried under Ar gas.

Structural Characterization

The morphology of the as-synthesized samples was examined by filed-emission scanning electron microscopy (SEM) using a JEOL JSM-7500F instrument. The elemental composition of the as-synthesized samples on CFP were investigated using energy-dispersive X-ray spectroscopy (EDS). The as-synthesized samples on CFP were ultrasonicated for 5 min in ethanol and the solution was drop-cast on a transparent copper grid. The deposited nanoflakes on grids were analyzed by using a transmission electron microscope (JEOL JEM-2010) operated at an accelerating voltage 200 kV. Phase assignments were enabled by Raman spectroscopy measurements performed using a Jobin-Yvon Horiba LabRAM HR800 instrument coupled to an Olympus BX41 microscope. Excitation from the 514.5 nm line of an Ar-ion laser was used to collect the Raman spectra; to minimize photo-oxidation, the laser power was kept below 10 mW. X-ray photoelectron spectroscopy (XPS, Omicron XPS) with Mg Kα radiation (1253.6 eV) was used to investigate the chemical composition and oxidation states of the as-synthesized samples. The measured spectra was calibrated by setting the C 1s line from the CFP (at 284.8 eV).

S K-edge, Mo L_3-edge, and Se K-edge XANES spectra were measured at the Advanced Light Source bending magnet beamline 10.3.2. The spectra were collected in fluorescence mode in the energy range of 2450–2580 eV for the S K-edge and Mo L_3-edge and 12600–12800 eV for the Se K-edge by continuously scanning a Si (111) monochromator (Quick XAS mode) from 20 eV below to 40 eV above the white line absorption. Deadtime correction, energy calibration, glitch removal, pre-edge subtraction,

and post-edge normalization were performed using a suite of custom LabVIEW programs. The XANES spectra were analyzed using the Athena suite of programs in the IFEFFIT package.[69]

Electrochemical Characterization

A three-electrode cell setup using a Bio-Logic potentiostat (SP-200) was used to measure the HER and the OER performance of the synthesized materials. For HER and OER measurements, a 0.5M aqueous solution of H_2SO_4 and 1.0M aqueous solution of KOH purged with N_2 gas were used, respectively. The as-prepared catalysts on CFP, MoS_2 powders (Sigma Aldrich, 99.0% purity, 90 nm diameter), and IrO_2 powders (Sigma Aldrich, 99.9% purity, 30 nm diameter) on CFP were used as the working electrodes. A saturated calomel electrode (SCE) and a glassy carbon electrode were used as reference and counter electrodes, respectively. For HER and OER analysis, the following relationship was used to convert the potential *versus* SCE (E_{SCE}) to the potential *versus* the reversible hydrogen electrode (RHE) (E_{RHE}): $E_{RHE} = E_{SCE} + (0.241 + 0.059 \times \text{pH})$.[17,47,49] Linear sweep voltammetry (LSV) was performed in the range between 0.0 to –0.5 V *vs.* RHE for HER and 1.0 to 2.0 *vs.* RHE for OER at a scan rate of 10 mV/s. Ohmic potential drop (iR) losses were accounted for during the measurement of polarization curve, where R is the series resistance of the electrochemical cell measured by performing electrochemical impedance spectroscopy (EIS). EIS was performed using a frequency range of 50 mHz to 200 kHz, with an ac amplitude of 25 mV at –0.15 V (*vs.* RHE in a 0.5M aqueous solution of H_2SO_4) and 1.6 V (*vs.* RHE in 1.0M aqueous solution of KOH).

Stability tests were performed using continuous cyclic voltammetry (CV) measurements within a potential range of 0 to – 0.6 V (*vs.* RHE in 0.5 M H_2SO_4) and 1.2 to 1.8 V (*vs.* RHE in 1.0 M KOH) with a scan rate of 100 mV/s for 1000 cycles. To estimate the electrochemically active surface area (ECSA), the double-layer capacitance (C_{dl}) of the samples were measured by cyclic voltammetry within a potential range of 0.1 to 0.3 V (*vs.* RHE in a 0.5M aqueous solution of H_2SO_4) and 0.3 to 0.5 V (*vs.* RHE in a 1.0M aqueous solution of KOH) at scan rates between 20 to 150 mV/s.

Computational Details

Electronic structure calculations were performed using DFT[70] as implemented in Vienna ab initio simulation package (VASP).[71,72] Generalized gradient approximation (GGA) of Perdew–Burke–Ernzerhof (PBE) functionals were used to implement electron exchange-correlation interactions.[73] Electron–ion interactions were implemented in our calculations by using the projector-augmented wave (PAW) formalism with a kinetic energy cutoff of 600 eV.[74] On-site Coulomb interactions were included by using the rotationally invariant density functional theory (DFT+*U*) formalism of Dudarev *et al.*[75] For molybdenum atoms, an on-site coulomb interaction parameter of U = 6.3 eV as suggested elsewhere in literature.[44] In calculating the density of states, a Γ-point-centered Monkhorst−Pack reciprocal grid of 2×2×2 k-points was used for first Brillouin zone sampling. A 2×2×2 k-points reciprocal grid was further used for relaxation of the structures. In order to model the interfaces, supercell structures of MoS_2 (001), $MoSe_2$ (001), and MoO_3 (010) surfaces were used. The lattice mismatch for such surfaces is less than 2%. The structures were considered to be relaxed when each Cartesian force

component was <0.1 eV/Å. To avoid interlayer interactions arising from periodic boundary conditions, the distance between the structures was kept at greater than 10Å. The cell size was kept fixed while the atoms were allowed to relax during the calculations of the structures. To accurately model the interlayer separation, van der Waals' interactions were included using the Grimme vdW-D2 approach.[76]

VI. 4. Conclusions

In summary, we have developed a concurrent sulfidation and selenization route combining sol—gel condensation with hydrothermal treatment that enables the preparation of $MoS_{2-x}Se_x/MoO_3$ heterostructures with varying chalcogenide stoichiometries integrated onto CFP. The heterostructures preserve the open framework of the CFP substrate and expose a high density of edge sites. These heterostructures show excellent electrocatalytic activity for both HER and OER as demonstrated by low overpotentials, high current densities, high turnover frequencies, and prolonged operation. $MoS_{2-x}Se_x/MoO_3$ with $x \sim 0.45$ exhibits excellent HER performance with an overpotential (η_{10}) of 0.12 V, a Tafel slope of 47.6 mV/dec, and TOF of 6.2 H_2/s per active site at –0.2 V *vs* RHE. $MoS_{2-x}Se_x/MoO_3$ with $x \sim 0.77$ exhibits excellent OER performance with an overpotential (η_{10}) of 0.28 V, a Tafel slope of 75.1 mV/dec, and TOF of 1.3 O_2/s per active site at 0.42 V *vs* RHE. The improved activity is seen to derive not from the increase in ECSA but from modulation of the intrinsic electronic structure of MoS_2 resulting from Se incorporation and hybridization with MoO_3. Se incorporation gives rise to shallow valence band states that facilitate adsorption of oxygen intermediates and reduce the overpotential for OER, whereas interfacing with MoO_3 contributes low-lying states that reduces the

effective CBM engendering facile hydrogen adsorption. The results demonstrate a systematic means of modulating crystal structure and electronic band structure to enhance electrocatalytic function.

VI.5. References

(1) Barber, J.; Tran, P. D. From Natural to Artificial Photosynthesis. *J. Royal Soc. Inter.* **2013**, *10*, 20120984.

(2) Facchetti, A. π-Conjugated Polymers for Organic Electronics and Photovoltaic Cell Applications. *Chem. Mater.* **2010**, *23*, 733-758.

(3) Green, M. A.; Ho-Baillie, A.; Snaith, H. J. The Emergence of Perovskite Solar Cells. *Nat. Photonics* **2014**, *8*, 506.

(4) Jeon, N. J.; Noh, J. H.; Yang, W. S.; Kim, Y. C.; Ryu, S.; Seo, J.; Seok, S. I. Compositional Engineering of Perovskite Materials for High-Performance Solar Cells. *Nature* **2015**, *517*, 476.

(5) Chen, X.; Mao, S. S. Titanium Dioxide Nanomaterials: Synthesis, Properties, Modifications, and Applications. *Chem. Rev.* **2007**, *107*, 2891-2959.

(6) Jaramillo, T. F.; Jørgensen, K. P.; Bonde, J.; Nielsen, J. H.; Horch, S.; Chorkendorff, I. Identification of Active Edge Sites for Electrochemical H_2 Evolution from MoS_2 Nanocatalysts. *Science* **2007**, *317*, 100-102.

(7) Li, Y.; Wang, H.; Xie, L.; Liang, Y.; Hong, G.; Dai, H. MoS_2 Nanoparticles Grown on Graphene: An Advanced Catalyst for the Hydrogen Evolution Reaction. *J. Am. Chem. Soc.* **2011**, *133*, 7296-7299.

(8) Iulianelli, A.; Liguori, S.; Wilcox, J.; Basile, A. Advances on Methane Steam Reforming to Produce Hydrogen through Membrane Reactors Technology: A Review. *Catal. Rev.* **2016**, *58*, 1-35.

(9) Graedel, T. E.; Harper, E.; Nassar, N. T.; Nuss, P.; Reck, B. K. Criticality of Metals and Metalloids. *Proc. Natl. Acad. Sci. U.S.A.* **2015**, *112*, 4257-4262.

(10) Thompson, S. T.; Wilson, A. R.; Zelenay, P.; Myers, D. J.; More, K. L.; Neyerlin, K.; Papageorgopoulos, D. ElectroCat: DOE's Approach to PGM-Free Catalyst and Electrode R&D. *Solid State Ion.* **2018**, *319*, 68-76.

(11) Mistry, H.; Varela, A. S.; Kuehl, S.; Strasser, P.; Cuenya, B. R. Nanostructured Electrocatalysts with Tunable Activity and Selectivity. *Nat. Rev. Mater.* **2016**, *1*, 16009.

(12) Bockris, J.; Ammar, I.; Huq, A. The Mechanism of the Hydrogen Evolution Reaction on Platinum, Silver and Tungsten Surfaces in Acid Solutions. *J. Phys. Chem.* **1957**, *61*, 879-886.

(13) Parsons, R. Hydrogen Evolution on Platinum Electrodes. The Heats of Activation for the Component Reactions. *Trans. Faraday Soc.* **1960**, *56*, 1340-1350.

(14) Greeley, J.; Jaramillo, T. F.; Bonde, J.; Chorkendorff, I.; Nørskov, J. K. Computational High-Throughput Screening of Electrocatalytic Materials for Hydrogen Evolution. *Nat. Mater.* **2006**, *5*, 909-913.

(15) Li, X.; Hao, X.; Abudula, A.; Guan, G. Nanostructured Catalysts for Electrochemical Water Splitting: Current State and Prospects. *J. Mater. Chem. A* **2016**, *4*, 11973-12000.

(16) Cherevko, S.; Geiger, S.; Kasian, O.; Kulyk, N.; Grote, J.-P.; Savan, A.; Shrestha, B. R.; Merzlikin, S.; Breitbach, B.; Ludwig, A. Oxygen and Hydrogen Evolution Reactions

on Ru, RuO_2, Ir, and IrO_2 Thin Film Electrodes in Acidic and Alkaline Electrolytes: A Comparative Study on Activity and Stability. *Catal. Today* **2016**, *262*, 170-180.

(17) Choi, Y.-H.; Lee, J.; Parija, A.; Cho, J.; Verkhoturov, S. V.; Al-Hashimi, M.; Fang, L.; Banerjee, S. An in Situ Sulfidation Approach for the Integration of MoS_2 Nanosheets on Carbon Fiber Paper and the Modulation of Its Electrocatalytic Activity by Interfacing with *n*C_{60}. *ACS Catal.* **2016**, *6*, 6246-6254.

(18) Parija, A.; Choi, Y.-H.; Liu, Z.; Andrews, J. L.; De Jesus, L. R.; Fakra, S. C.; Al-Hashimi, M.; Batteas, J. D.; Prendergast, D.; Banerjee, S. Mapping Catalytically Relevant Edge Electronic States of MoS_2. *ACS Cent. Sci.* **2018**, *4*, 493-503.

(19) Li, H.; Tsai, C.; Koh, A. L.; Cai, L.; Contryman, A. W.; Fragapane, A. H.; Zhao, J.; Han, H. S.; Manoharan, H. C.; Abild-Pedersen, F. Activating and Optimizing MoS_2 Basal Planes for Hydrogen Evolution through the Formation of Strained Sulphur Vacancies. *Nat. Mater.* **2016**, *15*, 48.

(20) Lin, H.; Shi, Z.; He, S.; Yu, X.; Wang, S.; Gao, Q.; Tang, Y. Heteronanowires of MoC−Mo_2C as Efficient Electrocatalysts for Hydrogen Evolution Reaction. *Chem. Sci.* **2016**, *7*, 3399-3405.

(21) Ma, F. X.; Wu, H. B.; Xia, B. Y.; Xu, C. Y.; Lou, X. W. Hierarchical β-Mo_2C Nanotubes Organized by Ultrathin Nanosheets as a Highly Efficient Electrocatalyst for Hydrogen Production. *Angew. Chem. Int. Ed.* **2015**, *127*, 15615-15619.

(22) Ma, R.; Zhou, Y.; Chen, Y.; Li, P.; Liu, Q.; Wang, J. Ultrafine Molybdenum Carbide Nanoparticles Composited with Carbon as a Highly Active Hydrogen-Evolution Electrocatalyst. *Angew. Chem. Int. Ed.* **2015**, *127*, 14936-14940.

(23) Kibsgaard, J.; Jaramillo, T. F. Molybdenum Phosphosulfide: An Active, Acid-Stable, Earth-Abundant Catalyst for the Hydrogen Evolution Reaction. *Angew. Chem. Int. Ed.* **2014**, *53*, 14433-14437.

(24) Xiao, P.; Sk, M. A.; Thia, L.; Ge, X.; Lim, R. J.; Wang, J.-Y.; Lim, K. H.; Wang, X. Molybdenum Phosphide as an Efficient Electrocatalyst for the Hydrogen Evolution Reaction. *Energy Environ. Sci.* **2014**, *7*, 2624-2629.

(25) Liu, Y.; Xiao, C.; Lyu, M.; Lin, Y.; Cai, W.; Huang, P.; Tong, W.; Zou, Y.; Xie, Y. Ultrathin Co_3S_4 Nanosheets that Synergistically Engineer Spin States and Exposed Polyhedra that Promote Water Oxidation under Neutral Conditions. *Angew. Chem. Int. Ed.* **2015**, *127*, 11383-11387.

(26) Wang, H.; Li, Z.; Li, G.; Peng, F.; Yu, H. Co_3S_4/NCNTs: A Catalyst for Oxygen Evolution Reaction. *Catal. Today* **2015**, *245*, 74-78.

(27) Ma, T. Y.; Dai, S.; Jaroniec, M.; Qiao, S. Z. Metal−Organic Framework Derived Hybrid Co_3O_4-Carbon Porous Nanowire Arrays as Reversible Oxygen Evolution Electrodes. *J. Am. Chem. Soc.* **2014**, *136*, 13925-13931.

(28) Smith, R. D.; Prévot, M. S.; Fagan, R. D.; Zhang, Z.; Sedach, P. A.; Siu, M. K. J.; Trudel, S.; Berlinguette, C. P. Photochemical Route for Accessing Amorphous Metal Oxide Materials for Water Oxidation Catalysis. *Science* **2013**, *340*, 60-63.

(29) Ouyang, C.; Wang, X.; Wang, C.; Zhang, X.; Wu, J.; Ma, Z.; Dou, S.; Wang, S. Hierarchically Porous Ni_3S_2 Nanorod Array Foam as Highly Efficient Electrocatalyst for Hydrogen Evolution Reaction and Oxygen Evolution Reaction. *Electrochim. Acta* **2015**, *174*, 297-301.

(30) Feng, L.-L.; Yu, G.; Wu, Y.; Li, G.-D.; Li, H.; Sun, Y.; Asefa, T.; Chen, W.; Zou, X. High-Index Faceted Ni_3S_2 Nanosheet Arrays as Highly Active and Ultrastable Electrocatalysts for Water Splitting. *J. Am. Chem. Soc.* **2015**, *137*, 14023-14026.

(31) Morales-Guio, C. G.; Stern, L.-A.; Hu, X. Nanostructured Hydrotreating Catalysts for Electrochemical Hydrogen Evolution. *Chem. Soc. Rev.* **2014**, *43*, 6555-6569.

(32) Hinnemann, B.; Moses, P. G.; Bonde, J.; Jørgensen, K. P.; Nielsen, J. H.; Horch, S.; Chorkendorff, I.; Nørskov, J. K. Biomimetic Hydrogen Evolution: MoS_2 Nanoparticles as Catalyst for Hydrogen Evolution. *J. Am. Chem. Soc.* **2005**, *127*, 5308-5309.

(33) Zheng, X.; Xu, J.; Yan, K.; Wang, H.; Wang, Z.; Yang, S. Space-Confined Growth of MoS_2 Nanosheets within Graphite: The Layered Hybrid of MoS_2 and Graphene as an Active Catalyst for Hydrogen Evolution Reaction. *Chem. Mater.* **2014**, *26*, 2344-2353.

(34) Yan, Y.; Ge, X.; Liu, Z.; Wang, J.-Y.; Lee, J.-M.; Wang, X. Facile Synthesis of Low Crystalline MoS_2 Nanosheet-Coated CNTs for Enhanced Hydrogen Evolution Reaction. *Nanoscale* **2013**, *5*, 7768-7771.

(35) Guo, Y.; Zhang, X.; Zhang, X.; You, T. Defect-and S-rich Ultrathin MoS_2 Nanosheet Embedded N-Doped Carbon Nanofibers for Efficient Hydrogen Evolution. *J. Mater. Chem. A* **2015**, *3*, 15927-15934.

(36) Zheng, W.; Lin, J.; Feng, W.; Xiao, K.; Qiu, Y.; Chen, X.; Liu, G.; Cao, W.; Pantelides, S. T.; Zhou, W. Patterned Growth of P-Type MoS_2 Atomic Layers Using Sol–Gel as Precursor. *Adv. Funct. Mater.* **2016**, *26*, 6371-6379.

(37) Mouri, S.; Zhang, W.; Kozawa, D.; Miyauchi, Y.; Eda, G.; Matsuda, K. Thermal Dissociation of Inter-Layer Excitons in $MoS_2/MoSe_2$ Hetero-Bilayers. *Nanoscale* **2017**, *9*, 6674-6679.

(38) Zhang, K.; Zhang, T.; Cheng, G.; Li, T.; Wang, S.; Wei, W.; Zhou, X.; Yu, W.; Sun, Y.; Wang, P. Interlayer Transition and Infrared Photodetection in Atomically Thin Type-II $MoTe_2/MoS_2$ van der Waals Heterostructures. *ACS Nano* **2016**, *10*, 3852-3858.

(39) Chiu, M.-H.; Li, M.-Y.; Zhang, W.; Hsu, W.-T.; Chang, W.-H.; Terrones, M.; Terrones, H.; Li, L.-J. Spectroscopic Signatures for Interlayer Coupling in MoS_2–WSe_2 van der Waals Stacking. *ACS Nano* **2014**, *8*, 9649-9656.

(40) Gong, Q.; Cheng, L.; Liu, C.; Zhang, M.; Feng, Q.; Ye, H.; Zeng, M.; Xie, L.; Liu, Z.; Li, Y. Ultrathin $MoS2_{(1-x)}Se_{2x}$ Alloy Nanoflakes for Electrocatalytic Hydrogen Evolution Reaction. *ACS Catal.* **2015**, *5*, 2213-2219.

(41) Kiran, V.; Mukherjee, D.; Jenjeti, R. N.; Sampath, S. Active Guests in the $MoS_2/MoSe_2$ Host Lattice: Efficient Hydrogen Evolution Using Few-Layer Alloys of $MoS_{2(1-x)}Se_{2x}$. *Nanoscale* **2014**, *6*, 12856-12863.

(42) Ren, X.; Ma, Q.; Fan, H.; Pang, L.; Zhang, Y.; Yao, Y.; Ren, X.; Liu, S. A Se-Doped MoS_2 Nanosheet for Improved Hydrogen Evolution Reaction. *Chem. Commun.* **2015**, *51*, 15997-16000.

(43) Cao, P.; Peng, J.; Liu, S.; Cui, Y.; Hu, Y.; Chen, B.; Li, J.; Zhai, M. Tuning the Composition and Structure of Amorphous Molybdenum Sulfide/Carbon Black Nanocomposites by Radiation Technique for Highly Efficient Hydrogen Evolution. *Sci. Rep.* **2017**, *7*, 16048.

(44) Li, H.; Yu, K.; Tang, Z.; Fu, H.; Zhu, Z. High Photocatalytic Performance of a Type-II α-MoO_3@MoS_2 Heterojunction: From Theory to Experiment. *Phys. Chem. Chem. Phys.* **2016**, *18*, 14074-14085.

(45) Lin, Y.-C.; Zhang, W.; Huang, J.-K.; Liu, K.-K.; Lee, Y.-H.; Liang, C.-T.; Chu, C.-W.; Li, L.-J. Wafer-Scale MoS_2 Thin Layers Prepared by MoO_3 Sulfurization. *Nanoscale* **2012**, *4*, 6637-6641.

(46) Song, S. H.; Kim, B. H.; Choe, D. H.; Kim, J.; Kim, D. C.; Lee, D. J.; Kim, J. M.; Chang, K. J.; Jeon, S. Bandgap Widening of Phase Quilted, 2D MoS_2 by Oxidative Intercalation. *Adv. Mater.* **2015**, *27*, 3152-3158.

(47) Choi, Y.-H.; Cho, J.; Lunsford, A. M.; Al-Hashimi, M.; Fang, L.; Banerjee, S. Mapping the Electrocatalytic Activity of MoS_2 across its Amorphous to Crystalline Transition. *J. Mater. Chem. A* **2017**, *5*, 5129-5141.

(48) Gao, Y.; Mi, L.; Wei, W.; Cui, S.; Zheng, Z.; Hou, H.; Chen, W. Double Metal Ions Synergistic Effect in Hierarchical Multiple Sulfide Microflowers for Enhanced Supercapacitor Performance. *ACS Appl. Mater. Inter.* **2015**, *7*, 4311-4319.

(49) Guo, Y.; Tang, J.; Qian, H.; Wang, Z.; Yamauchi, Y. One-Pot Synthesis of Zeolitic Imidazolate Framework 67-Derived Hollow Co_3S_4@MoS_2 Heterostructures as Efficient Bifunctional Catalysts. *Chem. Mater.* **2017**, *29*, 5566-5573.

(50) Jalilehvand, F. Sulfur: Not a "Silent" Element Any More. *Chem. Soc. Rev.* **2006**, *35*, 1256-1268.

(51) Patridge, C. J.; Whittaker, L.; Ravel, B.; Banerjee, S. Elucidating the Influence of Local Structure Perturbations on the Metal–Insulator Transitions of $V_{1-x}Mo_xO_2$

Nanowires: Mechanistic Insights from an X-ray Absorption Spectroscopy Study. *J. Phys. Chem. C* **2012**, *116*, 3728-3736.

(52) Itthibenchapong, V.; Ratanatawanate, C.; Oura, M.; Faungnawakij, K. A Facile and Low-Cost Synthesis of MoS_2 for Hydrodeoxygenation of Phenol. *Catal. Commun.* **2015**, *68*, 31-35.

(53) Tian, L.-J.; Peng, Y.; Chen, D.-L.; Ma, J.-Y.; Yu, H.-Q.; Li, W.-W. Spectral Insights into the Transformation and Distribution of CdSe Quantum Dots in Microorganisms during Food-Chain Transport. *Sci. Rep.* **2017**, *7*, 4370.

(54) Gao, D.; Xia, B.; Zhu, C.; Du, Y.; Xi, P.; Xue, D.; Ding, J.; Wang, J. Activation of the $MoSe_2$ Basal Plane and Se-Edge by B Doping for Enhanced Hydrogen Evolution. *J. Mater. Chem. A* **2018**, *6*, 510-515.

(55) Anjum, M. A. R.; Jeong, H. Y.; Lee, M. H.; Shin, H. S.; Lee, J. S. Efficient Hydrogen Evolution Reaction Catalysis in Alkaline Media by All-in-One MoS_2 with Multifunctional Active Sites. *Adv. Mater.* **2018**, *30*, 1707105.

(56) Helm, M. L.; Stewart, M. P.; Bullock, R. M.; DuBois, M. R.; DuBois, D. L. A Synthetic Nickel Electrocatalyst with a Turnover Frequency above 100,000 s^{-1} for H_2 Production. *Science* **2011**, *333*, 863-866.

(57) Mohanty, B.; Ghorbani-Asl, M.; Kretschmer, S.; Ghosh, A.; Guha, P.; Panda, S. K.; Jena, B.; Krasheninnikov, A. V.; Jena, B. K. MoS_2 Quantum Dots as Efficient Catalyst Materials for the Oxygen Evolution Reaction. *ACS Catal.* **2018**, *8*, 1683-1689.

(58) Shao, M.; Chang, Q.; Dodelet, J.-P.; Chenitz, R. Recent Advances in Electrocatalysts for Oxygen Reduction Reaction. *Chem. Rev.* **2016**, *116*, 3594-3657.

(59) Suntivich, J.; Gasteiger, H. A.; Yabuuchi, N.; Nakanishi, H.; Goodenough, J. B.; Shao-Horn, Y. Design Principles for Oxygen-Reduction Activity on Perovskite Oxide Catalysts for Fuel Cells and Metal–Air Batteries. *Nat. Chem.* **2011**, *3*, 546.

(60) Lima, F.; Zhang, J.; Shao, M.; Sasaki, K.; Vukmirovic, M.; Ticianelli, E.; Adzic, R. Catalytic Activity− d-Band Center Correlation for the O_2 Reduction Reaction on Platinum in Alkaline Solutions. *J. Phys. Chem. C* **2007**, *111*, 404-410.

(61) Cho, J.; Sheng, A.; Suwandaratne, N.; Wangoh, L.; Andrews, J. L.; Zhang, P.; Piper, L. F.; Watson, D. F.; Banerjee, S. The Middle Road Less Taken: Electronic-Structure-Inspired Design of Hybrid Photocatalytic Platforms for Solar Fuel Generation. *Acc. Chem. Res.* **2018**, *52*, 645-655.

(62) Wu, J.; Yadav, R. M.; Liu, M.; Sharma, P. P.; Tiwary, C. S.; Ma, L.; Zou, X.; Zhou, X.-D.; Yakobson, B. I.; Lou, J. Achieving Highly Efficient, Selective, and Stable CO_2 Reduction on Nitrogen-Doped Carbon Nanotubes. *ACS Nano* **2015**, *9*, 5364-5371.

(63) Liu, Y.; Wu, J.; Hackenberg, K. P.; Zhang, J.; Wang, Y. M.; Yang, Y.; Keyshar, K.; Gu, J.; Ogitsu, T.; Vajtai, R. Self-Optimizing, Highly Surface-Active Layered Metal Dichalcogenide Catalysts for Hydrogen Evolution. *Nat. Energy* **2017**, *2*, 17127.

(64) Akbashev, A.; Zhang, L.; Mefford, J.; Park, J.; Butz, B.; Luftman, H.; Chueh, W.; Vojvodic, A. Activation of Ultrathin $SrTiO_3$ with Subsurface $SrRuO_3$ for the Oxygen Evolution Reaction. *Energy Environ. Sci.* **2018**, *11*, 1762-1769.

(65) Andrews, J. L.; Cho, J.; Wangoh, L.; Suwandaratne, N.; Sheng, A.; Chauhan, S.; Nieto, K.; Mohr, A.; Kadassery, K. J.; Popeil, M. R.; Thakur, P. K.; Sfeir, M.; Lacy, D. C.; Lee, T.-L.; Zhang, P.; Watson, D. F.; Piper, L. F. J.; Banerjee, S. Hole Extraction by

Design in Photocatalytic Architectures Interfacing CdSe Quantum Dots with Topochemically Stabilized Tin Vanadium Oxide. *J. Am. Chem. Soc.* **2018**, *140*, 17163-17174.

(66) Swesi, A. T.; Masud, J.; Liyanage, W. P.; Umapathi, S.; Bohannan, E.; Medvedeva, J.; Nath, M. Textured $NiSe_2$ Film: Bifunctional Electrocatalyst for Full Water Splitting at Remarkably Low Overpotential with High Energy Efficiency. *Sci. Rep.* **2017**, *7*, 2401.

(67) Pelcher, K. E.; Milleville, C. C.; Wangoh, L.; Cho, J.; Sheng, A.; Chauhan, S.; Sfeir, M. Y.; Piper, L. F.; Watson, D. F.; Banerjee, S. Programming Interfacial Energetic Offsets and Charge Transfer in β-$Pb_{0.33}V_2O_5$/Quantum-Dot Heterostructures: Tuning Valence-Band Edges to Overlap with Midgap States. *J. Phys. Chem. C* **2016**, *120*, 28992-29001.

(68) McEvoy, T. M.; Stevenson, K. J. Electrochemical Quartz Crystal Microbalance Study of the Electrodeposition Mechanism of Molybdenum Oxide Thin Films from Peroxo-Polymolybdate Solution. *Anal. Chim. Acta* **2003**, *496*, 39-51.

(69) Ravel, B.; Newville, M. ATHENA, ARTEMIS, HEPHAESTUS: Data Analysis for X-ray Absorption Spectroscopy using IFEFFIT. *J. Synchrotron Rad.* **2005**, *12*, 537-541.

(70) Kohn, W.; Sham, L. J. Self-Consistent Equations Including Exchange and Correlation Effects. *Phys. Rev.* **1965**, *140*, A1133-A1138.

(71) Kresse, G.; Hafner, J. Ab Initio Molecular Dynamics for Liquid Metals. *Phys. Rev. B* **1993**, *47*, 558.

(72) Kresse, G.; Furthmüller, J. Efficiency of *Ab-Initio* Total Energy Calculations for Metals and Semiconductors Using a Plane-Wave Basis Set. *Comput. Mater. Sci.* **1996**, *6*, 15-50.

(73) Perdew, J. P.; Burke, K.; Ernzerhof, M. Generalized Gradient Approximation Made Simple. *Phys. Rev. Lett.* **1996**, *77*, 3865.

(74) Kresse, G.; Joubert, D. From Ultrasoft Pseudopotentials to the Projector Augmented-Wave Method. *Phys. Rev. B* **1999**, *59*, 1758−1775.

(75) Dudarev, S.; Botton, G.; Savrasov, S.; Humphreys, C.; Sutton, A. Electron-Energy-Loss Spectra and the Structural Stability of Nickel Oxide: An LSDA+U Study. *Phys. Rev. B* **1998**, *57*, 1505−1509.

(76) Grimme, S. Accurate Description of van der Waals Complexes by Density Functional Theory including Empirical Corrections. *J. Comput. Chem.* **2004**, *25*, 1463-1473.

CHAPTER VII

DISSERTATION SUMMARY AND OUTLOOK

VII. 1 Conclusions

Chapter I highlights several aspects of a richly diverse emerging area of the chemical sciences, periodic solids away from equilibrium. A fundamental thesis underpinning the exploration of metastability is that composition does not result in structural destiny–that structure can be controlled independently from composition. Metastable phase space thus holds opportunities for unprecedented tuning of properties and functionality based on the exploration of multiple structural variations for the same composition. Improved understanding of metastability will enable a fundamental re-evaluation of canonical chemical concepts such as allowed and preferred oxidation states, coordination geometries, and the nature of chemical bonding, many of which are thus far informed greatly by equilibrium ideas.

Several of the governing principles and synthetic strategies underpinning stabilization of metastable compounds have been outlined, emphasizing the need to traverse energy landscapes with synthetic methods that can carefully deposit materials within local minima or transformation pathways that take materials across specific trajectories. Dopants, defects, interfaces, dimensional confinement, and strain/pressure can modify the landscapes and trajectories and thus facilitate stabilization of metastable polymorphs. Topochemical modification, dimensional confinement (typically to sub-10 nm dimensions), pressure (mechanical or chemical), and templated methods can provide

access to wide range of metastable polymorphs with an abiding guiding principle being the stabilization of a compound under a constraint (temperature, pressure, chemical potential), where it represents the most energetically stable species, followed by the removal of the constraint to "trap" the material under ambient conditions.[1] What is urgently required is a clear framework for the predictive design, synthesis, and evaluation of the properties of metastable compounds. Such a framework requires addressing issues spanning the range from predictive design rules for identifying viable metastable polymorphs to a toolset of synthetic methods for preparing such structures, a clear understanding of the relative positioning of polymorphs along energy landscapes, and a fundamental understanding of chemical bonding and structural motifs that result in excursions away from the thermodynamic minimum. The stabilization of an expanded palette of V_2O_5 polymorphs provides illustrative examples of both synthetic strategies as well as mechanistic elucidation of transformations and unprecedented functionality.[2-5] Novel metastable polymorphs have enabled unprecedented function inaccessible within thermodynamic minima such as promising reversible intercalation of Mg-ions (ζ-V_2O_5),[4] and efficient metal-insulator transitions in β'-$Cu_xV_2O_5$.[6,7]

Chapter II contrasts the thermodynamics and kinetics of the insertion of Li, Na, Mg, and Al ions in two synthetically accessible metastable phases of V_2O_5, ζ- and ε-V_2O_5, with the relevant parameters for the thermodynamically stable α-phase of V_2O_5 using density functional theory calculations. The metastability of the frameworks results in a higher open circuit voltage for multivalent ions, exceeding 3 V for Mg-ion intercalation. Multivalent ions inserted within these structures encounter suboptimal coordination

environments and expanded transition states, which facilitate easier ion diffusion. Specifically, a nudged elastic band examination of ion diffusion pathways suggests that migration barriers are substantially diminished for Na- and Mg-ion diffusion in the metastable polymorphs. More generally, the results indicate that topochemically derived metastable polymorphs represent an interesting class of compounds for realizing multivalent cation diffusion because many such compounds place cations in "frustrated" coordination environments that are known to be useful for realizing low diffusion barriers.

Supplementing the above result **Chapter III**, explores multivalent cation insertion in three metastable polymorphs, γ′, δ′, and ρ′ phases of V_2O_5, using density functional theory calculations. The calculations allow for evaluation of the influence of distinctive structural motifs in mediating multivalent cation insertion. In particular, we contrasted the influence of single versus condensed double layers, planar versus puckered single layers, and the specific stacking sequence of the double layers. The study demonstrates that metastable phases offer some specific advantages with respect to thermodynamically stable polymorphs in terms of a higher chemical potential difference (giving rise to a larger open-circuit voltage) and in providing access to diffusion pathways that are highly dependent on the specific structural motif. The three polymorphs are found to be especially promising for Ca-ion intercalation, which is particularly significant given the exceedingly sparse number of viable cathode materials for this chemistry. The findings here demonstrate the ability to define cation diffusion pathways within layered metastable polymorphs by alteration of the stacking sequence or the thickness of the layers. Future work will focus on stabilization of these polymorphs through topochemical methods and

examination of chemical and electrochemical insertion of monovalent and multivalent cations. Expanding this palette of compounds will allow for systematic delineation of the correlation between specific structural motifs and the covalency, extent of electron correlation, and charge delocalization.

Chapter IV demonstrates that metastable β′-$Cu_xV_2O_5$ exhibits a metal-insulator transition with a critical temperature that is extremely sensitive to the copper stoichiometry, *x*.[6,7] The β/β′ phase is a quasi-1D tunnel structure in which the metal cation, in this case, Cu (I) resides within the tunnel and partially reduces specific V^{5+} sites in the V_2O_5 framework to V^{4+}, resulting in charge-ordered framework. Synchrotron powder X-ray diffraction and variable-temperature single-crystal X-ray diffraction, X-ray absorption and emission spectroscopy, temperature-dependent photoemission spectroscopy, and first-principles density functional theory calculations have been used to probe the mechanistic underpinnings of the metal-insulator transition. We find that melting of a charge-ordered state because of a subtle ionic rearrangement in the position of the copper ions results in the delocalization of the electrons in the charge ordered network, ultimately manifesting in metallic behavior. Insights into the structural and electronic properties underpinning this transition obtained during this study will allow for rational tuning of transition temperature and magnitude (by changing *x*). Ongoing work is focused on establishing independent control of transformation characteristics through compositional modification and on examining voltage-induced metal—insulator transitions in these materials.

Chapter V examines the specific edge sites of MoS_2 underpinning electro-catalytic function in the hydrogen evolution reaction. Using a combination of first-principles calculations, X-ray absorption spectroscopy, as well as scanning transmission X-ray microscopy (STXM) imaging, we find that edge corrugations yield distinctive spectroscopic signatures corresponding to increased localization of hybrid Mo 4d states. Independent spectroscopic signatures of such edge states were identified in both S $L_{2,3}$ and S K-edge X-ray absorption spectra; distinctive spatial localization of such states was observed in S $L_{2,3}$-edge STXM imaging. The presence of such low-energy hybrid states at the edge of the conduction band was further seen to correlate with substantially enhanced electrocatalytic activity in terms of a lower Tafel slope and higher exchange current density. These results illuminate the nature of the edge electronic structure and provide a clear framework for its rational manipulation to enhance catalytic activity. Ongoing work is focused on selective ligand modification of edge sites to explore the influence of inductive and steric effects as well as second sphere effects on catalytic function.

Supplementing the above effort, **Chapter VI** demonstrates modification of the electronic structure of MoS_2 by incorporation of Se as a substitutional dopant for greatly enhanced catalytic activity. Selenium doping onto S sites and interfacial modification of MoS_2 by MoO_3 yields an effective bifunctional catalyst for H_2 and O_2 generation. We have synthesized core-shell hierarchical nanostructures of interfacial $MoSe_2$ or selenium-doped MoS_2 on MoO_3 with high-edge-density for enhanced water splitting. These heterostructures show high catalytic activity in terms of low overpotential, high current, high turnover frequency, and durability for both hydrogen and oxygen evolution. Further,

using detailed spectroscopic studies and electronic structure calculations we have unraveled the mechanistic origins of the observed enhancement in catalytic activity resulting from interfacial charge transfer and Fermi engineering. DFT calculations suggest an increased valance band maximum (VBM), decreased conduction band minimum (CBM), and decreased bandgap for Se-doped motifs ($MoS_xSe_yO_z$), Se-interfaced motifs ($MoSe_2/MoS_2/MoO_3$), or combinations of doping and interfacial modification (MoS_xSe_y/MoO_3), which ultimately yields superior HER and OER performance. Ongoing work is focused on designing specific edge site modification methods to enhance catalytic activity as well as on *operando* X-ray spectroscopy studies of the electrocatalysts.

In summary, the close integration of theory and experiment is imperative to transcend longstanding chemical bottlenecks in the prediction, rationalization, and realization of new chemical compounds outside of global thermodynamic minima. Efficient computational mapping of energy landscapes requires the development of reliable sampling and interpolation methods and further must be benchmarked to experimental observations of changes in the atomistic and geometric structure underpinning transformations between polymorphs. The spatial and temporal resolution to study such phase transformations is now accessible based on methods such as HAADF STEM imaging, dynamical TEM imaging, high resolution STXM, ptychography, *in situ* EXAFS, and X-ray absorption spectroscopy measurements. The predictive design of metastable structures will further provide new opportunities for emergent function in areas such as catalysis, computing and energy storage that most often require function under conditions far from equilibrium.

VII.2. References

(1) Sun, W.; Dacek, S. T.; Ong, S. P.; Hautier, G.; Jain, A.; Richards, W. D.; Gamst, A. C.; Persson, K. A.; Ceder, G. The Thermodynamic Scale of Inorganic Crystalline Metastability. *Sci. Adv.* **2016**, *2*, e1600225.

(2) Waetzig, G. R.; Horrocks, G. A.; Jude, J. W.; Zuin, L.; Banerjee, S. X-ray Excited Photoluminescence near the Giant Resonance in Solid-Solution $Gd_{1-x}Tb_xOCl$ Nanocrystals and their Retention upon Solvothermal Topotactic Transformation to $Gd_{1-x}Tb_xF_3$. *Nanoscale* **2016**, *8*, 979-986.

(3) Hudak, B. M.; Depner, S. W.; Waetzig, G. R.; Talapatra, A.; Arroyave, R.; Banerjee, S.; Guiton, B. S. Real-Time Atomistic Observation of Structural Phase Transformations in Individual Hafnia Nanorods. *Nat. Commun.* **2017**, *8*, 15316.

(4) Andrews, J. L.; Mukherjee, A.; Yoo, H. D.; Parija, A.; Marley, P. M.; Fakra, S.; Prendergast, D.; Cabana, J.; Klie, R. F.; Banerjee, S. Reversible Mg-Ion Insertion in a Metastable One-Dimensional Polymorph of V_2O_5. *Chem* **2018**, *4*, 564-585.

(5) Parija, A.; Liang, Y.; Andrews, J. L.; De Jesus, L. R.; Prendergast, D.; Banerjee, S. Topochemically De-Intercalated Phases of V_2O_5 as Cathode Materials for Multivalent Intercalation Batteries: A First-Principles Evaluation. *Chem. Mater.* **2016**, *28*, 5611-5620.

(6) Patridge, C. J.; Wu, T.-L.; Sambandamurthy, G.; Banerjee, S. Colossal Above-Room-Temperature Metal–Insulator Switching of a Wadsley-Type Tunnel Bronze. *Chem. Commun.* **2011**, *47*, 4484-4486.

(7) Patridge, C. J.; Jaye, C.; Zhang, H.; Marschilok, A. C.; Fischer, D. A.; Takeuchi, E. S.; Banerjee, S., Synthesis, Structural Characterization, and Electronic Structure of Single-Crystalline $Cu_xV_2O_5$ Nanowires. *Inorg. Chem.* **2009,** *48,* 3145-3152.

APPENDIX A

SUPPLEMENTARY FIGURES AND TABLES

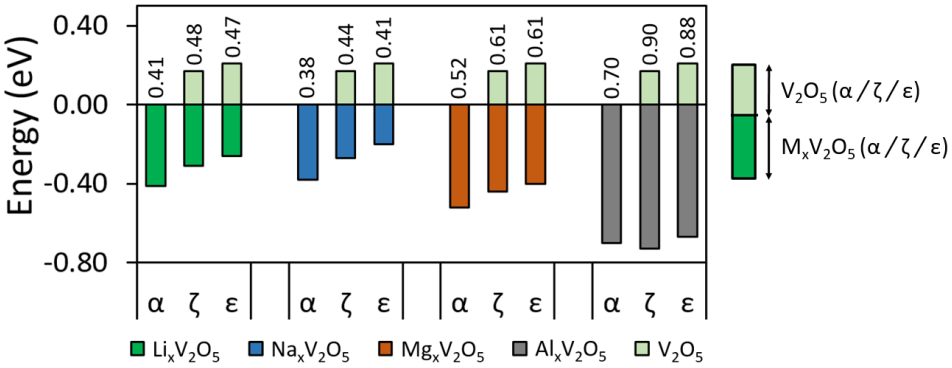

Figure A1. The relative energies of cation-intercalated polymorphs of V_2O_5 (in eV) are contrasted to the energy of α-V_2O_5. The energies in light green indicate the instability of the pristine metastable phases (ζ and ε-V_2O_5) in comparison to α-V_2O_5. The numerical sum of these two quantities, shown on the top of the bar, provides a measure of the open circuit voltage.

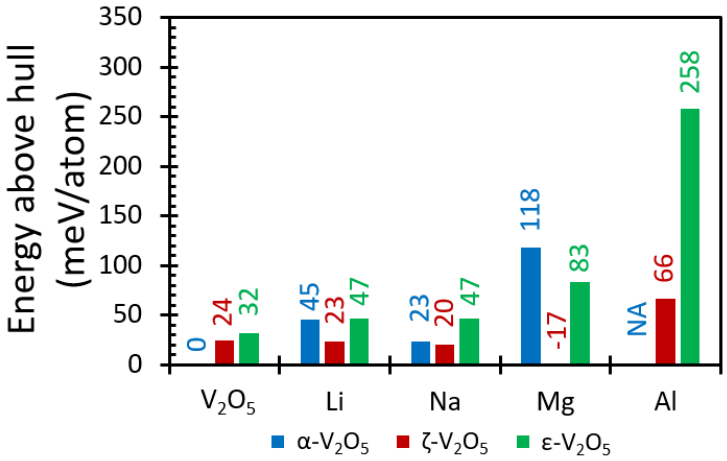

Figure A2. The energy-above-hull (E^{hull}), which quantifies the stability of the material with respect to its stable constituents at that chemical composition, in meV/atom. Note that the E^{hull} for ζ-MgV_2O_5 is 17 meV lower in energy than its stable constituents, implying that this compound represents the ground state configuration in Mg-V-O system.

The equations considered for energy (E^{hull}) calculation (Equations are obtained from https://www.materialsproject.org). All calculations have been performed using the same set of parameters across this study. A Hubbard parameter of U = 4.0 eV is used here as compared to 3.25 eV in the Materials Project database.

(1) (α-,ε-)LiV_2O_5 → γ- LiV_2O_5
ζ-$Li_2V_6O_{15}$ → γ- LiV_2O_5 + $LiVO_3$ +V_3O_7

(2) (α-,ε-)NaV_2O_5 → $NaVO_3$ + VO_2
ζ-NaV_6O_{15} → $NaVO_3$ + V_3O_7 + V_2O_5

(3) (α-,ε-)MgV_2O_5 → $MgVO_3$ + VO_2
ζ-MgV_6O_{15} → $MgVO_3$ + V_3O_7 + V_2O_5

(4) 2(ε-AlV_2O_5) → Al_2O_3 + V_3O_5 + VO_2
ζ-AlV_6O_{15} → $AlVO_4$ + V_3O_7 + 2VO_2

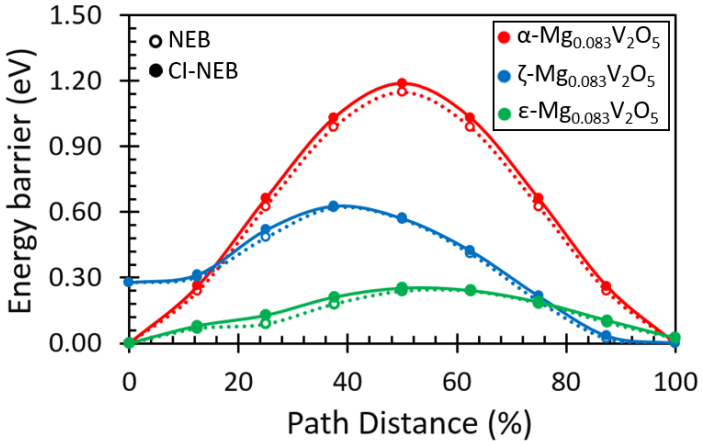

Figure A3. Comparison of the diffusion barrier calculated using two different methodologies, nudged elastic band (dotted) and climbing-image nudged elastic band (solid), for α-, ζ- and ε-$Mg_{0.083}V_2O_5$.

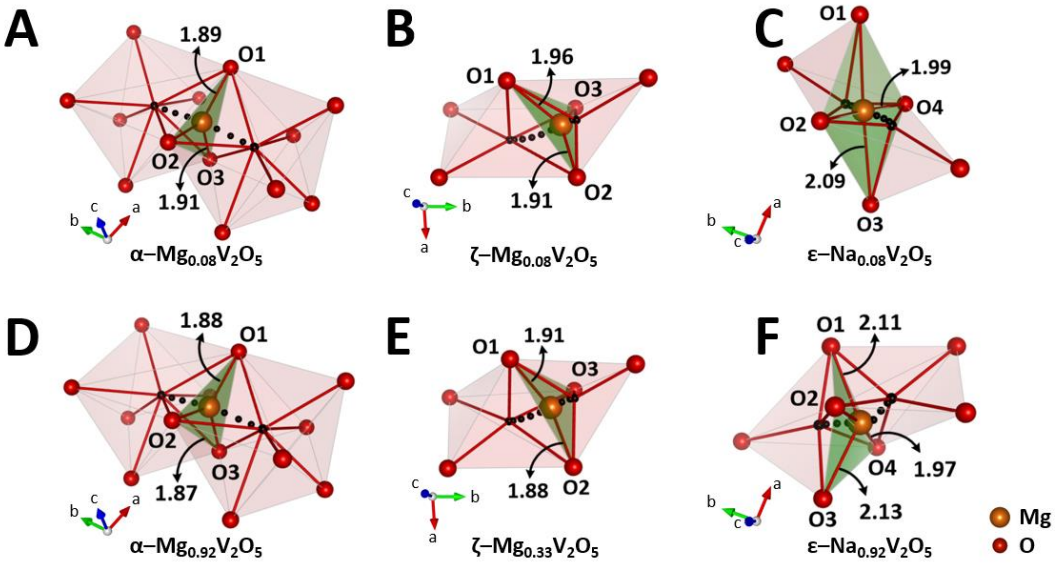

Figure A4. Comparison of the highest energy states in the diffusion pathway at low and high concentration limits in A, D) α-V_2O_5; B, E) ζ-V_2O_5; and C, F) ε-V_2O_5.

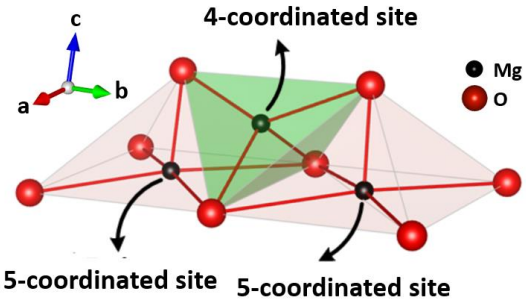

Figure A5. Illustration depicting alternating four-coordinated and five-coordinated Mg-ion sites along the energetically favored diffusion pathway of ε-$Mg_xV_2O_5$.

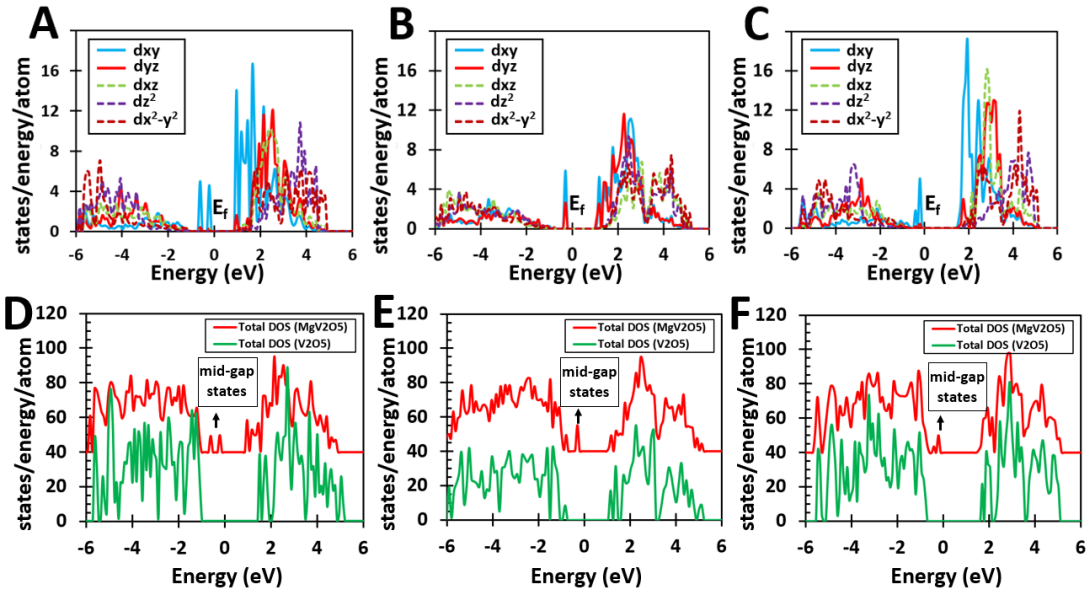

Figure A6. Orbital-projected density of states plots for vanadium 3d orbitals plotted for A) α-V_2O_5; B) ζ-V_2O_5; and C) ε-V_2O_5. The comparison of total density of states for V_2O_5 and $Mg_xV_2O_5$, showing the appearance of mid-gap states in $Mg_xV_2O_5$ are plotted for D) α-V_2O_5; E) ζ-V_2O_5; and F) ε-V_2O_5. Note in figure D, E and F the total density of states for V_2O_5 are aligned to the valence band.

Plot of difference in charge density

The difference in charge density plotted in **Figure II. 4** and **Figure A9** corresponds to the following expression,

$$\Delta\rho_{total} = \rho(Mg_xV_2O_5) - \rho(V_2O_5) - \rho(x\text{Mg})$$

where $\Delta\rho_{total}$ is the difference in charge density, $\rho(Mg_xV_2O_5)$ is the charge density of a V_2O_5 supercell with a single intercalated Mg-ion, $\rho(V_2O_5)$ is the charge density of the V_2O_5 supercell with the same structural parameters as Mg-intercalated V_2O_5 but without the magnesium ion and $\rho(x\text{Mg})$ is the charge density of Mg with same position as the Mg-ions in the final relaxed structure.

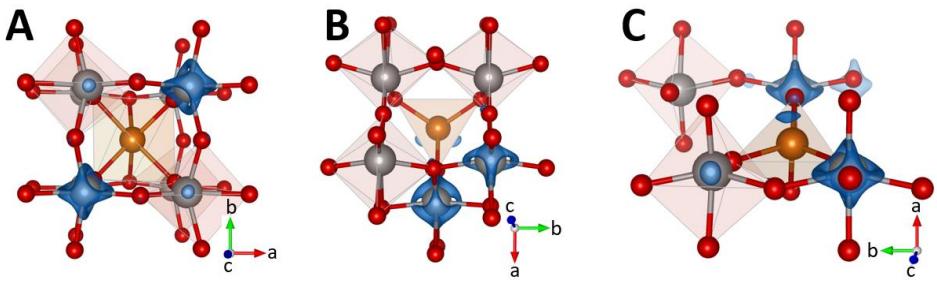

Figure A7. Decrease in charge density due to the formation of a small polaron upon the intercalation of a single Mg-ion plotted for A) α-V_2O_5; B) ζ-V_2O_5; and C) ε-V_2O_5.

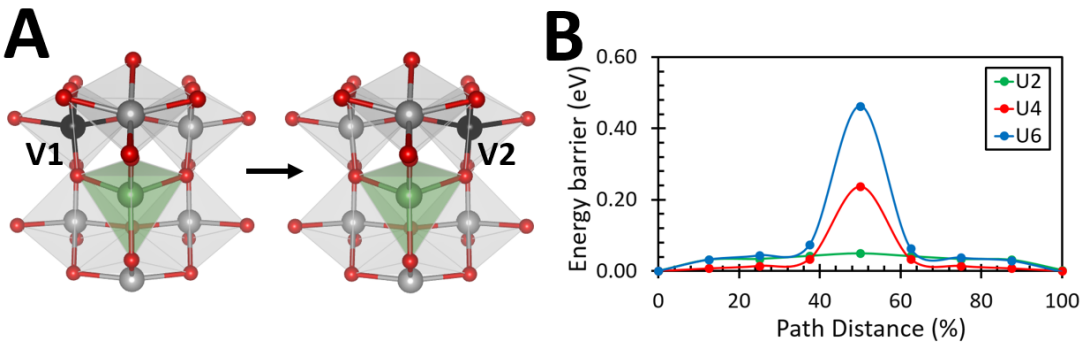

Figure A8. (A) The migration of polaron from V1 to V2 in ζ-$Li_{0.083}V_2O_5$. (B) An evaluation of the polaron diffusion barrier in ζ-$Li_{0.083}V_2O_5$ with increasing value of the Hubbard-U parameter.

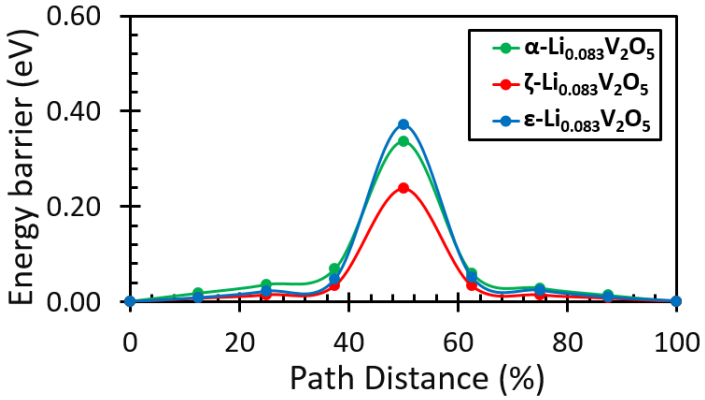

Figure A9. An evaluation of the polaron diffusion barrier in α-$Li_{0.083}V_2O_5$, ζ-$Li_{0.083}V_2O_5$, and ε-$Li_{0.083}V_2O_5$ calculated using a Hubbard-U value of 4.0 eV.

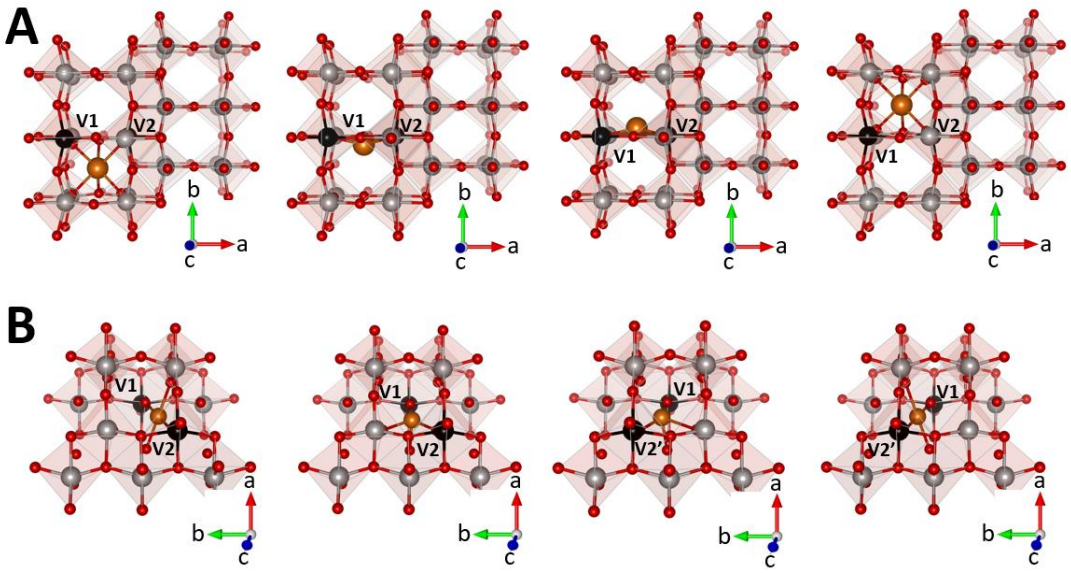

Figure A10. Coupled diffusion of an Mg-ion and a small polaron in A) α-V_2O_5 and B) ε-V_2O_5. In ε-V_2O_5, one of the small polarons diffuses from a V2 to a V2' site.

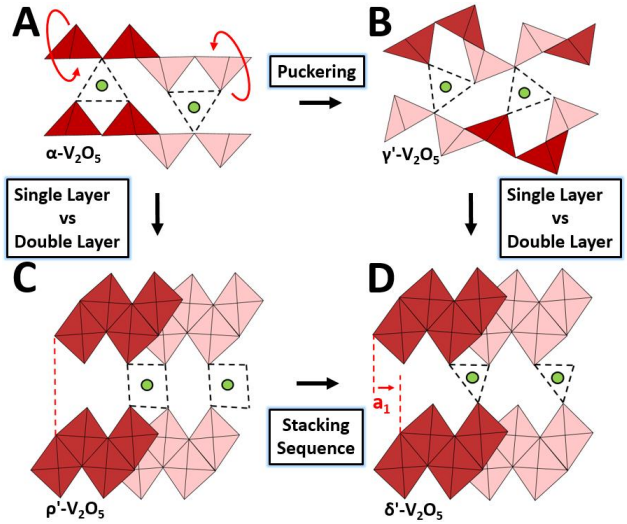

Figure A11. Depiction of crystallographic relationships between the metastable V_2O_5 polymorphs examined here. The study examines the specific role of puckering, number of layers, and the stacking sequence in influencing multivalent cation insertion.

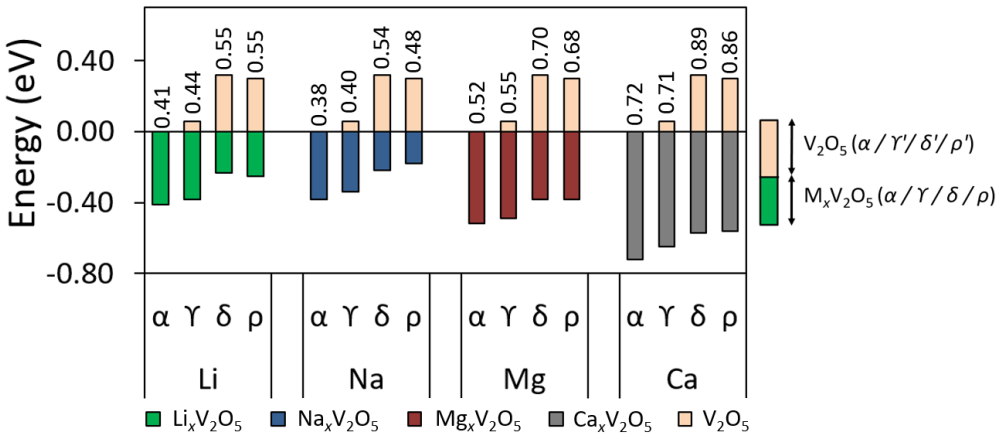

Figure A12. A comparison of the relative energies of the metastable polymorphs of V_2O_5 (in eV) with α-V_2O_5 for both the charged and discharged states. The relative instability of the metastable phases of V_2O_5 with respect to α-V_2O_5 are plotted using light orange bars. The numerical sum of these two values (shown on top of the bars) provides a measure of the open circuit voltage

Equations used for calculations of E_{hull}

The equations that are used for the calculation of E_{hull} are provided below. All calculations have been performed using the same set of parameters. A Hubbard parameter of U = 4.0 eV is used here as compared to 3.25 eV in the Materials Project database [The Materials Project Database. https://www.materialsproject.org (accessed April 14, 2017)].

(1) Li-ion Intercalation

(α–, γ–, δ–)LiV_2O_5 (s) → γ–LiV_2O_5 (s)

ρ–LiV_4O_{10} (s) → $LiVO_3$ (s) +V_3O_7 (s)

(2) Na-ion Intercalation

(α–, γ–, δ–)NaV_2O_5 (s) → $NaVO_3$ (s) + VO_2 (s)

ρ–NaV_4O_{10} (s) → NaV_3O_8 (s) + VO_2 (s)

(3) Mg-ion Intercalation

(α–, γ–, δ–)MgV_2O_5 (s) → $MgVO_3$ (s) + VO_2 (s)

ρ–$2MgV_4O_{10}$ (s) → $Mg_2V_2O_7$ (s) + V_3O_7 (s) + $3VO_2$ (s)

(4) Ca-ion Intercalation

(α–, γ–, δ–)CaV_2O_5 (s) → α–CaV_2O_5 (s)

ρ–CaV_4O_{10} (s) → CaV_2O_6 (s) + $2VO_2$ (s)

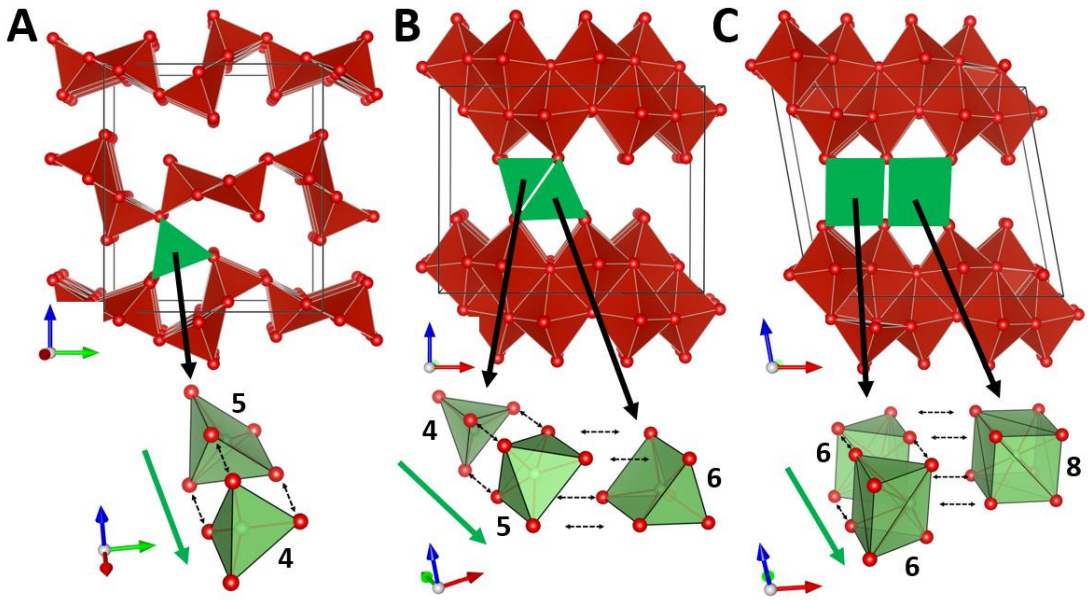

Figure A13. Potential local coordination environments accessible by cations in A) γ-$M_xV_2O_5$; B) δ-$M_xV_2O_5$; and C) ρ-$M_xV_2O_5$. A magnified view of the coordination environments is shown in the lower panel. The green arrow shows the lowest energy diffusion pathways; the numbers represent the change in coordination number along this pathway.

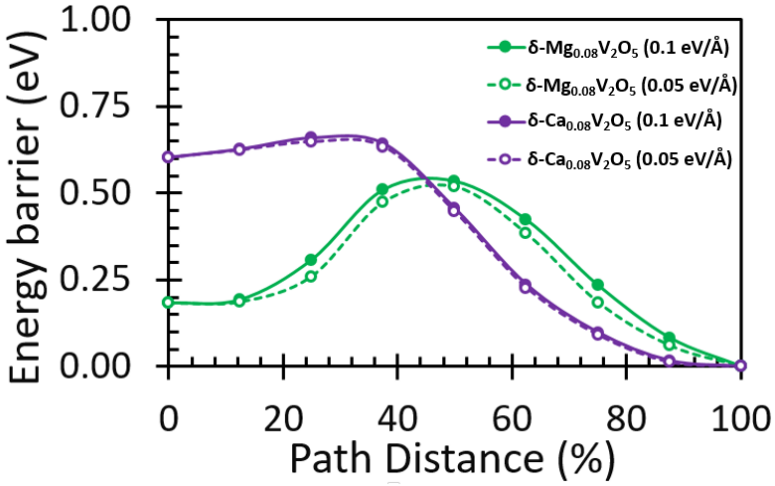

Figure A14. Difference in the diffusion barriers for Mg- and Ca-ions in δ'-V_2O_5 at NEB force threshold of 0.1 eV/Å and 0.05 eV/Å.

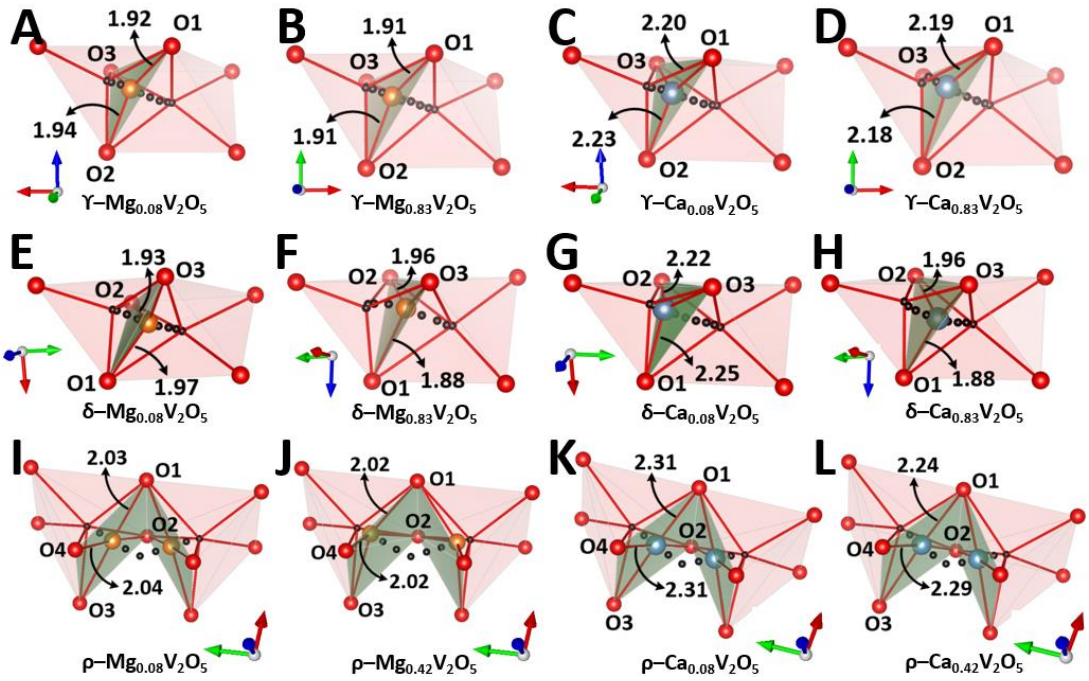

Figure A15. Comparison of the highest energy states in the diffusion pathway at low and high concentration limits of magnesium in A, B) γ'-V_2O_5; E, F) δ'-V_2O_5; and I, J) ρ'-V_2O_5 and of calcium in C, D) γ'-V_2O_5; G, H) δ'-V_2O_5; and K, L) ρ'-V_2O_5

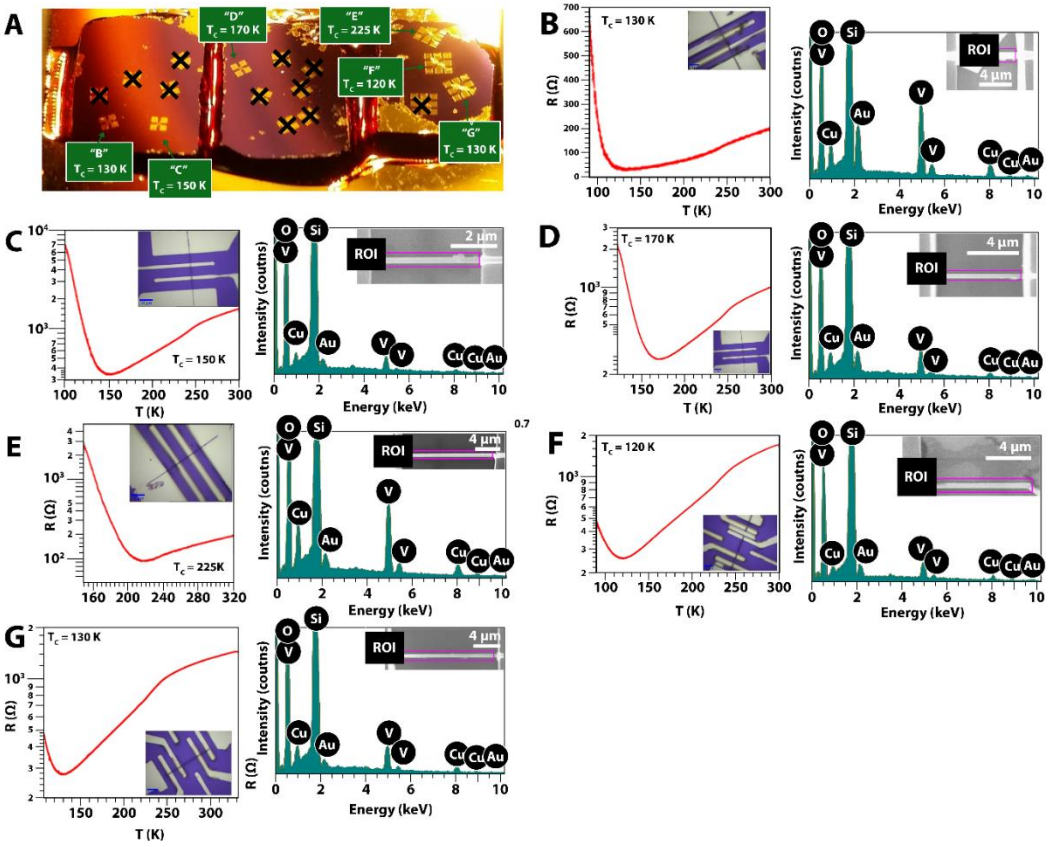

Figure A16. EDX correlation of transformation temperatures to Cu stoichiometry. **(A)** Optical image of a SiO_2/Si wafer containing several devices each fabricated from an individual β'-$Cu_xV_2O_5$ nanowire. Transport data was collected from devices delineated by green arrows. **(B-G)** Resistance versus temperature data for each of the devices marked in **(A)**. An SEM image and corresponding EDX spectrum is provided with an optical microscopy image of each device shown in the inset.

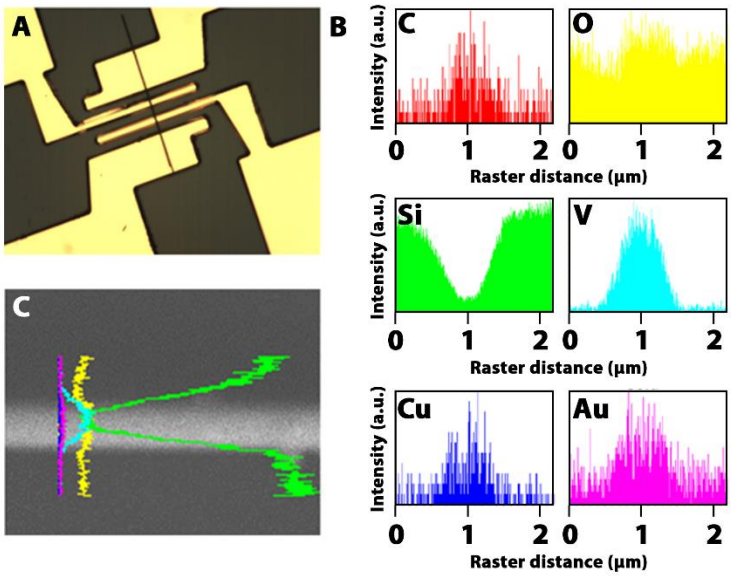

Figure A17. Example of single-nanowire EDX mapping. **(A)** Optical microscopy image of an individual nanowire device. **(B)** EDX spectra mapped for individual elements across the area indicated in **(C)**, which further shows co-localization of Cu and V signals on the nanowire. EDX spectra were collected for a series of devices using the mapping approach shown in **(B, C) (**and are plotted in **Figure A17**).

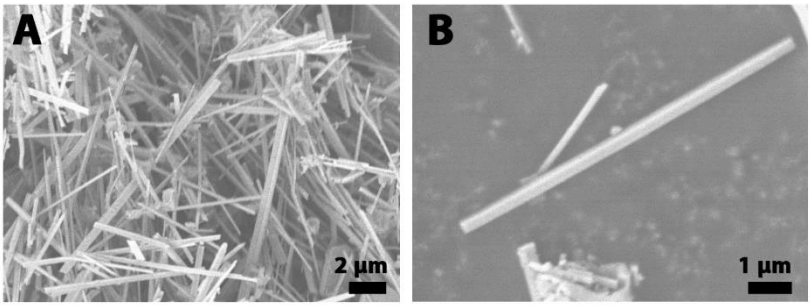

Figure A18. Characterization of β'-$Cu_xV_2O_5$ Nanowires. **(A)** SEM image of β'-$Cu_xV_2O_5$ nanowires prepared by solid-state synthesis of bulk β'-$Cu_xV_2O_5$ nanowires followed by hydrothermal treatment for 24 h. **(B)** The nanowires exhibit a rectangular cross-section.

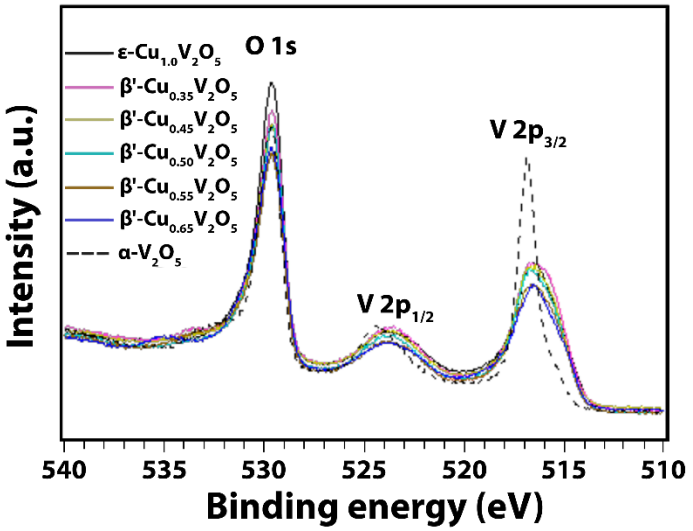

Figure A19. X-ray photoelectron spectra collected for the β'-$Cu_xV_2O_5$ (0.35<x<0.65, 1.0) nanowires. Reduction of the vanadium-oxygen framework is evidenced upon Cu-intercalation. A monotonic increase in $V^{4+}/(V^{4+}+V^{5+})$ is observed.

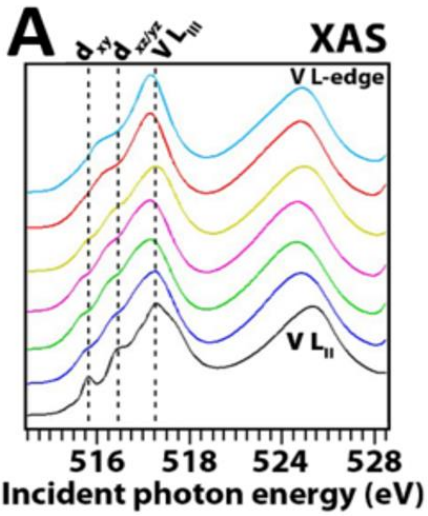

Figure A20. Electronic structure characterization of β'-$Cu_xV_2O_5$ series. **(A)** V L-edge X-ray absorption near-edge structure (XANES) spectra evidencing a concomitant reduction of the vanadium sublattice with increasing copper content. With increasing copper content, features ascribed to transitions to V $3d_{xy}$ states situated at the bottom edge of the conduction band are diminished in intensity as they become filled by electrons donated from Cu to V upon intercalation.

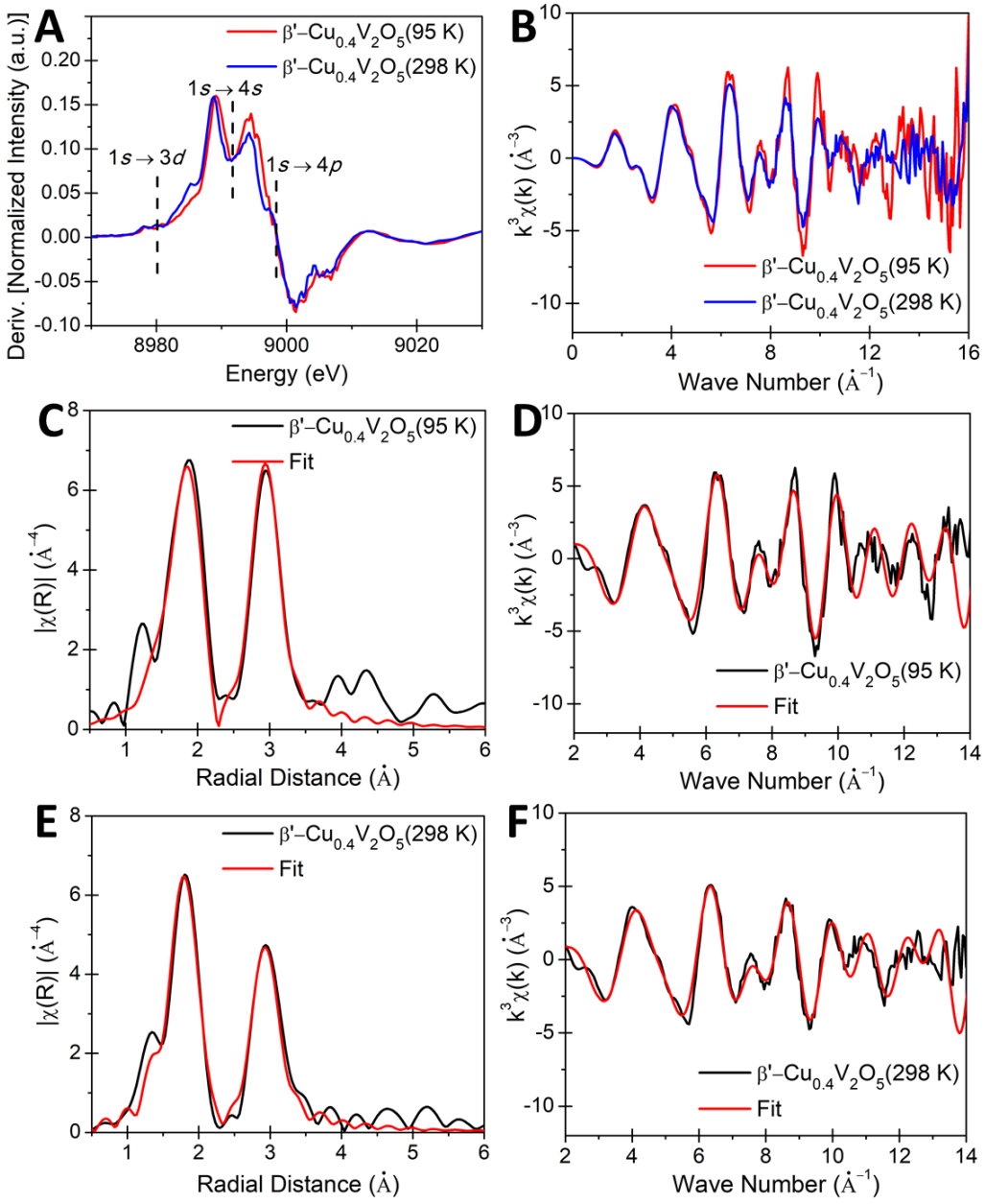

Figure A21. Fitting results of the EXAFS spectra of β'–$Cu_{0.4}V_2O_5$ at 95 K and 298 K. The first derivative of the Cu K-edge XANES spectra of β'-$Cu_{0.4}V_2O_5$ at 95 K and 298 K is shown in **(A)**. The decrease in intensity of the primary-edge (at ca. 8998.4 eV) when the sample is heated to 298K, can be attributed to the decrease of multiple scattering owing to increased thermal vibrations of the lattice and the absorbing atom, which diminishes long-range order. Comparison of the k-space EXAFS spectra at 95K and 298K is shown in **(B)**. Fitted R-space and k-space EXAFS spectra at 95K are shown in **(C**, **D)**, respectively; corresponding spectra acquired at 298K are plotted in **(E**, **F)**, respectively. A radial distance of 1.1–3.1Å is used to fit the experimental EXAFS data. The positioning of the Cu-ion at both Cu(1) and Cu(2) sites are taken into account for the fitted results.

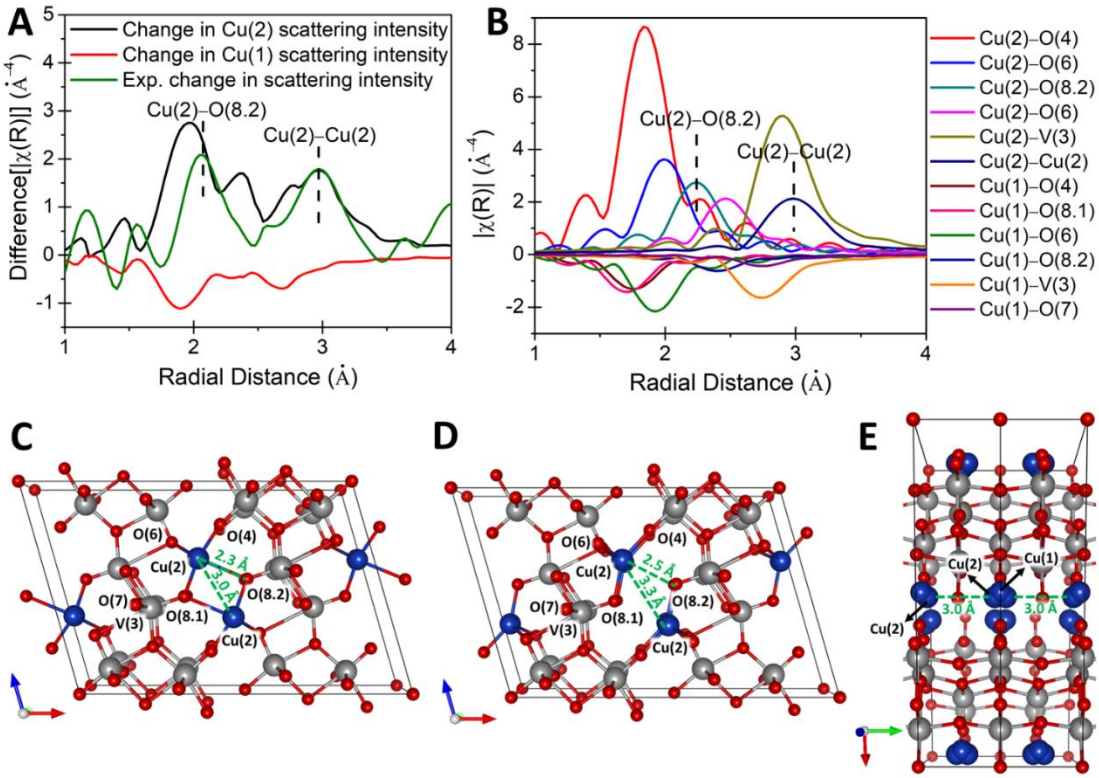

Figure A22. (A) Difference in intensity of the fitted Fourier transform spectra at 95K and 298 K. This difference spectra is further split into components originating from the Cu-ion being positioned at Cu(1) (red) and at Cu(2) sites (black). For clarity, the Cu(1) component is shown on a negative intensity scale. The corresponding difference curve for the experimental EXAFS spectra collected at 95K and 298K, which is identical to the plot shown in **Figure 2E**. **(B)** Plot of individual scattering paths for β'-$Cu_{0.6}V_2O_5$. The change in bond distances with neighboring atoms when the Cu-atom is at the Cu(2)-site in **(C)** or at the Cu(1)-site in **(D)** or at both Cu(1) and Cu(2)-sites in **(E)**. The bond distances which shows the most change are Cu(2)–O(8.2) and Cu(2)–Cu(2). After comparing the difference spectra, shown as green curve in **(A)**, with the plot of individual scattering paths in **(B)**, we infer all the scattering paths cancel each other except the Cu(2)–O(8.2) and Cu(2)–Cu(2) scattering paths.

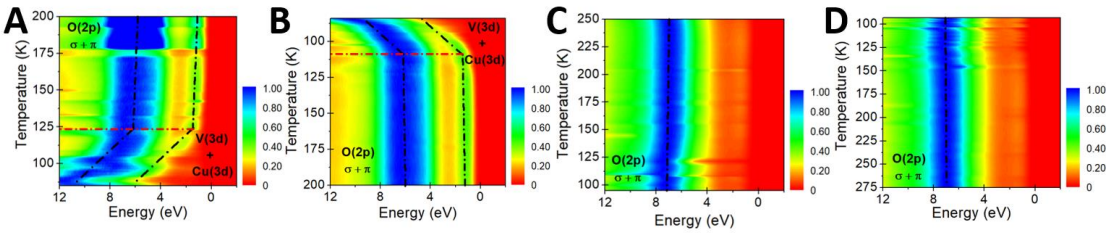

Figure A23. (A, B) Temperature-variant angle-integrated valence band photoemission spectra for β'-$Cu_{0.60}V_2O_5$, showing an abrupt energy gap opening at ca. 124K upon heating in **(A)**, and at ca. 108K during cooling in **(B)**; **(C, D)** temperature-variant angle-integrated valence band photoemission spectra for ζ-V_2O_5, indicating that the band gap remains essentially constant upon heating in **(C)** and cooling in **(D)**.

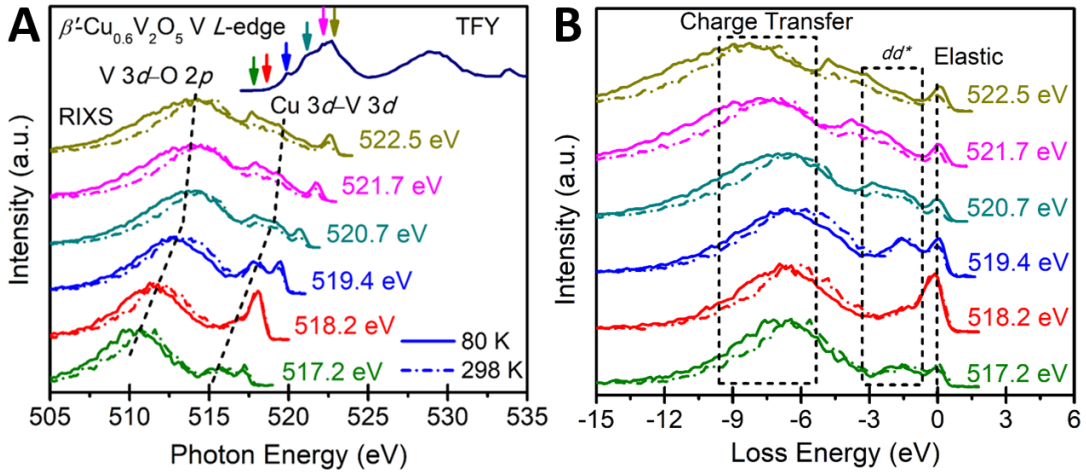

Figure A24. (A) RIXS spectra, normalized to the maximum of the CT peak, acquired at the V L_3-edge for β'-$Cu_{0.60}V_2O_5$ nanowires; the corresponding XAS (TFY) spectra is shown as a dark blue curve. The RIXS excitation energy is increased from the absorption onset to the main V L_2-edge, which is shown as colored arrows on the XAS peak and the normalized RIXS spectra for the corresponding excitation energies follow the same color pattern as the arrows; **(B)** Normalized V L_3-edge RIXS spectra displayed on the loss energy scale.

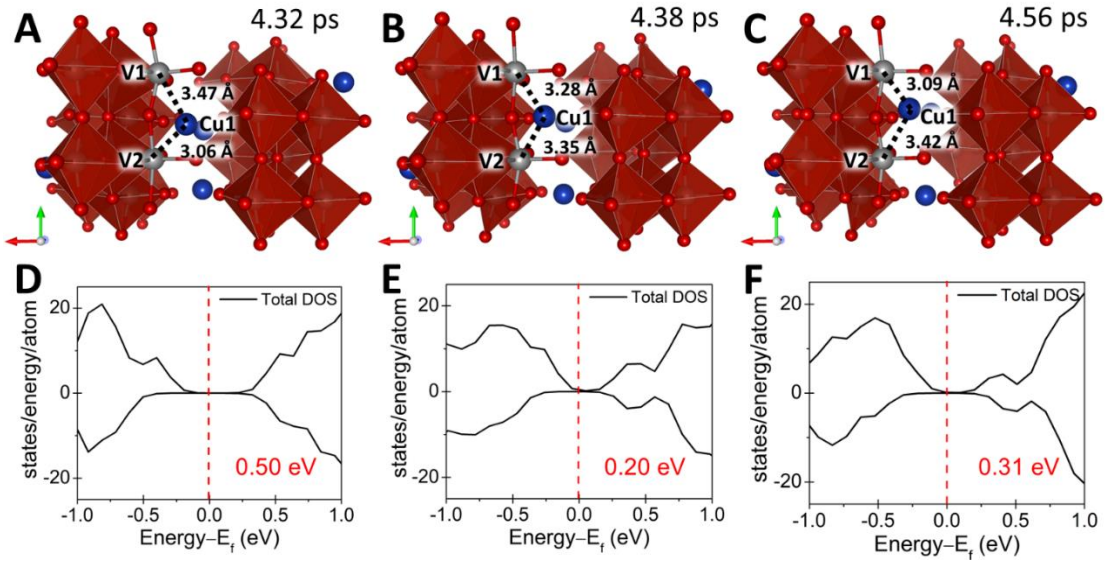

Figure A25. MD simulations of the migration of Cu-ions between the Cu(1) and the Cu(2) sites of β'-$Cu_{0.41}V_2O_5$. Snapshots of the trajectory for the diffusion of one of the Cu-ions from the Cu(2) site in **(A)**, to the Cu(1) site in **(B)**, and back again to the Cu(2) site in **(C)**. The corresponding total DOS is shown in panels **(D-F)**, respectively.

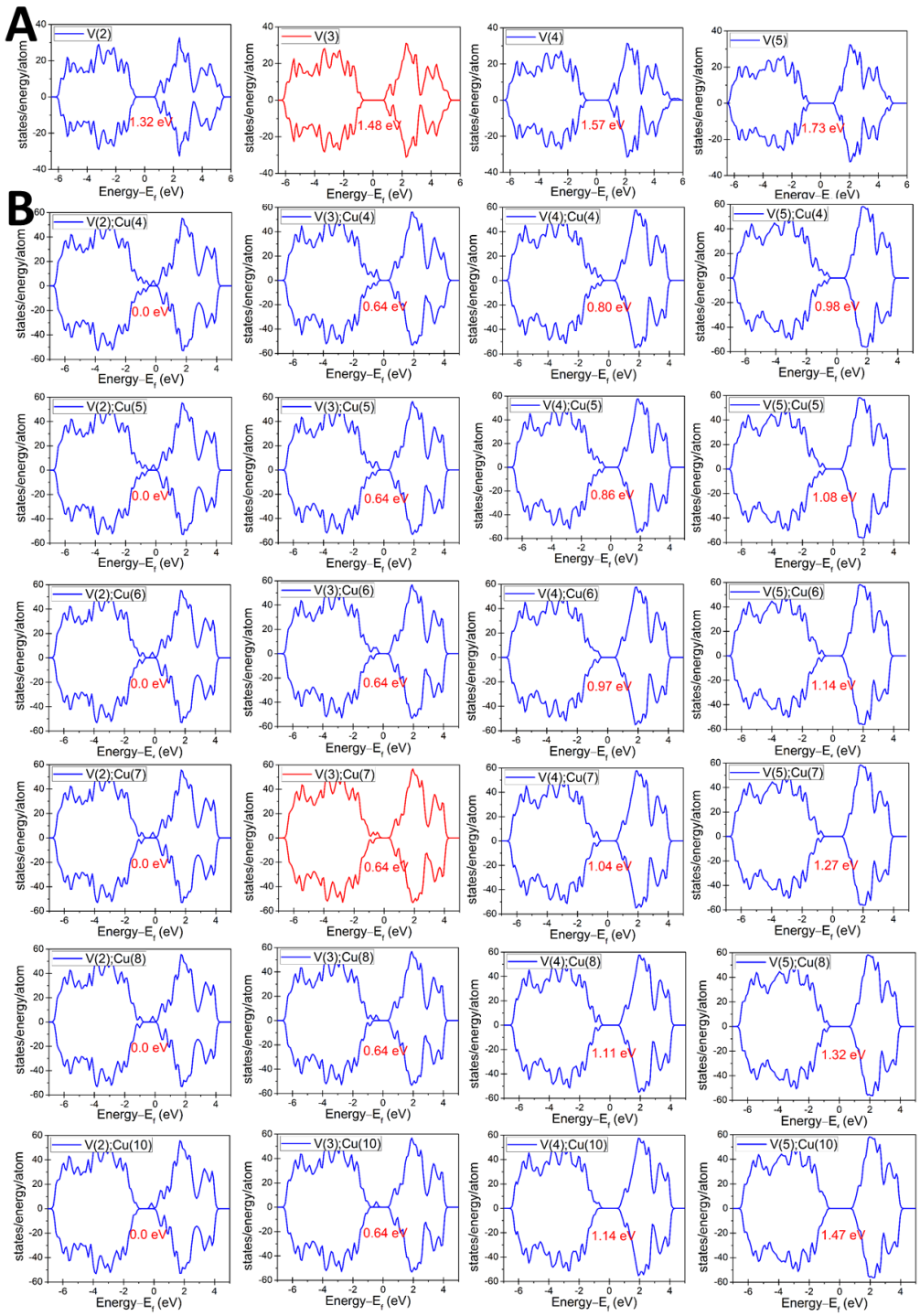

Figure A26. (A) The plot of total density of states for ζ-V_2O_5 at U (Vanadium) = 2, 3, 4, and 5. **(B)** The plot of total density of states for β'-$Cu_{0.1}V_2O_5$ at U (vanadium) = 2, 3, 4, 5 and U (copper) = 4, 5, 6, 7, 8, 10. The bandgaps are provided in red font on each individual plot. The two plots considered for the choice of U-parameter in our calculations are displayed in red curve.

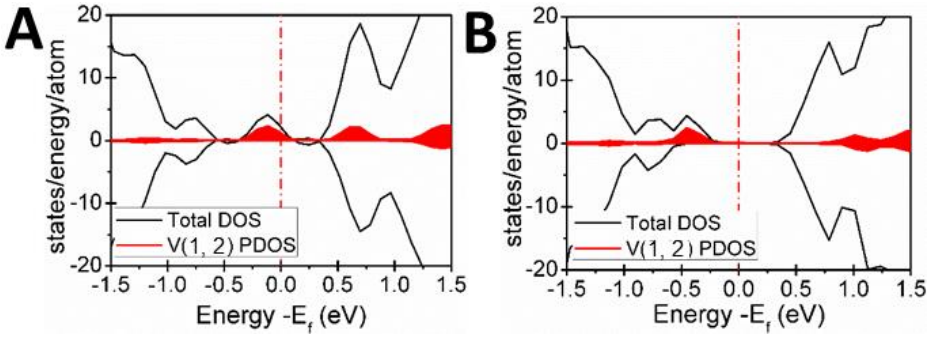

Figure A27. The total density of states and PDOS for V atoms delineated as V1 and V2 in the initial state **(Figure IV. 5H)** and transition state **(Figure IV. 5I)** are represented in panels **(A)** and **(B)**, respectively.

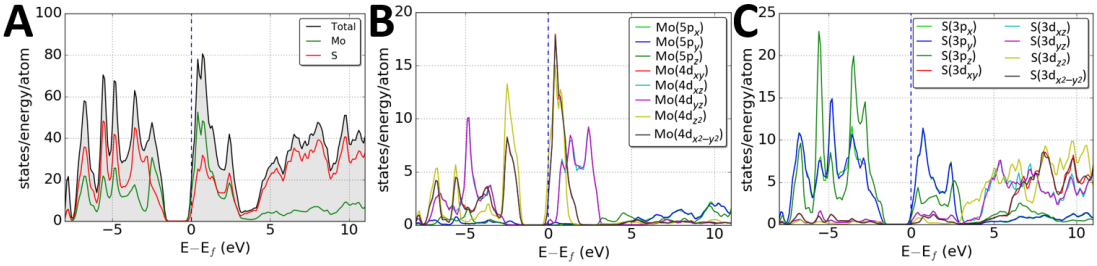

Figure A28. Calculated density of states for all sulfur atoms in a monolayer of 2H-MoS_2 with excitation of a sulfur core-level electron. (A) Total density of states and atom-projected density of states plots delineating Mo and S contributions; Orbital-projected density of states for (B) Mo and (C) S atoms in 2H-MoS_2.

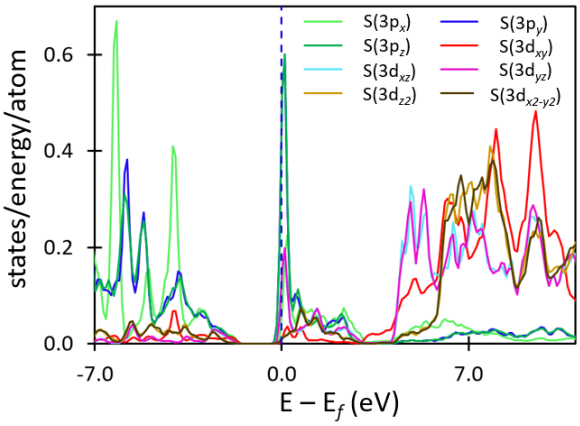

Figure A29. Calculated atom projected density of states for the excited sulfur atom in a monolayer of 2H-MoS_2. Orbital-projected density of states for the excited S-atom in 2H-MoS_2.

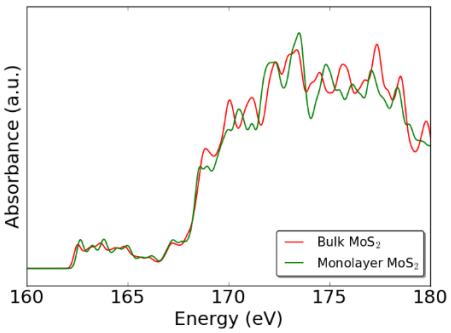

Figure A30. Contrasting the calculated sulfur $L_{2,3}$-edge XANES spectra of monolayer 2H-MoS_2 and bulk 2H-MoS_2.

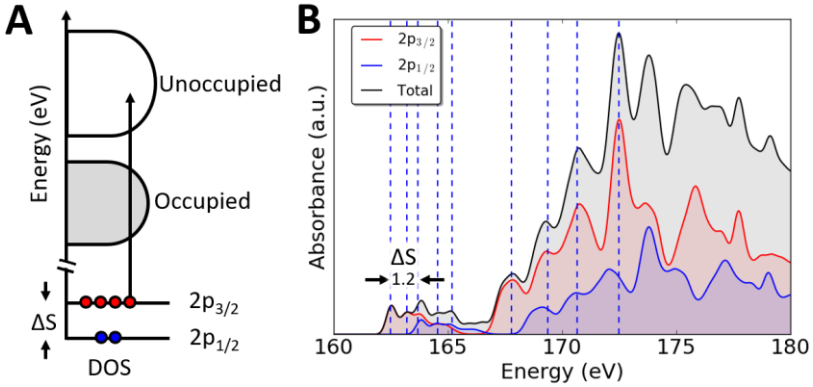

Figure A31. Schematic depiction of approach adopted for modeling the sulfur $L_{2,3}$-edge XANES spectrum of MoS_2. (A) Schematic depiction of transitions of $2p_{1/2}$ and $2p_{3/2}$ core-level electrons of sulfur to the lowest-energy unoccupied state in the electronic structure of MoS_2; (B) calculated sulfur $L_{2,3}$-edge spectrum (black curve) for MoS_2, which is the summation of spectra individually derived from excitation of $2p_{1/2}$ (blue) and $2p_{3/2}$ (red) core-level electrons of sulfur. The summation weights the excitation from $2p_{3/2}$ core levels twice that from the $2p_{1/2}$ core levels in terms of intensity; ΔE represents the spin–orbit splitting.

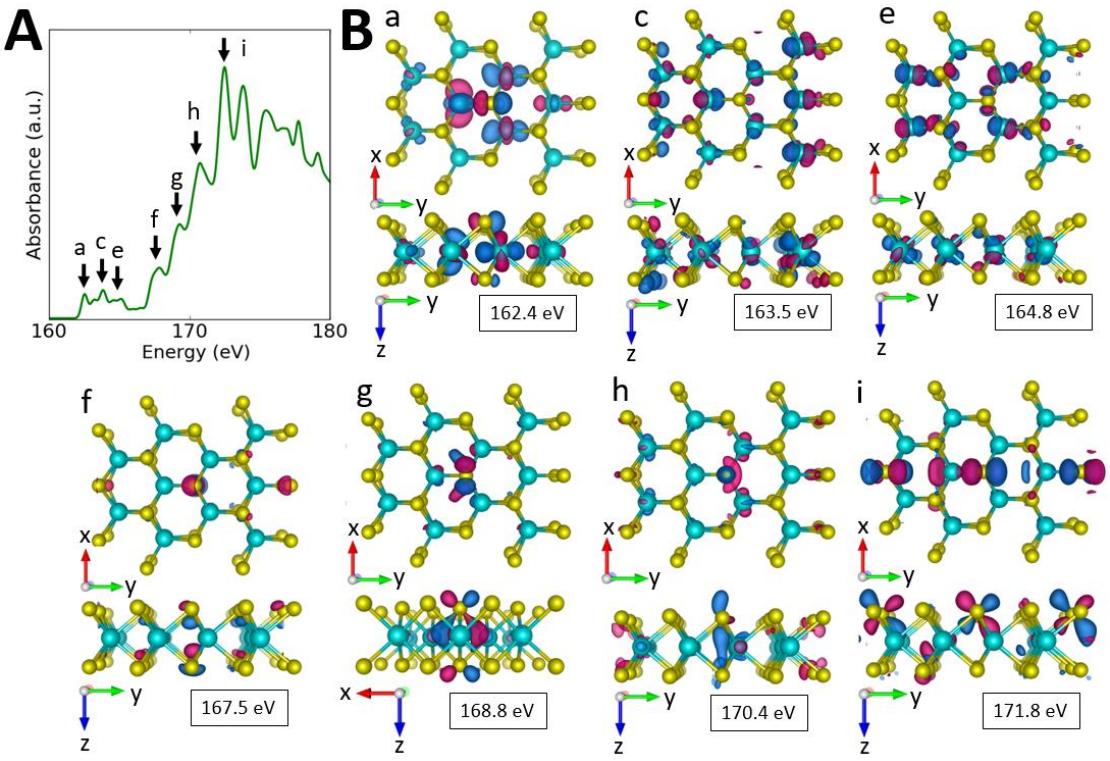

Figure A32. Orbital character of final states observed in S $L_{2,3}$-edge spectra of MoS_2. (A) Sulfur $L_{2,3}$-edge XANES spectra calculated using the XCH-XAS method; the absorption features are labeled (a)—(i); (B) isosurfaces representing the wavefunction squared corresponding to the final states to which core-level electrons are excited giving rise to absorption features (a)—(i). The labeling and energy position of the absorption feature is specified in each case. Mo atoms are depicted as light blue spheres and S atoms as yellow spheres. Opposite phases of the wavefunctions are represented as violet and dark blue lobes.

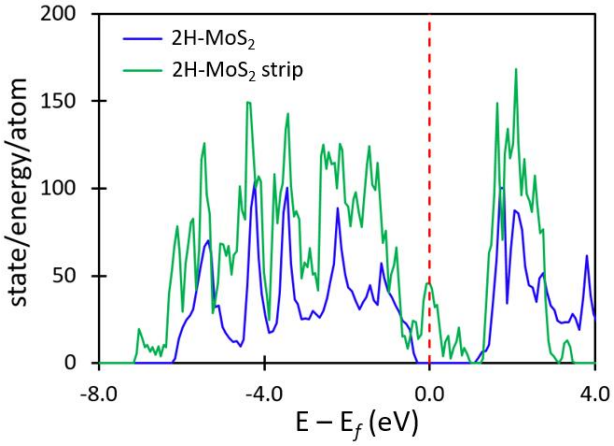

Figure A33. Total density of states (DOS) calculated for monolayer of 2H-MoS_2 (blue) and a 2H-MoS_2 semi-infinite strip (green). The conduction band minimum is decreased by 1.2 eV in the case of semi-infinite strip in comparison to monolayer 2H-MoS_2.

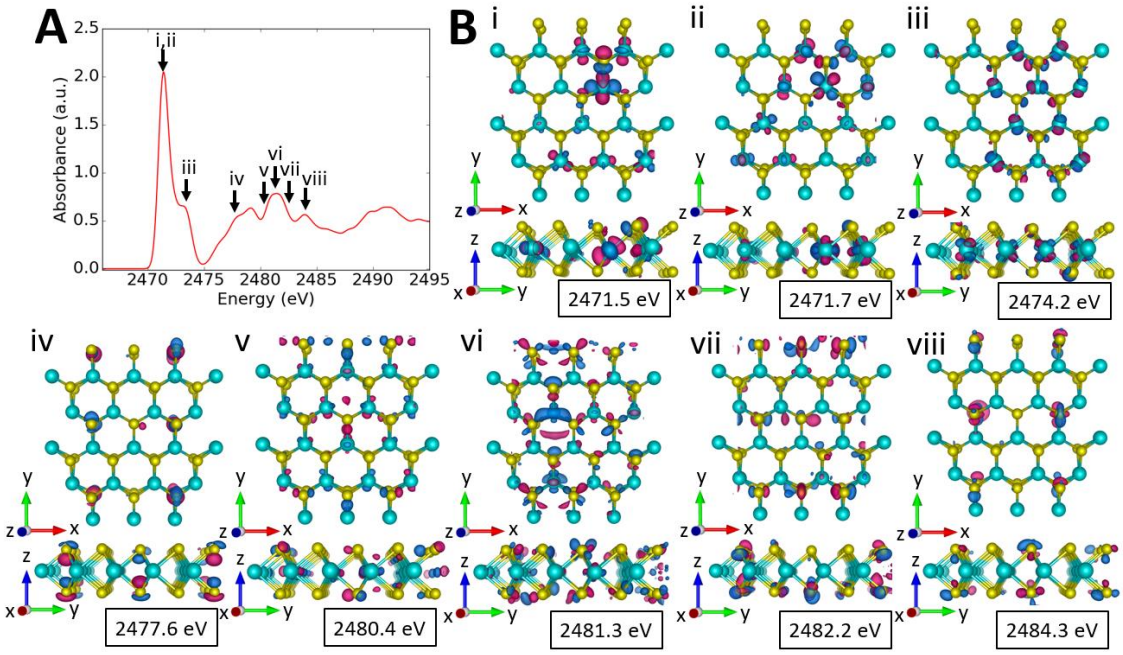

Figure A34. Orbital character of final states observed in S K-edge spectra of MoS_2. (A) S K-edge XANES spectrum for monolayer 2H-MoS_2 calculated using the XCH-XAS method; (B)(i—viii) isosurfaces representing the square of the wavefunction and delineating the charge density distribution of the final states corresponding to the specific absorption features (i)—(viii) observed in S K-edge spectra. Mo atoms are depicted as light blue spheres and S atoms as yellow spheres. Opposite phases of the wavefunctions are represented as violet and dark blue lobes.

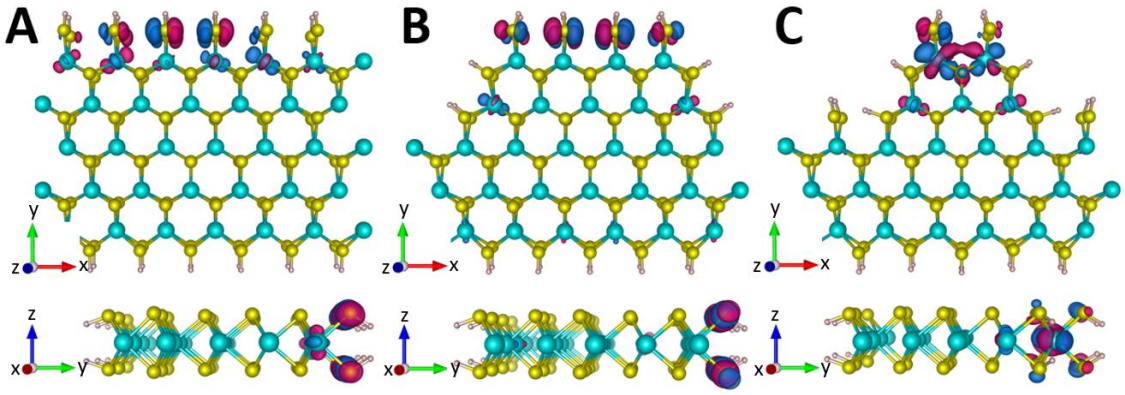

Figure A35. Influence of edge corrugation on S K-edge X-ray absorption spectra. The orbitals involved for the pre-edge absorption feature "pe" at 2469.8 eV demarcated with an arrow in **Figure V. 4F**. The orbital character for the pre-edge absorption feature is shown for MoS_2 with (A) an intact edge; (B) partial edge corrugation; and (C) substantial edge corrugation. Mo atoms are depicted as light blue spheres and S atoms as yellow spheres. Opposite phases of the wavefunctions are represented as violet and dark blue lobes.

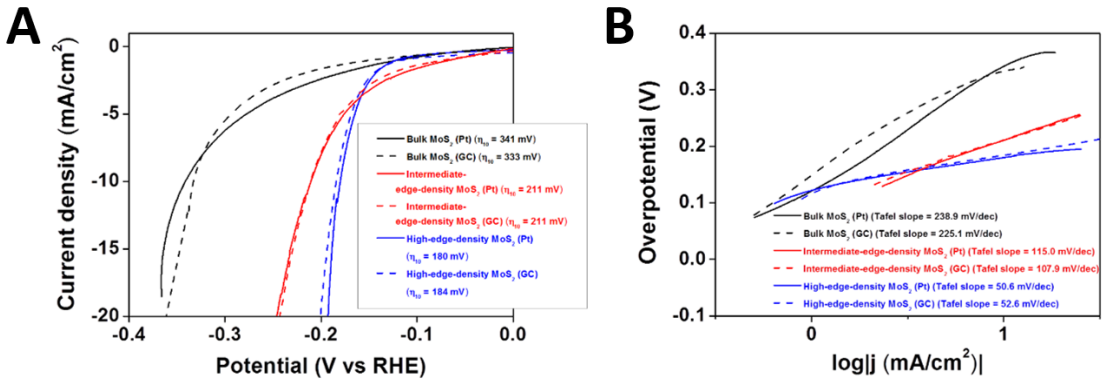

Figure A36. Contrasting the electrocatalytic activity when Pt or glassy carbon is used as the counter electrode. (A) Polarization curves and (B) Tafel plots contrasted for bulk 2H-MoS_2, intermediate-edge-density MoS_2, and high-edge-density MoS_2 integrated onto carbon fiber paper. HER measurements performed using Pt and glassy carbon counter electrodes are denoted as solid and dashed lines, respectively.

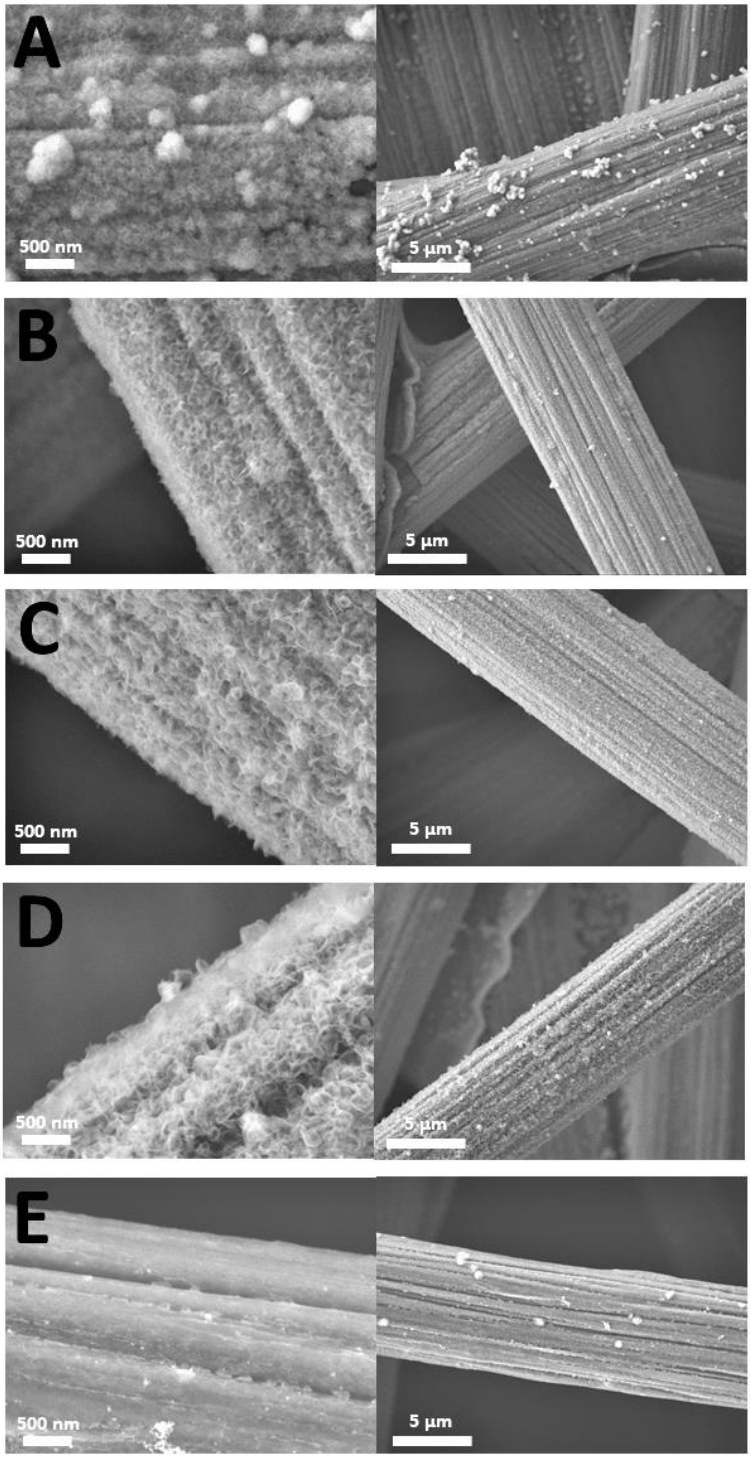

Figure A37. High- (left) and low-magnification (right) SEM images of **A)** sample S1, **B)** sample S2, **C)** sample S3, **D)** sample S4, and **E)** sample S5. The $MoS_{2-x}Se_x$ nanosheets increase in size from samples S1 to S4, whereas sample S5 is devoid of nanosheets and show layered $MoO_3/MoSe_2$ structure.

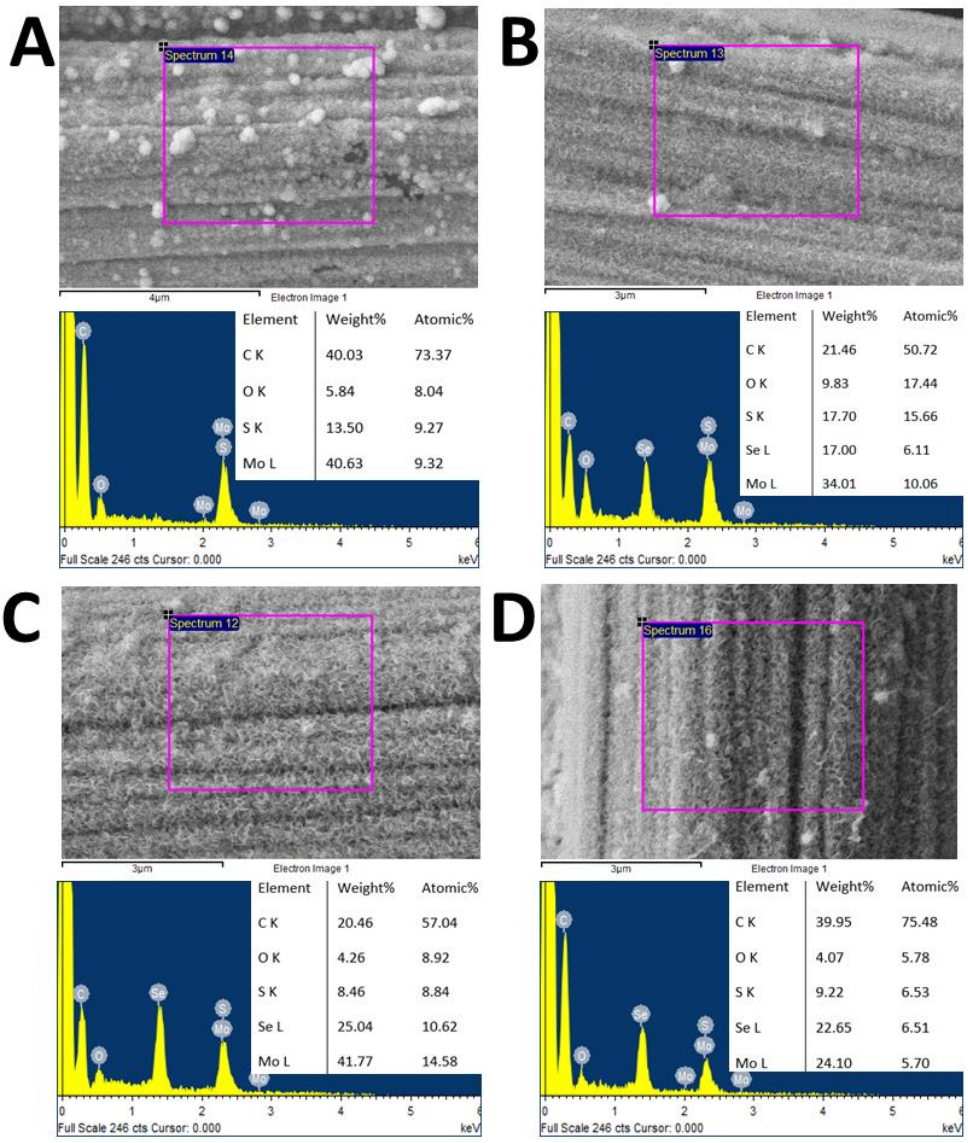

Figure A38. SEM image and corresponding energy-dispersive X-ray (EDX) spectrum with atomic percentages for molybdenum, sulfur, selenium, oxygen, and carbon in **(A)** sample S1, **(B)** sample S2, **(C)** sample S3, and **(D)** sample S4.

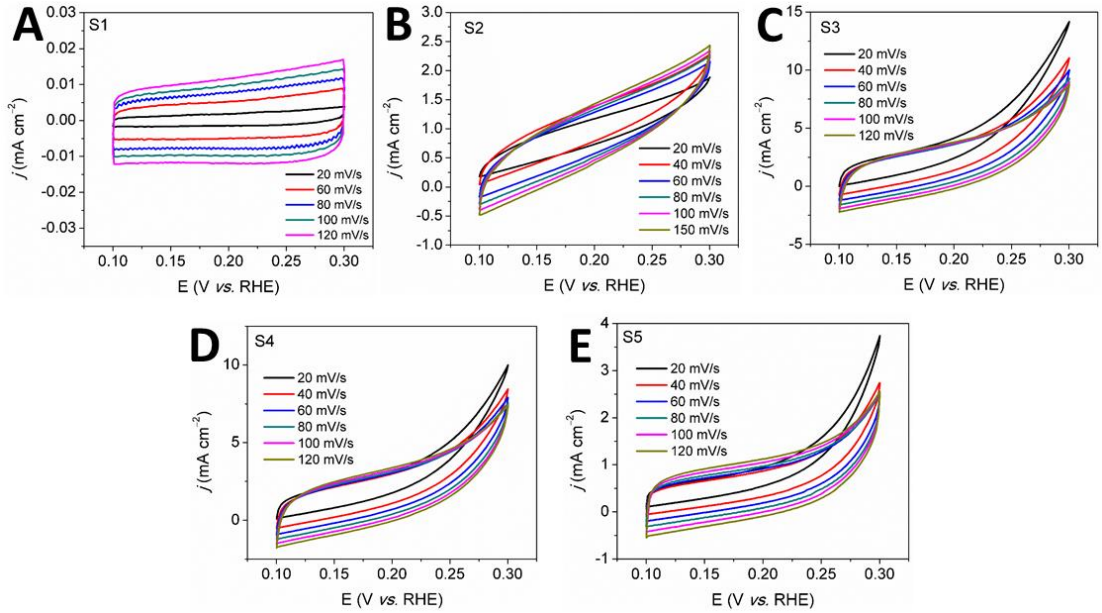

Figure A39. Cyclic voltammograms (CV) acquired in the range between 0.1–0.3 V vs. RHE in a 0.5M aqueous solution of H_2SO_4 for samples S1–S5. The CV data have been acquired at scan rates of 20–120 mV/s.

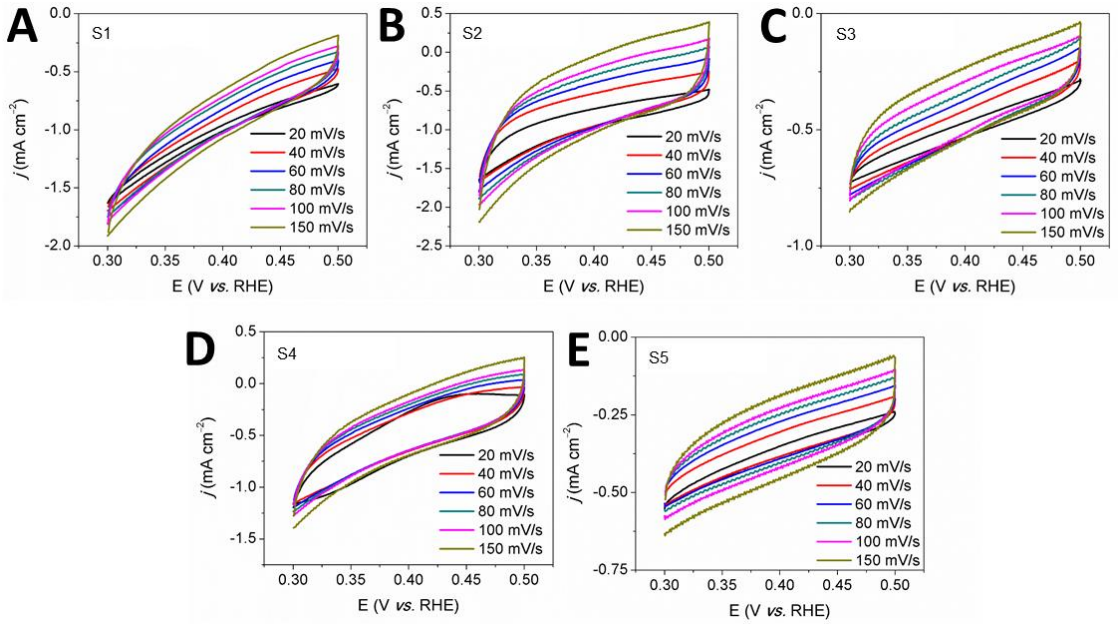

Figure A40. CV acquired in the range between 0.3–0.5 V vs. RHE in a 1.0M aqueous solution of KOH for samples S1–S5. The CV data have been acquired at scan rates of 20–150 mV/s.

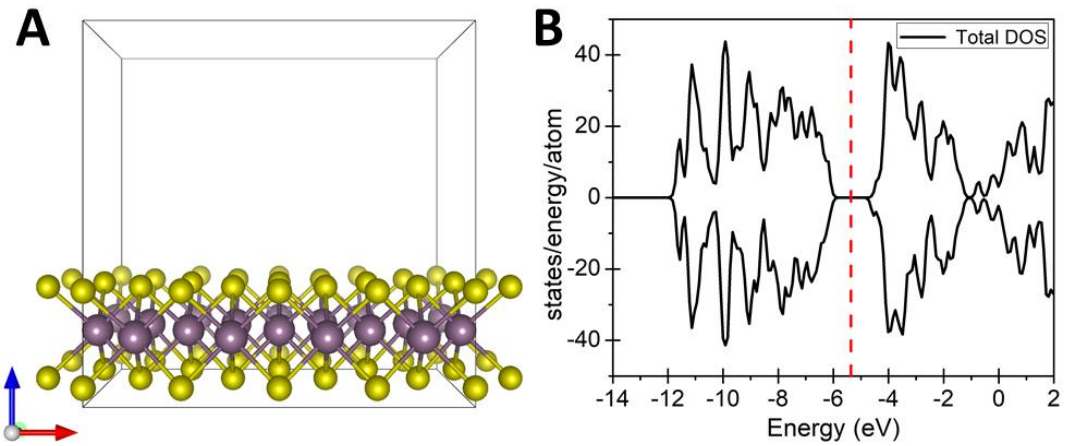

Figure A41. (A) Supercell and (B) the total density of states (DOS) for 2H-MoS_2. All energies are referenced to the vacuum level and the Fermi level is indicated by the red dashed line. Mo and S atoms are represented as violet and yellow spheres, respectively.

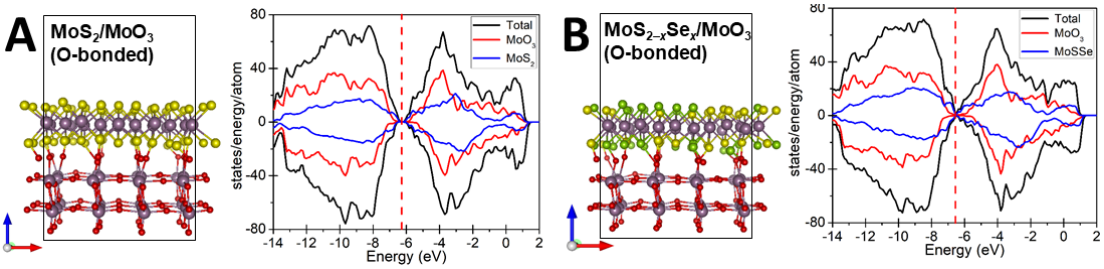

Figure A42. The supercell geometry and the corresponding DOS and PDOS for MoS_2/MoO_3 (O-bonded) and $MoS_{2-x}Se_x/MoO_3$ (O-bonded) are represented in (A) and (B) respectively. All energies are referenced to the vacuum level and the Fermi level is indicated by the red dashed line. The molybdenum, selenium, sulfur, and oxygen atoms are represented as violet, green, yellow, and red spheres respectively.

	α-V_2O_5		ζ-V_2O_5		ε-V_2O_5	
	k points	Energy (eV/atom)	k points	Energy (eV/atom)	k points	Energy (eV/atom)
Unit Cell	2×2×2	-7.00315	2×2×2	-6.97835	2×2×2	-6.97203
	2×4×4	-7.02242	2×4×2	-6.97835	2×4×2	-6.99258
	4×4×4	-7.02240	2×6×2	-6.99810	2×6×2	-6.99226
			4×4×4	-6.99810	**4×4×4**	-6.99258
Supercell	**2×2×2**	-7.02234	**2×2×2**	-6.99844	**2×2×2**	-6.99247
	4×4×4	-7.02216	4×4×4	-6.99844	4×4×4	-6.99263

Table A1. The energies of α-V_2O_5, ζ-V_2O_5, and ε-V_2O_5 polymorphs at various k-points contrasted for the unit cells and the supercells. The supercells considered for α-V_2O_5, ζ-V_2O_5, and ε-V_2O_5 are 1×3×2, 1×2×1, and 1×3×1 respectively.

Lattice parameters	α-V_2O_5			ζ-V_2O_5			ε-V_2O_5		
	Exp.[1] [Å]	PBE+U [Å]	vdW+ DF2 [Å]	Exp.[2] [Å]	PBE+U [Å]	vdW+ DF2 [Å]	Exp.[3] [Å]	PBE+U [Å]	vdW+ DF2 [Å]
a	11.512	11.489 (-0.2)	11.746 (2.0)	15.382	15.586 (1.3)	15.735 (2.3)	11.65	11.720 (0.6)	11.901 (2.2)
b	3.564	3.636 (2.0)	3.665 (2.8)	3.614	3.666 (1.4)	3.696 (2.3)	3.68	3.686 (0.2)	3.722 (1.1)
c	4.368	4.790 (9.7)	4.593 (4.9)	10.069	10.269 (2.0)	10.394 (3.1)	13.5[a]	9.541 (-29.3)[a]	9.128 (-32.4)[a]

[a] The experimental lattice parameter corresponds to a hydrated species with water intercalated between the layers; the *c* parameter is known to be greatly reduced upon dehydration although a complete structure solution of the dehydrated phase is not thus far available.

[1] Enjalbert, R.; Galy, J., A refinement of the structure of V_2O_5. *Acta Crystallogr. C: Crystal Struct. Commun.* **1986,** *42*, 1467-1469.
[2] Marley, P. M.; Abtew, T. A.; Farley, K. E.; Horrocks, G. A.; Dennis, R. V.; Zhang, P.; Banerjee, S., Emptying and filling a tunnel bronze. *Chem. Sci.* **2015,** *6*, 1712-1718.
[3] Tepavcevic, S.; Xiong, H.; Stamenkovic, V. R.; Zuo, X.; Balasubramanian, M.; Prakapenka, V. B.; Johnson, C. S.; Rajh, T., Nanostructured bilayered vanadium oxide electrodes for rechargeable sodium-ion batteries. *ACS Nano* **2011,** *6*, 530-538.

Table A2. Comparison of the predicted lattice parameters of relaxed structures obtained from GGA+U calculations with experimental data for the charged (empty) V_2O_5 polymorphs. All the values are in units of Å. The percent deviations are parenthetically denoted.

ε-$Mg_xV_2O_5$	Coordination Number	Relative Energy (meV)
Discharged Limit	4	0
	5	154
Charged Limit	4	0
	5	14

Table A3. Tabulated results comparing the difference in energy for Mg-ions residing at four-coordinated site *versus* five-coordinated sites near the discharged and charged limits of ε-$Mg_xV_2O_5$ as shown in **Figure A5**.

Lattice Para-meters	γ'-V_2O_5			δ'-V_2O_5			ρ'-V_2O_5		
	PBE+U [Å]	vdW +DF2 [Å]	opt B86b-vdW[Å]	PBE+U [Å]	vdW +DF2 [Å]	opt B86b-vdW[Å]	PBE+U [Å]	vdW +DF2 [Å]	opt B86b-vdW[Å]
a	3.65	3.68	3.62	11.74	11.92	11.68	11.68	11.88	11.67
b	10.06	10.25	9.80	3.69	3.72	3.68	3.68	3.72	3.68
c	11.40	10.41	9.51	9.14	9.10	8.76	9.80	9.76	9.32
	γ-MgV_2O_5			δ-$Mg_{0.5}V_2O_5$			ρ-MgV_2O_5		
a	3.58	3.62	3.56	12.51	12.73	12.43	11.97	12.16	11.93
b	9.92	10.06	9.85	3.73	3.75	3.70	3.71	3.75	3.70
c	11.16	11.28	11.11	8.42	8.50	8.29	9.05	9.19	8.94
	γ-CaV_2O_5			δ-$Ca_{0.5}V_2O_5$			ρ-CaV_2O_5		
a	3.75	3.79	3.73	12.59	12.76	12.59	11.95	12.08	11.88
b	9.93	10.06	9.84	3.83	3.86	3.83	3.78	3.82	3.77
c	12.11	12.22	12.03	8.32	8.44	8.09	9.23	9.38	9.12

Table A4. Predicted lattice parameters of relaxed structures obtained from GGA+U, vdw+DF2 and optB86b-vdW calculations for the charged (empty) V_2O_5 polymorphs and fully intercalated magnesium and calcium V_2O_5 polymorphs. All values are in units of Å.

Lattice Para-meters	γ'-V_2O_5				γ-$Li_1V_2O_5$			
	Exp.[1]	PBE+U [Å]	vdW +DF2 [Å]	opt B86b-vdW[Å]	Exp.[1]	PBE+U [Å]	vdW +DF2 [Å]	opt B86b-vdW[Å]
a	3.59	3.65 (1.3)	3.68 (2.5)	3.62 (0.8)	3.63	3.66 (0.8)	3.68 (1.4)	3.64 (0.2)
b	10.11	10.06 (-0.5)	10.25 (1.4)	9.80 (-3.1)	9.82	9.85 (0.3)	9.97 (1.5)	9.79 (-0.3)
c	10.48	11.40 (8.8)	10.41 (-0.7)	9.51 (-9.3)	10.80	10.93 (1.2)	10.96 (1.5)	10.70 (-0.9)

[1] Rocquefelte, X.; Boucher, F.; Gressier, P.; Ouvrard, G., First-Principle Study of the Intercalation Process in the $Li_xV_2O_5$ System. *Chem. Mater.* **2003,** *15*, 1812-1819.

Table A5. Comparison of lattice parameters of relaxed structures obtained from PBE+U, vdW+DF2 and optB86b-vdW calculations with experimental values for γ'-V_2O_5 and γ-$Li_1V_2O_5$. The percentage change in lattice parameters in comparison to experimental values are provided in parenthesis.

	γ-$M_xV_2O_5$		δ-$M_xV_2O_5$			ρ-$M_xV_2O_5$	
Ion/Coordination number	Four	Five	Four	Five	Six	Six	Eight
Li	**0.00**	0.10	**0.00**	0.06	0.11	**0.00**	0.42
Na	0.12	**0.00**	0.20	**0.00**	0.05	**0.00**	0.15
Mg	0.20	**0.00**	0.18	**0.00**	0.18	**0.00**	0.85
Ca	0.31	**0.00**	0.60	**0.00**	0.04	**0.00**	0.01

Table A6. Calculated formation energies for cations residing in different coordination environments with respect to the lowest energy metal ion coordination site as shown for γ-$M_xV_2O_5$, δ-$M_xV_2O_5$, and ρ-$M_xV_2O_5$, respectively. The lowest energy coordination environments are marked as null values in the table above. Migration pathways with the lowest barrier for each polymorph are shown in **Figure III. 3**.

a = 15.169453(14) Å, b = 3.635130(3)Å, c = 10.073962(8) Å, β = 106.057(0)°, V = 533.836(1)Å^3 χ^2 = 3.743, wRp = 13.65%, wRp = 10.03%					
Atom	***x***	***y***	***z***	**Occupancy**	**Uiso**
Cu(1)	0.54152(13)	0.0000000(0)	0.34396(19)	0.440(2)	0.00763(44)
Cu(2)	0.52806(14)	0.0706(6)	0.36123(21)	0.201(1)	0.00079(54)
V(1)	0.33238(5)	0.0000000(0)	0.09034(7)	1.000(0)	0.00110(16)
V(2)	0.11367(5)	0.0000000(0)	0.11994(8)	1.000(0)	0.00311(16)
V(3)	0.28670(5)	0.0000000(0)	0.40627(7)	1.000(0)	0.00127(15)
O(1)	0.0000000(0)	0.0000000(0)	0.0000000(0)	1.000(0)	0.00258(86)
O(2)	0.18865(16)	0.0000000(0)	-0.04653(24)	1.000(0)	0.00176(56)
O(3)	0.36658(16)	0.0000000(0)	-0.08519(25)	1.000(0)	0.00007(57)
O(4)	0.43178(16)	0.0000000(0)	0.20220(25)	1.000(0)	0.00301(62)
O(5)	0.26087(16)	0.0000000(0)	0.22355(25)	1.000(0)	0.00173(58)
O(6)	0.09672(16)	0.0000000(0)	0.27701(24)	1.000(0)	0.00167(59)
O(7)	0.24441(17)	0.0000000(0)	0.57662(26)	1.000(0)	0.00376(62)
O(8)	0.39839(17)	0.0000000(0)	0.45898(26)	1.000(0)	0.00544(62)

Table A7. Atom positions for β′-$Cu_{0.55}V_2O_5$ at 100K as refined from high-resolution synchrotron X-ray diffraction. Refinement statistics, lattice parameters, and atom positions as obtained from Rietveld refinement of the X-ray diffraction pattern collected for β′-$Cu_{0.55}V_2O_5$ at 100 K, shown in **Figure IV.1D,** light blue.

V-O Polyhedra	V-O	Distance (Å)	O-V-O	Angle (°)
V(1)O_6 Octahedra	V(1)_O(2)	2.2343(24)	O(2)_V(1)_O(2)	77.38(7)
			O(2)_V(1)_O(2)	77.38(7)
	V(1)_O(2)	1.8768(6)	O(2)_V(1)_O(3)	84.30(9)
			O(2)_V(1)_O(4)	174.22(11)
	V(1)_O(2)	1.8768(6)	O(2)_V(1)_O(5)	77.91(9)
			O(2)_V(1)_O(2)	151.14(14)
	V(1)_O(3)	1.9758(25)	O(2)_V(1)_O(3)	81.91(8)
			O(2)_V(1)_O(4)	103.27(7)
	V(1)_O(4)	1.6135(24)	O(2)_V(1)_O(5)	94.09(7)
			O(2)_V(1)_O(3)	81.91(8)
	V(1)_O(5)	1.9449(24)	O(2)_V(1)_O(4)	103.27(7)
			O(2)_V(1)_O(5)	94.09(7)
			O(3)_V(1)_O(4)	101.49(12)
V(2)O_6 Octahedra	V(2)_O(1)	1.8113(7)	O(1)_V(2)_O(3)	92.68(8)
			O(1)_V(2)_O(3)	92.68(8)
	V(2)_O(2)	2.2718(24)	O(1)_V(2)_O(5)	167.42(8)
			O(1)_V(2)_O(6)	105.31(9)
	V(2)_O(3)	1.8904(7)	O(3)_V(2)_O(3)	148.08(14)
			O(3)_V(2)_O(5)	83.99(8)
	V(2)_O(3)	1.8904(7)	O(3)_V(2)_O(6)	104.42(7)
			O(3)_V(2)_O(5)	83.99(8)
	V(2)_O(5)	2.1877(24)	O(3)_V(2)_O(6)	104.42(7)
	V(2)_O(6)	1.6718(24)	O(5)_V(2)_O(6)	87.27(11)
V(3)O_5 Square Pyramid	V(3)_O(5)	1.7728(25)	O(5)_V(3)_O(7)	149.71(11)
	V(3)_O(7)	1.9913(26)	O(5)_V(3)_O(7)	96.04(8)
	V(3)_O(7)	1.8976(8)	O(5)_V(3)_O(8)	104.45(12)
	V(3)_O(7)	1.8976(8)	O(7)_V(3)_O(7)	76.95(8)
	V(3)_O(8)	1.6294(25)	O(7)_V(3)_O(8)	105.84(11)
			O(7)_V(3)_O(7)	146.60(15)
			O(7)_V(3)_O(8)	103.45(8)

V-O Polyhedra	V-O	Distance (Å)	O-V-O	Angle (°)
Cu(1)O_4 Distorted Seesaw	O(4)_Cu(1)	1.8696(30)	O(8)_Cu(1)_O(6)	101.77(14)
			O(8)_Cu(1)_O(6)	101.77(14)
	O(6)_Cu(1)	2.1846(16)	O(8)_Cu(1)_O(4)	148.0(5)
			O(6)_Cu(1)_O(6)	112.6(4)
	O(6)_Cu(1)	2.1846(16)	O(6)_Cu(1)_O(4)	95.77(15)
	O(8)_Cu(1)	1.9419(31)	O(6)_Cu(1)_O(4)	95.77(15)
Cu(2)O_5 Distorted square pyramid	O(4)_Cu(2)	1.8631(32)	O(6)-Cu(2)-O(4)	96.2930(15)
			O(6)-Cu(2)-O(8)	139.2948(9)
	O(8)_Cu(2)	1.8631(32)	O(6)-Cu(2)-O(8)	104.7991(9)
			O(6)-Cu(2)-O(6)	99.7302(15)
	O(6)_Cu(2)	2.1748(24)	O(4)-Cu(2)-O(8)	78.7631(16)
	O(6)_Cu(2)	2.5684(28)	O(4)-Cu(2)-O(8)	158.8836(16)
			O(4)-Cu(2)-O(6)	84.1315(11)
	O(8)_Cu(2)	2.4447(31)	O(8)-Cu(2)-O(8)	85.7656(8)
			O(8)-Cu(2)-O(6	119.5544(8)

Table A8. Bond angles and lengths for β′-$Cu_{0.55}V_2O_5$ at 100K. Bond angles and bond lengths for MO_x polyhedra as obtained from Rietveld refinement of the synchrototon X-ray diffraction pattern collected for β′-$Cu_{0.55}V_2O_5$ at 100K, shown in **Figure IV.1D**, light blue.

a = 15.212392(23) Å, b = 3.633579(4)Å, c = 10.092637(13)Å, β = 106.245(0)°, V = 535.602(1)Å^3 χ^2 = , Rw = , wRp = %					
Atom	***x***	***y***	***z***	**Occupancy**	**Uiso**
Cu(1)	0.54333(15)	0.0000000(0)	0.34244(21)	0.368(6)	0.01592(52)
Cu(2)	0.52584(13)	0.0864(5)	0.36216(19)	0.232(3)	0.01542(57)
V(1)	0.33288(5)	0.0000000(0)	0.09244(7)	1.0000(0)	0.00380(17)
V(2)	0.11354(5)	0.0000000(0)	0.11929(8)	1.0000(0)	0.00677(18)
V(3)	0.28692(5)	0.0000000(0)	0.40664(7)	1.0000(0)	0.00546(17)
O(1)	0.0000000(0)	0.0000000(0)	0.0000000(0)	1.0000(0)	0.0068(90)
O(2)	0.18863(16)	0.0000000(0)	-0.04566(24)	1.0000(0)	0.00179(57)
O(3)	0.36784(15)	0.0000000(0)	-0.08541(23)	1.0000(0)	0.00027(55)
O(4)	0.43145(16)	0.0000000(0)	0.20285(24)	1.0000(0)	0.00858(66)
O(5)	0.25941(15)	0.0000000(0)	0.22085(23)	1.0000(0)	0.0034(57)
O(6)	0.09531(15)	0.0000000(0)	0.27536(24)	1.0000(0)	0.00715(65)
O(7)	0.24415(16)	0.0000000(0)	0.57423(25)	1.0000(0)	0.00797(67)
O(8)	0.39888(17)	0.0000000(0)	0.45905(26)	1.0000(0)	0.01440(69)

Table A9. Atom positions for β′-$Cu_{0.55}V_2O_5$ at 295 K. Refinement statistics, lattice parameters, and atom positions as obtained from Rietveld refinement of the X-ray diffraction pattern collected for β′-$Cu_{0.55}V_2O_5$ at 295K, shown in **Figure IV.1D**, orange.

V-O Polyhedra	V-O	Distance (Å)	O-V-O	Angle (°)
V(1)O_6 Octahedra	V(1)_O(2)	2.2465(24)	O(2)_V(1)_O(2)	76.90(8)
			O(2)_V(1)_O(2)	76.90(8)
	V(1)_O(2)	1.8826(6)	O(2)_V(1)_O(3)	84.41(11)
			O(2)_V(1)_O(4)	174.55(14)
	V(1)_O(2)	1.8826(6)	O(2)_V(1)_O(5)	76.6070(11)
			O(2)_V(1)_O(2)	149.60(14)
	V(1)_O(3)	2.0097(23)	O(2)_V(1)_O(3)	81.19(7)
			O(2)_V(1)_O(4)	103.78(7)
	V(1)_O(4)	1.5985(23)	O(2)_V(1)_O(5)	94.34(7)
			O(2)_V(1)_O(3)	81.19(7)
	V(1)_O(5)	1.9338(23)	O(2)_V(1)_O(4)	103.78(7)
			O(2)_V(1)_O(5)	94.34(7)
			O(3)_V(1)_O(4)	101.05(11)
V(2)O_6 Octahedra	V(2)_O(1)	1.8082(7)	O(1)_V(2)_O(3)	92.48(7)
			O(1)_V(2)_O(3)	92.48(7)
	V(2)_O(2)	2.2671(23)	O(1)_V(2)_O(5)	167.26(7)
			O(1)_V(2)_O(6)	104.34(9)
	V(2)_O(3)	1.8847(6)	O(3)_V(2)_O(3)	149.16(13)
			O(3)_V(2)_O(5)	84.26(7)
	V(2)_O(3)	1.8847(6)	O(3)_V(2)_O(6)	104.09(7)
			O(3)_V(2)_O(5)	84.26(7)
	V(2)_O(5)	2.1684(23)	O(3)_V(2)_O(6)	104.09(7)
	V(2)_O(6)	1.6741(24)	O(5)_V(2)_O(6)	88.40(10)
V(3)O_5 Square Pyramid	V(3)_O(5)	1.8033(23)	O(5)_V(3)_O(7)	148.68(10)
	V(3)_O(7)	1.9748(25)	O(5)_V(3)_O(7)	76.24(8)
	V(3)_O(7)	1.9006(7)	O(5)_V(3)_O(8)	104.72(12)
	V(3)_O(7)	1.9006(7)	O(7)_V(3)_O(7)	76.24(8)
	V(3)_O(8)	1.6360(25)	O(7)_V(3)_O(8)	103.48(7)
			O(7)_V(3)_O(7)	145.83(15)
			O(7)_V(3)_O(8)	103.48(7)

V-O Polyhedra	V-O	Distance (Å)	O-V-O	Angle (°)
Cu(1)O_4 Distorted Seesaw	O(4)_Cu(1)	1.8815(31)	O(8)_Cu(1)_O(6)	102.84(10)
			O(8)_Cu(1)_O(6)	102.84(10)
	O(6)_Cu(1)	2.1642(17)	O(8)_Cu(1)_O(4)	145.37(16)
			O(6)_Cu(1)_O(6)	114.17(14)
	O(6)_Cu(1)	2.1642(17)	O(6)_Cu(1)_O(4)	95.68(10)
	O(8)_Cu(1)	1.9497(33)	O(6)_Cu(1)_O(4)	95.68(10)
Cu(2)O_5 Distorted square pyramid	O(4)_Cu(2)	1.8584(31)	O(6)-Cu(2)-O(4)	105.71(12)
			O(6)-Cu(2)-O(8)	98.0837(11)
	O(8)_Cu(2)	1.8735(30)	O(6)-Cu(2)-O(8)	79.4345(10)
			O(6)-Cu(2)-O(6)	157.09(12)
	O(6)_Cu(2)	2.1589(23)	O(4)-Cu(2)-O(8)	96.5471(11)
	O(6)_Cu(2)	2.63485(26)	O(4)-Cu(2)-O(8)	86.0373(10)
			O(4)-Cu(2)-O(6)	88.4681(10)
	O(8)_Cu(2)	2.4170(29)	O(8)-Cu(2)-O(8)	105.71(12)
			O(8)-Cu(2)-O(6	98.0837(13)

Table A10. Bond angles and bond lengths for β′-$Cu_{0.55}V_2O_5$ at 295K. Bond angles and bond lengths for MO_x polyhedra as obtained from Rietveld refinement of the X-ray diffraction pattern collected for β′-$Cu_{0.55}V_2O_5$ at 295 K, shown in **Figure IV.1D,** orange.

***a* = 15.282535(16) Å, b = 3.633482(3) Å, c = 10.112663(9) Å, β = 106.514(0) Å, V = 538.381(1) Å^3 χ^2 = 6.983, wRp = 15.69%, Rp = 9.53%**					
Atom	**x**	**y**	**z**	**Occupancy**	**Uiso**
Cu(1)	0.5478(4)	0.0000(0)	0.3415(4)	0.295(13)	0.0144(15)
Cu(2)	0.52597(31)	0.0855(11)	0.35963(31)	0.269(6)	0.0256(9)
V(1)	0.33275(5)	0.0000(0)	0.09329(8)	1.0000(0)	0.00657(21)
V(2)	0.11384(6)	0.0000(0)	0.11828(9)	1.0000(0)	0.00928(22)
V(3)	0.28671(6)	0.0000(0)	0.40694(9)	1.0000(0)	0.00684(20)
O(1)	0.0000(0)	0.0000(0)	0.0000(0)	1.0000(0)	0.0112(11)
O(2)	0.18902(18)	0.0000(0)	-0.04512(29)	1.0000(0)	0.00559(70)
O(3)	0.36697(18)	0.0000(0)	-0.08362(28)	1.0000(0)	0.00580(70)
O(4)	0.43312(20)	0.0000(0)	0.20288(30)	1.0000(0)	0.01513(83)
O(5)	0.26039(19)	0.0000(0)	0.22123(28)	1.0000(0)	0.00698(73)
O(6)	0.09934(19)	0.0000(0)	0.27506(29)	1.0000(0)	0.01361(84)
O(7)	0.24568(20)	0.0000(0)	0.57645(30)	1.0000(0)	0.01463(84)
O(8)	0.39590(20)	0.0000(0)	0.45975(31)	1.0000(0)	0.01704(84)

Table A11. Atom positions for β′-$Cu_{0.55}V_2O_5$ at 400 K. Refinement statistics, lattice parameters, and atom positions as obtained from Rietveld refinement of the X-ray diffraction pattern collected for β′-$Cu_{0.55}V_2O_5$ at 400 K, shown in **Figure IV.1D**, red.

V-O Polyhedra	V-O	Distance (Å)	O-V-O	Angle (°)
V(1)O_6 Octahedra	V(1)_O(2)	2.2442(28)	O(2)_V(1)_O(2)	76.67(8)
			O(2)_V(1)_O(2)	76.67(8)
	V(1)_O(2)	1.8858(8)	O(2)_V(1)_O(3)	84.30(11)
			O(2)_V(1)_O(4)	175.64(14)
	V(1)_O(2)	1.8858(8)	O(2)_V(1)_O(5)	76.81(11)
			O(2)_V(1)_O(2)	148.89(17)
	V(1)_O(3)	2.0015(28)	O(2)_V(1)_O(3)	80.84(9)
			O(2)_V(1)_O(4)	103.91(8)
	V(1)_O(4)	1.6169(29)	O(2)_V(1)_O(5)	94.63(9)
			O(2)_V(1)_O(3)	80.84(9)
	V(1)_O(5)	1.9262(28)	O(2)_V(1)_O(4)	103.91(8)
			O(2)_V(1)_O(5)	94.63(9)
			O(3)_V(1)_O(4)	100.06(14)
V(2)O_6 Octahedra	V(2)_O(1)	1.8095(8)	O(1)_V(2)_O(3)	92.76(9)
			O(1)_V(2)_O(3)	92.76(9)
	V(2)_O(2)	2.2650(29)	O(1)_V(2)_O(5)	167.85(9)
			O(1)_V(2)_O(6)	105.47(11)
	V(2)_O(3)	1.8889(8)	O(3)_V(2)_O(3)	148.23(16)
			O(3)_V(2)_O(5)	84.04(9)
	V(2)_O(3)	1.8889(8)	O(3)_V(2)_O(6)	104.29(9)
			O(3)_V(2)_O(5)	84.04(9)
	V(2)_O(5)	2.1851(28)	O(3)_V(2)_O(6)	104.29(9)
	V(2)_O(6)	1.6620(29)	O(5)_V(2)_O(6)	86.68(13)
V(3)O_5 Square Pyramid	V(3)_O(5)	1.8054(28)	O(5)_V(3)_O(7)	145.38(18)
	V(3)_O(7)	1.9857(30)	O(7)_V(3)_O(7)	76.70(9)
	V(3)_O(7)	1.9029(9)	O(5)_V(3)_O(8)	105.49(14)
	V(3)_O(7)	1.9029(9)	O(7)_V(3)_O(7)	76.70(9)
	V(3)_O(8)	1.6011(29)	O(7)_V(3)_O(8)	104.07(9)
			O(7)_V(3)_O(7)	145.38(18)
			O(7)_V(3)_O(8)	104.07(9)

V-O Polyhedra	V-O	Distance (Å)	O-V-O	Angle (°)
Cu(1)O_4 Distorted Seesaw	Cu(1)_O(4)	1.908(5)	O(8)_Cu(1)_O(6)	103.17(15)
			O(8)_Cu(1)_O(6)	103.17(15)
	Cu(1)_O(6)	2.162(5)	O(8)_Cu(1)_O(4)	143.3(5)
			O(6)_Cu(1)_O(6)	114.4(4)
	Cu(1)_O(6)	2.162(5)	O(6)_Cu(1)_O(4)	96.39(14)
	Cu(1)_O(8)	1.948(5)	O(6)_Cu(1)_O(4)	96.39(14)
Cu(2)O_5 Distorted square pyramid	O(4)_Cu(2)	1.829(4)	O(6)-Cu(2)-O(4)	97.79(14)
			O(6)-Cu(2)-O(8)	88.35(12)
	O(8)_Cu(2)	1.9022(34)	O(6)-Cu(2)-O(8)	103.64(15)
			O(6)-Cu(2)-O(6)	96.61(10)
	O(6)_Cu(2)	2.1914(31)	O(4)-Cu(2)-O(8)	79.57(10)
	O(6)_Cu(2)	2.657(7)	O(4)-Cu(2)-O(8)	157.69(13)
			O(4)-Cu(2)-O(6)	97.78(8)
	O(8)_Cu(2)	2.493(6)	O(8)-Cu(2)-O(8)	86.85(8)
			O(8)-Cu(2)-O(6)	88.35(11)

Table A12. Bond angles and lengths for β′-$Cu_{0.55}V_2O_5$ at 400 K. Bond angles and lengths for MO_x polyhedra as obtained from Rietveld refinement of the X-ray diffraction pattern collected for β′-$Cu_{0.55}V_2O_5$ at 400 K, shown in **Figure IV.1D**, red.

	Relative Cu occupancies			
	110K		250K	
Total Cu Occupancy	**Cu(1)**	**Cu(2)**	**Cu(1)**	**Cu(2)**
0.37	0.097	0.273	0.092	0.279
0.64	0.239	0.406	0.121	0.523

Table A13. Refined Relative Cu Occupancies per V_2O_5 as determined by single-crystal X-ray diffraction of β′-$Cu_xV_2O_5$, where x = 0.37 and 0.64.

Sample	Shell	N	S_0^2	*R* (Å)	ΔE_0 (eV)	Ratio Cu(1):Cu(2)	*R*-factor (%)
β'–$Cu_{0.40}V_2O_5$ (95K)	Cu(2)–O(4.1)	2	1.01 ± 0.09	1.92 ± 0.01	0.752 ± 0.092	0.21 ± 0.08	2.2
	Cu(2)–O(6.1)	1	1.01 ± 0.09	2.08 ± 0.01			
	Cu(2)–O(8.2)	1	1.01 ± 0.09	2.33 ± 0.01			
	Cu(2)–O(6.2)	1	1.01 ± 0.09	2.57 ± 0.01			
	Cu(2)–V(3.1)	1	1.01 ± 0.09	2.99 ± 0.01			
	Cu(2)–Cu(2)	2	0.17 ± 0.02	3.00 ± 0.01			
	Cu(1)–O(4.1)	1	0.22 ± 0.09	1.79 ± 0.07			
	Cu(1)–O(8.1)	1	0.22 ± 0.09	1.78 ± 0.02			
	Cu(1)–O(6.1)	2	0.22 ± 0.09	2.00 ± 0.03			
	Cu(1)–O(8.2)	1	0.22 ± 0.09	2.50 ± 0.03			
	Cu(1)–V(3.1)	1	0.22 ± 0.09	2.82 ± 0.04			
	Cu(1)–O(7.1)	1	0.22 ± 0.09	2.86 ± 0.04			
β'–$Cu_{0.40}V_2O_5$ (298K)	Cu(2)–O(4.1)	2	0.79 ± 0.06	1.90 ± 0.01	-0.673 ± 1.519	0.35 ± 0.09	2.9
	Cu(2)–O(6.1)	1	0.79 ± 0.06	2.07 ± 0.01			
	Cu(2)–O(8.2)	1	0.79 ± 0.06	2.33 ± 0.01			
	Cu(2)–O(6.2)	1	0.79 ± 0.06	2.57 ± 0.01			
	Cu(2)–V(3.1)	1	0.79 ± 0.06	2.99 ± 0.01			
	Cu(2)–Cu(2)	2	0.13 ± 0.01	2.99 ± 0.01			
	Cu(1)–O(4.1)	1	0.28 ± 0.08	1.91 ± 0.01			
	Cu(1)–O(8.1)	1	0.28 ± 0.08	1.78 ± 0.02			
	Cu(1)–O(6.1)	2	0.28 ± 0.08	2.00 ± 0.02			
	Cu(1)–O(8.2)	1	0.28 ± 0.08	2.50 ± 0.02			
	Cu(1)–V(3.1)	1	0.28 ± 0.08	2.82 ± 0.03			
	Cu(1)–O(7.1)	1	0.28 ± 0.08	2.86 ± 0.03			

Table A14. Results of fits to β'–$Cu_{0.40}V_2O_5$ Cu K-edge EXAFS data collected at 95K and 298K. The coordination number (N) is kept fixed at 1 or 2 in the modeling of the EXAFS data. Atomic positions obtained from high-resolution synchrotron powder X-ray diffraction are to fit the EXAFS data.

Energy	Molybdenum						Sulfur				
	5s		5p				3s		3p		
	s		p_x	p_y	p_z		s		p_x	p_y	p_z
162.4 (a)	0.9		0.1	0.2	0.2		2.7(0.14)		9.0(0.09)	8.9(0.07)	5.4(0.07)
163.5 (c)	0.2		0.0	0.3	0.3		3.9(0.11)		11.9(0.14)	12.4(0.12)	7.2(0.10)
164.8 (e)	0.0		0.0	0.0	0.0		3.6(0.07)		**17.7**(0.15)	**17.3**(0.10)	9.5(0.09)
167.5 (f)	3.9		2.0	1.8	1.9		3.1(0.14)		1.1(0.13)	1.2(0.02)	4.5(0.02)
168.8 (g)	3.5		0.3	2.2	2.4		9.8(0.24)		1.9(0.12)	1.9(0.05)	5.2(0.05)
170.4 (h)	3.6		0.9	2.8	3.1		5.0(0.10)		2.3(0.04)	2.3(0.06)	2.8(0.06)
171.8 (i)	1.9		3.8	3.4	3.7		2.6(0.06)		2.1(0.02)	2.1(0.07)	0.9(0.07)
	4d						3d				
	d_{xy}	d_{xz}	d_{yz}	d_{z2}	d_{x2-y2}		d_{xy}	d_{xz}	d_{yz}	d_{z2}	d_{x2-y2}
162.4 (a)	**16.6**	1.6	1.7	**26.0**	**16.5**		0.4(0.03)	2.1(0.04)	2.1(0.04)	0.9(0.09)	0.4(0.08)
163.5 (c)	9.5	**16.1**	**15.6**	2.2	9		2.2(0.01)	2.8(0.14)	2.9(0.14)	0.3(0.11)	2.1(0.12)
164.8 (e)	0	**22**	**22**	0	0		0.7(0.01)	2.6(0.08)	2.7(0.08)	0.4(0.03)	0.7(0.03)
167.5 (f)	1.5	0.2	0.1	1	1.4		3.3(0.37)	**23.7**(0.82)	**23.2**(1.00)	**19.5**(0.11)	3.3(0.09)
168.8 (g)	0.6	0.3	0.3	0.5	0.7		9.5(0.75)	**14.0**(0.65)	12.8(0.58)	**17.8**(0.80)	10.8(0.73)
170.4 (h)	0.7	0.7	0.6	0.7	0.7		**17.3**(0.94)	8.1(0.31)	8.1(0.31)	**18.1**(0.66)	**18.1**(0.76)
171.8 (i)	0.6	0.5	0.5	0.7	0.6		**14.5**(1.17)	10.7(0.61)	11.9(0.66)	**19.1**(0.56)	**15.6**(0.56)

Table A15. Calculated percentages of S 3s, S 3p, S 3d, Mo 5s, Mo 5p, and Mo 4d character in excited states corresponding to specific intense absorption features observed in the S $L_{2,3}$-edge XANES spectrum of 2H-MoS_2. The percentage contribution of the excited S atom (red circle in **Figure V. 2C**) to the total DOS is shown in parentheses.

Energy	Molybdenum						Sulfur				
	5s		5p				3s		3p		
	s		p_x	p_y	p_z		s		p_x	p_y	p_z
161.4 (*p*)	0.7		0.0	0.6	0.2		1.0(0.01)		4.7(0.09)	**30.1**(0.12)	1.2(0.01)
161.3 (*p'*)	0.4		0.0	0.5	0.4		0.7(0.02)		7.4(0.02)	**22.4**(0.21)	4.0(0.02)
161.7 (*p''*)	0.6		0.0	0.7	0.2		0.5(0.01)		7.7(0.04)	**14.2**(5.31)	7.1(2.26)
	4d						3d				
	d_{xy}	d_{xz}	d_{yz}	d_{z2}	d_{x2-y2}		d_{xy}	d_{xz}	d_{yz}	d_{z2}	d_{x2-y2}
161.4 (*p*)	**20.0**	0.0	0.0	**13.1**	**12.4**		--	--	--	--	--
161.3 (*p'*)	**20.7**	0.1	0.2	**25.1**	**16.1**		--	--	--	--	--
161.7 (*p''*)	**22.7**	3.3	1.5	**10.9**	**29.3**		--	--	--	--	--

Table A16. Calculated percentages of S 3s, S 3p, Mo 5s, Mo 5p, and Mo 4d character in excited states corresponding to p, p', and p" absorption features observed in the S $L_{2,3}$-edge XANES spectra of **Figure V. 3**. The percentage contribution of the excited S atom (red circles in **Figure V. 3B-D**) to the total DOS is shown in parentheses.

	Mo^{4+} (eV)		$Mo^{4+<x<6+}$ (eV)		Mo^{6+} (eV)	
	$3d_{5/2}$	$3d_{3/2}$	$3d_{5/2}$	$3d_{3/2}$	$3d_{5/2}$	$3d_{3/2}$
S1	228.9	232.1	229.7	232.9	232.9	236.1
S2	229.1	232.3	230.5	233.7	233.4	236.6
S3	229.0	232.2	229.7	232.9	233.4	236.6
S4	229.0	232.2	229.5	232.7	233.2	236.4
S5	228.8	232.0	230.1	233.3	232.8	236.0
Spin-orbit splitting	3.2		3.2		3.2	
	Se^{2-} (eV)		S^{2-} (eV)		SO_4^{2-} (eV)	
	$3p_{3/2}$	$3p_{1/2}$	$3p_{3/2}$	$3p_{1/2}$	$3p_{3/2}$	$3p_{1/2}$
S1	N.A.	N.A.	161.9	163.1	168.5	169.7
S2	160.8	166.6	162.0	163.2	169.3	170.5
S3	160.9	166.7	162.1	163.3	169.1	170.3
S4	160.9	166.7	162.1	163.3	168.9	170.1
S5	160.9	166.7	N.A.	N.A.	168.5	169.7
Spin-orbit splitting	5.8		1.2		1.2	
	Se^{2-} (eV)					
	$3d_{5/2}$	$3d_{3/2}$				
S1	N.A.	N.A.				
S2	54.9	55.6				
S3	54.7	55.4				
S4	54.8	55.5				
S5	54.5	55.2				
Spin-orbit splitting	0.7					

Table A17. Mo 3d, S 2p, Se 3p, and Se 3d peak positions derived from fitting of XPS spectra measured for samples S1-S5. The spin-orbit splitting is also indicated in each case